Engineering Phthalocyanine-Based Organic Thin-Film Transistors for Cannabinoid Sensing & Chemotyping

By

Zachary John Comeau

Thesis submitted to the University of Ottawa in partial fulfillment of the requirements for the Doctorate of Philosophy in Chemical Engineering

Chemical and Biological Engineering
Faculty of Engineering
University of Ottawa

PhD in Chemical Engineering (2022)

Chemical and Biological Engineering

University of Ottawa

TITILE:	Engineering Phthalocyanine-Based Organic Thin-Film Transistors for Cannabinoid Sensing & Chemotyping
AUTHOR:	Zachary Comeau, BSc. (Biochemistry), BASc. (Chemical Engineering)
SUPERVISORS:	Adam Shuhendler & Benoît Lessard
PAGES:	201

Abstract

The development and implementation of biosensors as an integral and growing part of our modern world has prompted the push for precision health as the next step in medicine. Adapted from aircraft engine monitoring, where an array of sensors is used to build a digital twin to preemptively predict problems, precision health requires an increase in molecular monitoring. Organic thin-film transistors (OTFTs), as sensitive, low-cost, and adaptable devices are well suited to meet this need. Phthalocyanines (Pcs), as an organic semiconducting layer for OTFTs, are easily synthesized and highly tunable small molecules which can be deposited through both solution and physical vapor deposition techniques, enhancing their utility. This work presents Pc-based OTFTs for cannabinoid sensing and chemotyping to meet the quality control needs of a growing Canadian and International cannabis industry, and to broadly demonstrate the sensitivity and selectivity attainable with Pc-based OTFTs incorporating molecular analyte sensors. Spectroelectrochemistry is established as a screening technique for Pc-based OTFT sensors and, in combination with thin-film characterization, is used to propose a mechanism for Pc-cannabinoid interactions and OTFT cannabinoid sensitivity with and without a cannabinoid-sensitive chromophore. Thin-film morphologies and polymorphs, pre- and post-analyte exposure, are demonstrated as key drivers of Pc-based OTFT sensing responses and are further explored through controlled deposition conditions and post deposition annealing techniques. Through material screening and thin-film engineering, part-per-billion cannabinoid sensitivity is achieved with Pc-based OTFTs. This report documents several strategies for sensitizing Pc-based OTFT sensors to organic analytes, and the results herein serve as a basis for continued development of Pc-based OTFT biosensors.

Abstrait

Le développement et la mise en œuvre de biocapteurs en tant que partie intégrante et croissante de notre monde moderne ont incité à faire de la santé de précision la prochaine étape de la médecine. Adaptée de la surveillance des fusées d'avion, où un réseau de capteurs est utilisé pour créer un jumeau numérique afin de prédire les problèmes de manière préventive, la santé de précision nécessite une augmentation de la surveillance moléculaire. Les transistors organiques à couches minces (OTFT), en tant que dispositifs sensibles, peu coûteux et adaptables, sont bien adaptés pour répondre à ce besoin. Les phtalocyanines (Pc), en tant que couche semi-conductrice organique pour les OTFT, sont de petites molécules facilement synthétisées et hautement accordables qui peuvent être déposées à la fois par des techniques de dépôt en solution et en phase vapeur, ce qui améliore leur utilité. Ce travail présente des OTFT basés sur Pc pour la détection des cannabinoïdes afin de répondre aux besoins spécifiques de la détection des cannabinoïdes et, plus largement, de démontrer la sensibilité et la sélectivité réalisables avec les OTFT basés sur Pc. La spectroélectrochimie est établie comme technique de triage pour les capteurs OTFT à base de Pc et, en combinaison avec la caractérisation des couches minces, est utilisée pour proposer un mécanisme de sensibilité aux cannabinoïdes OTFT à base de Pc. La morphologie et les polymorphes des couches minces avant et après l'exposition à l'analyte sont démontrés comme réponses de détection OTFT basées sur Pc et sont explorés plus en détail par des conditions de dépôt contrôlées et des techniques de recuit post-dépôt. Grâce aux sélections des matériaux et à l'ingénierie des couches minces, une sensibilité aux cannabinoïdes d'une partie par milliard est obtenue avec les OTFT basés sur Pc. Ce rapport décrit un certain nombre de stratégies pour sensibiliser les capteurs OTFT à base de PC aux analytes organiques, et les résultats ici servent de base pour le développement continu de biocapteurs OTFT à base de Pc.

Acknowledgments

Without the help and prior work of many people, my projects would not have been possible. I would like to first thank my co-supervisors, Dr. Benoît Lessard & Dr. Adam Shuhendler, for their guidance and encouraging my deep love of research and science. Thank you for your trust, understanding, and patience to let me try new, and sometimes wacky, ideas. It was a pleasure to be exposed to so many interesting projects in the great lab groups that you have grown.

I would also like to thank all of the collaborators and support staff for their knowledge and expertise. Special thanks to Dr. Cory Harris, for providing materials and a welcoming lab space to test my cannabinoid sensors. Thanks to Dr. Glenn Facey and Dr. Peter Pallister who trained and assisted me in the dark arts of NMR and to Franco Ziraldo and Dr. Jeffrey Ovens for helping me try new experiments and keeping so many key pieces of equipment functioning.

I would like to thank all of the members of the Shuhendler and Lessard research groups past and present. Special thanks to Dr. Owen Melville, who's development of our electrical characterization set-up laid the foundation for my own research, but also Nick Calvert and Rosemary Cranston for their friendship and entertaining my PowerPoint design ideas.

Finally, I express my heartfelt gratitude to my family for all their love and support throughout my degree; my parents Marc and Christina Comeau, my sister Lizzy, and my grandparents Mémère, Pépère, and Cookie.

Thank you to my thesis committee for your consideration of this report.

Table of Contents

Table of Figures

Table[2]

List of Key Abbreviations

AlClPc:	Aluminum chloride phthalocyanine
CBD:	Cannabidiol
CuPc:	Copper phthalocyanine
CoPc:	Cobalt phthalocyanine
DNA:	Deoxyribonucleic acid
EGOFET:	Electrolyte gated organic thin film transistor
F_{16}-MPc:	Peripherally fluorinated metal phthalocyanine
H_2Pc:	Metal free phthalocyanine
ISOFET:	Ion-sensitive field effect transistor
$I_{ON/OFF}$:	On/off current
MPc:	Metal phthalocyanine
MOSFET:	Metal oxide semiconductor field effect transistor
MRI:	Magnetic resonance imaging
NMR:	Nuclear magnetic resonance
OSC:	Organic semiconducting layer
OLED:	Organic light emitting diode
OFET:	Organic field effect transistor
OPV:	Organic photovoltaic
OTFT:	Organic thin-film transistor
OTS:	Octyl trichlorosilane
Pc:	Phthalocyanine
PVD:	Physical vapor deposition
SAM:	Self-assembled monolayer
THC:	Tetrahydrocannabinol
V_{GS}:	Gate-source voltage
V_{SD}:	Drain-source voltage
V_T:	Voltage threshold
µ:	Mobility
ZnPc:	Zinc phthalocyanine

Chapter 1. Introduction

Overview and Biosensors

Biosensors, or devices which detect the concentration of a specific biological moiety with a physicochemical detector, are critical to many modern scientific and medical applications. From disease diagnostics to environmental monitoring to food inspection, biosensors are an integral and expanding part of the modern world[1–3]. Enzymatic glucose sensing was one of the first biosensors to see widespread use, such that the enzymatic activity of immobilized glucose oxidase produces hydrogen peroxide which, upon decomposition, measurably alters conductivity[4]. The benefits of rapid glucose monitoring for diabetes management were profound, and more recently, continual glucose monitors, paired with integrated insulin pumps have greatly improved diabetes monitoring and therapy[5]. The overwhelming benefits of continuous disease monitoring have prompted a shift in modern healthcare towards a concept known as precision health[6–9]. Borrowed from the idea of aircraft engine monitoring, where an array of sensors is used to create a digital twin to allow preventative maintenance, precision health seeks to reimagine the clinical paradigm, using molecular monitoring to preventatively diagnose and treat diseases before the onset of acute symptoms. Realizing this goal requires the development of biosensors and their integration into more aspects of our lives.

In its simplest form, a biosensor transduces a biological physicochemical event into an interpretable signal. Optical, piezoelectric, and electrochemical processes can then all be transduced into measurable signals, enabling a wide range of possible biosensor modalities[10–13] (**Figure 1.1**). Organic thin-film transistors (OTFTs) are a promising biosensor platform, due to their facile integration into integrated circuits, mechanical flexibility, and ease of manufacture[2,14,15]. Sensitivity and selectivity are key elements to a biosensor, which can be improved through the use of a bioreceptor or molecular probe. Such receptors and probes include, but are not limited to, antibodies, protein receptors, enzymes, nucleic acids, and small molecules. Probe molecules are then usually immobilized on, or adsorbed to, the sensing surface. This report focuses on the demonstration of phthalocyanine (Pc) -based OTFTs for sensing and differentiating cannabinoids, with solution and thin-film characterization techniques used to interrogate and elucidate the molecular and physical mechanisms that govern Pc-based OTFT sensing responses. My hope is that the information learned and presented here can help inform future Pc-based OTFT biosensing projects.

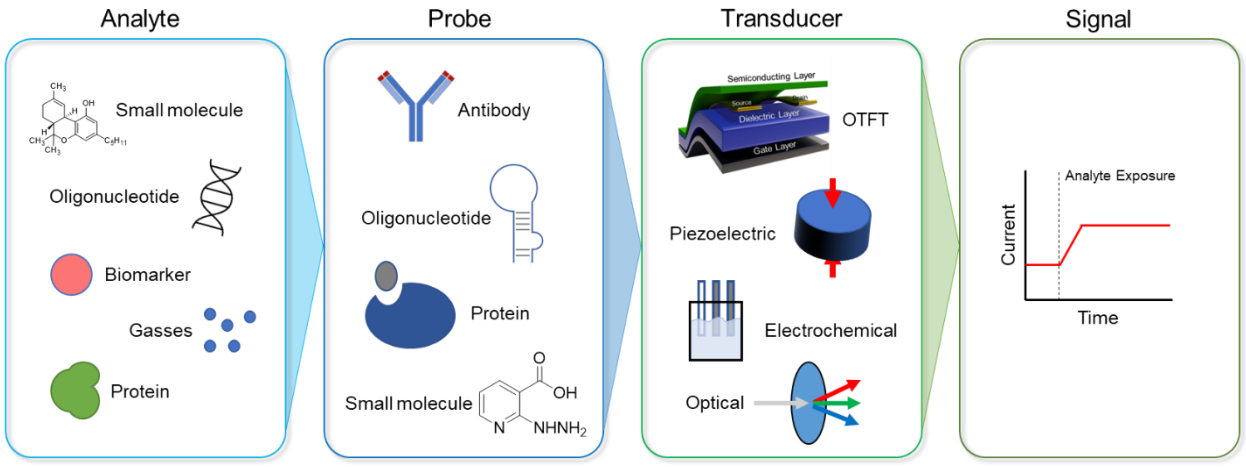

Figure 1.1. *Elements of a biosensor. In typical biosensor operation, analytes are captured by, or interact with, a probe molecule which induces a change in the transducer, generating an interpretable signal. A broad range of analyte, probes, and transducer architectures can be combined, demonstrating the near endless possibilities of biosensor applications.*

Organic Thin-Film Transistors

Organic electronics, or the integration and application of organic molecules and polymers into electronics, is a rapidly expanding branch of materials science with a broad range of applications[16]. Organic electronics are already integrated into the daily lives of people around the world in technologies such as organic light emitting diodes (OLEDs) present in many smartphones and displays, and organic photovoltaic (OPV) energy harvesting. OTFTs are an exciting element of the organic electronics umbrella, bringing the manufacturing, form, and cost advantages of organic molecules over existing traditional silicon-based transistors[17–19]. Enabling flexible, low-cost, and environmentally friendly mass manufacture processes, OTFTs have been demonstrated in a range of architectures for an even broader range of uses, including flexible displays[2,20–22], printable electronics[23–25], and biocompatible health-sensors[11,26,27].

In typical OTFT operation, a bias is applied between a source and gate electrode (V_{GS}), polarizing an insulating dielectric layer, which can, with an additional source-drain electrode bias (V_{SD}), drive charge transport. Measured as source-drain current (I_{SD}), charge transport increases through the semiconducting layer with increased biases, rendering the OTFT in an “on” state[28]. As three-terminal electrical devices, OTFT can have multiple transistor configurations and often be further classified as organic electrochemical transistors (OECTs), electrolyte gated field effect transistors (EGOFETs), or ion-sensitive field effect transistors (ISOFETs)[2]. The device architecture, or relative position and orientation of each terminal and layer can vary, but the fundamental principle, that a relationship between the applied biases and the drain current can be established, remains the same.

With an applied V_{SD}, at low V_{GS} there is a small concentration of mobile charge carriers within the organic semiconductor (OSC) which limits the I_{SD}. This state can be defined as the off current (I_{OFF}). As V_{GS} is increased, a mobile sheet of charge carriers forms at the OSC-dielectric interface with a concentration proportional to the mobile charge density, increasing I_{SD} linearly relative to V_{GS}. At certain bias conditions, the charge density of the channel becomes saturated, limiting further charge injection, and levelling off I_{SD}. As the output in accumulation mode is like that of a metal oxide semiconductor field effect transistor (MOSFET) device, the operational mechanism of OTFTs is often modeled similarly[18,28]. While these models[29,30] are widely used to characterize MOSFETs, they are often not ideally suited to OTFTs, due to non-ideal performance and limited charge injection into the device channel, however, for the purposes of this thesis, they can still provide a reasonable estimation of small-molecule OTFT mobility[31,32]. Leveraging the π-conjugated electron systems of organic molecules, OTFTs can be either electron transporting (n-type), hole transporting (p-type), or both (ambipolar) such that charge transport is heavily dependent on the structure, morphology, and energetics of the OSC layer.[33] Thus, changes to the OSC layer or terminal electrodes can induce large changes in electrical characteristics that can be interpreted as a sensing response, while the self-amplifying nature of semiconductor operation and charge transport additionally makes OTFTs typically highly sensitive[2]. Specificity however is often the limiting factor, though this can be overcome with the inclusion of molecular probes and using multiple OTFT characterization parameters to determine sensor response.

OTFT Characterization and Charge Transport

Transistors, as a fundamental building block of computer circuitry, form the basis of our modern computing age. Composed of a semiconducting material and at least three electrode terminals, transistors function as switches or amplifiers in circuits, facilitating logic gates and complex modern circuitry. MOSFETs are the most commonly employed transistors in operation today, typically using silicon, germanium, gallium arsenide, or a blend of inorganic materials, and report carrier mobilities on the order to 1000, 4000, and even 10,000 cm^2/Vs respectively[34]. As a measure of the speed at which charge carriers can move through a semiconducting material, mobility determines the frequency response, and thus the possible applications of a given material as a thin-film transistor. In comparison, the best organic thin-film transistors have reported mobilities on the order of 50 cm^2/Vs, but most are typically below 1 cm^2/Vs, currently limiting their uses[35]. The process of charge transport between molecules in an OTFT can occur as charge hopping or band bending, but in both cases, whether a charge moves from one molecule to another is dictated by the transfer integral[36]. Described by the degree of orbital overlap, the transfer integral is directly related to the molecular structure and packing of the semiconducting

molecules[37]. This highlights the importance of thin-film morphology and polymorphism to OSC carrier mobility and other charge transport parameters.

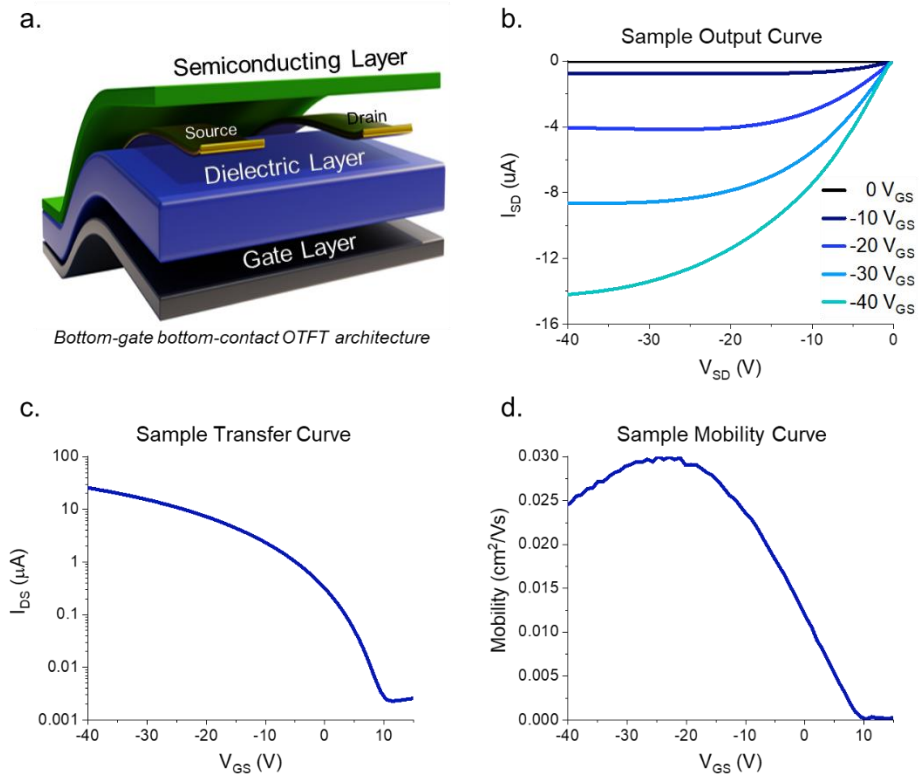

Figure 1.2. *Example of bottom-gate bottom-contact OTFT architecture, output, transfer, and mobility curves. (a) Example bottom-gate bottom-contact OTFT architecture. (b) Sample output curves obtained by maintaining a constant V_{GS} and sweeping V_{SD}. (c) Sample transfer curve obtained with a constant V_{SD} and sweeping V_{GS}. (d) Calculated mobility curve from the sample transfer curve.*

Carrier mobility is not the only relevant parameter however, as other operating conditions, such as voltage threshold (V_T), On/Off current and ratio, hysteresis, subthreshold swing (S), and contact resistance can also determine the operational suitability of a given transistor. Operating conditions can be obtained by generating output curves, where V_{GS} is held constant, and V_{SD} is varied with the flow of charge carriers between the source and drain measured as I_{SD}. These curves enable the characterization of the linear and saturation regimes of charge transport, the identification of operating biases, and can be used to estimate contact resistance[38–40]. Transfer curves can then be obtained by maintaining a constant V_{SD}, sweeping V_{GS}, and measuring I_{SD}. From the transfer data, saturation mobility can be calculated as shown in equation (1):

(1) $$I_{SD} = \frac{\mu C_i W}{2L}(V_{GS} - V_T)^2$$

A function of the rate of change in I_{SD}, saturation mobility is also dependent on fixed channel dimensions (width, W, and length, L), dielectric capacitance (C_i), the gate-source bias (V_{GS})

required to drive charge transport, and the voltage threshold (V_T) at which it occurs. Similar to μ, transconductance (g_m) can also be determined as the derivative of current over voltage. In comparison however, g_m does not incorporate any additional parameters such as device architecture or dielectric capacitance, though as a pure measure of current amplification over potential it is not susceptible to errors that can result nonideal OTFT behavior[31]. Additionally, from the transfer data, the subthreshold swing (S) and defect density (N) can be calculated as further discussed in **Chapter 4**. These parameters can give information about the quality of the charge transport pathways, such that an "ideal" transistor that rapidly enters an "on" state will have a low subthreshold swing, suggesting a low number of defects or charge traps. Hysteresis and on-off currents ($I_{ON/OFF}$), which are similarly dependent on charge transport conditions and trap formation, can additionally be extracted from the transfer data. Charge transport in OTFTs is rarely ideal, with the aforementioned charge transport characteristics heavily dependent on the incidence of charge traps within the film.

Charge Trapping and Dopants

A charge trap is often simply defined as a location which restricts the movement of charge carriers and can result from irregular spacing of the OSC molecules. The irregular OSC spacings are defined as intrinsic traps, and chemical impurities in the film are defined as extrinsic traps. Charge carrier traps can then be termed as shallow or deep, with the latter causing charges to remain fixed within an organic semiconducting film even after the device is turned off[41]. This can induce bias stress effects, which can be observed by temporally evolving shifts in the voltage threshold[42].

Unlike inorganic semiconductors, which form covalently bonded tightly packed crystal structures, organic small molecule semiconductors form van der Waals solids with fully occupied and unoccupied molecular orbitals respectively[36,41]. Thus, isolated organic small molecules, such as those at grain boundaries within semiconducting films are themselves not expected to serve as intrinsic traps due to breaks in the band structure, but instead can lead to intrinsic charge trapping within crystallite domains. Oxygen, water, other atmospheric gases, and material impurities are often sources of deep extrinsic traps within OTFTs and for typical OTFT operation it is sought to minimize these negative effects[36,42,43].

Dopants are then extrinsic additives which, rather than acting as, or inducing traps, instead improve OTFT charge transport[44]. Widely used in inorganic semiconductors, dopants can reduce contact resistance by lowering the barrier for charge injection by band bending. In OTFTs, dopants have also been demonstrated to improve bias stress stability, mobility, and voltage

threshold, however, practical implementation issues prevent widespread use. In OSCs, potential dopants can often present deleterious disruptions to the host lattice, decreasing mobility. The process of OTFT-based sensing, whereby the thin-film is exposed to an analyte is often effectively the controlled introduction of extrinsic traps or dopants to the film. However, rather than a controlled improvement in charge transport parameters, the goal is to maximize the observed responses.

OTFT Sensing

Overview

Through a variety of sensor architectures and molecular probes, OTFT devices have been demonstrated as flexible sensor platforms for an exceptionally broad range of analytes in both liquid and vapor phases[3,20,22]. Many OTFT materials are also innately biorthogonal, facilitating integration or immobilization of organic probes, including but not limited to, enzymes[45], antibodies[46], oligonucleotides[47], or small molecules[48]. The relatively small size of OTFTs can enable arrays of sensors be printed on a single device for "lab-on-a-chip" applications. Low carrier mobility, in comparison to traditional silicon TFTs, is less of an issue for sensor applications as even comparatively longer operating times are still on the order of seconds or minutes. Thus, the cost and fabrication advantages afforded OTFTs over metal TFTs positions them well for single-use or disposable devices to deliver on-the-spot sensor readings.

While any element of the OTFT device architecture can be used as a sensing area, provided the resulting electrochemical changes can be used to drive a sensing response, this report will focus on OTFT sensors where the sensing area is the semiconducting channel. In this paradigm, chemical or biological detection with OTFTs occurs when an analyte interacts with the organic semiconductor or the active transport layer, with direct interactions resulting in a change in conductivity that is ultimately transduced as a sensing response. Analytes then generally adsorb and diffuse along grain boundaries, causing either charge trapping or doping-like effects, however, these mechanisms are rarely fully explored and utilized. Incorporating molecular probes can enhance these interactions, increasing sensitivity and selectivity to specific analytes. For practical operations, transduction of analyte interaction events is typically monitored in constant "on" bias conditions such that changes in operating current (ΔI_{SD}) can be measured. In the process, the gate bias (V_{GS}) can be used to modulate the conductivity of the semiconducting layer and the site of analyte-sensor interactions, providing a dynamic sensing window, and amplifying the signal. While more complex to implement than two-electrode chemiresistor architectures, in comparison, gate modulation allows multiparametric charge transport characteristics to be

extracted from a single analyte condition. As many electronic sensors are single use, due to irreversible or destructive sensing mechanism, this allows additional data to be extracted from a single measurement, presenting a further advantage for OTFTs as sensors. Continuous sensors are highly sought after, however, the realities of environmental wear factors and long term OTFT operation has limited their implementations. Nonetheless, high-throughput manufacture, innate sensitivity, and tunable selectivity positions OTFTs well as a platform for molecular sensors.

Vapor Sensing

MOSFETs have been well characterized and demonstrated as gas sensors[49], however, they are often limited in their ability to be miniaturized and necessitate heating of the sensing area[50]. Early characterization of OTFT devices revealed that many organic semiconducting materials are susceptible to ambient environmental conditions and gases[10]. Pentacene, as well as Pc-based OTFTs, have been shown to exhibit large decreases in saturation current when exposed to high relative humidity[51]. Thus, one of the main limitations for OTFT vapor sensing is finding appropriate semiconducting materials that are both suitable for bottom-gate architecture, such that the electrodes are not exposed to the analyte, but are also both sensitive and selective enough for practical implimentations[3,52]. Additionally, due to the kinetic limitations inherent to vapor sensing with a solid phase device, it is often challenging to incorporate molecular probes to increase sensitivity or selectivity. To overcome this challenge, arrays of sensors or “electronic noses” are often implemented for analyzing more complex gas mixtures[52]. Alcohols, amines, and nitriles are popular compounds for this type of analysis[14,53,54], and while their molecular interactions with Pcs have been well simulated, allowing inferences towards the observed changes in OTFT sensor response, the precise sensing mechanisms are often unclear[55]. Similarly, explosives detection, specifically the detection of toluene derivatives, has also shown promise[56]. Surface engineering has also been demonstrated to improve both sensitivity and selectivity, generally such that an increase in grain boundaries increases analyte-semiconductor interactions and thus the sensing response[57]. Additionally, Roberts et al. demonstrated that sensing mechanisms for the same analyte are conserved in both liquid and vapor phases[58]. Vapor phase sensing with OTFTs shows promise for environmental monitoring however, for many biosensing applications, the challenges associated with breath collection (discussed further in **Chapter 6**) and the relative concentration of analytes involved, limits current implementations.

Liquid Sensing

Compared to vapor phase sensing, solution interactions provide a broader range of molecular probes for sensing in liquid environments. However, many inorganic TFT materials

require high processing and operating temperatures which can limit the use and integration of protein and oligonucleotide-based probes. Thus, OTFTs are well-suited for biosensing applications in solution due to their biocompatible processing and ease by which molecular probes can be integrated. Aqueous sensing with TFTs can be a challenge due to incompatibilities between water and the electrode materials. Hydrophobic interlayers and microfluidic systems have been demonstrated as methods to control the flow of water through the semiconducting channel and overcome these challenges. Alternatively, the device architecture can be modified such that the solution contacts, or acts as, the gate or dielectric layer, as demonstrated in EGOFETs, ISOFETs, or extended gate OTFTs. Extended gate architectures can be readily functionalized, typically through silane treatments, which in turn allows click-chemistry of a variety of molecular probes. Enzymes[42], antibodies[43], proteins[44], oligonucleotides[45], and small molecules[22] have all been demonstrated as recognition elements for OTFT biosensors, highlighting the versatility of the platform.

As mentioned, enzymatic glucose sensing is one of the first, and most well characterized examples of biosensing[2], however, a number of other enzyme-based OTFT sensing systems have been developed that use the byproducts of enzyme activity to drive sensing response. In 2012, Buth et al. reported solution gated surface functionalized OFETs where penicillinase activity liberated protons to drive a sensing response[27]. Similarly, in 2013, Khodagholy et al. demonstrated lactate oxidase functionalized ionogels, such that enzyme activity liberated electrons, allowing detection of lactate concentrations to 10 mM[26]. Nickel et al. reported in 2015 urease-functionalized OFETs where enzyme activity drove local changes in pH which was detected in mM ranges[59]. Enzyme-based OFET biosensors for nitrates and histamines have also been demonstrated, leveraging liberated electrons from enzymatic activity to drive the sensing response[45,60]. Thus, enzymes which alters pH or generate electrons as a byproduct of its activity are promising targets to enable sensing of the substrate molecule through OTFT-based sensors.

While enzymes are often highly selective, they are limited in tunability. Antibodies, by comparison, can be generated to target a specific analyte, and fragmented to facilitate a broad range of functionalization chemistry. In 2018, Jang et al., demonstrated an antibody-embedded polymer as a recognition agent for cortisol in an OTFT, achieving detection as low as 1 pg/mL in 1xPBS and 1 ng/mL in artificial sweat[12]. Antibody-paired organic electrochemical transistors (OCETs) have also been demonstrated pg/mL detection limits for prostate specific antigen (PSA)[46]. Recently, Minamiki et al. demonstrated a flexible, micron-thick, OTFT where a self-assembled monolayer (SAM) biotin-streptavidin complex was used to immobilized antibodies to

achieve sensing responses on par with conventional immunoassays[20]. Yu et al. demonstrated a system where a surface-functionalized antibody was used to capture cancer biomarkers which in turn enabled OCET detection and quantification with a secondary, enzyme-functionalized, nanoprobe[61]. In addition to acting as a molecular probe, antibodies are also of interest as molecular biomarkers themselves, particularly for autoimmune diseases[62]. Detection of antibodies is typically accomplished through immobilization of the antigen to a surface, with a fluorophore paired secondary antibody to provide optical transduction, however, this can be limited in sensitivity. Vallee-Belisle et al. reported a technique whereby an antibody binding event induces a conformational change in an electrode-immobilized strand of deoxyribonucleic acid (DNA), alerting operating current[47]. The large-scale conformational change induced by the binding event served to further sensitize the architecture, achieving nM detection, and demonstrating that a combination of electrochemical and physical changes can be used to achieve high sensitivities.

In the same way as antibodies, DNA is also of interest as both a recognition agent as well as a biomarker. Incorporating single-stranded DNA as a recognition element has allowed detection to concentrations as low as 1 uM while peptide bound nucleic acids as a recognition element demonstrated DNA sensitivities as low as 1 nM[3]. Additionally, the use of aptamers as a recognition element for sensing is a popular area of research for OTFT-based biosensors as they can be readily generated and incorporated into a variety of architectures while providing high sensitivity and selectivity. As a recent example, Liang et al. reported fM sensitivity to dopamine with aptamer functionalized OCETs, highlighting the value of the intrinsic signal amplification inherent to OTFTs[63].

Wearables and Implantable OTFT Sensors

While single, use on-the-spot, biosensors can meet some current clinical needs, wearable, or implantable, continual sensors could allow additional insights into disease pathogenesis and increase opportunities for preventative medicine. The now ubiquity of modern smartphones is a prime example of the potential for integration of consumer electronics into the daily lives of individuals. Smartwatches can provide clinical level physical data on key metrics such as heart rate, blood pressure, and activity, but the translation of devices to the consumer market that can provide continual analysis of other biomarkers remains an ongoing challenge. Recently, a variety of epidermal, oral, and implantable biosensors have been demonstrated. Additional discussion, potential integration of established molecular imaging probes, as well as biosensor design considerations can be found in **Chapter 6**.

Phthalocyanine-based OTFTs

Phthalocyanine Thin-Film Manufacture

Pcs are large, macrocyclic organic molecules with two-dimensional geometry and extensively delocalized π-electrons. It is this π-electron delocalization that lends Pcs their brilliant colors and interesting electrical properties, enabling their use in OPVs and OTFTs. Changes to the central metal, its axial substituents, and the Pc's peripheral substituents can be easily performed, enabling material tuning for specific applications. The size of the central atom of the Pc is a determining factor in its molecular geometry and eventual thin film packing structure. As examples, Pcs with a centrally held copper, zinc, or cobalt yield planar configurations, while larger centrally held metals, such as titanium, or aluminum yield cone-like configurations with an axial substituent. Very large metals can still be held by the Pc ring, forming complexes, such as $LuPc_2$ or Eu_2Pc_3, or distorted planar structures. High thermal stability of Pcs allows physical vapor deposition (PVD), and material-tuned solubility enables solution processing. As a result, Pcs are an excellent candidate material for flexible, high-throughput electronics.

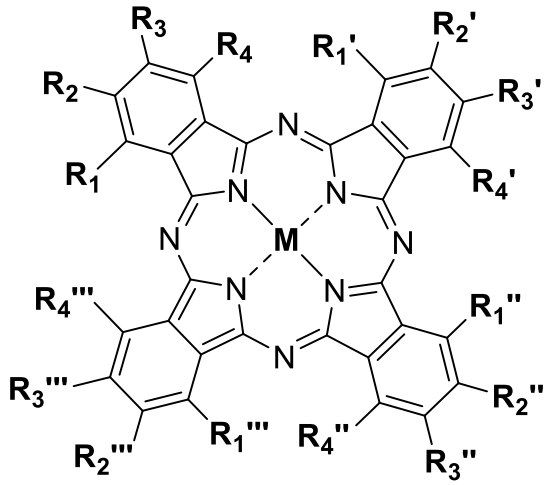

Figure 1.3. *Illustration of the general chemical structure of a phthalocyanine.*

An advantage of Pcs as semiconducting materials is their ability to be manufactured through both solution processing and PVD. An active area of study, solution processing offers the potential of extremely high-throughput device manufacture, though consistency can be an issue[24,64]. PVD, while lower through-put, offers increased consistency and was the method I used throughout my studies to deposit thin-films. Batch-to-batch variations in OTFT performance and thin-film characteristics were monitored and the control measures taken are additionally discussed in **Chapters 2-5**. Generally, for this thesis, at least two separate batches of four or more replicate OTFTs were characterized to ensure batch-to-batch reproducibility, and data was

displayed as either the min-max range (**Chapters 2 and 3**) or with an average and standard deviation (**Chapters 4 and 5**).

Pcs, with their high thermal stability, are particularly well suited to PVD as they readily sublime at moderate temperatures (~400ºC) under vacuum. In a typical PVD process, a source (boat, crucible, etc.) is heated in a chamber held under high vacuum ($<10^{-5}$ torr). At some temperature the material may sublime, forming a plume which travels upwards and collides with the substrates. A quartz crystal microbalance can be placed within line of sight to measure the deposition rate, facilitating rate control through tooling factors. As sublimed molecules collide with the substrate, some deposit as either layers, islands, or a combination of both, depending on the intermolecular forces of the deposited molecules relative to themselves and the surface[64]. Adsorbed atoms, or adatoms, can be mobile on the surface while they retain kinetic energy, able to join other adatoms to form islands[65]. Larger islands afford a greater number of sites with greater degrees of coordination, further promoting their growth. Furthermore, Ostwald ripening describes the process whereby small islands can diffuse across the surface, themselves joining or forming larger islands. In general, where adatoms are more strongly attracted to each other island growth is preferred, while layer growth occurs when adatoms are more strongly attracted to the surface[66]. Combinations of both island and layer growth are possible, with Pcs typically fitting into this latter category, such that one or more initial monolayers are formed, but subsequent 2D growth is unfavorable and instead 3D island growth becomes dominant[64,66].

Substrate temperature can be controlled to yield more favorable deposition kinetics, with higher temperatures generally yielding larger grains, more uniform orientation in metal-phthalocyanine (MPc) thin films and resulting in improved OTFT charge transport characteristics. Similarly, deposition rate can also be used to control film growth, with greater deposition rates resulting in kinetically dominated film growth, typified by amorphous films with low crystallinity and often poor OTFT transfer characteristics (**Figure 1.4**). For the fabrication of MPc thin-films, relatively low deposition rates of 0.1 – 5 A/s are typically used as they result in larger crystallites with more favorable π-π stacking which is typically desired for OTFTs.

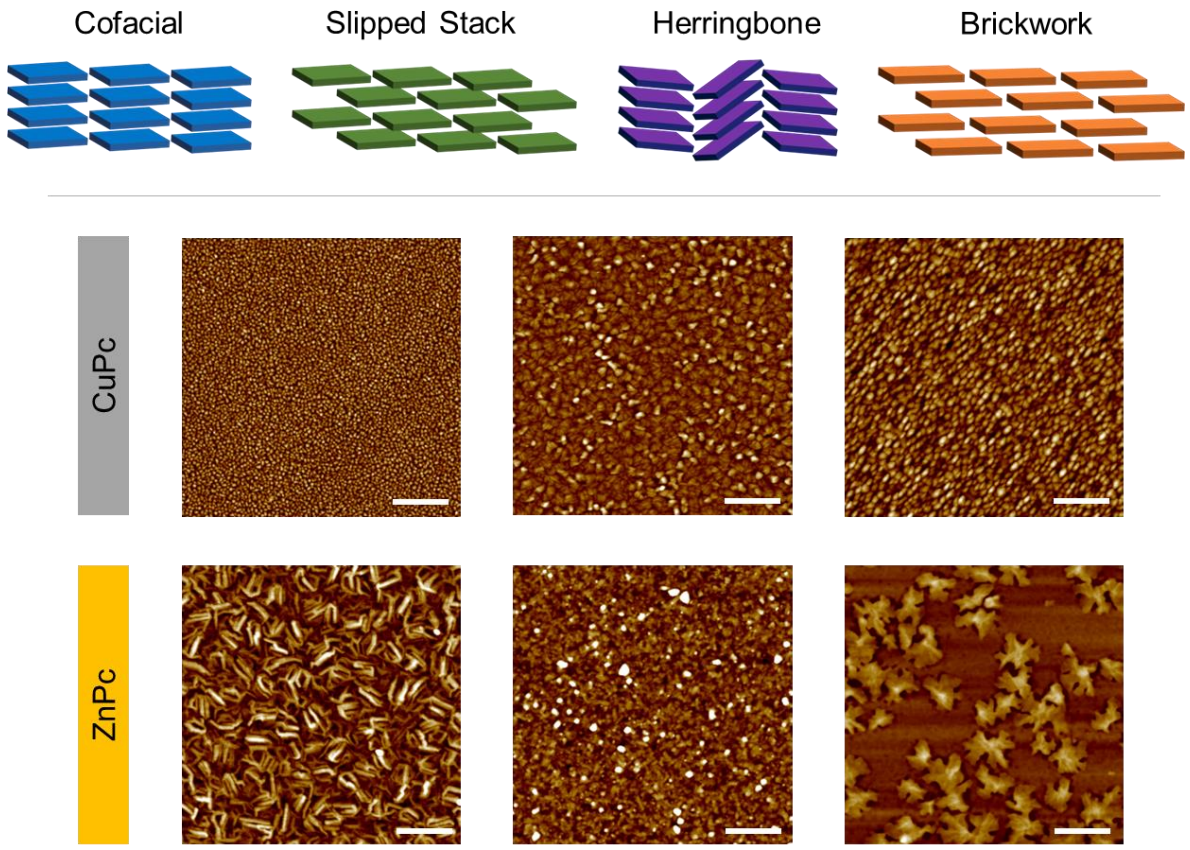

Figure 1.4. *Stacking profiles and AFM images of phthalocyanine thin films. Top: cofacial, slipped stack, herringbone, and brickwork type packing structures. Bottom: AFM images of CuPc and ZnPc thin films on Si/SiO_2 substrates. Varied deposition conditions and post-deposition annealing techniques were used to generate the altered morphologies visible. Scale bars represent 1 nm.*

As the orientation and spacing of the initial deposited monolayers guides future film growth, substrate surface modifications are a popular choice in OTFT manufacture to improve deposition conditions. Reducing surface defects yields more optimal MPc film growth which improves MPc-OTFT performance. On Si/SiO_2 substrates, such as those demonstrated in this thesis, silanes can be easily bonded to the surface through solution or vapor phase reactions, forming SAMs. In both cases, a combination of hydrolysis and condensation reactions can occur, ideally yielding a well-ordered monolayer through horizontal polymerization. A smooth, well-ordered surface can induce favorable Pc thin-film growth in addition to shielding the OSC from electronic coupling with the dielectric and rejecting water. Octyl trichlorosilane (OTS), as a SAM for dielectric surface treatment, has been consistently found to yield excellent OTFT performance when compared to other silanes and is used throughout this thesis[67]. Thus, it is important to highlight that every element of Pc-based OTFT manufacturing conditions has an impact on the final device performance.

Polymorphs and Morphology

Where many inorganic materials can form well understood covalent bonds, and thus well understood packing geometries in thin-films, the packing geometry of Pcs is more variable as anisotropic geometry and van der Waals forces govern the final thin-film morphology and polymorph. Planar, unsubstituted MPcs typically form stacks which arrange in a herringbone packing pattern (**Figure 1.4**), arranging in a variety of polymorphic forms, but generally depositing as either an α or β packing geometry, characterized by their phase angle relative to the surface[68–70] (**Figure 1.5**). Non-planer Pcs, such as AlClPc, form π-stacks enabling a wider array of geometries[71]. It is important to make the distinction between polymorphism and thin-film morphology, which, while closely related, describe different elements of the thin-film microstructure. Polymorphism describes structural features, such as the intermolecular spacing and alignment of Pcs, while morphology describes surface topology and larger packing domains. As a result, two thin films can have the same polymorph but significantly different morphologies (**Figure 1.4**). As an example, unsubstituted Pcs, deposited at room temperature typically generate small, rounded grains while substrate heating yields larger, ribbon-like structures. Both instances can be the same α-phase Pc polymorph, however, the surface morphology can be dramatically different. Non-planar MPcs such as AlClPc or TiOPc, can instead have larger, rectangular plate-like features as a result of their different π-stacked packing structures.

Phase transitions between polymorphs can occur through altered deposition conditions or post-deposition processing and are characterized by a change in tilt angle between adjacent Pc molecules, altering the degree of face-face and edge-edge Pc interactions[68]. In the pigment industry, controlled phase transitions between Pc polymorphs are used to tune color, with blue α-CuPc shifting to a rich purple as β-CuPc (**Figure 1.5**), and near red ε-CuPc[72]. These physical changes between polymorphs, in addition to optical effects, have significant effects on the charge transport properties of Pcs. As an example, β-CuPc, by the nature of increased face-face interactions and reduced intermolecular spacing, though highly crystalline, is a poor semiconductor (μ_H ~10^{-5} cm^2/Vs) in comparison to α-CuPc (μ_H ~10^{-2} cm^2/Vs)[73]. Thus, post-deposition annealing is frequently used in OTFT manufacture to obtain more favorable polymorphs for charge transport but also thin-film morphology.

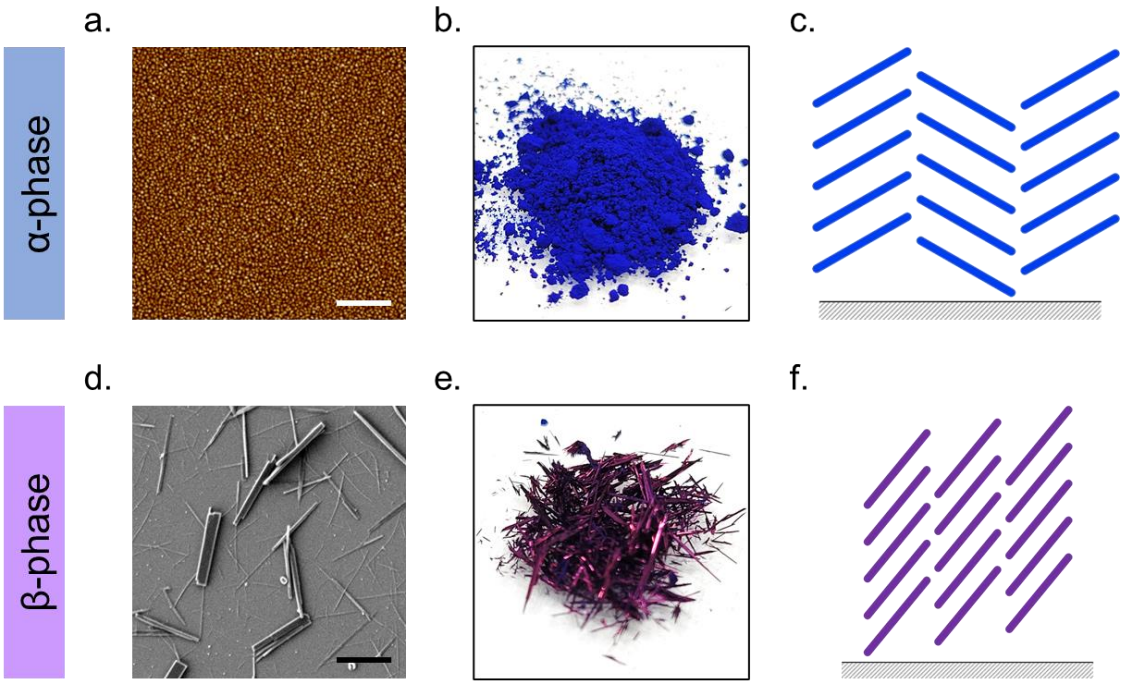

Figure 1.5. *Crystallite images, color, and crystalline structure of alpha and beta phases of copper phthalocyanine. (a) AFM image of α-CuPc, (d) SEM image of β-CuPc, (b, e) images of α and β-CuPc powders, (c, f) schematics of the general packing structure of α- or β-CuPc. White scale bar represents 1 nm, black scale bar represents 3 µm.*

Characterizing Phthalocyanines

Thin-Film Characterization

Given the impacts of thin-film morphology and polymorphism on OTFT performance, thin-film characterization techniques are a key component of OTFT research. For the projects in this thesis a combination of X-ray techniques, allowing for the interrogation of the bulk thin-film polymorphs and morphologies, and imaging techniques, examining the surface of thin-films were used. While both techniques individually have their limitations, the combination of both imaging and X-ray characterization allows a more complete overview of the physical properties of thin films.

X-ray diffraction (XRD) and grazing incident wide angle X-ray scattering (GIWAXS) both function by directing a beam of X-rays at a sample and collecting the diffraction pattern relative to the angle of the X-ray beam. XRD is a rapid technique, where the diffraction data of an individual sample can be collected in <20 minutes. For material characterization, XRD allows powerful, rapid identification of homogenous samples, however for thin-films, XRD is limited to providing crystal d-spacings and a relative diffraction intensity[74,75]. While both d-spacing and signal intensity can

suggest a specific thin-film polymorph and morphology, it is impossible without a complementary technique to precisely assign thin-film characteristics. To this end, GIWAXS, in combination with single crystal XRD, allows the determination of both the degree of thin-film crystallinity, but also the bulk molecular orientation relative to the substrate. A more powerful technique, GIWAXS requires a powerful beamline, limiting its use to a handful of synchrotron beamline facilities.

While X-ray techniques can give significant insight towards the molecular structures within thin films, they are often paired with an imaging technique to provide a visualization of the surface microstructures. Brightfield microscopy is one of the easier ways to visualize thin-films however, limits in optical resolution means only µm-scale features can be visualized. Scanning electron microscopy (SEM), where a beam of electrons is used to determine surface topology, then allows for the visualization of smaller features, but it can be limited in resolution relative to the considerations of thin-film characterization. Atomic force microscopy (AFM) enables the resolution of nm scale features, allowing visualization of nm sized grains commonly found in Pc thin films.

As highly colorful molecules, UV-Vis can be used to characterize both solutions and thin-films of Pcs, with the latter necessitating deposition on a transparent substrate. Pcs lend themselves well to this type of analysis as they typically have three distinct spectral regions, typically defined as the B-band (~300 nm), Q-band (550-750 nm), and M-band (350-450 nm)[76]. It is suggested the B-band, or Soret band, indicates the presence of a *d*-band that is a result of *π*-*d* transitions with lower wavelength B-band peaks at 275-210 nm suggesting *π**-*d* transitions. The Q-band is then responsible for the brilliant blue-green-purples of Pcs and has generally been interpreted as *π*-*π** excitation between bonding and anti-bonding molecular orbitals. For MPcs, this band often displays characteristic splitting, with the high-energy peak assigned to the first π-*π** transition in the Pc macrocycle while the second, smaller, and Davydov split peaks are the second *π*-*π** transition and a result of metal out-of-plane bonding. Molecular substitutions at the metal center, its axes, or the periphery of Pcs will alter these spectral properties, shifting, and in some cases, resulting in new absorbance peaks[77,78]. Coordination, or strong molecular interactions, between a Pc and an analyte will also induce altered spectral properties[79].

Electron paramagnetic resonance, or EPR, is analogous to NMR, in so far that electron spins are excited instead of atomic nuclei. Particularly useful for characterizing metal complexes and organic radicals, EPR uses microwaves and an external magnetic field to expand the energy gap between unpaired electrons, which, as they move between spin-states, generates a measurable signal. In Pcs metal-metal interactions can often cause significant line broadening, however, analysis of H_2Pc, or MPcs chilled to low K temperatures, will demonstrate hyperfine

coupling peaks via isoindole nitrogen interactions[80]. Pcs, particularly CuPc can also often hold long lasting radical species, which can be detected by EPR, and potentially have use in quantum computing[81,82].

Electrochemistry

Electrochemistry is a powerful technique that allows the probing of electron transfer between molecules, relating the flow of electrons to chemical changes[83]. Typically utilizing a three-electrode system, a potential bias is applied in a solution with an electrolyte between the working and counter electrode and monitored with a reference electrode. At specific potential biases, molecular species will be locally oxidized or reduced at the working electrode, changing the measured operating current and thus, electron transfers between electrodes and species within the solution can be monitored. By sweeping through a series of potential biases, cyclic voltammetry measurements can be collected, allowing for the interrogation of redox potentials in solution or a thin film.

With an applied potential, the concentration of unreacted species near the electrode is depleted, a diffusion layer of reacted species builds, and current becomes dictated by diffusion rate, causing current to decrease. This can be visualized as a single peak in a graph of current versus potential. For a reversible redox reaction, where electrons can be transferred reversibly from the electrode to the analyte, a peak will again appear as the scan direction is reversed. Faster scan rates then limit the size of the diffusion layer, increasing the measured current, but at the risk of missing the reverse peak of freely diffusing redox species. By maintaining a constant bias and measuring current over time, chronoamperometry measurements can be performed to study diffusion layer coefficients. Chronopotentiometry, square wave voltammetry, or linear sweep voltammetry can also be carried out by varying galvanostatic parameters, allowing further characterization of redox kinetics and reaction mechanisms.

As electron transfers occur at the electrodes, a supporting electrolyte is necessary to increase solution conductivity to balance charge and complete the circuit. Without a high concentration of supporting electrolyte the solution can become resistive to charge transfer. Additionally, a high relative concentration of support electrolyte limits migration as a means of mass transport through the solution, improving the resolution of electrochemical peaks. Ammonium salts, as demonstrated in this thesis, are a popular choice as they are often highly soluble in most organic solvents, are chemically and electrochemically inert, and can be highly purified.

Electrode material and geometry are also important factors for electrochemical activity. For typical electrochemical characterization, an inert electrode material is desired, with popular choices being gold, platinum, or glassy carbon in a consistent and most often in a smooth geometry to facilitate experimental repeatability. Significant research has been devoted to improving electrochemical catalysis for a variety of industrial applications where material tuning and nano-scale alterations to electrode surfaces can significantly improve the rate of reaction. Similar concepts have been employed for electrochemical sensing, where molecular probes have been functionalized to engineered nano-architectures to achieve impressive sensing responses.

Spectroelectrochemistry and Magnetoelectrochemistry

By combining an electrochemical technique with a spectral characterization technique, spectroeletrochemical measurements can be acquired, where, for some materials, including Pcs, changes in color can be observed with redox processes[84]. By pairing spectral analyses to characterize the physical properties of a film or a solution with the electrical characterization of time-dependent chemical properties, a more complete analysis of electron transfer processes can be achieved. UV-Vis is the most commonly paired spectral technique, but IR, Raman, fluorescence, X-ray, and even NMR visualizations have also been demonstrated. In addition to advances in spectral characterization techniques, advances have also been made towards optically transparent electrodes and spectroelectrochemical cells that can be used with a broader range of equipment. The spectral characteristics of Pcs, specifically the relation of different segments of the Pc molecules to the B, M, and Q bands, lends Pcs well to spectroelectrochemical characterization (**Figure 1.6**). Solubility and defined electrochemical characteristics further facilitate spectroelectrochemical Pc characterization. In **Chapter 3**, analyte induced alterations to these processes are demonstrated to change the resulting spectra, allowing spectroeletrochemistry to be used as a rapid screening technique for Pc-analyte interactions.

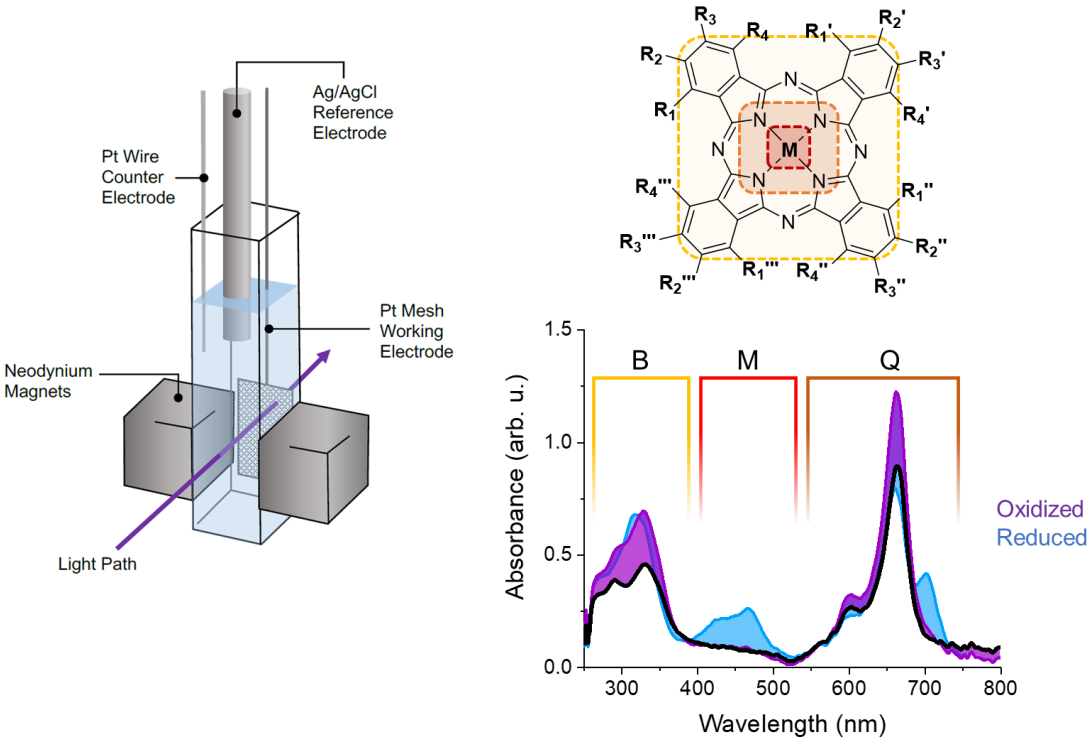

Figure 1.6. *Spectroelectrochemisty and magnetoelectrochemistry set up, general phthalocyanine structure and spectra of CoPc. Electrochemical biases can be applied and controlled by a platinum micromesh working electrode and counter electrode and Ag/AgCl reference electrode. Spectral properties can be monitored by a light beam through the micromesh electrode. A 1T static magnetic field can be applied across the working electrode with neodymium magnets. The absorbance spectra with labelled B, M, and Q bands of CoPc as it is electrochemically oxidized and reduced.*

The paired spectral technique does not solely need to be used for characterization, but rather can be used to drive photopolymerization and other surface reactions. In a similar manner, electrochemical experiments can be carried out in a magnetic field, termed magnetoelectrochemistry, which can be used to alter reaction rates and yield unique electro-deposited structures. Whether a magnetic field is alternating or static in addition to its direction can yield a variety of different, but often concurrent, phenomena. In solution, a magnetic field can induce magnetohydrodynamic effects through the Lorenz force, acting much in the same way as conductive effects, reducing the size of the diffusion layer in electrochemical cells, and increasing the operating current during redox processes. This has been demonstrated to promote hydrolysis reactions as well as facilitate selective deposition of enantiomers. The Kelvin force can similarly induce convective effects on paramagnetic species and is particularly relevant to redox and reaction processes of free radicals. However, the precise mechanisms governing these effects are still not fully explained[85]. Pcs, as well as MRI contrast agents, often incorporate paramagnetic or diamagnetic transition metals and can hold long lasting radical species. Thus, a further

understanding of the effects of magnetic fields on these molecules is a promising and largely unexplored area of interest.

Cannabinoids

Since 2012 there has been a growing international trend of *cannabis* legalization and decriminalization[86]. The plant, *Cannabis sativa*, produces cannabinoids in great abundance, particularly in the inflorescence, of up to 30% by weight. While tetrahydrocannabinol (THC) and cannabidiol (CBD) are the most well-known, thanks to their relative abundance in the plant and their pharmacological effects in humans, over 100 species of cannabinoids are produced[87]. Used both recreationally and medicinally, THC and CBD act on CB1 and CB2 receptors in humans, with the differences in pharmacological effects necessitating accurate speciation and identification through chemotyping techniques[88]. Comparing the molecular structures of THC and CBD, it is only relatively small structural differences at the 6' carbon which confer the different pharmacological effects, in addition to allowing the aromatic rings of CBD to rotate around the 1-1' C-C bond. This free rotation has electronic consequences, altering the distribution of charge through the molecule and the respective redox properties[89], but the overall similarities make THC and CBD difficult to speciate with conventional methods.

A significant direction of cannabinoid research is focused on detection of cannabinoids and their by-products for drug-testing purposes or further understanding of human endocannabinoid systems. To this end, gas chromatography-mass-spectrometry (GC-MS) as well as high performance liquid chromatography (HPLC) are still the preferred techniques, with additional work demonstrated to further sensitize the techniques[87]. Electrochemical systems have also been demonstrated; however, they are often limited in their potential to either quantify or speciate cannabinoids, particularly in complex samples. For rapid detection of cannabinoids, colorimetric probes have been developed, such as fast blue BB (FBBB), however, with high reactivity, often to the phenol group of the cannabinoid, comes a lack of specificity[90]. Colorimetric cannabinoid probes, without pairing a secondary technique, can yield false positives with other cannabinoids or plant material. Currently, speciation and quantification of cannabinoids is often accomplished by HPLC or GC-MS, however, these techniques require expensive equipment and trained technicians which limits their consumer and commercial use. Thus, there is a present and growing need for low cost on-the-spot devices for rapid detection and speciation of cannabinoids.

Scope of the Thesis

This thesis will focus on the fabrication and characterization of Pc OTFTs for cannabinoid sensing within the broader context of Pc-based biosensor development. To this end, the main questions explored were as follows:

1. *Can Pc-OTFTs be useful cannabinoid sensors?*
2. *What are the mechanisms behind Pc-OTFT cannabinoid sensing responses?*
    - *What are the intermolecular interactions?*
    - *Do these interactions have physical implications for solid-state devices?*
3. *Can we use the mechanisms established to make a better cannabinoid sensor?*

In **Chapter 2**, as my first examination of copper phthalocyanines (CuPcs) as OTFTs and cannabinoid sensors, I sought to validate the effects of cannabinoids on OTFTs against a variety of other potentially confounding factors. The highlight of this study was finding consistent responses with varying ratios of cannabinoids and developing standard curves which were able to predict THC/CBD ratios in rapid cannabinoid extractions from *Cannabis* inflorescence. Additionally, I performed a cursory examination of the effects of vaporized cannabinoids against other interfering compounds. While exciting practically, demonstrating the potential utility of these sensors and answering the first question, the results of these experiments did not provide significant insight into the mechanisms by which we were achieving a sensing response.

To further examine cannabinoid-Pc interactions and the mechanisms behind the observed sensing responses, I developed a spectroelectrochemistry set-up and procedure for our laboratory. In **Chapter 3**, I describe the findings of these results, additionally performing NMR experiments which provided corroborative and additional insights into the hypothesized intermolecular interactions between Pcs and cannabinoids. The overarching goal of this study was however to relate solution effects to thin-film sensing effects and in this regard, there were still questions and some unexplained observations made during thin-film characterization, particularly in respect to thin-film morphology post analyte exposure.

Building from the previous spectroelectrochemical work, in **Chapter 4** I focused on furthering my understanding of physical Pc thin-film effects with exposure to analytes. Using XRD to assay crystal morphology and polymorphs and imaging techniques such as AFM and SEM, I examined the semiconducting layer, revealing that the observed sensing effects were a combination of both electrochemical interactions and physical recrystallization effects. EPR experiments further revealed the formation of Pc radical species with exposure to cannabinoids, corroborating observed analyte-induced disruptions to the Pc-crystallites and strong Pc-

cannabinoid electrochemical interactions. Finally, a deeper analysis of the transfer data, particularly in the subthreshold region, demonstrated interesting changes in charge transport characteristics with analyte exposure, highlighting the importance of material selection and thin-film morphology to sensor response. This study presented a satisfactory answer to the questions posed in **Chapters 2** and **3** and prompted further optimization studies, described **in Chapter 5** and **Chapter 7**.

To conclude my cannabinoid sensing studies, using the techniques practiced and information learned from the previous works, I sought to improve cannabinoid sensing performance through material selection, tuned surface morphology, and OSC layer thickness. As described in **Chapter 5**, I was able to further sensitize ZnPc OTFT devices by over 100x in comparison to the devices characterized in **Chapter 2**. Furthermore, I developed a system to explore real-time sensing of vaporized cannabinoids and was able to observe both the hypothesized electrochemical and physical effects that drive the sensing response.

Chapter 6 presents a review of current biosensor implementations and attempts to make the case that incorporating existing biosensor architectures with molecular imaging probes is potentially an untapped avenue to new and improved molecular sensors. This fits within the broader concepts of precision health, a powerful idea which necessitates an increased use of sensors and sensor data within the clinical paradigm. In **Chapter 7**, I provide abstracts and context to papers I have contributed to during my PhD in addition to preliminary and ongoing research towards phthalocyanine thin-film engineering and biosensor development.

References

1. Van Dorst, B. *et al.* Recent advances in recognition elements of food and environmental biosensors: A review. *Biosens. Bioelectron.* **26**, 1178–1194 (2010).
2. Elkington, D., Cooling, N., Belcher, W., Dastoor, P. & Zhou, X. Organic Thin-Film Transistor (OTFT)-Based Sensors. *Electronics* **3**, 234–254 (2014).
3. Lin, P., Yan, F., Lin, P. & Yan, F. Organic Thin-Film Transistors for Chemical and Biological Sensing. *Adv. Mater.* **24**, 34–51 (2012).
4. Macaya, D. J. *et al.* Simple glucose sensors with micromolar sensitivity based on organic electrochemical transistors. *Sensors Actuators B Chem.* **123**, 374–378 (2007).
5. Peeks, F. *et al.* A retrospective in-depth analysis of continuous glucose monitoring datasets for patients with hepatic glycogen storage disease: Recommended outcome parameters for glucose management. *J. Inherit. Metab. Dis.* **44**, 1136–1150 (2021).
6. Collins, F. S. & Varmus, H. A New Initiative on Precision Medicine. *N. Engl. J. Med.* **372**, 793–795 (2015).
7. Gambhir, S. S., Ge, T. J., Vermesh, O. & Spitler, R. Toward achieving precision health. *Science Translational Medicine* vol. 10 3612 (2018).
8. Scott, R. T. *et al.* Beyond Low Earth Orbit: Biomonitoring, Artificial Intelligence, and Precision Space Health.
9. Gambhir, S. S., Ge, T. J., Vermesh, O., Spitler, R. & Gold, G. E. Continuous health monitoring: An opportunity for precision health. *Sci. Transl. Med.* **13**, (2021).
10. Sokolov, A. N., Roberts, M. E. & Bao, Z. Fabrication of low-cost electronic biosensors. *Mater. Today* **12**, 12–20 (2009).
11. Bandodkar, A. J. & Wang, J. Non-invasive wearable electrochemical sensors: a review. *Trends Biotechnol.* **32**, 363–371 (2014).
12. Jang, H. J. *et al.* Electronic Cortisol Detection Using an Antibody-Embedded Polymer Coupled to a Field-Effect Transistor. *ACS Appl. Mater. Interfaces* **10**, 16233–16237 (2018).
13. Abdulbari, H. A. & Basheer, E. A. M. Electrochemical Biosensors: Electrode Development, Materials, Design, and Fabrication. *ChemBioEng Rev.* **4**, 92–105 (2017).
14. Torsi, L., Dodabalapur, A., Sabbatini, L. & Zambonin, P. . Multi-parameter gas sensors based on organic thin-film-transistors. *Sensors Actuators B Chem.* **67**, 312–316 (2000).
15. Gelinck, G., Heremans, P., Nomoto, K. & Anthopoulos, T. D. Organic transistors in optical displays and microelectronic applications. *Adv. Mater.* **22**, 3778–3798 (2010).
16. Friederich, P. *et al.* Toward Design of Novel Materials for Organic Electronics. *Adv. Mater.* **31**, 1808256 (2019).
17. Reese, C., Roberts, M., Ling, M. M. & Bao, Z. Organic thin film transistors. *Mater. Today* **7**, 20–27 (2004).
18. Melville, O. A., Lessard, B. H. & Bender, T. P. Phthalocyanine-Based Organic Thin-Film Transistors: A Review of Recent Advances. *ACS Appl. Mater. Interfaces* **7**, 13105–13118 (2015).
19. Sirringhaus, H. 25th Anniversary Article: Organic Field-Effect Transistors: The Path Beyond Amorphous Silicon. *Adv. Mater.* **26**, 1319–1335 (2014).
20. Minamiki, T. *et al.* Flexible organic thin-film transistor immunosensor printed on a one-micron-thick film. *Commun. Mater. 2021 21* **2**, 1–8 (2021).
21. Sekine, T., Fukuda, K., Kumaki, D. & Tokito, S. The effect of mechanical strain on contact resistance in flexible

printed organic thin-film transistors. *Flex. Print. Electron.* **1**, 035005 (2016).
22. Schwartz, G. *et al.* Flexible polymer transistors with high pressure sensitivity for application in electronic skin and health monitoring. *Nat. Commun.* **4**, 1859 (2013).
23. Kim, S. H. *et al.* High performance ink-jet printed diketopyrrolopyrrole-based copolymer thin-film transistors using a solution-processed aluminium oxide dielectric on a flexible substrate. *J. Mater. Chem. C* **1**, 2408–2411 (2013).
24. Jacob, S. *et al.* High performance printed N and P-type OTFTs enabling digital and analog complementary circuits on flexible plastic substrate. *Solid. State. Electron.* **84**, 167–178 (2013).
25. Shimoda, T. *et al.* Solution-processed silicon films and transistors. *Nature* **440**, 783–786 (2006).
26. Khodagholy, D. *et al.* Organic electrochemical transistor incorporating an ionogel as a solid state electrolyte for lactate sensing. *J. Mater. Chem.* **22**, 4440–4443 (2012).
27. Buth, F., Donner, A., Sachsenhauser, M., Stutzmann, M. & Garrido, J. A. Biofunctional Electrolyte-Gated Organic Field-Effect Transistors. *Adv. Mater.* **24**, 4511–4517 (2012).
28. Zaumseil, J. & Sirringhaus, H. Electron and ambipolar transport in organic field-effect transistors. *Chemical Reviews* vol. 107 1296–1323 (2007).
29. Shockley, W. A unipolar “field-effect” transistor*. *Proc. IRE* **40**, 1365–1376 (1952).
30. Shichman, H. & Hodges, D. A. Modeling and Simulation of Insulated-Gate Field-Effect Transistor Switching Circuits. *IEEE J. Solid-State Circuits* **3**, 285–289 (1968).
31. Dallaire, N. J., Brixi, S., Claus, M., Blawid, S. & Lessard, B. H. Benchmarking contact quality in N-type organic thin film transistors through an improved virtual-source emission-diffusion model. *Appl. Phys. Rev.* **9**, 011418 (2022).
32. Paterson, A. F. *et al.* Recent Progress in High-Mobility Organic Transistors: A Reality Check. *Adv. Mater.* **30**, 1801079 (2018).
33. Li, H., Li, Y., Li, H. & Brédas, J. L. Organic Field-Effect Transistors: A 3D Kinetic Monte Carlo Simulation of the Current Characteristics in Micrometer-Sized Devices. *Adv. Funct. Mater.* **27**, 1605715 (2017).
34. Choi, J. Y. & Lee, S. Y. Comprehensive review on the development of high mobility in oxide thin film transistors. *J. Korean Phys. Soc. 2017 719* **71**, 516–527 (2017).
35. Paterson, A. F. *et al.* Recent Progress in High-Mobility Organic Transistors: A Reality Check. *Adv. Mater.* **30**, 1801079 (2018).
36. Troisi, A. & Orlandi, G. Dynamics of the intermolecular transfer integral in crystalline organic semiconductors. *J. Phys. Chem. A* **110**, 4065–4070 (2006).
37. Marinov, O., Deen, M. J., Jiménez-Tejada, J. A. & Chen, C. H. Variable-range hopping charge transport in organic thin-film transistors. *Phys. Rep.* **844**, 1–105 (2020).
38. Horowitz, G. Interfaces in Organic Field-Effect Transistors. *Adv Polym Sci* **223**, 113–153 (2009).
39. Nautiyal, S., Nautiyal, P., Negi, S. & Mittal, P. Contact resistance-dependent OTFT behaviour: Effect of channel length. *Adv. Intell. Syst. Comput.* **624**, 107–113 (2018).
40. Liu, C., Xu, Y. & Noh, Y. Y. Contact engineering in organic field-effect transistors. *Mater. Today* **18**, 79–96 (2015).
41. Kaake, L. G., Barbara, P. F. & Zhu, X. Y. Intrinsic charge trapping in organic and polymeric semiconductors: A physical chemistry perspective. *J. Phys. Chem. Lett.* **1**, 628–635 (2010).
42. Sirringhaus, H. Reliability of Organic

Field-Effect Transistors. *Adv. Mater.* **21**, 3859–3873 (2009).
43. Koch, N. Organic Electronic Devices and Their Functional Interfaces. *ChemPhysChem* **8**, 1438–1455 (2007).
44. Lüssem, B. *et al.* Doped Organic Transistors. *Chem. Rev.* **116**, 13714–13751 (2016).
45. Minami, T., Sato, T., Minamiki, T. & Tokito, S. An Extended-gate Type Organic FET Based Biosensor for Detecting Biogenic Amines in Aqueous Solution. *Anal. Sci.* **31**, 721–724 (2015).
46. Kim, D. J. *et al.* Organic electrochemical transistor based immunosensor for prostate specific antigen (PSA) detection using gold nanoparticles for signal amplification. *Biosens. Bioelectron.* **25**, 2477–2482 (2010).
47. Vallée-Bélisle, A., Ricci, F., Uzawa, T., Xia, F. & Plaxco, K. W. Bioelectrochemical switches for the quantitative detection of antibodies directly in whole blood. *J. Am. Chem. Soc.* **134**, 15197–15200 (2012).
48. Comeau, Z. J. *et al.* On-the-Spot Detection and Speciation of Cannabinoids Using Organic Thin-Film Transistors. *ACS Sensors* **4**, 2706–2715 (2019).
49. Arshak, K., Moore, E., Lyons, G. M., Harris, J. & Clifford, S. A review of gas sensors employed in electronic nose applications. *Sens. Rev.* **24**, 181–198 (2004).
50. Hong, S. *et al.* FET-type gas sensors: A review. *Sensors Actuators B Chem.* **330**, 129240 (2021).
51. Zhu, Z. T., Mason, J. T., Dieckmann, R. & Malliaras, G. G. Humidity sensors based on pentacene thin-film transistors. *Appl. Phys. Lett.* **81**, 4643 (2002).
52. Roberts, M. E., Sokolov, A. N. & Bao, Z. Material and device considerations for organic thin-film transistor sensors. *J. Mater. Chem.* **19**, 3351–3363 (2009).
53. Klyamer, D., Sukhikh, A., Gromilov, S., Krasnov, P. & Basova, T. Fluorinated metal phthalocyanines: Interplay between fluorination degree, films orientation, and ammonia sensing properties. *Sensors (Switzerland)* **18**, (2018).
54. Polat, M. P. *et al.* Sensing alcohol vapours with novel unsymmetrically substituted metallophthalocyanines. *Dalt. Trans.* **48**, 9194–9204 (2019).
55. Bouvet, M. Phthalocyanine-based field-effect transistors as gas sensors. *Anal. Bioanal. Chem.* **384**, 366–373 (2006).
56. Huang, J. *et al.* Response diversity and dual response mechanism of organic field-effect transistors with dinitrotoluene vapor. *J. Mater. Chem.* **20**, 2644–2650 (2010).
57. Roberts, M. E., Mannsfeld, S. C. B., Tang, M. L. & Bao, Z. Influence of molecular structure and film properties on the water-stability and sensor characteristics of organic transistors. *Chem. Mater.* **20**, 7332–7338 (2008).
58. Roberts, M. E. *et al.* Water-stable organic transistors and their application in chemical and biological sensors. *Proc. Natl. Acad. Sci. U. S. A.* **105**, 12134–12139 (2008).
59. Werkmeister, F. X., Koide, T. & Nickel, B. A. Ammonia sensing for enzymatic urea detection using organic field effect transistors and a semipermeable membrane. *J. Mater. Chem. B* **4**, 162–168 (2015).
60. Minami, T. *et al.* Selective nitrate detection by an enzymatic sensor based on an extended-gate type organic field-effect transistor. *Biosens. Bioelectron.* **81**, 87–91 (2016).
61. Fu, Y. *et al.* Highly Sensitive Detection of Protein Biomarkers with Organic Electrochemical Transistors. *Adv. Mater.* **29**, 1703787 (2017).
62. Pollak, T. A. *et al.* Antibodies in the Diagnosis, Prognosis, and Prediction of Psychotic Disorders. *Schizophr.*

Bull. **45**, 233 (2019).
63. Liang, Y., Guo, T., Zhou, L., Offenhäusser, A. & Mayer, D. Label-Free Split Aptamer Sensor for Femtomolar Detection of Dopamine by Means of Flexible Organic Electrochemical Transistors. *Materials (Basel).* **13**, (2020).
64. Cranston, R. R., It, B. & Lessard, H. Metal phthalocyanines: thin-film formation, microstructure, and physical properties. (2021) doi:10.1039/d1ra03853b.
65. Antczak, G., Kamiński, W., Sabik, A., Zaum, C. & Morgenstern, K. Complex Surface Diffusion Mechanisms of Cobalt Phthalocyanine Molecules on Ag(100). *J. Am. Chem. Soc.* **137**, 14920–14929 (2015).
66. Vetter, T., Iggland, M., Ochsenbein, D. R., Hänseler, F. S. & Mazzotti, M. Modeling nucleation, growth, and ostwald ripening in crystallization processes: A comparison between population balance and kinetic rate equation. *Cryst. Growth Des.* **13**, 4890–4905 (2013).
67. Melville, O. A., Rice, N. A., Therrien, I. & Lessard, B. H. Organic thin-film transistors incorporating a commercial pigment (Hostasol Red GG) as a low-cost semiconductor. *Dye. Pigment.* **149**, 449–455 (2018).
68. Xu, J. *et al.* Effect of solvent-vapour annealing on morphology, structure of copper(II) phthalocyanine thin films and device performance. *Bull. Mater. Sci.* **41**, 1–7 (2018).
69. Hoshino, A., Takenaka, Y. & Miyaji, H. Redetermination of the crystal structure of α-copper phthalocyanine grown on KCl. *Acta Crystallogr. Sect. B Struct. Sci.* **59**, 393–403 (2003).
70. Gonzalez Arellano, D. L. *et al.* Phase Transition of Graphene-Templated Vertical Zinc Phthalocyanine Nanopillars. *J. Am. Chem. Soc.* **140**, 8185–8191 (2018).
71. Lessard, B. H. *et al.* From chloro to fluoro, expanding the role of aluminum phthalocyanine in organic photovoltaic devices. *J. Mater. Chem. A* **3**, 5047–5053 (2015).
72. Fryer, J. R., McKay, R. B., Mather, R. R. & Sing, K. S. W. The technological importance of the crystallographic and surface properties of copper phthalocyanine pigments. *J. Chem. Technol. Biotechnol.* **31**, 371–387 (1981).
73. McAfee, T. *et al.* Morphological, Optical, and Electronic Consequences of Coexisting Crystal Orientations in β-Copper Phthalocyanine Thin Films. *J. Phys. Chem. C* **120**, 18616–18621 (2016).
74. Bunaciu, A. A., Udriştioiu, E. gabriela & Aboul-Enein, H. Y. X-Ray Diffraction: Instrumentation and Applications. *http://dx.doi.org/10.1080/10408347.2014.949616* **45**, 289–299 (2015).
75. Kobayashi, N. & Fukuda, T. Recent progress in phthalocyanine chemistry: Synthesis and characterization. *Funct. Dye.* 1–45 (2006) doi:10.1016/B978-044452176-7/50002-4.
76. Denes, G. Phthalocyanines: Properties and Applications, Volume 4 Edited by C. C. Leznoff and A. B. P. Lever (York University, Canada). VCH: New York, 1996. vi + 524 pp. $150.00. ISBN 1-56081-916-2. *J. Am. Chem. Soc.* **120**, 241–242 (1998).
77. Mack, J. & Stillman, M. J. Transition Assignments in the Ultraviolet−Visible Absorption and Magnetic Circular Dichroism Spectra of Phthalocyanines. *Inorg. Chem.* **40**, 812–814 (2001).
78. Tu Gba Saka, E. *et al.* Electrochemical and spectroelectrochemical properties of new metal free, nickel(II), lead(II) and zinc(II) phthalocyanines. (2016) doi:10.1016/j.synthmet.2016.04.004.
79. Yanagisawa, S. *et al.* Intermolecular Interaction as the Origin of Red Shifts in Absorption Spectra of Zinc-Phthalocyanine from First-Principles.

J. Phys. Chem. A **117**, 11246–11253 (2013).
80. Warner, M. *et al.* Spin-based diagnostic of nanostructure in copper phthalocyanine-C 60 solar cell blends. *ACS Nano* **6**, 10808–10815 (2012).
81. Warner, M. *et al.* Potential for spin-based information processing in a thin-film molecular semiconductor. *Nat. 2013 5037477* **503**, 504–508 (2013).
82. Claessens, C. G., Hahn, U. & Torres, T. Phthalocyanines: From outstanding electronic properties to emerging applications. *Chem. Rec.* **8**, 75–97 (2008).
83. Demir, E., Silah, H. & Uslu, B. Phthalocyanine Modified Electrodes in Electrochemical Analysis. *https://doi.org/10.1080/10408347.2020.1806702* **52**, 425–461 (2020).
84. Gouterman, M., Wagni~re', G. H. & Sxyder, L. C. *Spectra of Porphyrins Part II. Four Orbital Model*. *JOURNAL OF MOLECULAR SPECTROSCOPY* vol. 11 (1963).
85. Monzon, L. M. A. & Coey, J. M. D. Magnetic fields in electrochemistry: The Kelvin force. A mini-review. *Electrochem. commun.* **42**, 42–45 (2014).
86. Russo, E. B. History of Cannabis and Its Preparations in Saga, Science, and Sobriquet. *Chem. Biodivers.* **4**, 1614–1648 (2007).
87. Leghissa, A., Hildenbrand, Z. L. & Schug, K. A. A review of methods for the chemical characterization of cannabis natural products. *Journal of Separation Science* vol. 41 398–415 (2018).
88. Gowran, A., Noonan, J. & Campbell, V. A. The Multiplicity of Action of Cannabinoids: Implications for Treating Neurodegeneration. *CNS Neurosci. Ther.* **17**, 637–644 (2011).
89. Kumer, A., Sarkar, N., Paul, S. & Zannat, A. The Theoretical Prediction of Thermophysical properties, HOMO, LUMO, QSAR and Biological Indics of Cannabinoids (CBD) and Tetrahhdrocannabinol (THC) by Computational Chemistry. *Bangladesh Adv. J. Chem. A* **2**, 190–202 (2019).
90. dos Santos, N. A. *et al.* Evaluating the selectivity of colorimetric test (Fast Blue BB salt) for the cannabinoids identification in marijuana street samples by UV–Vis, TLC, ESI(+)FT-ICR MS and ESI(+)MS/MS. *Forensic Chem.* **1**, 13–21 (2016).

Chapter 2. On-The-Spot Detection and Speciation of Cannabinoids Using Organic Thin-Film Transistors

This chapter is taken from: ***Z. J. Comeau****, N. T. Boileau, T. Lee, O. A. Melville, N. A. Rice, Y. Troung, C. S. Harris, B. H. Lessard, A. J. Shuhendler, ACS Sens., 2019, 4, 10, 2706-2715*

Preamble and Context

During the first stage of my graduate studies, I learned my groups' established protocols for fabricating and characterizing CuPc and F_{16}-CuPc OTFTs and, building on previous DNA sensing work, I tested the potential of these devices for sensing cannabinoids. The results were immediate and exciting, with both CuPc and F_{16}-CuPc OTFTs demonstrating large OTFT characterization changes in response to cannabinoids both with and without cannabinoid sensitive chromophores. This work is the result of those initial characterization studies where we performed a broad range of controls to establish that, in a basic environment, the combination of FBBB and a cannabinoid produced large electrical effects in OTFTs, particularly reductions in μ and shifts in V_T. By developing standard μ vs concentration curves I was able to determine THC:CBD ratios within rapidly extracted plant samples with OTFTs on par with HPLC accuracy. Additionally, I performed and reported preliminary vapor experiments, examining the effects of cannabinoids against a range of potential airborne contaminants. This work served as the foundation of my subsequent examinations of cannabinoid sensing with Pc-based OTFTs.

Contribution

I performed the majority of device fabrication and OTFT characterization. NTB performed some device fabrication and characterization. NAR performed AFM measurements. OAM assisted with device characterization and OTFT data interpretation. TL, YT, and I performed cannabinoid characterization. I authored the manuscript and all co-authors provided editorial contributions. This work was supervised by AJS and BHL.

Abstract

Quality control is imperative for Cannabis since the primary cannabinoids, Δ^9-tetrahydrocannabinol (THC) and cannabidiol (CBD), elicit very different pharmacological effects. THC/CBD ratios are currently determined by techniques not readily accessible by consumers or dispensaries and which are impractical for use in the field by law-enforcement agencies. CuPc- and F_{16}-CuPc-based organic thin-film transistors have been combined with a cannabinoid-

sensitive chromophore for the detection and differentiation of THC and CBD. The combined use of these well-characterized and inexpensive p- and n-type materials afforded the determination of the CBD/THC ratio from rapid plant extracts, with results indistinguishable from high-pressure liquid chromatography. Analysis of the prepyrolyzed sample accurately predicted postpyrolysis THC/CBD, which ultimately influences the psychotropic and medicinal effects of the specific plant. The devices were also capable of vapor-phase sensing, producing a unique electrical output for THC and CBD relative to other potentially interfering vaporized organic products. The analysis of complex medicinal plant extracts and vapors, normally reserved for advanced analytical infrastructure, can be achieved with ease, at low cost, and on the spot, using organic thin-film transistors.

Introduction

Since 2012, there has been a growing international trend toward the legalization of Cannabis for recreational and/or medicinal use, in some cases with limitations, restrictions, and government control, in over 40 countries worldwide, with others in the process of legalization[1−4]. While the plant, *Cannabis sativa*, is also used for fiber and seed/oil (hemp), the drug-like properties are generally associated with the inflorescence, which contains a variety of unique cannabinoids[5], often in high concentrations. Cannabinoids are produced by the plant as carboxylic acids that can be decarboxylated into their more pharmacologically active homologs by exposure to heat, light, or prolonged storage[6]. Among over 100 identified cannabinoids[7,8], Δ^9-tetrahydrocannabinol (THC) and cannabidiol (CBD), the decarboxylated forms of Δ^9-tetrahydrocannabinolic acid (THCa) and cannabidiolic acid (CBDa) are the most abundant and, due to their psychoactive and therapeutic effects, the most sought after by consumers (**Figure 2.1a**). The psychogenic effects of THC may be attributed to the engagement of cannabinoid receptor 1 (CB1), making it recreationally useful, but challenging as a therapeutic agent[9]. CBD is nonpsychoactive and has a very low affinity for cannabinoid receptors but provides a variety of clinically validated and experimental indications for therapeutic use[10−13]. Therefore, THC and CBD content labeling of Cannabis and related products is mandatory in Canada as it is in the best interest of consumers, industry, and regulators alike, for reasons of safety and efficacy as well as quality control and law enforcement.

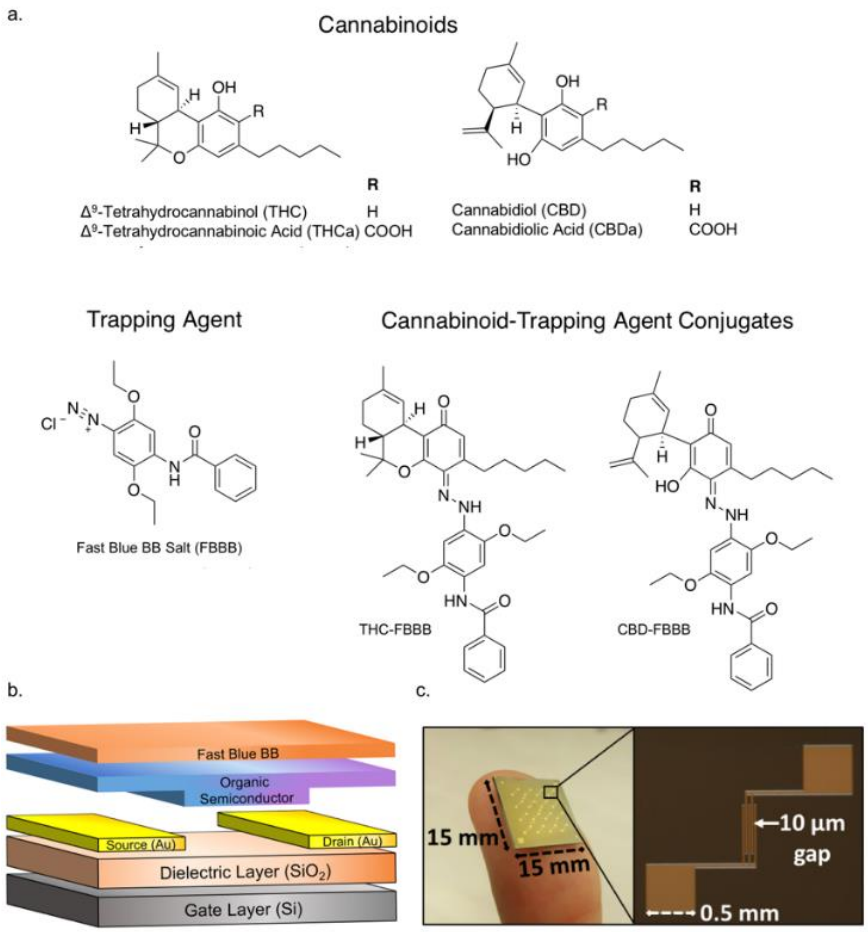

***Figure 2.1**. Molecular structures of primary cannabinoids, trapping agent (FBBB), and cannabinoid-trapping agent conjugates. (b) Electronic device architecture cross section. (c) Image of a Fraunhofer IPMS chip and enlarged brightfield microscopy image of a single bottom-gate bottom-contact (BGBC) device substrate with a 10 µm channel width. (d) Atomic force microscopy (AFM) images of (i) CuPc and (ii) F_{16}-CuPc substrates. Black scale bars represent 500 nm.*

Currently, the most common and accurate methods of measuring cannabinoids employ high-pressure liquid or gas chromatography (HPLC or GC); however, for many companies and most consumers with limited resources and expertise, these instruments are not an accessible option. Fee-for-service cannabinoid testing is increasingly available but expensive and results may be delayed by shipping or backlogs. Law-enforcement officials have similarly struggled with establishing a definitive analytical field method to detect Cannabis and Cannabis impairment[14–17]. Recently, smaller GC and Fourier-transform near-infrared technologies have been developed as alternatives but there is a present and growing need for rapid, on-the-spot, and low-cost differentiation of cannabinoids. Small molecules have been reported for cannabinoid detection, the majority of which are chromogenic in nature. Fast blue BB (4-amino-2,5-diethoxybenzanilide diazotated zinc double salt, or FBBB) has emerged as the most well-characterized molecular

sensor, undergoing covalent modification by cannabinoids under alkaline conditions to afford a rapid colorimetric test to detect THC (**Figures 2.1a and A.2.1**)[18–20], which is still in use by law-enforcement agencies[20]. While the very high limit of detection and rapid rate of reaction of FBBB with cannabinoids is ideally suited as a cursory sampling tool, critically, the method in its optical form is limited by its lack of specificity[21–23]. However, the color change that occurs upon the reaction of FBBB with cannabinoids suggests alterations in band-gap energies between free FBBB and the FBBB–cannabinoid complex, which, we hypothesize, will translate to differential modulation of charge transport with the layering of an alkaline FBBB-based thin film onto organic thin-film transistors (OTFTs).

OTFTs have shown promise as low-cost, disposable, and mechanically robust sensors[24]. They are operated by applying a fixed source-drain voltage (V_{SD}) across an organic semiconductor (OSC) while modulating the current that flows through it (I_{SD}) with bias from an insulated gate electrode (V_{GS}) (**Figure 2.1b,c**). OSC materials can transport either holes (p-type) or electrons (n-type) at a rate quantified by the field-effect mobility, μ_H or μ_E, respectively, which increases sharply when V_{GS} exceeds the threshold voltage (V_T) and continues to vary as a function of V_{GS}[25,26]. Molecular structure, frontier orbital energies, film crystallinity, device engineering, and characterization environment all have been shown to affect OTFT performance, including both μ and V_T[25,27,28]. In addition, changes in these sensitive electrical properties can be measured in response to the introduction of interactive chemical species. To date, OTFTs have been developed for the detection of a variety of medically relevant fluid-based analytes[29–34] and environmental gases[35–37], with selectivity being attained by assembling multiple sensors into an array. However, the application of OTFTs for the detection and/or differentiation of Cannabis components from crude plant extracts or vapor-phase plant samples is unprecedented.

In this study, we demonstrate the rapid sensing of cannabinoids in FBBB-sensitized OTFTs and evaluate the hypothesis that the energy changes of FBBB upon analyte binding are responsible for significant OTFT performance variations that could yield practical analytical capabilities. p-type copper phthalocyanine (CuPc) and n-type copper hexadecafluorophthalocyanine (F_{16}-CuPc) were selected as the OSCs for these devices as they are air-stable, well characterized, and inexpensive materials with different energetics and majority charge carriers that might differentiate their sensing responses to cannabinoid analytes. We examine the effects these primary cannabinoids have on device performance and use these results to develop a method for determining the primary cannabinoid ratio in unprocessed liquid extracts of plant material with accuracy indistinguishable to that obtained by HPLC analysis. We

also apply our devices to sensing vaporized cannabinoids and demonstrate a method for their selective detection. Finally, we investigate the mechanisms for cannabinoid detection in FBBB-integrated OTFT devices by solid-state UV–vis spectroscopy. The current work establishes the potential utility of OTFTs for expeditious, low-cost, on-the-spot quality control assessment for the Cannabis producer and consumer, as well as for law enforcement and border protection services. More broadly, this work demonstrates the utility of integrating chromogenic substrates into OTFTs with the potential to enhance analyte sensitivity, sensor portability, and analytical selectivity.

Results and Discussion

Device Architecture and Detection of Cannabinoids

Bottom-gate bottom-contact (BGBC) OTFTs were fabricated by the physical vapor deposition of 150 Å semiconducting films of either CuPc or F_{16}-CuPc on octyltrichlorosilane (OTS)-treated Si/SiO_2 substrates with prepatterned gold source-drain electrodes (**Figure 2.1b,c**). OTS was used as a pretreatment as it forms a self-assembled monolayer that helps promote consistent surface morphology, improving the overall device performance[26,38]. The deposited semiconductor films were confirmed to be homogenous by atomic force microscopy (AFM) with results consistent with literature values obtained under similar conditions (**Figure 2.1di,ii**)[39,40].

To sensitize the OTFTs to cannabinoid analytes, a thin film of alkaline FBBB (pH 9, NaOH as a base) in acetonitrile (ACN) was drop-cast on top of the semiconductor layer (**Figure 2.1b**). Device performance was analyzed in ambient conditions to reflect those in which Cannabis samples would most likely be tested. Due to small variations in the baseline device performance, the calculated peak baseline mobility (eq 2) of each device was linearly scaled to the overall average. Application of this vertical scaling factor yielded the adjusted mobility that facilitates direct comparison between devices prior to the addition of analytes. After the addition of a thin film of alkaline FBBB (20 μM, FBBB(B)) to these baseline CuPc and F_{16}-CuPc devices, the maximum current observed in their respective output curves does not change substantially (**Figure 2.2ai-ii,bi-ii**). However, the subsequent addition of an analytical standard THC (20 μM, plant extract concentrate, 97% purity) solution directly onto the OTFT surface caused a substantial reduction in the maximum current, roughly 20- and 2-fold for CuPc- and F_{16}-CuPc-based devices, respectively (**Figure 2.2aiii,biii**). In addition to a decrease in the maximum current, the application of analytical standards of either THC or CBD (plant extract concentrate, 99% purity) to the FBBB-sensitized devices resulted in a large negative V_T shift, particularly for F_{16}-CuPc, that can be observed as shifts to the left in their transfer curves (**Figure 2.2c,d**). Overall,

these significant changes in OTFT I_{SD} and V_T are indicative of altered charge transport properties caused by the addition of liquid samples of THC or CBD onto the device surface.

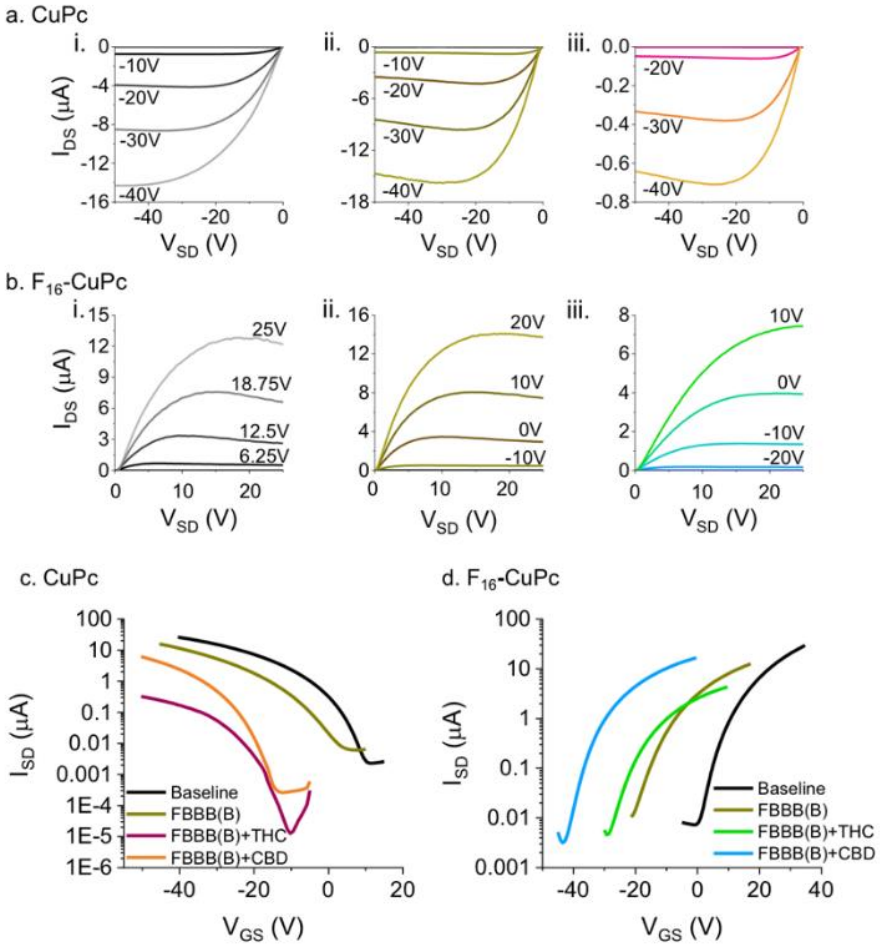

Figure 2.2. *Sample output and transfer curves of OTFT devices. Output curves obtained for characteristic (a) CuPc and (b) F_{16}-CuPc devices for (i) a semiconductor-only device, (ii) following the application of 20 μM FBBB with 50 μM NaOH in ACN (FBBB(B)), and (iii) following FBBB(B) deposition and after exposure to 20 μM THC in ACN. Transfer curves, (c, d), obtained for CuPc and F_{16}-CuPc devices with various treatments (20 μM THC or CBD). Note the differences in the y-axis scales between panels.*

To more thoroughly examine the observed changes in the performance upon cannabinoid addition to FBBB-sensitized devices, CuPc and F_{16}-CuPc OTFTs were characterized after exposure to different combinations of detection components, including ACN, NaOH (base), FBBB, FBBB with NaOH (FBBB(B)), and the cannabinoids themselves (THC and CBD). Repeated applications of ACN showed sequential decreases of 14.2 and 8.5% in μ_H on CuPc-based devices and 15.2 and 2.4% decreases in μ_E on devices comprising F_{16}-CuPc (**Figure A.2.2**). A single addition of NaOH showed a 29.2% decrease in μ_H and an 8.0% decrease in μ_E (**Figure A.2.2**). The addition of FBBB as a thin film overlying the semiconducting layer caused an approximate

46.5% decrease in μ_H on CuPc and a 59.5% decrease in μ_E on F_{16}-CuPc from the baseline, with an observed ±3 V shift in V_T (**Figure A2.3aii,bii**). The addition of alkaline FBBB (pH 9) resulted in a −11 and −15 ΔV_T, with an additional 7.1% drop in μ_H and a 10.1% drop in μ_E from FBBB on CuPc- and F_{16}-CuPc-based OTFTs, respectively (**Figure A2.3ai,bi**). THC alone, THC with NaOH, and THC with FBBB all displayed a combined average 53.0 ± 6.9% decrease in μ_H and 61.1± 2.4% decrease in μ_E from the baseline (**Figure A2.3aiii,biii**). The addition of any impurity typically causes a reduction in mobility; however, only in the presence of a thin film of alkaline FBBB did the subsequent addition of THC induce a significant decrease in both μ_H and μ_E (96.0 and 98.9%, respectively) from that observed with FBBB alone (**Figure A2.3ai,bi**). The addition of CBD (plant extract concentrate, 99% purity) to devices with alkaline FBBB resulted in a ΔV_T of roughly −20 V with an 81% decrease in μ_H and 58.1% decrease in μ_E relative to baseline (**Figure 2.3ai,bi**), distinct changes from those observed for THC.

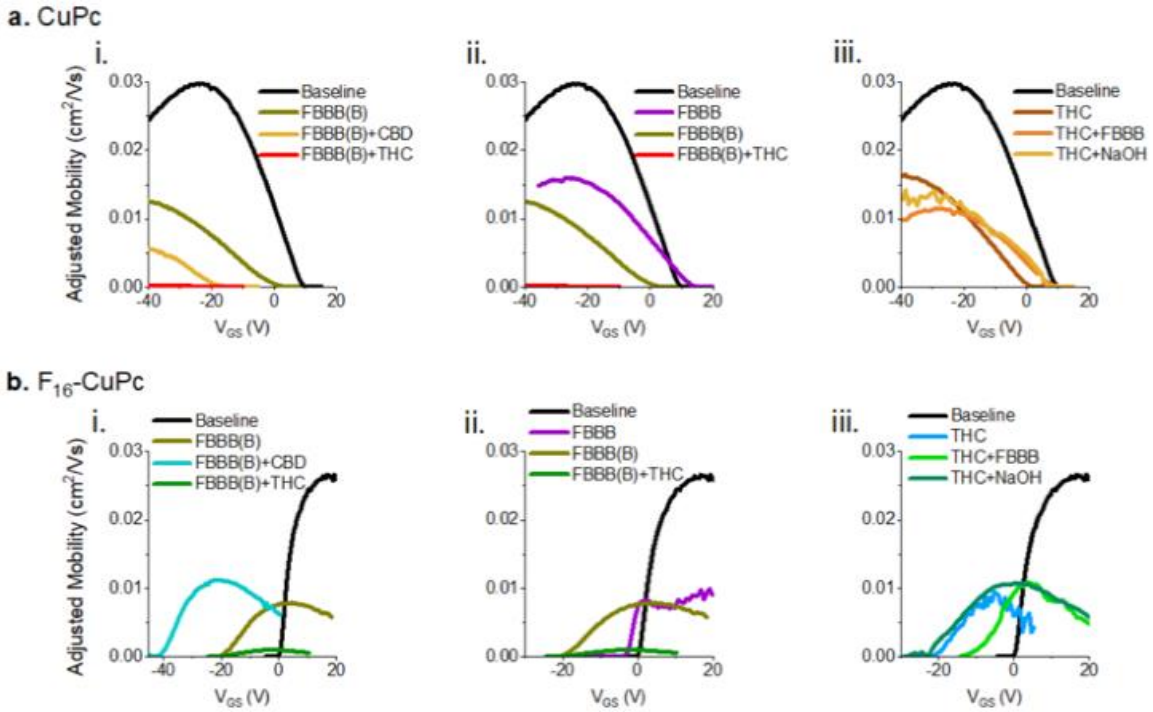

Figure 2.3. *Effect of applied analyte on the field-effect mobility of OTFTs with respect to the applied gate-source voltage (V_{GS}). Field-effect mobility was evaluated for OTFTs consisting of (a) CuPc or (b) F_{16}-CuPC semiconductors prior to further manipulation (baseline), following 20 µM FBBB deposition (FBBB), 20 µM alkaline (pH 9) FBBB deposition (FBBB(B)), deposition of alkaline FBBB and the subsequent addition of 0.5 µL of 20 µM analytical standard solutions of THC or CBD (FBBB(B) + THC, (FBBB)B + CBD), following deposition of THC standards (THC) or alkaline THC standards (THC + NaOH). Data represent the mean (solid line) and data range (i.e., min. to max. values, shaded region) of three V_{GS} sweeps at saturation across eight devices. Mobilities were calculated between adjacent points of the transfer data.*

To provide evidence that the reaction between FBBB and the phenolic center is necessary for cannabinoid sensing by OTFT, device performance after treatment with the model phenols resorcinol and 3-methoxyphenol was assessed (**Figure A.2.3**). As was observed with THC and CBD, a substantial decrease in the adjusted mobility ($\Delta\mu_H$ = −76.8 and −73.9%, $\Delta\mu_E$ = −82.9 and −80.3%) and voltage threshold (CuPc ΔV_T = −5 and 0, F_{16}-CuPC ΔV_T = 0 and 10) were recorded for devices bearing alkaline FBBB when exposed to resorcinol and 3-methoxyphenol, respectively (**Figure A2.3bii,cii**). Device responses (μ and V_T) recorded were easily differentiable from those observed with THC and CBD, likely due, in part, to differences in π-conjugation and hydrophobicity of the phenols. Further support for molecular determinants of analyte detection by alkaline FBBB-bearing OTFTs was obtained by testing the device against cannabigerol (CBG), a biosynthetic intermediate to THC and CBD bearing an alkyl-substituted resorcinol moiety (**Figure A2.3a,bi,ci**). CBG produced a response more closely matching that of resorcinol than THC and CBD, with a decrease of 77.8 and 88.7% in μ_H and μ_E, respectively, and of 5 and 0 V in ΔV_T on CuPc and F_{16}-CuPc, respectively (**Figure A.2.3**). While all of the components of the thin film deposited on the semiconductor have some effect on μ and V_T relative to uncoated devices, alterations in the device performance are amplified by the reaction of the phenol moiety of the analyte with the alkaline FBBB of the device. Furthermore, this reaction facilitates analyte differentiation by specific alterations of performance parameters related to the specific chemical structures of the analyte.

Determination of THC/CBD Ratios from Liquid Samples

From the μ–V_{GS} curves obtained from the transfer data, it was noted that the OTFT readouts were characteristic of the cannabinoid type applied, with THC and CBD yielding differential responses on both CuPc and F_{16}-CuPc (**Figure 2.3ai vs bi**). From this observation, we hypothesized that CuPc and F_{16}-CuPc could be used in parallel as the active materials in OTFT-based sensors for the differential detection of THC and CBD when using a thin film of alkaline FBBB as cannabinoid complexing agent. To test this hypothesis, THC and CBD mixtures comprising of analytical standard plant extract concentrates were prepared in 1:3, 1:1, and 3:1 molar ratios and were applied to the surface of devices coated with alkaline FBBB. For CuPc-based devices, the adjusted mobility varied inversely with higher THC to CBD content, with limited changes in V_T of < 5 V (**Figure 2.4ai**). In contrast, for F_{16}-CuPc-based OTFTs, adjusted mobility varied inversely, and V_T varied directly with increasing THC to CBD content (**Figure 2.4bi**). These electrical differences between THC and CBD outputs could be due to variations in the molecular structure of the FBBB–cannabinoid complexes. The FBBB–THC complex is more planar in character, has increased π electron delocalization, and may better align between grain

boundaries, further limiting charge transfer, while FBBB–CBD may form lower density aggregates[27,41]. Overall, the adjusted mobility maxima for each intermediate ratio (1:3, 1:1, and 3:1) were found to lie between those obtained for pure THC and CBD extract solutions, with the total device output dependent upon the relative cannabinoid content, suggesting that the alkaline FBBB-integrated OTFTs may be capable of rapid cannabinoid speciation.

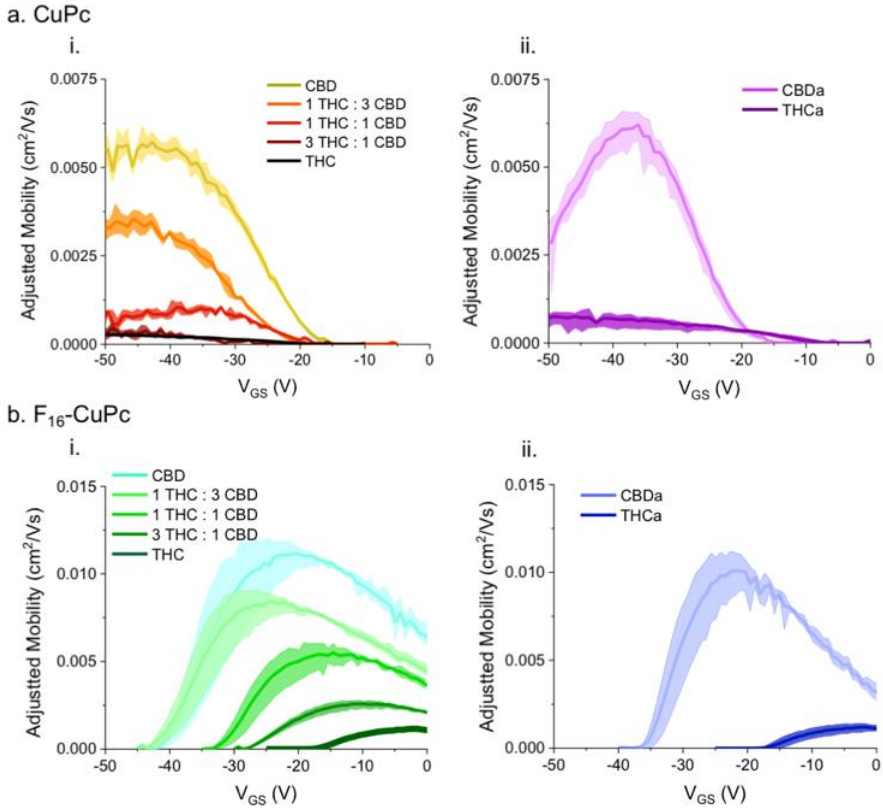

Figure 2.4. *Effect of primary cannabinoid ratios on field-effect mobility of alkaline FBBB-treated OTFTs with respect to gate-source voltage (V_{GS}). Field-effect mobility was evaluated for OTFTs consisting of alkaline FBBB (20 µM)-treated (a) CuPc or (b) F_{16}-CuPc semiconductors following the addition of 0.5 µL of a 20 µM analytical standard in ACN of THC to CBD as a ratio (i), or pure THCa or CBDa (ii). Data represent the mean (solid line) and data range (shaded region) of three V_{GS} sweeps at saturation across eight devices. Mobilities were calculated between adjacent points of the transfer data using eq 2.*

An important consideration for cannabinoid analysis is that cannabinoids from plants are effectively in a “prodrug” form, existing as cannabinolic acids that must be decarboxylated, often by pyrolysis, to their respective cannabinol form to have pharmacological effects. To evaluate the effect of these cannabidiolic acids on the device performance, analytical standard solutions of THCa and CBDa were applied to the OTFTs. The corresponding mobility curves were found to approximate those of pure THC and CBD, respectively (CuPc: THC/THCa $\Delta\mu = -4.5 \times 10^{-4}$ cm^2/(V s), ΔV_T = 6 V, CBD/CBDa $\Delta\mu = -4.0 \times 10^{-5}$ cm^2/(V s), ΔV_T = −1 V; F_{16}-CuPc: THC/THCa $\Delta\mu = -4.9 \times 10^{-5}$ cm^2/(V s), ΔV_T = −2 V, CBD/CBDa $\Delta\mu = 1.0 \times 10^{-3}$ cm^2/(V s), ΔV_T = 7 V) (**Figure**

2.4aii,bii). While pharmacologically distinct from the decarboxylated cannabinoid compounds, our results show that, through extract analysis via OTFT, the cannabinolic acid is undifferentiable from the respective cannabinol form. Since heating (i.e., baking or smoking) induces decarboxylation[6], we hypothesize that the total complement of (THC + THCa)/(CBD + CBDa) in a sample prepyrolysis can be determined by alkaline FBBB-coated OTFTs and furthermore can predict postpyrolysis THC/CBD content.

To test this hypothesis and apply the alkaline FBBB-coated OTFT to the analysis of real-world Cannabis plants, small samples (~3 mg) were harvested from the inflorescence of two different plants, both confirmed by the supplier to contain approximately 20% w/v primary cannabinoids (Hydropothecary). A simple extraction on the naïve Cannabis bud samples was carried out where approximately 3 mg of the plant material in ACN (1 mg/mL) was manually agitated for 2 min, filtered, and diluted 20-fold in ACN prior to addition directly to the device surface (**Figure 2.5a**). The dilution step was necessary to avoid overloading the devices, which were found to have a sensitivity range below 1.5 pg to a maximum of 3.15 ng of cannabinoid (**Figure A.2.4**). Concentrations greater than 3.15 ng of THC resulted in no field effect being observed, and concentrations at 1.58 pg had a minimal effect (<5%) relative to that already observed from the alkaline FBBB treatment. Longer and mechanically agitated extractions of plant material in ACN or 80:20 MeOH/H_2O, a gold standard solvent for extraction of bioactive compounds from plants[42], did not improve the 90–95% extraction efficiency obtained by short manual agitation (**Figure A.2.5**). A portion of the obtained plant extract was heated at 115 °C for 45 min to decarboxylate cannabinolic acids to their cannabinol form[43], while another portion was left unheated. HPLC analysis of these extracts confirmed that 73 and 85 wt% of samples 1 and 2, respectively, were decarboxylated (**Figure 2.5biii, ciii**). Peak identities were confirmed by comparing retention times against those resulting from authentic cannabinoid standard samples (**Figure A.2.6**). Mobility curves were obtained after applying a drop (approximately 0.5 µL) of plant extracts with and without pyrolysis treatment directly onto CuPc and F_{16}-CuPc devices (**Figure 2.5a**), and the ratio of THC to CBD was determined by linear interpolation of the average μ–V_{GS} curve for each Cannabis plant sample extract between the standard curves generated from analytically pure THC/CBD solutions (**Figure 2.5bi-ii,ci-ii**, dashed lines, and Table 1).

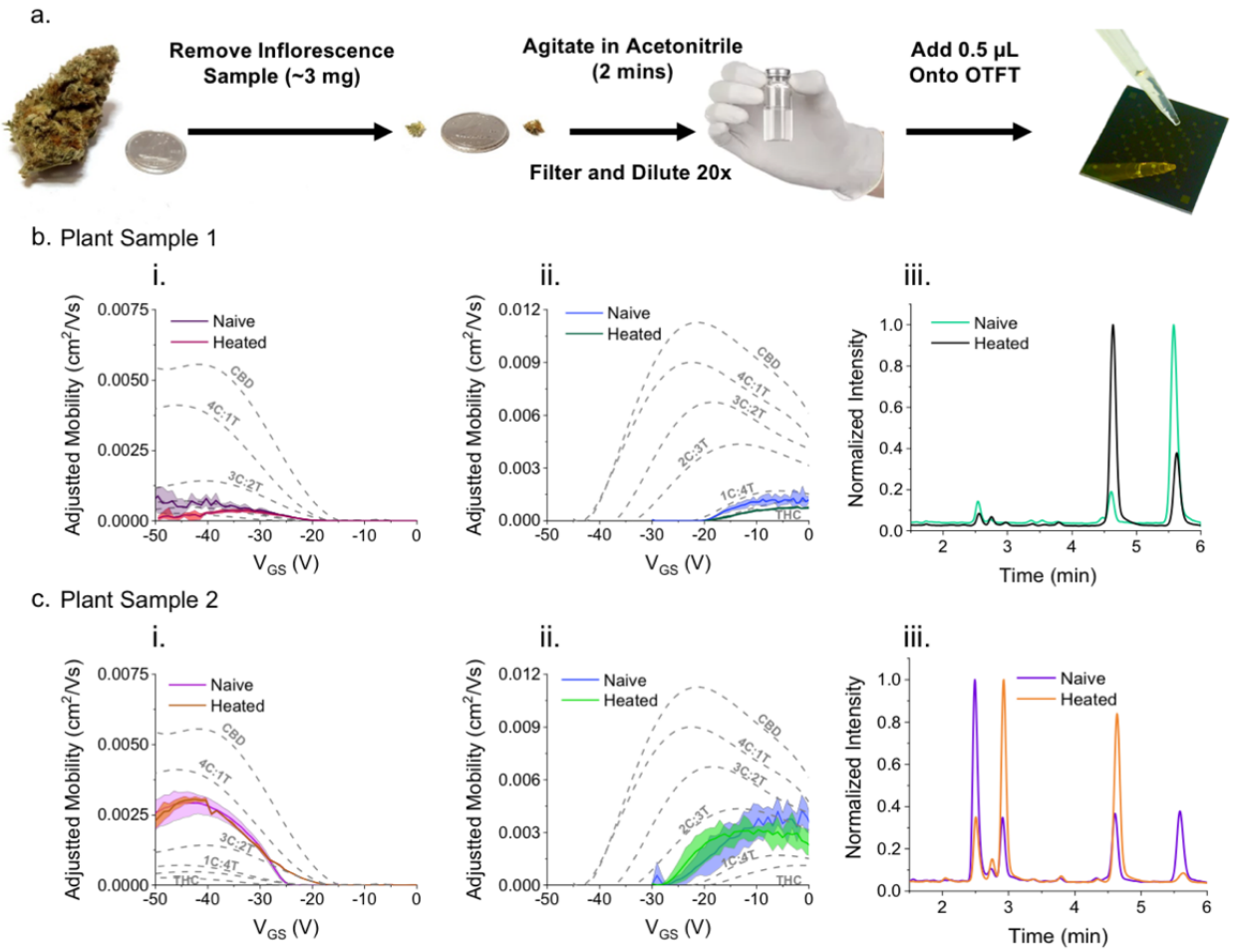

Figure 2.5. *Estimating primary cannabinoid ratios by OTFT mobility from simple plant sample extractions. (a) Extraction workflow. (b, c) Samples of Cannabis inflorescence were ground, and 1 mg/mL was agitated for 2 min in ACN before microfiltration and 20× dilution. Heated samples were baked at 115 °C for 45 min. Filtered extract (0.5 µL) was applied to the surface of alkaline FBBB-treated (bi, ci) CuPc and (bii, cii) F_{16}-CuPc OTFTs and the field-effect mobility was linearly compared (Table 1) to linear fit fifth-order polynomial standard curves obtained from the analytical standard cannabinoid ratios (Figure 2.4a). Data represent the mean (solid line) and data range (shaded region) of three V_{GS} sweeps at saturation across eight devices. (biii, ciii) HPLC-DAD analysis was performed on 2 µL of filtered extract prior to dilution. Samples were eluted at 0.25 mL/min in 50–100% H_2O/ACN with 0.1% FA at 65 °C. Chromatograms were detected at 210 nm and intensity-normalized. HPLC ratios were determined by areas under the curve.*

Table 2.1. Comparison of estimates by OTFT of primary cannabinoid ratios to HPLC-DAD from simple plant sample extractions. Mobilities from -40 to -50 V_{GS} for CuPc and -10 to 0 V_{GS} for F_{16}-CuPc OTFTs were linearly fit to fifth order polynomial standards curves and averaged for each plant sample. Also shown is standard deviation. Ratios for each material were averaged again to give OTFT average. HPLC ratios were determined by direct comparison of peak area.

Measurement Method	**Measured Cannabinoid Ratio (CBD:THC)**	
	Plant Sample 1	Plant Sample 2
CuPc	11:89±4.5	66:34±0.7
F_{16}-CuPc	5:95±0.5	36:64±0.4
OTFT Average	*8:92*	*51:49*
HPLC	3:97	57:43

CuPc-based devices consistently predicted ratios slightly greater than those determined by HPLC for each plant sample, while F_{16}-CuPc-based devices consistently predicted smaller values. The THC/CBD ratio determined by averaging CuPc- and F_{16}-CuPc-based analyses resulted in an error rate of 5.5%, matching the accuracy of ratios determined by HPLC that fall within 3–10% of the real value due to extraction inefficiencies, variations in inflorescence composition, and varying maximal absorbances of the primary cannabinoids assayed[44,45]. These results suggest that CuPc- and F_{16}-CuPc-based OTFTs can be used to identify the ratio of THC to CBD following simple Cannabis plant extractions and that the analysis of preheated samples (i.e., majority cannabinoids in an acid form) predict THC and CBD content postpyrolysis (i.e., in the decarboxylated and medicinally/recreationally efficacious bioactive form).

Detection of Vaporized Cannabinoids

While on-the-spot plant extract analysis is of interest to producers, dispensaries, and consumers, cannabinoid detection from the vapor phase is of special interest to law enforcement seeking objective measures of Cannabis use in prohibited environments (e.g., automobiles). To this end, alkaline FBBB thin-film-bearing OTFT devices were exposed to THC or CBD vapor, as well as a variety of vaporized materials that were previously indicated to interfere with FBBB-mediated cannabinoid detection (coffee grounds or wood smoke)[18], or that might be found alongside Cannabis (cigarette or e-cigarette smoke). Following 1.5 min exposure to equivalent vapor volumes, μ–V_{GS} curves for the CuPc- and F_{16}-CuPc-based OTFTs were obtained (**Figure 2.6a,b**). Exposure to THC vapor (3.125 mg/L) resulted in a substantially reduced μ_H and μ_E on both CuPc- and F_{16}-CuPc-based devices and a $-\Delta V_T$ of 35 V on F_{16}-CuPc (**Figure 2.6**). Devices exposed to CBD vapor (3.125 mg/L) behaved similarly to those exposed to liquid samples, with a decrease in μ_H and μ_E on both CuPc- and F_{16}-CuPc-based devices, with a $-\Delta V_T$ of 18 V on F_{16}-CuPc. This greater $-\Delta V_T$ shift on F_{16}-CuPc-based devices when exposed to THC, compared to

those exposed to CBD, could be due to noncomplexed THC and CBD interacting with the devices, with the former found to cause a deeper $-V_T$ shift on its own (**Figure A.2.7**). In an effort to understand the interactions of the alkaline FBBB-coated OTFT devices with cannabinoids that result in the observed detection and speciation capabilities, solid-state absorbance spectroscopy was performed. Absorbance spectra show decreasing Q-band intensities in CuPc when treated with alkaline FBBB, with a further decrease when subsequently exposed to THC vapor (**Figure A.2.8**). Such Q-band intensity reduction is characteristic of an interruption in π–π* interactions, supporting the observed loss of hole-transport capability of CuPc upon the formation of the FBBB–THC complex[46,47]. For F_{16}-CuPc, only a minimal decrease in the Q-band absorbance is observed, possibly due to the protective nature of the axial fluorines. A slight increase in the Soret band points to electron doping and interactions with the central copper, expected due to the large $-\Delta V_T$ shifts observed[46,47]. Our research group has found that F_{16}-CuPc-based OTFTs are more susceptible to large V_T shifts relative to CuPc-based OTFTs when exposed to an analyte[31]. With a larger observed grain size and smoother surface (**Figure 2.1**), the variations in response of F_{16}-CuPc versus CuPc OTFTs may also be partially explained by morphological differences between the films.

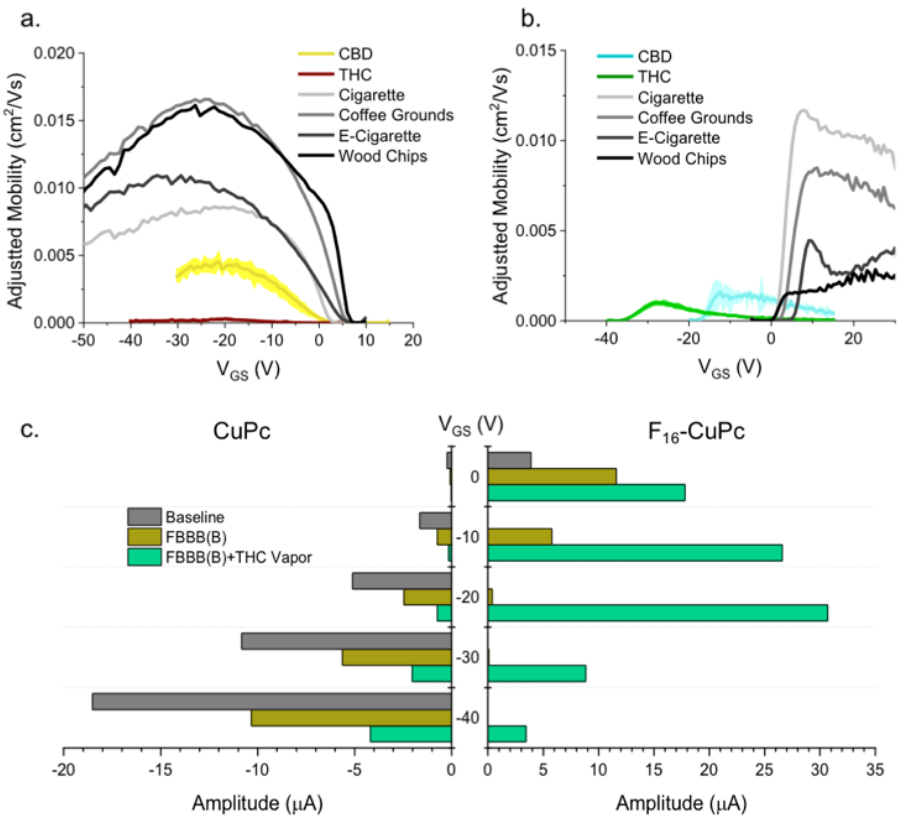

Figure 2.6. *Effects of vapor treatments and single current output on field-effect OTFTs with respect to gate-source voltage (V_{GS}). Field-effect mobility was evaluated for OTFTs consisted of alkaline FBBB (20 μM)-coated (a) CuPc or (b) F_{16}-CuPc semiconductors following exposure to vaporized THC, CBD, cigarette, coffee grounds, e-cigarette solution, or wood chips. The analyte (25 mg) was completely vaporized at 210 °C into an 8 L bag and allowed to flow over the devices for 90 s. Data represent the mean (solid line) and data range (shaded region) of three V_{GS} sweeps at saturation across eight devices. Mobilities were calculated between adjacent points of the transfer data. (c) Gate-source (V_{GS}) and source-drain (−50 V for CuPc (left) and 25 V for F_{16}-CuPc (right)) voltages were held constant and the current was measured over 10 s and averaged. Bars represent the average of 10 readings; minimum and maximum current is <0.017 μA from the average and are not visible on the plot.*

Interfering vapor compounds (e-cigarette smoke, wood smoke, and burnt coffee grounds) were evaluated for their effects on alterations in device performance for both CuPc and F_{16}-CuPc OTFTs. e-Cigarette smoke caused the greatest $+\Delta V_T$ shift, likely due to its high concentration of propylene glycol[48], which contains many electron-trapping hydroxyl groups (**Figure 2.6a**). Wood smoke and burnt coffee grounds, despite being high in phenolic compounds and interacting with alkaline FBBB in liquid[18], may have done so in a limited fashion in the vapor phase, resulting in smaller property changes (**Figure 2.6b**). For CuPc-based devices (μ_H), the mobility reduction caused by the cannabinoids was substantially greater (10- and 2-fold for THC and CBD, respectively) than any of the interfering compounds. Similarly, interfering vapors were readily

differentiable from CBD and THC vapor by their effects on V_T on F_{16}-CuPc-based devices. Only THC and CBD resulted in ΔV_T <0 V, with $V_{T,THC}$ = −35 V and $V_{T,CBD}$ = −23 V (**Figure 2.6b**).

Due to the specific response of both types of OTFT, elicited at V_{GS} < 0 V when exposed to vapor-phase THC compared to other interfering compounds, a simple device implementation scheme for vapor-phase THC detection was tested. Rather than capturing the full range of electrical data in a μ–V_{GS} curve and compared to standards, the signal output (I_{SD}) of the devices was measured before and after the THC vapor exposure at specific electrical inputs (**Figure 2.6c**). CuPc-based devices sensitized with an alkaline FBBB layer showed the highest change in signal when V_{GS} = −20 V, with a 5-fold decrease in the current after THC exposure. On the other hand, F_{16}-CuPc-based alkaline FBBB-coated devices demonstrated a maximum 30-fold increase in I_{SD} at V_{GS} = −20 V after exposure. This turn-on response is generally desirable for sensing as changes that cause increases in the current are harder to cause incidentally and easier to detect[49]. When combined, a CuPc- and F_{16}-CuPc-based device array with V_{GS} = −20 V could detect both changes in the current for a more sensitive or specific detection of THC. Although the applied biases may seem high, fine-tuning the device architecture and dimensions could reduce them to more reasonable levels for practical use. Overall, CuPc- and F_{16}-CuPc-based devices produced an electrical fingerprint that uniquely identified cannabinoids over other interfering compounds in the vapor phase, with the potential to detect and speciate CBD from THC when analyzing both extrinsic semiconductors in an array.

Conclusions

Herein, we present an OTFT-based sensor consisting of two well-known organic semiconducting materials, CuPc and F_{16}-CuPc, coated with an alkaline FBBB-based thin film for the specific detection and speciation of the major cannabinoid components of the Cannabis plant. Detection and speciation were demonstrated for the direct analysis of simple liquid (**Figure 2.5**) and vapor-phase samples (**Figure 2.6**). The overlying thin film of alkaline FBBB on top of the semiconductor layer was found to be necessary to induce a substantial decrease in the charge transport mobility and threshold voltage on both semiconducting materials upon exposure to cannabinoids (**Figures 2.2 and 2.3**). The ratio of decarboxylated cannabinoids in the postpyrolyzed product was accurately predicted following a simple, manual plant extract procedure to within 5.5% of the CBD/THC obtained by HPLC analysis when averaged between CuPc and F_{16}-CuPc. Therefore, the postpyrolysis ratio of pharmacologically active THC and CBD can be predicted through the analysis of prepyrolyzed plant sample extract. Furthermore, the presence of THC vapor was readily detected through simple changes in the OTFT output current,

with F_{16}-CuPc devices showing a significant turn-on response when operating in reverse bias. Potentially interfering vapor compounds did not induce comparable changes to electrical properties relative to that of THC or CBD. This could be useful for the specific, rapid detection of vaporized THC in applications such as law enforcement.

The OTFT devices described herein afford on-the-spot cannabinoid analysis that is unprecedented among existing analytical techniques: compact, low cost, simple sample preparation, rapid analysis, and capable of liquid- or vapor-phase detection and speciation of THC and CBD, the main cannabinoids of interest for recreational and medicinal use, respectively. This work initiates the application of OTFT technologies for cannabinoid sensing upon which engineering of device architecture and the synthesis of new cannabinoid-sensitive materials could improve specificity and sensitivity, opening the door to full cannabinoid quantitation. In addition, the integration of the analyte-sensitive chromophores into the OTFT was shown to extend device-based sensing to complex, real-world samples and helps to lay the groundwork for expanding OTFT-based sensing through reactive chromophore integration.

Materials and Methods

All chemicals were used as received unless otherwise specified. Copper phthalocyanine (CuPc, 90%) and copper(II) 1,2,3,4,8,9,10,11,15,16,17,18,22,23,24,25-hexadecafluoro-29H,31H-phthalocyanine (F_{16}-CuPc, >99.9%) were obtained from TCI Chemicals. CuPc was purified twice by train sublimation before use. 4-Amino-2,5-diethoxybenzanilide diazotated zinc double salt (Fast Blue BB, FBBB), (octyl)trichlorosilane (OTS, 97%), resorcinol, and 3-methoxyphenol were obtained from Sigma-Aldrich. All solvents were HPLC grade and purchased from Fisher Scientific. Cannabis plant samples were supplied by Hydropothecary and cannabinoid standards were obtained from Toronto Research Chemicals.

Preparation of Devices

Prepatterned silicon substrates with a thermally grown, 230-nm-thick SiO_2 dielectric, and gold source-drain electrodes (W = 2000 µm, L = 10 µm) were purchased from Fraunhofer IPMS and used to make bottom-gate bottom-contact transistors. Each Fraunhofer contained four devices. Substrates were washed with acetone to remove the protective resist, rinsed with isopropanol, and dried with nitrogen, before oxygen plasma treatment for 15 min. Substrates were then washed with water, rinsed with isopropanol, and dried with nitrogen before being submerged in a solution of 0.1% v/v OTS in toluene for 1 h at 70 °C. The silane-treated substrates were then washed with toluene, rinsed with isopropanol, and dried with nitrogen. The substrates were further dried under vacuum at 70 °C for 1 h. Dried substrates were transferred into an Angstrom EvoVac

thermal evaporator and 150 Å of CuPc or F_{16}-CuPc was deposited at 25 °C and pressure below 2×10^{-6} torr at a rate of 0.3 Å/s by sublimation onto respective substrates. Devices were kept under nitrogen for up to 2 days prior to characterization.

Device Characterization

The source-drain electrodes were contacted with BeCu alloy probe tips, and electrical measurements were taken using a custom electrical probe station, oesProbe A10000-P290 (Element Instrumentation Inc. & Kreus Design Inc.) with a Keithley 2614B to set discrete V_{SD} and V_{GS} values, measuring I_{SD}. From these measurements, the saturation field-effect mobility, threshold voltage, and on/off current ratio were determined. The general expression relating current to field-effect mobility and gate voltage in the saturation region is as follows

$$I_{SD} = \frac{\mu C_i W}{2L}(V_{GS} - V_T)^2 \quad (1)$$

where I_{SD} is the source-drain current, μ is the field-effect mobility, C_i is the capacitance, W is the width of the channel, L is the length of the channel, V_{GS} is the gate-source voltage, and V_T is the threshold voltage. Eq 1 can be rearranged, giving eq 2, such that the mobility and threshold voltage can be calculated directly from the slope and x-intercept of the I_{SD} vs V_{GS} curve

$$\sqrt{I_{SD}} = \sqrt{\frac{\mu C_i W}{2L}}(V_{GS} - V_T) \quad (2)$$

Baseline mobility values were obtained for each device prior to adding analytes and averaged. The maximum baseline value for the individual device was linearly scaled to the average maximum baseline value, and this scaling factor was applied to the resulting analyte mobility curves for that device. Liquid analytes, dissolved in ACN, were pipetted directly onto the source-drain channel and allowed to dry for 3 min before device characterization. Maximum and minimum obtained mobilities are displayed in plots in lieu of standard deviation to better represent reproducibility in the device performance.

Vapor Experiments

Samples were vaporized at 210°C in a Volcano Medic Vaporizer by PharmaSystems in an 8 L bag. The vapor was allowed to cool for 1 min before being flowed over devices in a 500 mL container at an approximate rate of 90 mL/s. Wood chips were fine shavings of eastern white pine, cigarettes were Pall Mall Blue, e-cigarette fluid was Vapor Papi Original, and coffee grounds were President's Choice West Coast Dark Roast.

HPLC Analysis

Cannabinoid standards of CBD, CBDa, THC, and THCa were made to 1 mg/mL in methanol. Ground Cannabis plant material was extracted with 1 mg/mL of either ACN or 80:20 MeOH/H_2O and 1 mL of supernatant was filtered with a 0.22 µm PTFE syringe filter (Chromatographic Specialties Inc.) after 2, 15, 30, or 60 min of agitation in a solvent. Extracts (2 µL) were analyzed using a HPLC system (Agilent 1100 HPLC) with an inline photodiode array detector (series G1315). A polar C18 Phenomenex Luna Omega column (100 × 2.1 mm^2; particle size 1.6 µm; pore size 100 Å) was used for separation. The mobile phase consisted of water + 0.1% formic acid (mobile phase A) and ACN + 0.1% formic acid (mobile phase B). The gradient elution was the following: 0.0–1.0 min 75% B, 2.0–6.0 min 75–85% B, 6.0–7.0 min 85% B, 7.0–15.0 min 75% B, followed by a 5 min column equilibration after each run. The flow rate was set at 0.25 mL/min and the column temperature was maintained at 65 °C. The chromatograms were detected at 210 nm.

Thin-Film Characterization

UV–vis spectra were acquired on a Cary 100 spectrophotometer in a 3500 µL cuvette with a 10 mm path length (Thorlabs). Solutions of FBBB (0.1%) and FBBB (0.1%) with THC (40 µg/mL) and NaOH (0.15 M) were prepared in ACN.

AFM

Tapping mode atomic force microscopy images were obtained using a Bruker Dimension Icon AFM equipped with ScanAsyst-Air tips. Scans were performed at a scan rate of 1 Hz, with multiple locations on each surface investigated. Images were processed using NanoScope Analysis v.1.8.

Statistics

Data were analyzed by a binomial test using Prism (v.8.0.1., GraphPad Inc.).

Supplemental Information

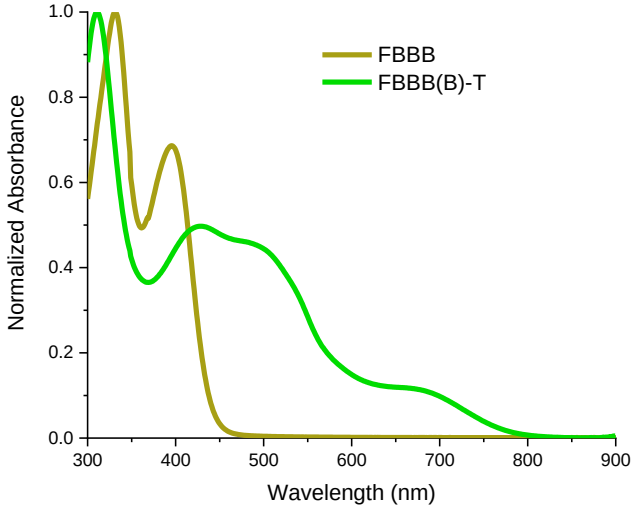

Figure A.2.1. *Normalized absorbance of FBBB and alkaline FBBB conjugated to THC.*

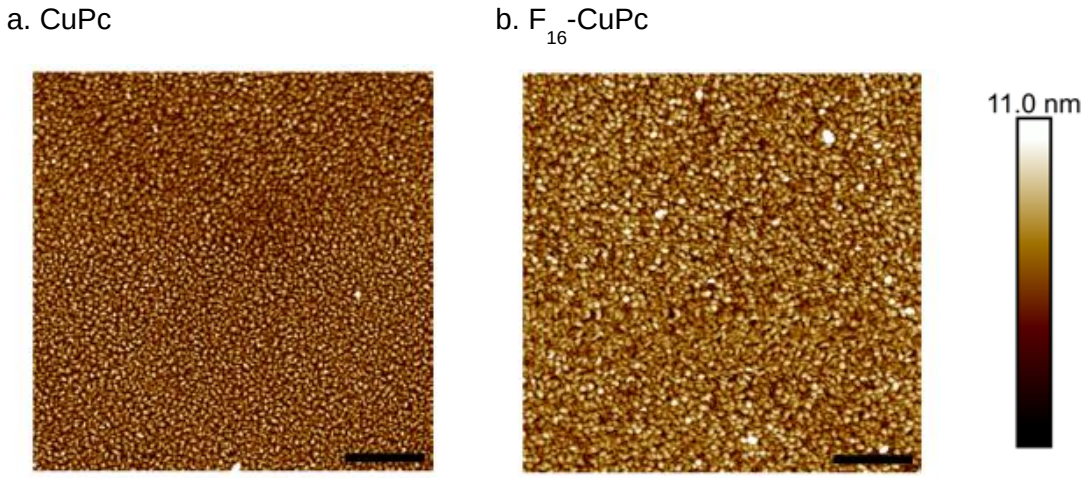

Figure A.2.2. *Atomic force microscopy (AFM) images of (a) CuPc and (b) F_{16}-CuPc substrates. Black scale bars represent 500 nm.*

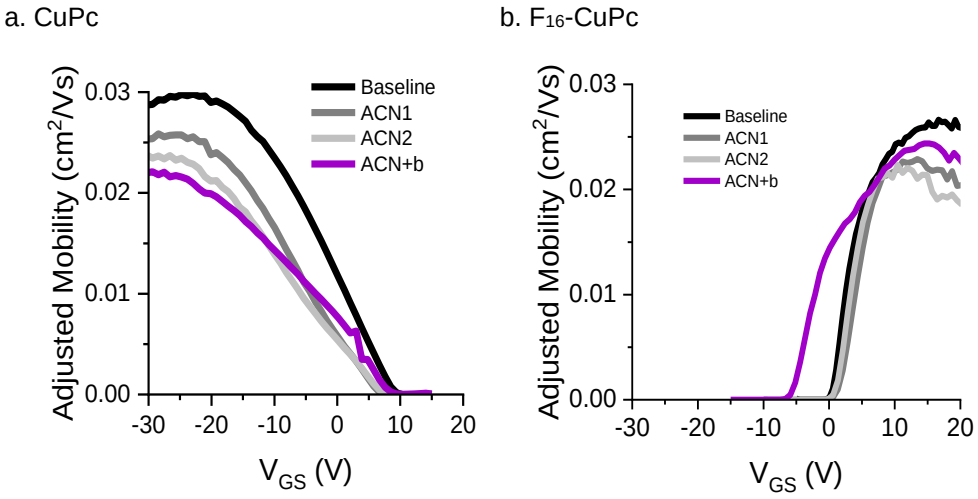

Figure A.2.3. *Solvent effects on field-effect mobility of characteristic OTFT devices. Field-effect mobility was evaluated for (a) CuPc and (b) F_{16}-CuPc devices after two repeat additions of 0.5 µL of ACN, and the separate addition of ACN with 50 µM NaOH. Mobilities were calculated between adjacent points of the transfer data.*

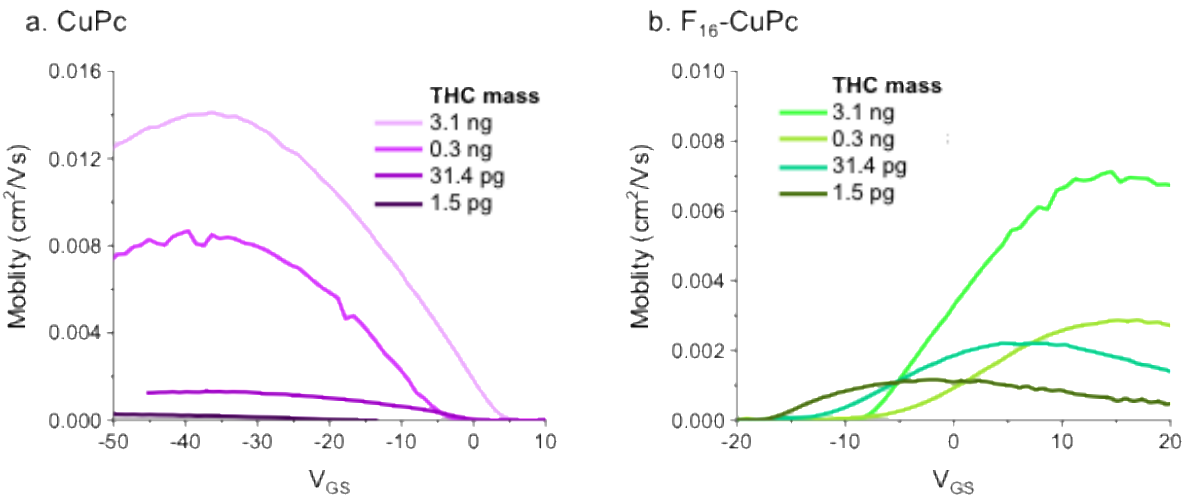

Figure A.2.4. *Effect of THC concentration on field-effect mobility of alkaline FBBB treated OTFTs with respect to gate-source voltage (V_{GS}). Field-effect mobility was evaluated for OTFTs comprised of alkaline FBBB (20 µM) treated (a) CuPc or (b) F_{16}-CuPc semiconductors following the addition of 0.5 µL of a 20 µM analytical standard in ACN of THC (1X, diluted 10X, diluted 100X, or diluted 2000X with ACN). Mobilities were calculated between adjacent points of the transfer data.*

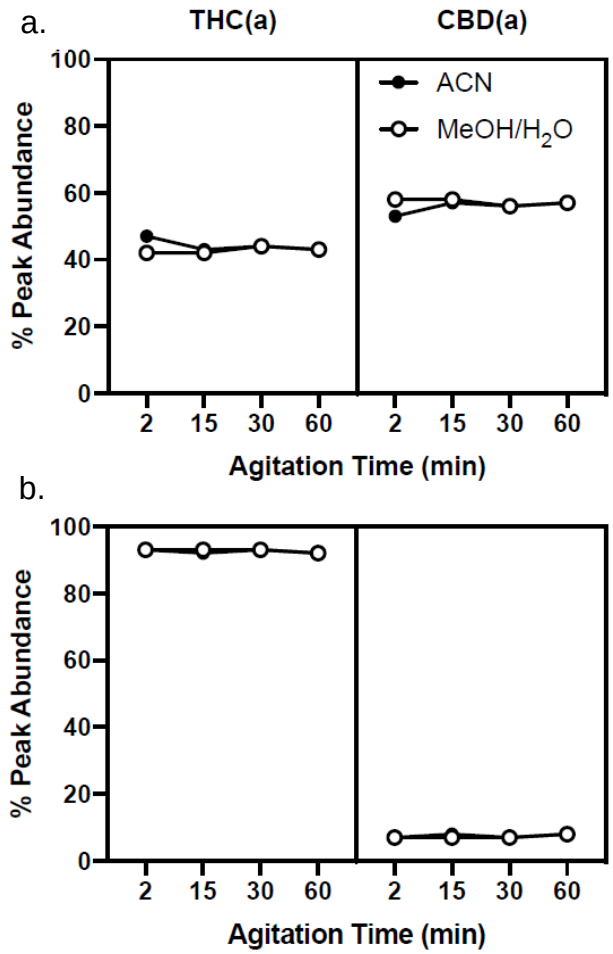

Figure A.2.5. *HPLC-DAD percentage of peak abundance of primary cannabinoids for plant samples 1 (b) and 2 (a) via extraction method and duration. Ground cannabis flower (1 mg/mL) was agitated in ACN or 80:20 MeOH/H_2O for a set time before the solution was microfiltered and characterized by HPLC-DAD. A binomial test found no significant difference between methods.*

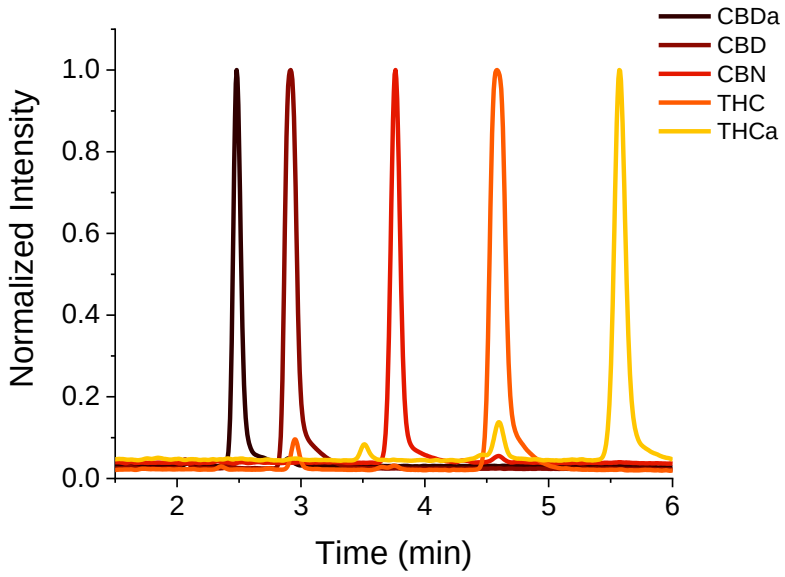

Figure A.2.6. *Normalized intensity of industrial HPLC cannabinoid standards. 2 µL of 1 mg/mL samples in ethanol were eluted at 0.25 mL/min in 50-100% H_2O/ACN with 0.1% FA at 65 ºC. Chromatograms were detected at 210 nm.*

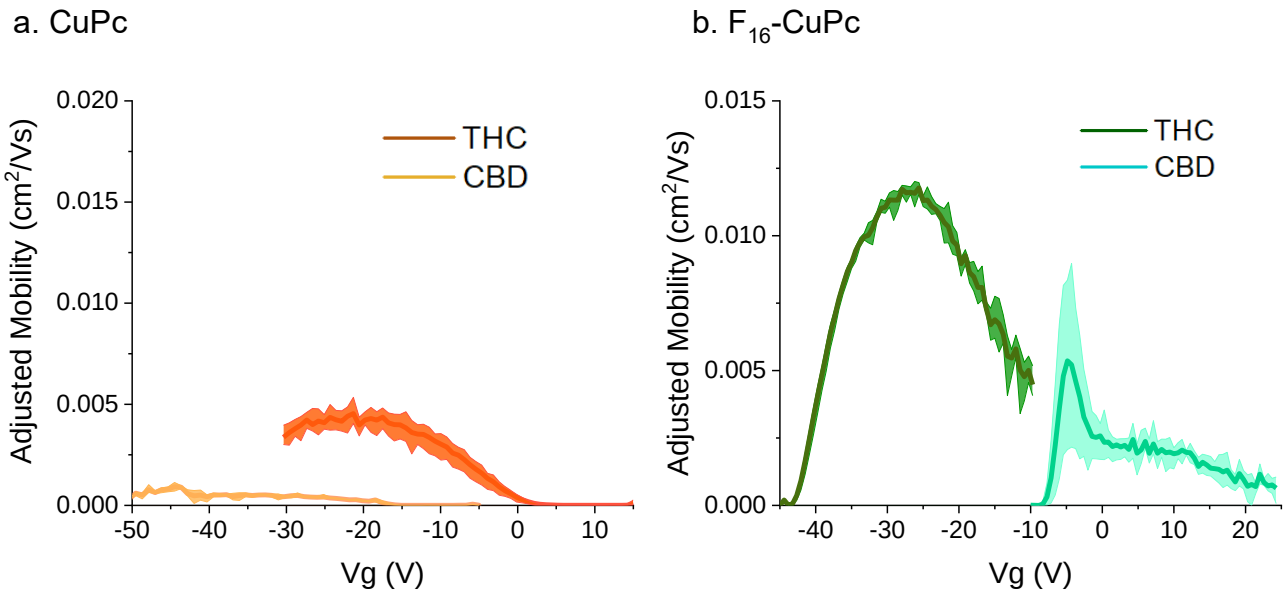

Figure A.2.7. *THC and CBD vapor exposed OTFTs. (a) CuPc and (b) F_{16}-CuPc OTFTs were exposed to vaporized THC and CBD (25 mg in 8 L) over a period of 1.5 min. Shaded regions represent the range of data points, encapsulating all data points for three V_{GS} sweeps at saturation across two devices with the bold center line representing the pooled average. Mobilities were calculated between adjacent points of the transfer data.*

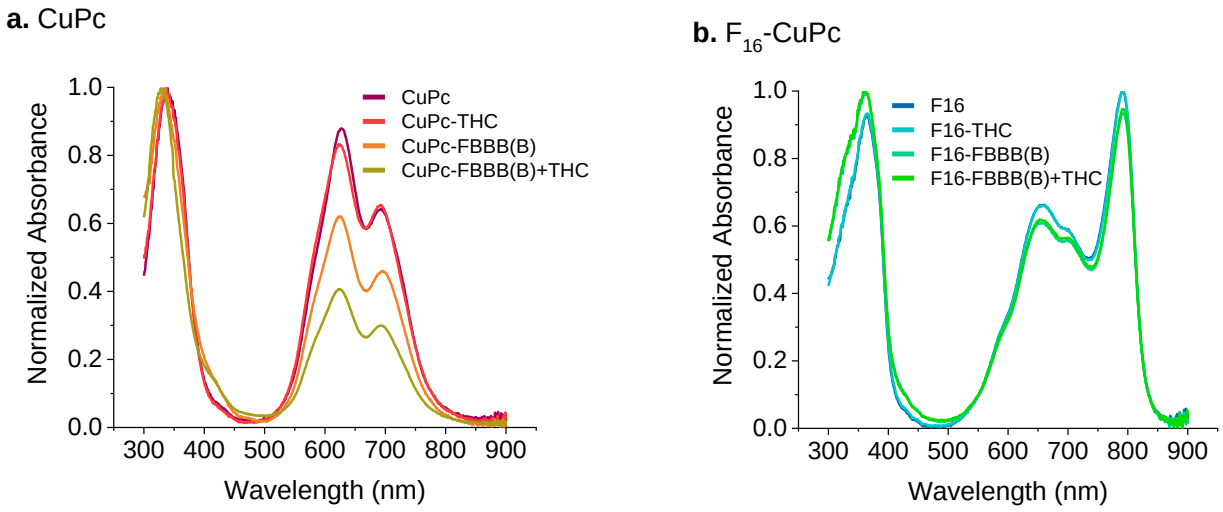

Figure A.2.8. *Normalized absorbance characterization of thin films. Thin films of (a) CuPc or (b) F_{16}-CuPc (200 Å) were deposited on glass for UV-Vis characterization and treated with either, or in combination, 50 mg in 8 L THC vapor over 90 seconds, and 20 µM FBBB with 50 µM NaOH.*

References

1. Abrams, D. I. The Therapeutic Effects of Cannabis and Cannabinoids: An Update from the National Academies of Sciences, Engineering and Medicine Report. Eur. J. Intern. Med. 2018, 49, 7– 11, DOI: 10.1016/j.ejim.2018.01.003
2. Hajizadeh, M. Legalizing and Regulating Marijuana in Canada: Review of Potential Economic, Social, and Health Impacts. Int. J. Heal. Policy Manag. 2016, 5, 453– 456, DOI: 10.15171/ijhpm.2016.63
3. Rehm, J.; Fischer, B. Cannabis Legalization With Strict Regulation, the Overall Superior Policy Option for Public Health. Clin. Pharmacol. Ther. 2015, 97, 541– 544, DOI: 10.1002/cpt.93
4. Hall, W.; Weier, M. Assessing the Public Health Impacts of Legalizing Recreational Cannabis Use in the USA. Clin. Pharmacol. Ther. 2015, 97, 607– 615, DOI: 10.1002/cpt.110
5. Turner, C. E.; Elsohly, M. A.; Boeren, E. G. Constituents of Cannabis sativa L. XVII. A Review of the Natural Constituents. J. Nat. Prod. 1980, 43, 169– 234, DOI: 10.1021/np50008a001
6. Veress, T.; Szanto, J. I.; Leisztner, L. Determination of Cannabinoid Acids by High-Performance Liquid Chromatography of Their Neutral Derivatives Formed by Thermal Decarboxylation: I. Study of the Decarboxylation Process in Open Reactors. J. Chromatogr. A 1990, 520, 339– 347, DOI: 10.1016/0021-9673(90)85118-F
7. Ahmed, S. A.; Ross, S. A.; Slade, D.; Radwan, M. M.; Khan, I. A.; ElSohly, M. A. Minor Oxygenated Cannabinoids from High Potency Cannabis sativa L.. Phytochemistry 2015, 117, 194– 199, DOI: 10.1016/j.phytochem.2015.04.007
8. ElSohly, M. A.; Gul, W. Constituents of Cannabis sativa. In Handbook of Cannabis; Oxford University Press, 2014; pp 3– 22.
9. Kunos, G.; Osei-Hyiaman, D.; Bátkai, S.; Sharkey, K. A.; Makriyannis, A. Should Peripheral CB1 Cannabinoid Receptors Be Selectively Targeted for Therapeutic Gain. Trends Pharmacol. Sci. 2009, 30, 1– 7, DOI: 10.1016/j.tips.2008.10.001
10. Mechoulam, R.; Peters, M.; Murillo-Rodriguez, E.; Hanuš, L. O. Cannabidiol – Recent Advances. Chem. Biodivers. 2007, 4, 1678– 1692, DOI: 10.1002/cbdv.200790147
11. Ujváry, I.; Hanuš, L. Human Metabolites of Cannabidiol: A Review on Their Formation, Biological Activity, and Relevance in Therapy. Cannabis Cannabinoid Res. 2016, 1, 90– 101, DOI: 10.1089/can.2015.0012
12. Seeman, P. Cannabidiol Is a Partial Agonist at Dopamine D2High Receptors, Predicting Its Antipsychotic Clinical Dose. Transl. Psychiatry 2016, 6, e920 DOI: 10.1038/tp.2016.195
13. Weiss, L.; Zeira, M.; Reich, S.; Har-Noy, M.; Mechoulam, R.; Slavin, S.; Gallily, R. Cannabidiol Lowers Incidence of Diabetes in Non-Obese Diabetic Mice. Autoimmunity 2006, 39, 143– 151, DOI: 10.1080/08916930500356674
14. Nissim, R.; Compton, R. G. Absorptive Stripping Voltammetry for Cannabis Detection. Chem. Cent. J. 2015, 9, 41, DOI: 10.1186/s13065-015-0117-0
15. Kintz, P.; Cirimele, V.; Ludes, B. Detection of Cannabis in Oral Fluid (Saliva) and Forehead Wipes (Sweat) from Impaired Drivers. J. Anal. Toxicol. 2000, 24, 557– 561, DOI: 10.1093/jat/24.7.557
16. Beck, O.; Sandqvist, S.; Dubbelboer, I.; Franck, J. Detection of 9-Tetrahydrocannabinol in Exhaled Breath Collected from Cannabis Users. J. Anal. Toxicol. 2011, 35,

541– 544, DOI: 10.1093/anatox/35.8.541
17. Hartman, R. L.; Huestis, M. A. Cannabis Effects on Driving Skills. Clin. Chem. 2013, 59, 478– 492, DOI: 10.1373/clinchem.2012.194381
18. Lau-Cam, C. A.; Pizzitola, V. Simple Field Test for Marijuana. J. Pharm. Sci. 1979, 68, 976– 978, DOI: 10.1002/jps.2600680815
19. Mali, B. D.; Parulekar, P. P. Diazotized Dapsone as a Reagent for the Detection of Cannabinoids on Thin-Layer Chromatograpic Plates. J. Chromatogr. A 1988, 457, 383– 386, DOI: 10.1016/S0021-9673(01)82088-4
20. dos Santos, N. A.; Souza, L. M.; Domingos, E.; França, H. S.; Lacerda, V.; Beatriz, A.; Vaz, B. G.; Rodrigues, R. R. T.; Carvalho, V. V.; Merlo, B. B.Evaluating the Selectivity of Colorimetric Test (Fast Blue BB Salt) for the Cannabinoids Identification in Marijuana Street Samples by UV–Vis, TLC, ESI(+)FT-ICR MS and ESI(+)MS/MS. Forensic Chem. 2016, 1, 13– 21, DOI: 10.1016/j.forc.2016.07.001
21. Nascimento, I. R.; Costa, H. B.; Souza, L. M.; Soprani, L. C.; Merlo, B. B.; Romão, W. Chemical Identification of Cannabinoids in Street Marijuana Samples Using Electrospray Ionization FT-ICR Mass Spectrometry. Anal. Methods 2015, 7, 1415– 1424, DOI: 10.1039/C4AY02355B
22. Watanabe, K.; Yamaki, E.; Yamamoto, I.; Yoshimura, H. A Colorimetric Method for the Determination of Cannabinoids with Fast Blue BB Salt. Eisei kagaku 1979, 25, 321– 326, DOI: 10.1248/jhs1956.25.321
23. Lester, G. E.; Lewers, K. S.; Medina, M. B.; Saftner, R. A. Comparative Analysis of Strawberry Total Phenolics via Fast Blue BB vs. Folin–Ciocalteu: Assay Interference by Ascorbic Acid. J. Food Compos. Anal. 2012, 27, 102– 107, DOI: 10.1016/j.jfca.2012.05.003
24. Torsi, L.; Dodabalapur, A. Organic Thin-Film Transistors as Plastic Analytical Sensors. Anal. Chem. 2005, 77, 380A– 387A, DOI: 10.1021/ac053475n
25. Melville, O. A.; Lessard, B. H.; Bender, T. P. Phthalocyanine-Based Organic Thin-Film Transistors: A Review of Recent Advances. ACS Appl. Mater. Interfaces 2015, 7, 13105– 13118, DOI: 10.1021/acsami.5b01718
26. Melville, O. A.; Grant, T. M.; Lessard, B. H. Silicon Phthalocyanines as N-Type Semiconductors in Organic Thin Film Transistors. J. Mater. Chem. C 2018, 6, 5482– 5488, DOI: 10.1039/C8TC01116H
27. Sirringhaus, H. Reliability of Organic Field-Effect Transistors. Adv. Mater. 2009, 21, 3859– 3873, DOI: 10.1002/adma.200901136
28. Brixi, S.; Melville, O. A.; Boileau, N. T.; Lessard, B. H. The Influence of Air and Temperature on the Performance of PBDB-T and P3HT in Organic Thin Film Transistors. J. Mater. Chem. C 2018, 6, 11972– 11979, DOI: 10.1039/C8TC00734A
29. Liu, J.; Agarwal, M.; Varahramyan, K. Glucose Sensor Based on Organic Thin Film Transistor Using Glucose Oxidase and Conducting Polymer. Sens. Actuators, B 2008, 135, 195– 199, DOI: 10.1016/j.snb.2008.08.009
30. Zhang, Q.; Subramanian, V. DNA Hybridization Detection with Organic Thin Film Transistors: Toward Fast and Disposable DNA Microarray Chips. Biosens. Bioelectron. 2007, 22, 3182– 3187, DOI: 10.1016/j.bios.2007.02.015
31. Boileau, N. T.; Melville, O. A.; Mirka, B.; Cranston, R.; Lessard, B. H. P and N Type Copper Phthalocyanines as Effective Semiconductors in Organic Thin-Film Transistor Based DNA Biosensors at Elevated Temperatures. RSC Adv. 2019, 9,

2133– 2142, DOI: 10.1039/C8RA08829B
32. Hammock, M. L.; Knopfmacher, O.; Naab, B. D.; Tok, J. B.-H.; Bao, Z. Investigation of Protein Detection Parameters Using Nanofunctionalized Organic Field-Effect Transistors. ACS Nano 2013, 7, 3970– 3980, DOI: 10.1021/nn305903q
33. Khan, H. U.; Jang, J.; Kim, J.-J.; Knoll, W. Effect of Passivation on the Sensitivity and Stability of Pentacene Transistor Sensors in Aqueous Media. Biosens. Bioelectron. 2011, 26, 4217– 4221, DOI: 10.1016/j.bios.2011.03.031
34. Huang, W.; Besar, K.; LeCover, R.; Dulloor, P.; Sinha, J.; Martínez Hardigree, J. F.; Pick, C.; Swavola, J.; Everett, A. D.; Frechette, J.Label-Free Brain Injury Biomarker Detection Based on Highly Sensitive Large Area Organic Thin Film Transistor with Hybrid Coupling Layer. Chem. Sci 2014, 5, 416– 426, DOI: 10.1039/C3SC52638K
35. Zhu, Z.-T.; Mason, J. T.; Dieckmann, R.; Malliaras, G. G. Humidity Sensors Based on Pentacene Thin-Film Transistors. Appl. Phys. Lett. 2002, 81, 4643– 4645, DOI: 10.1063/1.1527233
36. Xie, T.; Xie, G.; Su, Y.; Hongfei, D.; Ye, Z.; Jiang, Y. Ammonia Gas Sensors Based on Poly (3-Hexylthiophene)-Molybdenum Disulfide Film Transistors. Nanotechnology 2016, 27, 065502 DOI: 10.1088/0957-4484/27/6/065502
37. Zhuang, X.; Han, S.; Huai, B.; Shi, W.; Junsheng, Y. Sub-Ppm and High Response Organic Thin-Film Transistor NO2 Sensor Based on Nanofibrillar Structured TIPS-Pentacene. Sens. Actuators, B 2019, 279, 238– 244, DOI: 10.1016/j.snb.2018.10.002
38. Chaure, N. B.; Cammidge, A. N.; Chambrier, I.; Cook, M. J.; Cain, M. G.; Murphy, C. E.; Pal, C.; Ray, A. K. High-Mobility Solution-Processed Copper Phthalocyanine-Based Organic Field-Effect Transistors. Sci. Technol. Adv. Mater. 2011, 12, 025001 DOI: 10.1088/1468-6996/12/2/025001
39. Nénon, S.; Kanehira, D.; Yoshimoto, N.; Fages, F.; Videlot-Ackermann, C. Shelf-Life Time Test of p- and n-Channel Organic Thin Film Transistors Using Copper Phthalocyanines. Thin Solid Films 2010, 518, 5593– 5598, DOI: 10.1016/j.tsf.2010.04.035
40. Ji, Z.; Wong, K.; Tse, P.; Kwok, R. W.; Lau, W. Copper Phthalocyanine Film Grown by Vacuum Deposition under Magnetic Field. Thin Solid Films 2002, 402, 79– 82, DOI: 10.1016/S0040-6090(01)01702-3
41. Hailey, A. K.; Petty, A. J., II; Washbourne, J.; Thorley, K. J.; Parkin, S. R.; Anthony, J. E.; Loo, Y.-L. Understanding the Crystal Packing and Organic Thin-Film Transistor Performance in Isomeric Guest-Host Systems. Adv. Mater. 2017, 29, 1700048 DOI: 10.1002/adma.201700048
42. Eloff, J. Which Extractant Should Be Used for the Screening and Isolation of Antimicrobial Components from Plants. J. Ethnopharmacol. 1998, 60, 1– 8, DOI: 10.1016/S0378-8741(97)00123-2 [Crossref], [PubMed], [CAS], Google Scholar
43. Hazekamp, A.; Bastola, K.; Rashidi, H.; Bender, J.; Verpoorte, R. Cannabis Tea Revisited: A Systematic Evaluation of the Cannabinoid Composition of Cannabis Tea. J. Ethnopharmacol. 2007, 113, 85– 90, DOI: 10.1016/j.jep.2007.05.019
44. Aizpurua-Olaizola, O.; Omar, J.; Navarro, P.; Olivares, M.; Etxebarria, N.; Usobiaga, A. Identification and Quantification of Cannabinoids in Cannabis sativa L. Plants by High Performance Liquid Chromatography-Mass Spectrometry. Anal. Bioanal.

Chem. 2014, 406, 7549– 7560, DOI: 10.1007/s00216-014-8177-x
45. Stolker, A. A. M.; van Schoonhoven, J.; de Vries, A. J.; Bobeldijk-Pastorova, I.; Vaes, W. H. J.; van den Berg, R. Determination of Cannabinoids in Cannabis Products Using Liquid Chromatography–Ion Trap Mass Spectrometry. J. Chromatogr. A 2004, 1058, 143– 151, DOI: 10.1016/S0021-9673(04)01447-5 [
46. Zhang, X.; Chen, Y. A Sandwich Mixed (Phthalocyaninato) (Porphyrinato) Europium Triple-Decker: Balanced-Mobility, Ambipolar Organic Thin-Film Transistor. Inorg. Chem. Commun. 2014, 39, 79– 82, DOI: 10.1016/j.inoche.2013.10.040
47. Kumar, P.; Santhakumar, K.; Shin, P.-K.; Ochiai, S. Improving the Photovoltaic Parameters of Organic Solar Cell Using Soluble Copper Phthalocyanine Nanoparticles as a Buffer Layer. Jpn. J. Appl. Phys. 2014, 53, 01AB06 DOI: 10.7567/JJAP.53.01AB06
48. Margham, J.; McAdam, K.; Forster, M.; Liu, C.; Wright, C.; Mariner, D.; Proctor, C. Chemical Composition of Aerosol from an E-Cigarette: A Quantitative Comparison with Cigarette Smoke. Chem. Res. Toxicol. 2016, 29, 1662– 1678, DOI: 10.1021/acs.chemrestox.6b00188 [ACS Full Text ACS Full Text], [CAS], Google Scholar
49. Elkington, D.; Cooling, N.; Belcher, W.; Dastoor, P.; Zhou, X. Organic Thin-Film Transistor (OTFT)-Based Sensors. Electronics 2014, 3, 234– 254, DOI: 10.3390/electronics3020234

Chapter 3. Engineering Cannabinoid Sensors through Solution-Based Screening of Phthalocyanines

This chapter is taken from: ***Z. J. Comeau***, *G. A. Facey, C. S. Harris, B. H. Lessard, A. J. Shuhendler, ACS Appl. Mater. Interfaces 2020, 12, 45, 50692-50702*

Context

While the previous work was generally well controlled with regards to the effects of the analytes studied on OTFT performance, within the scope of the study it was unable to provide a precise mechanism by which those effects occurred. To that end, I developed a spectroelectrochemical set up and procedure, initially characterizing the redox induced spectroelectrochemical behavior of Pcs. The addition of cannabinoids and a colorimetric probe produced complex spectra which could be interpreted to determine sites of Pc-cannabinoid interactions and related to OTFT performance; however, I wanted a complimentary technique to corroborate my spectroelectrochemical observations. With the guidance of Dr. Glenn Facey, I experimented with 2D-NMR techniques, improving the conclusions I made between Pc-analyte electrochemical solution interactions and OTFT performance. I observed strong interactions between Pcs and cannabinoids in solution, suggesting a source of the Pc-cannabinoid sensitivity. Additionally, specific Pc-cannabinoid sites of molecular coordination suggested a mechanism for the specificity previously observed. More broadly, this work demonstrated the utility of spectroelectrochemistry as a potential rapid screening technique for sensing applications with conjugated aromatic small molecules.

Contribution

I performed all experiments and authored the manuscript. GAF assisted with NMR experiments and interpretation. All co-authors provided editorial contributions. This work was performed under the supervision of BHL and AJS.

Abstract

Organic thin-film transistors (OTFTs) have shown promise for a range of sensing applications, with phthalocyanine-based OTFTs demonstrated as sensors for atmospheric parameters, volatile gases, and small organic molecules including cannabinoids. However, the process of fabricating, testing, and optimizing OTFTs in a laboratory setting requires highly specialized equipment, materials, and expertise. To determine if sensor development can be

expedited and thus reduce manufacturing burden, spectroelectrochemistry is applied to rapidly screen for molecular interactions between metal-free phthalocyanines and a variety of metal phthalocyanines (MPcs) and the cannabinoids Δ^9-tetrahydrocannabinol (THC) or cannabidiol (CBD), with and without a cannabinoid-sensitive chromophore (Fast Blue BB). Spectral analyses are corroborated by 2D-NMR and related to measured OTFT performance. Spectroelectrochemical changes to the Q band region of the phthalocyanine spectra in the presence of analytes can be used to predict the response of OTFTs. Thus, with spectroelectrochemistry, a range of potential materials for OTFT small organic molecule-sensing applications can be quickly analyzed, and phthalocyanines with a preferred response can be selected.

Introduction

Phthalocyanines (Pcs) are aromatic, conjugated, macrocyclic molecules with high thermal stability and a variety of industrial applications[1]. Pcs typically absorb light at 300–400 and 600–700 nm, appearing visually as brilliant blues and purples, lending them for use in dyes and pigments[2]. Pcs have highly delocalized π electrons facilitating intermolecular charge transport, giving rise to applications in organic solar cells[3,4] and organic thin-film transistors (OTFTs)[5,6]. Metal-free Pc (H_2Pc) and a variety of metal-Pc (MPc) complexes are possible, which can be peripherally and axially substituted, depending on the metal, allowing for precision tuning of their material properties and optimization of device performance[5,7,8]. Charge transport of semiconducting Pcs in OTFTs can be affected by atmospheric parameters[9,10] or improved via doping with small molecules[11,12]. The interaction of analytes with the Pc-derived semiconducting layer can cause performance changes that can be interpreted as a sensing response[6,13,14]. Furthermore, changes to the central metal or substituents, axial or peripheral, can be used to improve the sensing response[8,15,16]. Pc semiconductors in OTFTs have been demonstrated for a variety of liquid- and gas-sensing applications[6,9,13,17], including our demonstration of the ratiometric detection and differentiation of Δ^9-tetrahydrocannabinol (THC) and cannabidiol (CBD)[18].

Produced by the plant *Cannabis sativa*, THC and CBD are sought after by consumers for their psychoactive and potentially therapeutic effects. However, industrial identification and separation of these bioactives without the use of higher order analytical techniques have proven to be a challenge[19]. Cannabinoid detection by Pc-based OTFTs offers a rapid, low-cost alternative; however, the mechanisms of sensing response are still not fully characterized. Furthermore, while there has been significant work to understand the effects of small, inorganic,

volatile gases on Pc-based OTFT performance, the effects of small organic compounds are not well understood[9,13,16,20].

In Pc-based OTFTs, device architecture, fabrication conditions, and molecular structure determine film crystallinity and morphology, affecting molecular interactions and dictating how well the film can transport charge[13,21–23]. Gas or liquid analytes can interact with the Pc semiconducting layer, causing changes in electrical output to elicit a sensing response[9,14,24]. However, the large number of variables involved with device engineering and manufacturing can complicate the identification of specific semiconductor materials possessing sensing potential. Spectroelectrochemistry affords the opportunity to easily and rapidly assay conduction mechanisms and molecular interactions in solution that may inform semiconductor–analyte pairing suitability without the need to fabricate and engineer a solid-state device. Pcs lend themselves well to spectral analysis as they have two well-defined spectral regions: the B or Soret band and the Q band which correspond to different $\pi \rightarrow \pi^*$ electron transitions[17,25,26]. Variations in wavelength and intensity of specifics peaks in the Q band region can give significant information about molecular orientation, coordination, reduction states, and the HOMO–LUMO band gap energies[27–30]. Additionally, in the 400–500 nm region, metal–ligand coordination peaks can be visualized, further elucidating molecular interactions[17]. By applying a reducing potential during spectroscopy, we can visualize changes to the Pcs as they accept and donate charges in the presence of analytes, which can be related to the sensing response of OTFT devices[8,22,31–33].

Herein, we examine the reduction processes of metal-free Pcs and a variety of metal-bound Pcs (**Figure 3.1a**) and the effects of cannabinoids (THC and CBD, **Figure 3.1b,c**) alone and in combination with 4-amino-2,5-diethoxybenzanilide diazoated zinc double salt (FBBB, **Figure 3.1d**), a colorimetric cannabinoid binding agent[34]. Solvents play a significant role in peak locations and intensity of Pc spectra in addition to their electrochemical processes[25,28]. In this work, we build on our previously established Pc-based OTFT cannabinoid sensors[18], correlating spectroelectrochemical changes of analyte–PC solutions to shifting ratios of Pc–Pc and Pc–analyte coordination configuration states, corroborating these opto-electronic signals with structural outcomes by 1D and 2D-NMR experiments. Ultimately, we validate our solution-based workflow for semiconductor–analyte pair optimization by relating spectroelectrochemical outcomes to OTFT device performance for practical sensing applications.

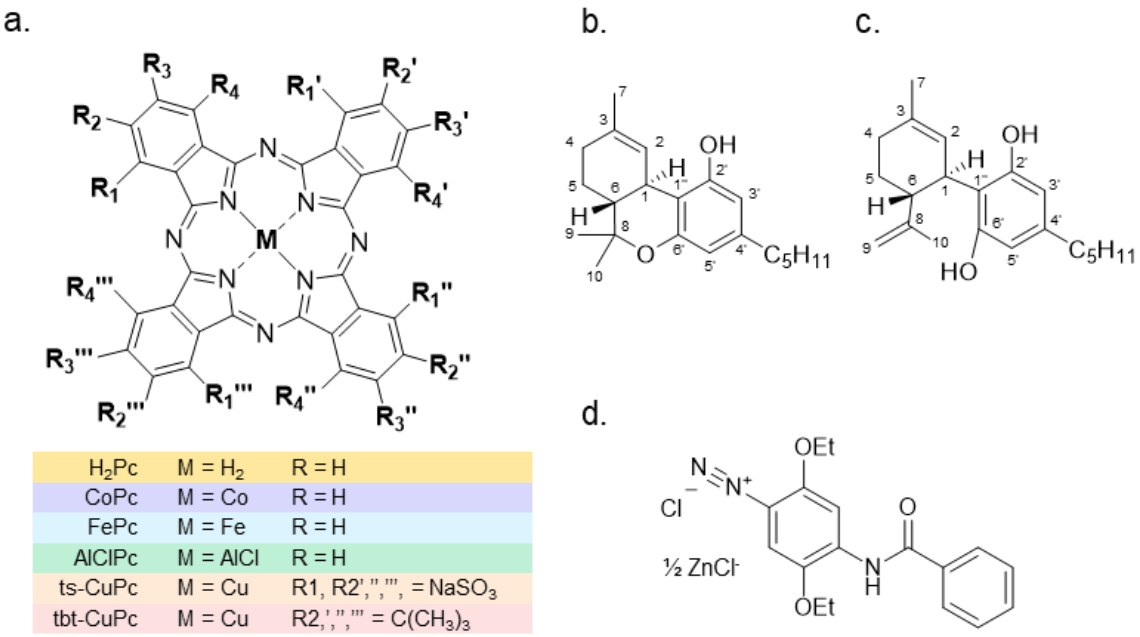

Figure 3.1. *Chemical structures of (a) metal Pc (MPc), (b) Δ⁹-tetrahydrocannabinol (THC), (c) cannabidiol (CBD), and (d) 4-amino-2,5-diethoxybenzanilide diazoated zinc double salt (FBBB). (a) Unless otherwise noted, R = H.*

Results and Discussion

Spectroelectrochemical Reduction Processes of Pcs

The spectroelectrochemical reduction responses of six Pcs were investigated in dimethyl sulfoxide (DMSO) with tetra-butyl ammonium perchlorate (TBAP) electrolyte (**Figure 3.2**). DMSO/TBAP was selected as a solvent/electrolyte system as it has a relatively wide negative potential window, and all analytes utilized are soluble to 0.1 μM. The reducing potential applied to each of the Pcs corresponded to the first reduction potential as indicated by in situ cyclic voltammetry (CV) (**Figure A.3.1**). Spectroscopically, H_2Pc and tbt-CuPc (**Figure 2a,b**) were characterized by having broad peaks with limited features which is typical of the Pc aggregation[35–37]. CoPc and FePc (**Figure 3.2c,d**) have more well-defined spectra, each with clear peaks in both the B band and Q band regions, though they still display broad features. ts-CuPc and AlClPc (**Figure 3.2e,f**), the most electronegative of the Pcs studied, appear highly monomeric with narrow, well-defined B and Q band peaks. For all Pcs studied herein, an increase in peak intensity is observed at the primary Q band peak with a negative applied cell potential, which is driven by increased π → π* transitions[27].

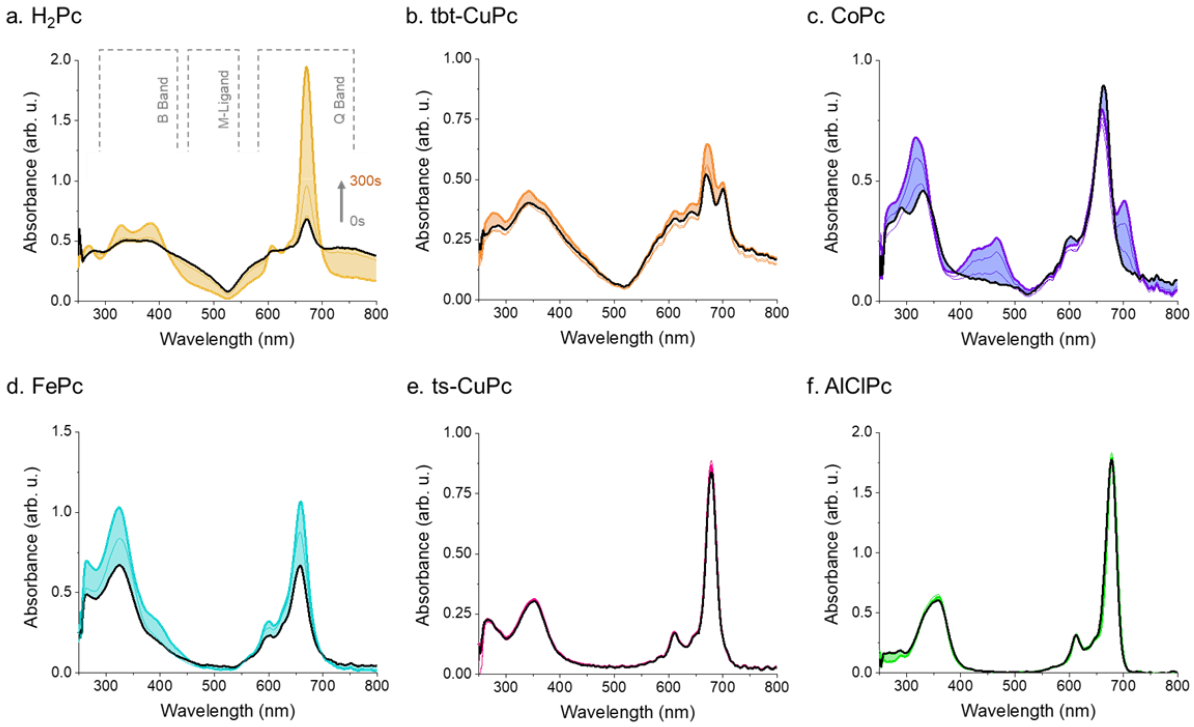

Figure 3.2. *Spectroelectrochemical reduction processes of different Pcs. Absorbance spectral baseline (black) and reducing potential responses at 100, 200, and 300 s from initial voltage application (colored) of 0.1 μM (a) metal-free Pc (H_2Pc), (b) 4,4′,4″4‴-tetra-tert-butyl CuPc (tbt-CuPc), (c) cobalt Pc (CoPc), (d) iron Pc (FePc), (e) 3,4′,4″,4‴-tetrasulfonic-acid CuPc (ts-CuPc), and (f) aluminum chloride Pc (AlClPc) in DMSO with 0.1 M TBAP electrolyte in a custom quartz SEC cell. The first reducing potential by in situ CV [(a) −0.70, (b) −0.75, (c) −0.55, (d) −0.40, (e) −0.74, and (f) −0.50 V] was applied between the platinum micromesh working electrode and platinum wire counter electrode against a Ag/AgCl reference electrode.*

While applying a reducing potential of −0.70 V, the spectra of H_2Pc (**Figure 3.2a**) shift significantly, with the spectra becoming more defined, developing a strong, narrow Q band peak at 671 nm. A pair of split peaks visible at 607 and 639 nm indicates that the reduced species is preferentially monomeric in DMSO/TBAP, adopting D_{4h} symmetry, suggesting coordination with either the solvent or electrolyte[25,38]. tbt-CuPc displays complex spectra (**Figure 3.2b**), with a Q band peak shoulder at 702 nm and broad background absorbance suggesting the presence of complex aggregates[39]. The main 668 nm Q band peak gains intensity and shifts to 673 nm upon reduction without a significant decrease in background absorbance, implying that the aggregating species are closely coordinated[36]. When applying a reducing potential to CoPc (**Figure 3.2c**), we observe a new peak at 702 nm; unique to the reduced cobalt species[9,17]. In addition, the main Q band peak at 664 nm shifts to 660 nm, suggesting metal–ligand interactions and an increased preference toward face-on Pc–Pc coordination (**Figure 3.2c**)[17,27]. Finally, the formation of peaks at 422 and 466 nm, corresponding to metal–ligand interactions, further corroborates reduction-driven face-on Pc–Pc interactions. A similar double peak is observed at 394 and 432 nm for FePc

(**Figure 3.2d**); however, these interactions are obscured by the B band as they are blue-shifted relative to those of CoPc, implying a slightly lower degree of coordination and less significant π electron sharing[27,40]. This shift is accompanied by a stronger increase in Q band absorbance, demonstrating a different Pc–Pc coordination configuration allowing for a greater degree of π to π* transitions (**Figure 3.2d**). ts-CuPc (**Figure 3.2e**), with its electronegative tetra-sulfonic acid groups promoting solubility and hindering aggregate formation, evidenced through a strong, narrow, 678 nm Q band peak and two split peaks at 610 and 644 nm, appear monomeric. AlClPc appears highly monomeric with a strong Q band at 679 nm and well-defined split peaks at 612 and 646 nm (**Figure 3.2f**). These spectral features are supported by the limited ability of AlClPc to form additional metal ligand interactions due to its flexed ring shape via axially substituted chlorine[41]. Overall, our results obtained regarding the spectroelectrochemical behavior of Pcs are in-line with those previously reported in the literature[17,42–44] and provide a response baseline for each Pc that can be compared to the more complex multi-component systems required for analyte sensing.

Reduction Processes of H_2Pc in the Presence of Cannabinoids

To assay the effects of cannabinoids on the spectroelectrochemical behavior of Pcs, specifically interactions with the Pc macrocycle, equimolar amounts of cannabinoid, either THC or CBD, were added to a solution containing H_2Pc. The cell was then exposed to the first reducing potential of the Pc as defined by CV and used to generate spectroelectrochemical baselines as was done previously for the individual Pc's (**Figure 3.3a,b**). Prior to the application of bias, the addition of THC does not substantially alter the spectrum relative to baseline (**Figure 3.3a**, black line); however, the addition of CBD slightly promotes the monomeric species of the Pc (**Figure 3.3b**, black line), possibly through a pseudo-reducing effect[45,46], visualized through sharper peaks and an increase in peak intensity at 671 nm. Upon the application of bias, an increase in absorbance of the Q band peaks at 671 nm and 619 nm as well as the formation and increase of two B band peaks at 324 and 383 nm are observed for H_2Pc with the addition of either cannabinoids, with a limited reduction in light scattering effects (**Figure 3.3a,b**). This result suggests that the cannabinoids are not donating electrons directly to H_2Pc but instead coordinating strongly, increasing electron density of the Pc ring and promoting $\pi \rightarrow \pi^*$ transitions. Such spectral responses have previously been attributed to slight increases in the HOMO level of H_2Pc[25,38]. DFT and QSAR studies of THC and CBD suggest that the electron density of CBD is spatially confined around carbons 8, 9, and 10, localizing electron density relative to THC[46], supporting the differences in spectroelectrochemical behavior observed. The cyclic voltammogram of H_2Pc + CBD corroborates this behavior (**Figure 3.3c**, green), with the reducing

potential peaks shifting by approximately −0.28 V and the current increasing relative to H_2Pc + THC, suggesting a smaller diffusion layer and less aggregate formation.

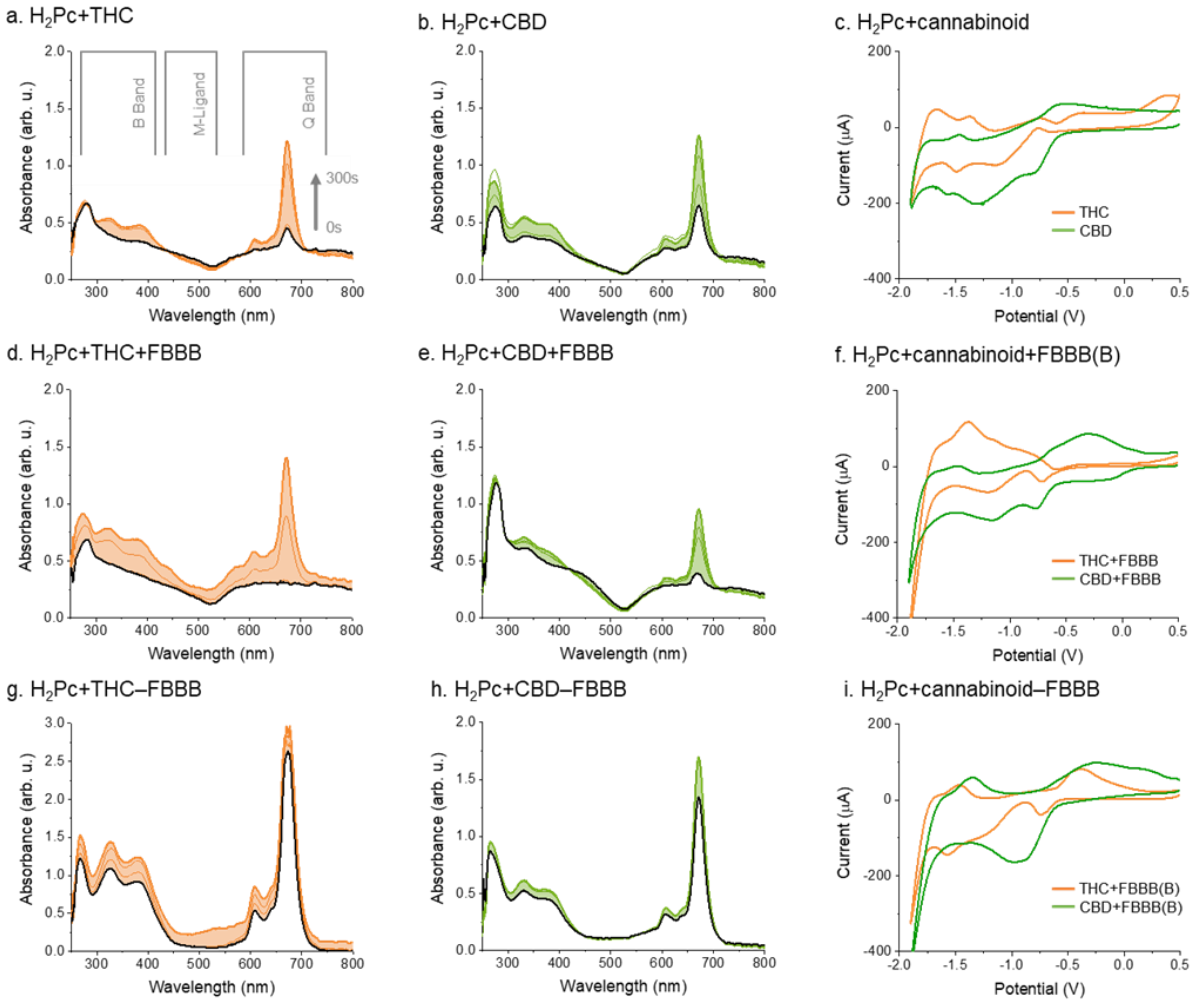

Figure 3.3. *Spectroelectrochemical reduction processes and cyclic voltammograms of H_2Pc with cannabinoids, cannabinoids and FBBB (neutral pH), and cannabinoid–FBBB conjugate (high pH). Absorbance spectral baseline (black) and reducing potential responses at 100, 200, and 300 s from initial voltage application (colored) of 0.1 μM H_2Pc in DMSO with 0.1 M TBAP electrolyte in a custom quartz SEC cell following equimolar additions of (a–c) THC or CBD, (d–f) FBBB, and (g–i) 50 μM NaOH. The first reducing potential by in situ CV [(a) −1.1, (d) −0.75, (g) −0.85, (b) −0.75, (e) −0.75, and (h) −0.80 V] was applied between the platinum micromesh working electrode and platinum wire counter electrode against an Ag/AgCl reference electrode. (c,f,i) A scan rate of 0.1 mV/s was applied.*

With equimolar H_2Pc, cannabinoid, and FBBB added to the sample solution, analysis under conditions that do not promote the formation of an FBBB–cannabinoid complex (i.e., neutral pH), a reduction in intensity of the baseline 671 nm Q band peak is observed relative to both those for the independent H_2Pc and equimolar H_2Pc, cannabinoid solutions (**Figure 3.3d,e**, black line). Upon application of bias, increases in the intensity of the Q and B band peaks are observed

similarly to the spectral changes noted upon cannabinoid addition alone; however, light scattering increases slightly suggesting aggregate formation persists or increases. Upon addition of FBBB under alkaline conditions, which is known to covalently bind to cannabinoids at their phenol moiety[34], and before the application of bias, the UV–vis spectrum of H_2Pc appears strongly monomeric (**Figure 3.3g,h**, black line). This implies that the cannabinoid–FBBB conjugate promotes H_2Pc coordination with the solvent or electrolyte resulting in strongly favored D_{4h} symmetry. With an applied reducing bias, the THC–FBBB conjugate with H_2Pc prompts an increase in light scattering and a 6 nm red-shift of the main Q band peak, implying the preference of an edge on species that can aggregate upon reduction[27,36]. Neither an increase in background absorbance nor peak shifts are observed for the reduction of H_2Pc in the presence of the CBD + FBBB(B) conjugate (**Figure 3.3h**), indicating preference to a differently orientated coordinated species that does not aggregate as readily.

Consistent with the spectra (**Figure 3.3d,e and A.3.3g,h**), cyclic voltammograms of H_2Pc + CBD and H_2Pc + CBD + FBBB show negatively shifted peaks (−0.28 and −0.15 V respectively) corresponding to the first order reduction process relative to those of THC and THC + FBBB (**Figure 3.3f,i**). With the H_2Pc + CBD–FBBB(B) sample, there is a limited shift but instead a substantial increase in the first reduction potential intensity (**Figure 3.3i,** green), while THC + FBBB(B) shows an increased negative potential shift (**Figure 3.3i**, orange). This further demonstrates that while both cannabinoid conjugates are coordinating with the Pc ring, they are doing so differently, and that these changes are reflected in both their spectral and electrical properties.

Reduction Processes of CoPc in the Presence of Cannabinoids

CoPc is similar in size and molecular properties to CuPc, the Pc we previously employed in our OTFT cannabinoid sensor[18], but, unlike CuPc, soluble in mild solvents and amenable to spectroelectrochemical analysis. Initially, the effect of adding equimolar concentration of THC or CBD to CoPc was studied under a negative bias (**Figure 3.4a,b**). With the addition of THC, the Q band intensity increased relative to the baseline CoPc spectra (**Figure 3.4a**, black line). Conversely, the addition of CBD reduced the intensity of the Q and B relative to the baseline CoPc spectra (**Figure 3.4b**, black line). In the presence of either cannabinoid, a similar shift in the Q band from 664 to 661 nm was observed, implying face-on Pc–ligand coordination[27]. In the presence of THC and upon the application of bias, the CoPc Q band shifts back to 664 nm, becoming less intense and slightly broader (**Figure 3.4a**). Metal–ligand peaks at 422 and 466 nm also develop, and a broad shoulder at 702 nm appears, corresponding to the reduced cobalt

species[17] (**Figure 3.4a**). This shoulder is of reduced intensity relative to the shoulder that appears upon application of bias to CoPc alone (**Figure 3.2c**). The Q band intensity increase observed in the CoPc–THC sample suggests that interactions between the Pc ring and THC provides a pseudo-electron donating effect, hindering the ability for Pc–Pc coordination. Upon reduction, the electron donating effect is lessened but the hindrance toward metal coordination persists (**Figure 3.4a**). In the presence of CBD and upon application of bias, the CoPc Q band peak decreases in intensity but does not shift, and the shoulder at 702 nm appears (**Figure 3.4b**). Unlike what was observed in the presence of THC, the shoulder at 702 nm appears unaltered by the presence of CBD. The B band at 380 nm significantly increases in intensity upon reduction, suggesting a unique interaction between CoPc and CBD limiting S_0 to S_1 transitions[16,29]. Additionally, compared to the addition of THC, with the addition of CBD, the metal-ligand coordination peaks red-shift from 422 to 426 nm, 466 to 470 nm, and a third peak at 445 nm develops. With the appearance of a new metal–ligand peak and considering the higher electron density of CBD[46], CBD could interact more directly with the central cobalt, drawing electronegativity away from the CoPc macrocycle to cause the overall observed spectral intensity decrease. Such an interaction is further supported by the CV curves, which show higher current at both the first and second reducing potentials, relative to THC, as well as −0.11 and −0.10 V shifts, respectively (**Figure 3.4c**, purple).

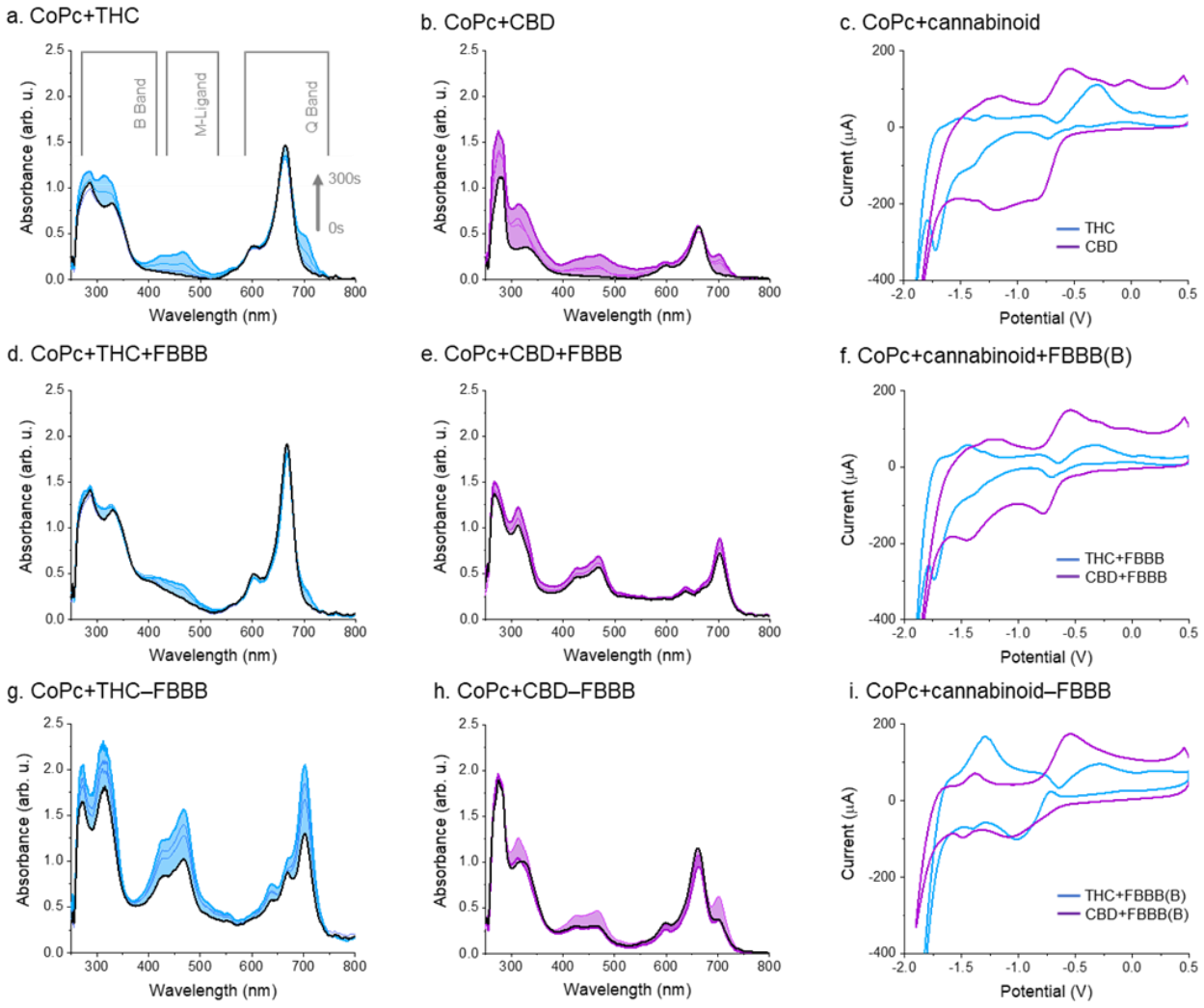

Figure 3.4. *Spectroelectrochemical reduction processes and cyclic voltammograms of CoPc with cannabinoids, FBBB, and cannabinoid–FBBB conjugate. Absorbance spectral baseline (black) and first reducing potential responses at 100, 200, and 300 s (colored) of 0.1 μM CoPc in DMSO with 0.1 M TBAP electrolyte in a custom quartz SEC cell following equimolar additions of (a–c) THC or CBD, (d–f) FBBB, and (g–i) 50 μM NaOH. The first reducing potential by in situ CV [(a) −1.1, (d) −0.75, (g) −0.85, (b) −0.75, (e) −0.75, and (h) −0.80 V] was applied between the platinum micromesh working electrode and platinum wire counter electrode against an Ag/AgCl reference electrode. (g,h,f) A scan rate of 0.1 mV/s was applied.*

In the presence of neutral FBBB and either cannabinoid before applied potential, metal–ligand coordination is observed (**Figure 3.4d,e**). Increasing intensity of the CoPc Q band peak is observed with the addition of THC and FBBB, which is accompanied by a red shift from 665 to 668 nm (**Figure 3.4d**). Upon reduction, Q band intensity decreases slightly with a similarly slight blue shift from 668 to 666 nm, a minor increase in the intensity of the 422 and 466 nm metal–ligand coordination peaks, and a reduction in the 702 nm cobalt peak. With the addition of CBD and neutral FBBB (**Figure 3.4e**), overall spectral intensity increases, pointing to the formation of

aggregate species[36,40], and a spectral shift in the Q band region is observed where the predominant Q band peak becomes that of the reduced cobalt at 702 nm. Both the original Q band peak and split peak are still visible but red-shifted to 669 and 634 nm, respectively. A reducing potential increases absorbance across the whole spectrum, pointing towards the promotion of aggregation. By CV, similar differences in the interaction of THC and CBD alone with CoPc were noted in the presence of neutral FBBB (**Figure 3.4f**): specifically, higher reducing current when CBD is present relative to THC, possibly through a smaller diffusion layer due to a lesser propensity towards aggregate formation.

Upon interaction with the THC–FBBB(B) conjugate, CoPc demonstrates high background absorbance and persistent metal–ligand coordination, and the 702 nm shoulder becomes more intense than the Q band peak that shifts from 664 to 669 nm (**Figure 3.4c**, black line). These data demonstrate preference of the reduced cobalt form in the presence of THC–FBBB(B), possibly through aggregate formation[47,48]. However, interaction of CoPc with the CBD + FBBB(B) conjugate causes the most predominant Q band peak to appear at 660 nm, which loses intensity and red-shifts to 663 nm with the application of reducing potential (**Figure 3.4f**). Furthermore, the 702 nm shoulder and the 422 and 466 nm metal coordination peaks are initially present and gain in intensity with reducing potential. Thus, the CBD + FBBB(B) conjugate also appears to coordinate with the central metal; however, the CBD–FBBB(B) conjugate has less of a reducing effect on the CoPc than the THC + FBBB(B) conjugate. By CV, the addition of the CBD–FBBB(B) conjugate to CoPc produces a similar current as the THC–FBBB(B) conjugate (**Figure 3.4i**); however, the THC–FBBB(B) conjugate demonstrates a high potential as the second reduction state is reversibly oxidized, suggesting a unique interaction between CoPc and the THC–FBBB(B) conjugate. The spectroelectrochemical differences indicative of coordinating activity between the two cannabinoids with and without FBBB is significantly more pronounced with CoPc over H_2Pc, suggesting that the central metal plays a key role in facilitating Pc–ligand interactions.

Reduction Processes of Metal Pcs in the Presence of THC + FBBB(B)

We next sought to examine the effects of the THC–FBBB(B) conjugate on other metal Pcs in efforts to determine if coordination effects are observed similar to those noted with CoPc. Prior to the application of bias, FePc displays an intensity increase and a Q band peak shift from 659 to 654 nm upon interaction with THC–FBBB(B) (**Figure 3.5a**, black line). Since Fe^{II} cannot easily be reduced, new Q band peaks are not observed. With an applied reducing potential, the Q band reduces in intensity, red-shifting to 657 nm while apparent metal–ligand coordination increases, visualized as peaks at 395 and 440 nm. Similar effects are observed with the soluble ts-CuPc

upon interaction with the THC–FBBB(B) conjugate (**Figure 3.5b**): an intensity increase in the 678 nm Q band absorbance is observed before application of bias, which reduces in intensity with applied potential concurrent with the appearance of a 527 nm metal–ligand coordination peak. A large B band increase is observed with the applied reducing bias, potentially pointing toward a unique cannabinoid–Pc interaction, similar to that of CBD with CoPc. The tbt-CuPc is another soluble form of the CuPc core, however, possessing bulky tert-butyl substitutions on the diiminoisoindoline moieties (**Figure 3.1**). The tbt-CuPc shows substantial spectral shifts from its baseline with the addition of the THC–FBBB(B) conjugate, becoming highly monomeric (**Figure 3.5c**), similar to what was observed with H_2Pc (**Figure 3.3g**). Steric hindrance of the tert-butyl groups likely limits metal–ligand coordination, supporting the role of metal–ligand interactions in the spectroelectrochemical responses of CoPc, FePc, and ts-CuPc in the presence of cannabinoid–FBBB(B) conjugates.

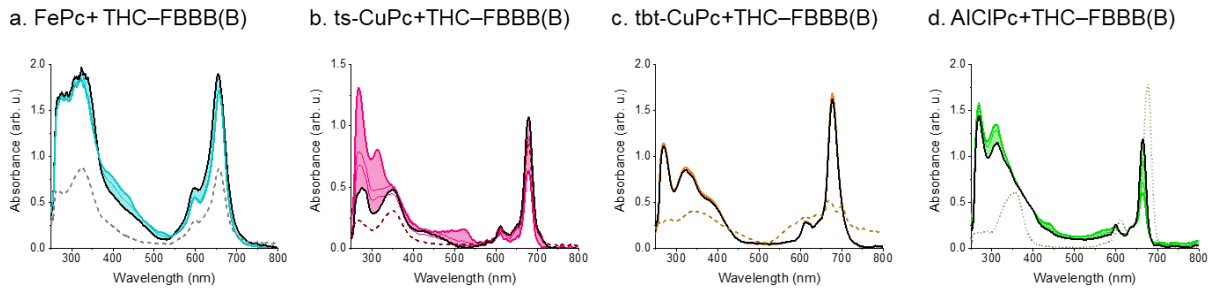

Figure 3.5. *Spectroelectrochemical reduction processes of Pcs with the THC–FBBB(B) conjugate. Absorbance spectral baseline of Pc only (dashed line), treated spectral baseline (black), and first reducing potential responses at 100, 200, and 300 s (colored) of 0.1 μM (a) FePc, (b) ts-CuPc, (c) tbt-CuPc, and (d) AlClPc in DMSO with 0.1 M TBAP electrolyte in a custom quartz SEC cell following equimolar additions THC and FBBB with 50 μM NaOH. The first reducing potential by in situ CV [(a) −1.2, (b) −0.50, (c) −0.75, and (d) −0.75 V] was applied between the platinum micromesh working electrode and platinum wire counter electrode against a Ag/AgCl reference electrode.*

AlClPc is highly monomeric in solution with a very narrow and intense Q band at 678 nm and two split peaks at 646 and 612 nm (**Figure 3.5d**). In the presence of the THC–FBBB(B) conjugate, a 14 nm blue-shift of the main Q band to 664 nm is observed alongside a reduction of intensity. The vibrational split peaks become further separated from the main Q band peak, each blue-shifting 12 to 634 and 600 nm, respectively. With the application of reducing potential, the 664 nm Q band peak becomes less intense, and a small metal coordination peak appears at 435 nm with an increase in light scattering. These large Q band peak shifts suggest that AlClPc is significantly altering its coordination states in the presence of the THC–FBB(B) conjugate[9,47,48].

THC and THC–FBBB Coordination with AlClPc

We performed a series of NMR experiments to elucidate Pc–Pc and Pc–ligand interactions observed from the solution-based spectroelectrochemical screening (**Figure 3.6**). AlClPc was analyzed as it is diamagnetic, and its main Q band peak shifts with additions of THC and the THC–FBBB(B) conjugate (**Figures 3.5d and A.3.2**), implying that interactions between the semiconductor and analyte species may be present. The ^{1}H NMR signal for the R2,3 protons of AlClPc (**Figure 3.1a**), centered at 8.52 ppm, appears as a large doublet of doublets with an adjacent lower frequency doublet of doublets and a high frequency doublet shoulder (**Figure 3.6a**), corresponding to different configurations or coordination orientations of AlClPc. These subspectra were shown to be in slow exchange with one another by using NMR exchange spectroscopy (EXSY, **Figure A.3.3**). With the addition of THC, a new set of doublet of doublets appears centered at 8.37 ppm, implying strong interaction of THC to AlClPc and resulting in a shielding effect. Increasing concentrations of THC increases the intensity of these new peaks (**Figure A.3.4**). Furthermore, on a normalized basis, the smaller set of doublet of doublets at ~8.50 ppm for AlClPc + THC is twice as intense relative to the larger set compared to AlClPc, indicating that the configuration of the AlClPc is affected by an interaction with THC (**Figure 3.6a**). A diffusion ordered NMR spectroscopy (DOSY) experiment (**Figure A.3.5**) also suggests strong coordination of THC with AlClPc. The diffusion constant for the THC in AlClPc + THC is measurably lower than that of THC on its own, indicating an associative interaction between THC and AlClPc (**Figure A.3.5**). Additionally, the 3′ proton signal of THC in the AlClPc + THC solution shifts to higher frequency by 0.02 ppm compared to THC. Similar shifts are also observed for the 5′ and 8 protons on THC again indicating a significant interaction between the THC and the AlClPc. With the addition of the THC–FBBB(B) conjugate, the normalized intensity of the second set of Pc doublets of doublets at 8.50 ppm shifts slightly to lower frequency and appears four times more intense than those of AlClPc and twice as intense as those of AlClPc + THC. Only a very small set of doublets of doublets at 8.37 ppm is visible in the ^{1}H-NMR spectra (**Figure 3.6a**). The 3′ proton of THC is shifted to higher frequency; however, the diffusion coefficient is comparable to that of AlClPc + THC, further demonstrating the level of coordination between those two species.

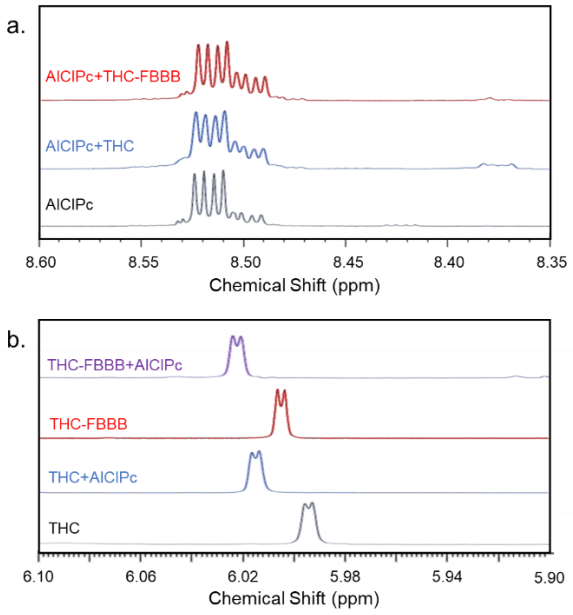

Figure 3.6. *^{1}H-NMR traces of AlClPc, THC, the THC–FBBB(B) conjugate, and AlClPc with THC or the THC–FBBB(B) conjugate. (a) Centered at 8.45 ppm and (b) centered at 6.00 ppm (3' THC proton). ^{1}H-NMR experiments were carried out on a Bruker AVANCE-IIIHD 600 MHz NMR spectrometer equipped with a cryoprobe using standard one-pulse programs.*

In order to investigate the structural effects of analyte–Pc interactions on cannabinoid conformation, NOESY experiments were performed (**Figure 3.7**). While THC can coordinate strongly with AlClPc, it does not significantly alter the optical spectral data (**Figure A.3.2**), showing a limited 3 nm blue shift. These results imply that the overall electrochemical properties of AlClPc are not significantly altered. Conversely, with the THC–FBBB(B) conjugate, significant AlClPc spectral shifts are observed. Thus, by analyzing the effects of THC and the THC–FBBB(B) conjugate by NMR, we can gain additional insights into their coordinating interactions with AlClPc, complementing the spectroelectrochemical analysis. The NOESY spectra show a reduction in intensity at specific cross peaks (**Figure 3.7**, labeled 1., 2., 3.) for both THC + AlClPc and the THC–FBBB conjugate + AlClPc. These spectral changes suggest that in the presence of AlClPc, THC, whether alone or conjugated to FBBB, is more planar in solution. This may be due to intermolecular interactions between the analytes and the semiconductor, further delocalizing the π electron cloud. This corroborates the spectroelectrochemical data, which suggests that adding THC or the THC–FBBB(B) conjugate changes the preference of Pc–Pc configurations, shifting their band gap, and altering the Pcs' electronic properties (**Figure 3.5d**).

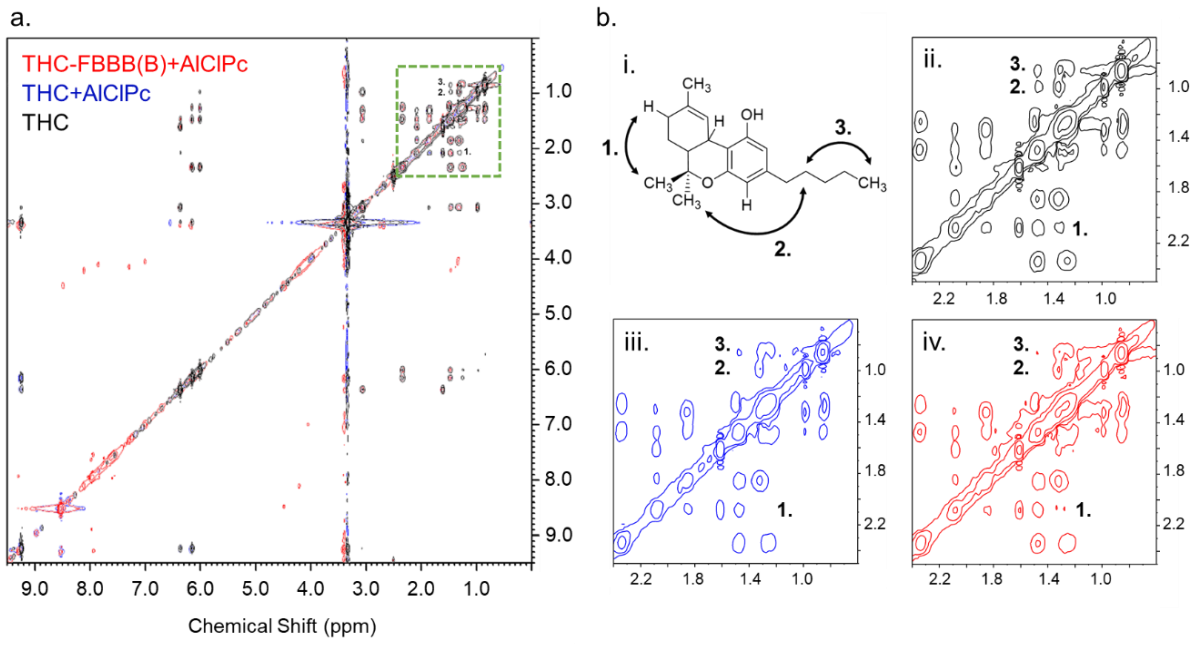

Figure 3.7. *NOESY spectra and assigned proton–proton interactions of THC. (a) Stacked NOESY spectra of THC (black), AlClPc with THC (blue), and AlClPc with the THC–FBBB(B) conjugate (red). Green box denotes inset area shown in (b). (b) (i) assigned THC proton–proton interactions and inset NOESY data between 0.6 and 2.4 ppm of (ii) THC, (iii) AlClPc with THC, and (iv) AlClPc with the THC–FBBB(B) conjugate. NOESY experiments were performed on a Bruker AVANCE II-400 MHz NMR using the standard gradient NOESY pulse programs.*

Effect of Analyte Composition and Pc on Device Performance

With applied source–drain (V_{SD}) and gate–source (V_{GS}) biases to generate a current (I_{SD}), charge can be moved through Pc semiconducting films between the source and the drain at a rate defined by mobility (μ, calculated from eq 1). The V_{GS} bias at which current significantly increases is known as the threshold voltage (V_T). The effects of THC, CBD, FBBB, and the cannabinoid–FBBB(B) conjugates on μ and V_T were explored for CuPc (**Figures 3.8a and A.3.6**) and, previously, on F_{16}-CuPc devices[18]. With the addition of THC, CBD, or FBBB(B) to CuPc devices, μ_H, the rate at which holes are transported across the semiconducting layer decreases by 61.0, 41.8, and 57.5%, while V_T shifts −5, −7, and −11 V respectively. The subsequent addition of THC or CBD to FBBB(B)-coated OTFTs causes a 98.5 and −86% decrease from the baseline, with a −16 and −11 V V_T shift from the baseline, respectively. In our previous work, characterizing CuPc and F_{16}-CuPc based-OTFT devices, cannabinoid sensitivities in the order of 100 nM and selectivity for rapid ratiometric speciation analysis of extracted plant cannabinoid samples were demonstrated, with results comparable to HPLC analysis[18].

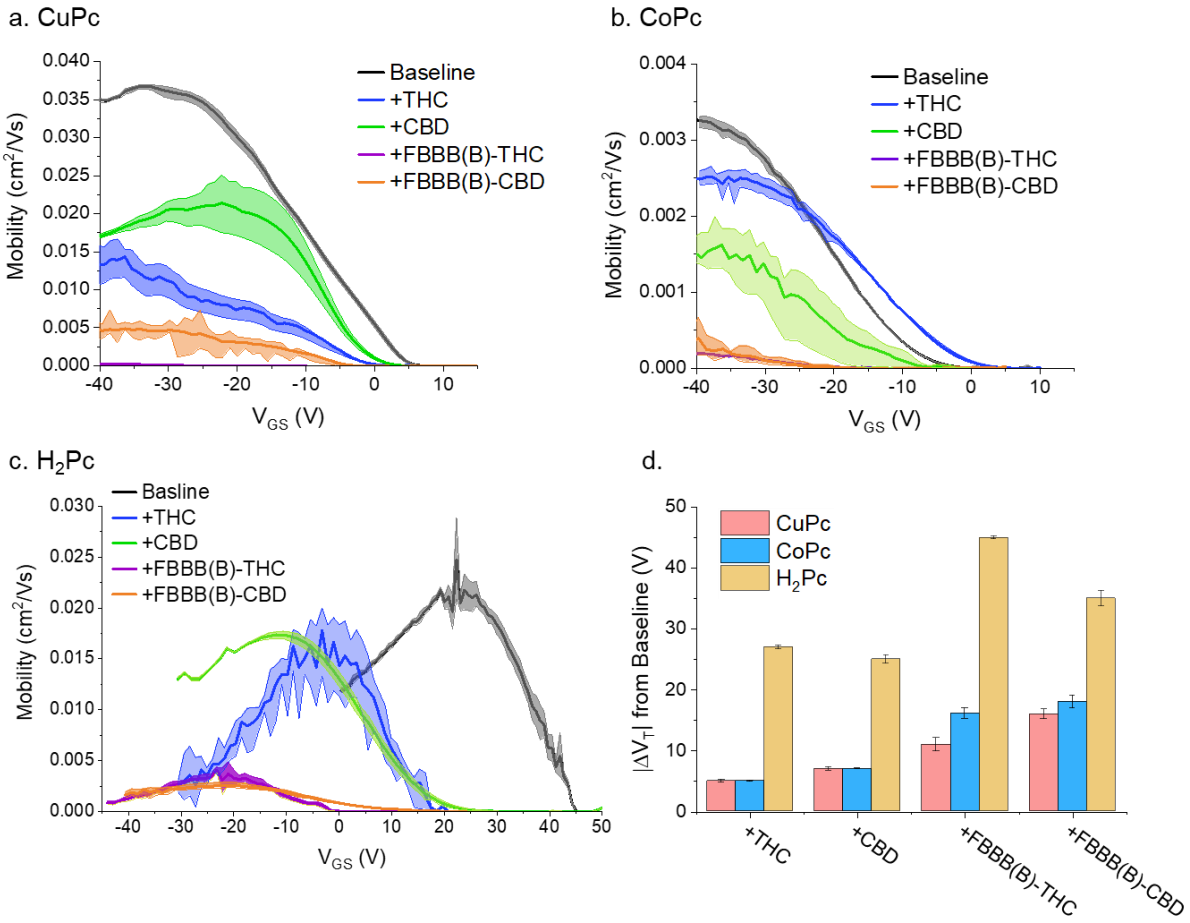

Figure 3.8. *Effect of THC and CBD on the field-effect mobility of alkaline FBBB-treated OTFTs with respect to gate–source voltage (V_{GS}).Field-effect mobility was evaluated for OTFTs consisting of native and alkaline FBBB (20 μM)-treated (a) CuPc, (b) CoPc, or (c) H_2Pc semiconductors following the addition of 0.5 μL of 20 μM THC or CBD in ACN. (d) Absolute voltage threshold shifts from the baseline for each treatment by material. Mobility curves represent the mean (solid line) and data range (shaded region) of three V_{GS} sweeps at saturation across four devices with an applied V_{SD} of −50 V. Mobilities were calculated between adjacent points of the transfer data using eq 1. Errors bars are standard deviation.*

Of the materials spectroelectrochemically analyzed, FePc is not air stable and ts-CuPc is incompatible with PVD, precluding either from use in our cannabinoid-sensing devices. Further, neither AlClPc nor tbt-CuPc demonstrated significant spectroelectrochemical alterations upon the application of bias, suggesting that they would be poor performing materials when incorporated into an OTFT sensor. Thus, CoPc and H_2Pc were selected through solution-based screening to fabricate OTFT devices on account of their substantial bias-induced spectroelectrochemical changes and their compatibility with our fabrication and characterization processes. With CoPc as the semiconducting material, performance changes from baseline of μ_H −23.4%, V_T +5 V with THC; μ_H −48.6%, V_T −7.0 V with CBD; ; μ_H −94.1%, V_T −16 V with FBBB(B)-THC; and μ_H −58.4%, V_T −18.1 V with FBBB(B)-CBD are observed, respectively (**Figure 3.8b**). H_2Pc has a high baseline

V_T of 45 V, shifting by −27, −25, and −30 V and μ_H decreasing by 30.1, 29.8, and 49.2% with the addition of THC, CBD, and FBBB(B), respectively. H_2Pc shifts another −15 or −35 V with μ_H decreasing an additional 34.4 or 59% with the subsequent addition of FBBB(B)-THC or FBBB(B)-CBD. With the addition of analytes, both on and off currents decrease (**Figure A.3.7**), with larger off-current decreases corresponding to larger V_T shifts. We surmise, these performance changes result from the formation of deep charge traps[21,49].

From the spectroelectrochemical data of H_2Pc and CoPc (**Figures 3.2 and 3.3** respectively), it can be inferred that both THC and FBBB interact broadly with the Pc macrocycle, irrespective of the central species, donating electron density to result in the observed increases in Q band intensity, possibly as a result of their planar shapes and delocalized π electrons[46]. This is reflected in the device data as all three materials display very similar trends. THC results in both moderate μ_H decreases and V_T shift, while FBBB(B) results in slightly greater μ_H decrease and V_T shifts relative to the baseline. Through spectrochemical analysis, CBD was observed to coordinate with H_2Pc similarly to THC (**Figure 3.3a,b**), resulting in similar device performance characteristics (**Figure 3.8c**). However, CBD promotes the reduction of CoPc to a greater extent than THC, likely through stronger coordination with the central cobalt as indicted by spectroelectrochemical changes (**Figure 3.4**) and displays a greater V_T shift in OTFT devices. The FBBB(B)–THC conjugate results in the greatest spectral Q band changes, closely mirrored by the FBBB(B)–CBD conjugate, respectively promotes the greatest and second greatest changes to OTFT performance.

Similar in molecular size, HOMO/LUMO levels, and electrochemical properties, cobalt and copper, and thus CoPc and CuPc, could be expected to coordinate similarly with the cannabinoid–FBBB(B) conjugates, forming aggregates and producing the observed similar sensing responses as OTFT devices. Without a central metal, H_2Pc becomes highly monomeric in the presence of the cannabinoid–FBBB(B) conjugates, with changes in OTFT performance manifesting primarily as a significant −45, and −35 V V_T shifts, for THC and CBD, respectively, through pseudo-doping effects[8,22,31,50,51]. Thus, the presence of a central metal allows for direct coordinating interactions that could cause the cannabinoid–FBBB(B) conjugates to preferentially act as a charge trap or promote a non-charge conducting aggregate Pc species. It could then be inferred that evidence of strong metal–analyte coordination correlates to large μ_H, and off current, decreases through charge trapping effects[49], while preferential Pc ring–analyte coordination results in V_T shifts by acting as a pseudo-dopant. This implies that, for screening potential materials for OTFT device

sensing, specific peak changes to the Q band region, aggregate formation, and signs of preferential M-ligand coordination can be used to guide material selection.

Conclusions

Herein, we demonstrate that spectroelectrochemistry can be used as a powerful technique to gain insights into interactions of Pcs with analytes that can be used to predict the degree of sensing response of Pc-based OTFT devices. Cannabinoids are shown to coordinate strongly with Pcs in solution with limited alterations to their electrochemical properties. The FBBB(B)–cannabinoid conjugate coordinates less strongly with Pcs; however, it significantly alters their electrochemical properties, with effects varying dependent on bound cannabinoid species. These spectroelectrochemical differences are reflected in the elicited sensing response of OTFT devices. THC and CBD, and their respective FBBB(B) conjugates, are shown to have varying interactions with both H_2Pc and CoPc, with improved selectivity in the presence of a central metal and the colorimetric probe. A screen of four additional Pcs (FePc, AlClPc, ts-CuPc, and tbt-CuPc) serves to demonstrate the effects of alterations to the central metal alongside peripheral and axial substitutions. AlClPc was further studied as an example due to its substantial spectral shifts in the presence of analytes, indicating complex interactions and the formation of new coordinated species. ^{1}H-NMR, 2D DOSY, and NOESY experiments were conducted to further characterize the structural underpinnings of the observed spectroelectrochemical changes, suggesting that analyte–Pc interactions promote analyte planarity and increased π electron delocalization. OTFT devices demonstrate differences in sensing response between H_2Pc, CoPc, and CuPc through significant variations in device performance upon interaction with THC–FBBB(B). This work further demonstrates the utility of Pc semiconductors for cannabinoid sensing and provides a straightforward solution-based screening tool for highly selective materials for sensor integration.

Materials

H_2Pc (metal free phthalocyanine), tbt-CuPc (copper(II) 2,9,16,23-tetra-tert-butyl-phthalocyanine), ts-CuPc (3,4′,4″,4‴-tetrasulfonic acid copper(II)phthalocyanine), 4-amino-2,5-diethoxybenzanilide diazotated zinc double salt (Fast Blue BB, FBBB), TBAP, and (octyl)trichlorosilane (OTS, 97%) were obtained from Sigma-Aldrich. CoPc, FePc, and AlClPc were obtained from TCI Chemicals. All Pcs were purified by train sublimation before use. All other materials were used as received unless otherwise noted. Cannabinoid standards were obtained from Toronto Research Chemicals. All solvents were of HPLC grade and purchased from Fischer Scientific.

Spectroelectrochemistry

10^{-4} M of Pc was thoroughly mixed in DMSO and filtered through a 0.2 μm syringe filter before the addition of 0.1 M TBAP electrolyte. 3 mL of solution was placed in a custom spectroelectrochemical cell, and a baseline absorbance measurement was taken with an Ocean Optics flame spectrometer with a filter width of 5 μm. A CV curve between 0.5 and −1.9 V was then collected with a Princeton Instruments VersaSTAT 3 Potentiostat Glavanostat at a rate of 0.1 mV/s with a platinum micromesh working electrode, platinum wire counter electrode, and Ag/AgCl reference electrode. UV–vis absorption measurements were then carried out at precise time intervals, while a constant voltage bias corresponding to first reducing peak of the previously obtained cyclic voltammogram was applied to the cell.

NMR

^{1}H-NMR and DOSY experiments were performed on a Bruker AVANCE IIIHD 600 MHz spectrometer equipped with a cryoprobe using the standard Bruker one-pulse program and stimulated echo DOSY pulse program, respectively. The one-pulse spectra were collected with 16 scans using a 30° pulse. The acquisition time was 4 s. DOSY experiments were carried out with gradient strengths varying quadratically over 32 increments from 2 to 98% of the maximum gradient strength (~50 T/m). The total diffusion gradient duration and diffusion time were 3 and 100 ms, respectively. Each increment was collected with 16 scans, a 4 s acquisition time and a 4 s recycle delay. NOESY spectra were performed on a Bruker AVANCE II 400 MHz spectrometer using the standard gradient NOESY pulse program with a mixing time of 1 s. Spectra consisted of 256 increments each with 16 scans and a 1 s recycle delay. In all spectra, the chemical scale was calibrated to the residual proton signal of DMSO-6 at 2.50 ppm.

Preparation and Device Characterization

Silicon substrates with thermally grown 230 nm thick SiO_2 dielectric and prepatterned gold-source drain electrodes (W = 2000 μm, L = 10 μm) were purchased from Fraunhofer IPMS and used to make bottom-gate bottom-contact transistors. Each Fraunhofer contained four devices. Substrates were first washed with acetone to remove the photoresist, then rinsed with isopropanol, and dried with a nitrogen gas stream. Substrates were then treated with oxygen plasma for 15 min and subsequently rinsed with water, isopropanol, and dried with a nitrogen gas stream before being immersed in a solution of 1% v/v OTS in toluene for 1 h at 70 °C. The OTS-treated substrates were washed with toluene, isopropanol, and dried with a nitrogen gas stream before being transferred into an Angstrom EvoVac thermal evaporator, and 200 Å of CuPc, CoPc,

or H_2Pc was deposited at 25 °C and pressure below 2×10^{-6} torr at a rate of 0.2 Å/s by sublimation onto the respective substrates.

The source–drain electrodes of each device were contacted with BeCu alloy probe tips, and electrical characterization was performed using a custom electrical probe station, oesProbe A10000-P290 (Element Instrumentation Inc. & Kreus Design Inc.) with a Keithley 2614B to discrete V_{GS} and V_{SD} values, while measuring I_{SD}. Using I_{SD} and V_{GS}, the saturation field-effect mobility, threshold voltage, and on/off current can be determined. The general expression relating current to saturation field-effect mobility and gate voltage is shown below

$$I_{SD} = \frac{\mu C_i W}{2L}(V_{GS} - V_T)^2 \quad (1)$$

where I_{SD} is the source–drain current, μ is the field effect mobility, C_i is the capacitance, W is the width of the channel, L is the length of the channel, V_{GS} is the gate–source voltage, and V_T is the threshold voltage. eq 1 can be rearranged to allow for mobility and threshold voltage to be calculated directly from the slope and x-intercept of the $\sqrt{I_{SD}}$ versus V_{GS} curve.

Liquid analytes were dissolved in ACN and pipetted directly on the semiconducting channel and allowed to dry for 3 min before device characterization. Maximum and minimum obtained mobilities are displayed in plots in lieu of standard deviation to better represent reproducibility in the device performance.

Supplemental Information

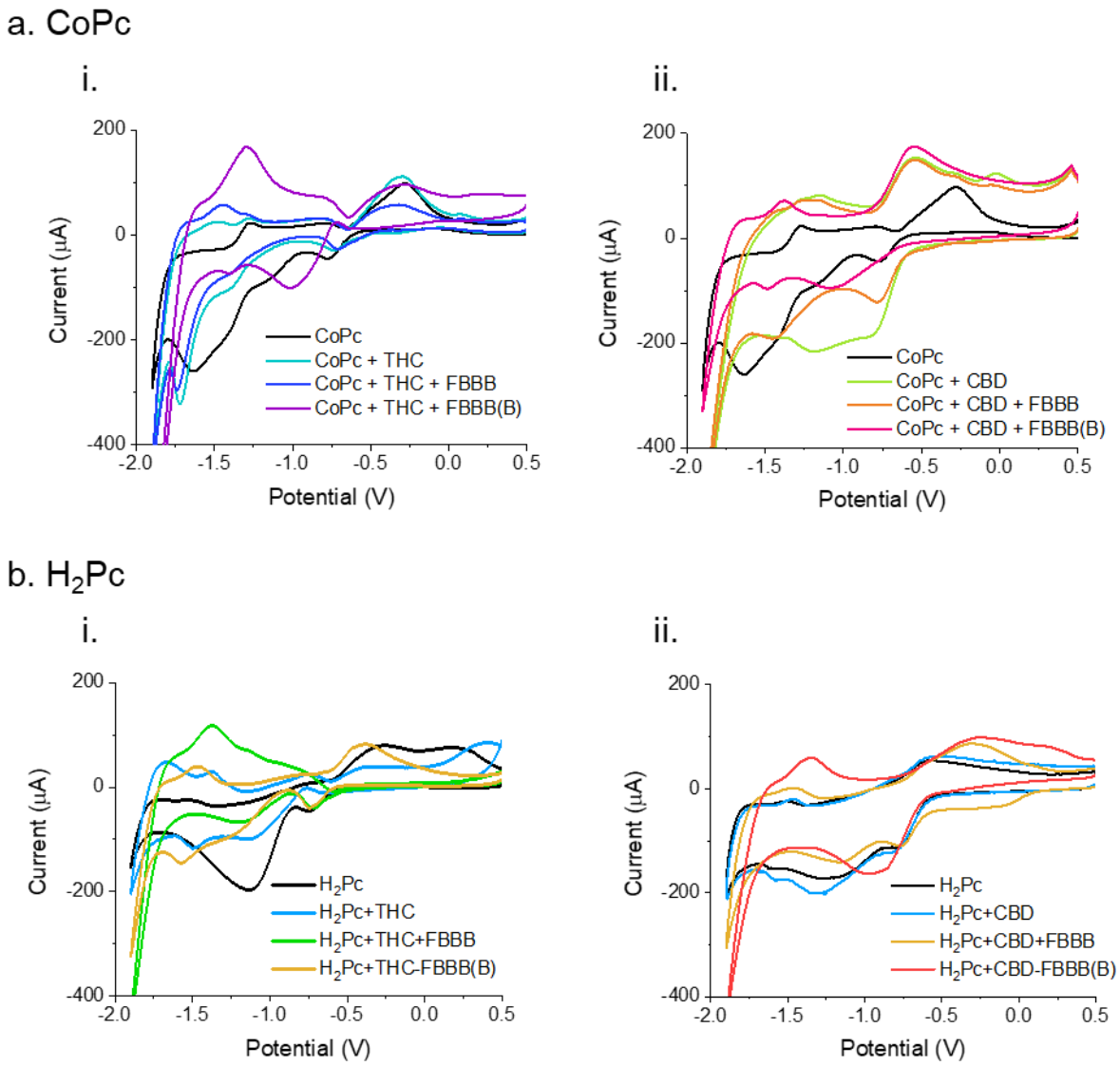

Figure A.3.1. *Cyclic voltammograms of CoPc and H_2Pc with cannabinoids and a colorimetric binding agent. A scan rate of 0.1 mV/s was applied between a platinum micromesh working electrode and platinum wire counter electrode against an Ag/AgCl reference electrode and data collected on a VersaSTAT 3 potentiostat.*

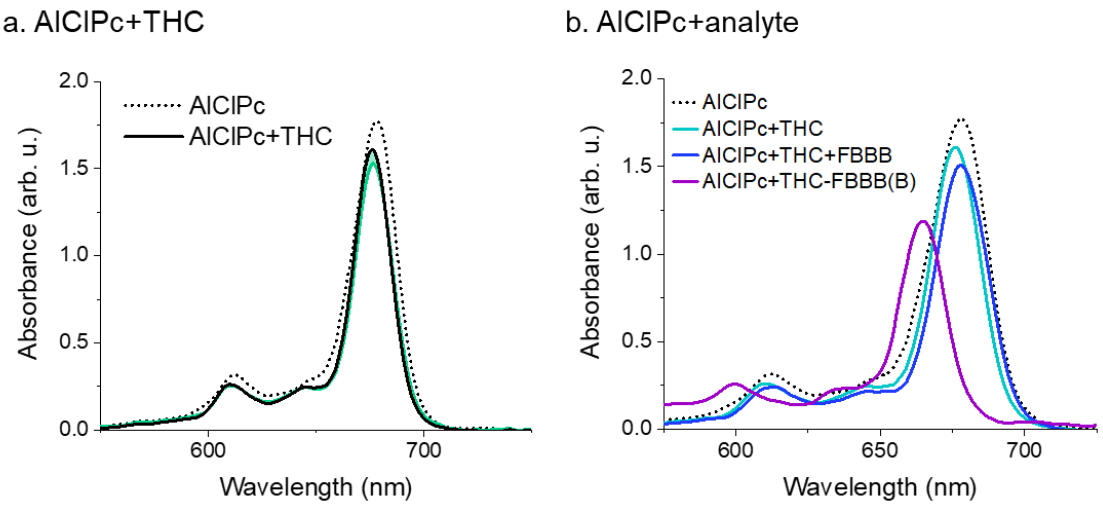

Figure A.3.2. *Q band absorbance of the spectroelectrochemical reduction of AlClPc+THC and UV-Vis spectra of AlClPc with analytes.*

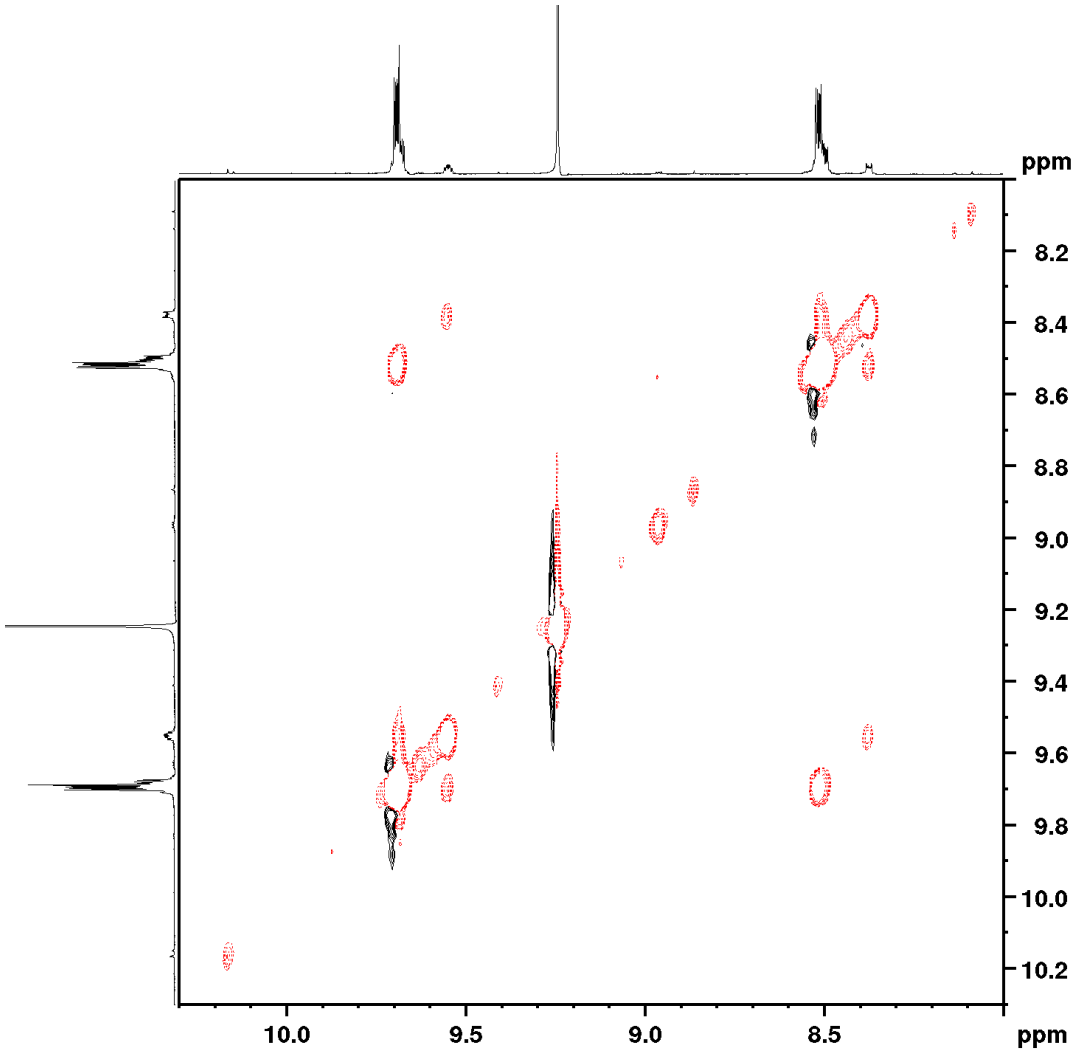

Figure A.3.3. *Partial EXSY spectra of AlClPc+THC. The experiment was carried out on a Bruker Avance-IIIHD 600 MHz spectrometer equipped with a cryoprobe using the standard gradient NOESY/EXSY pulse program with a mixing time of 1 second and a recycle time of 3 seconds. Each of 213 increments were collected with 4 scans. The cross peaks in the spectrum are of the same sign as the diagonal and are due to conformational exchange.*

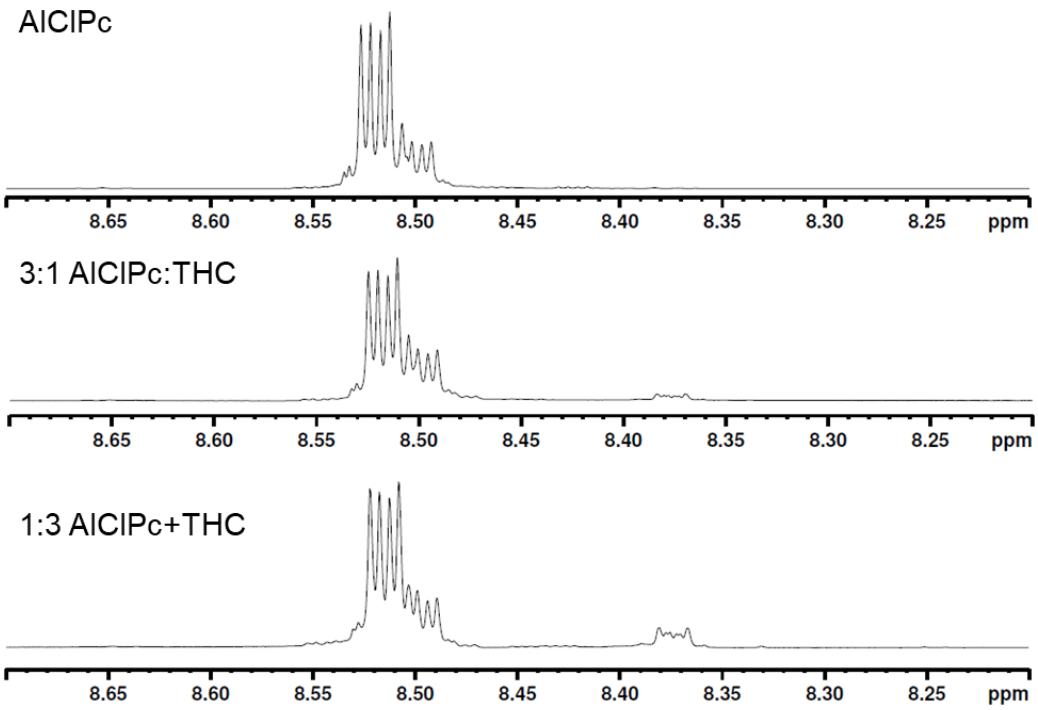

Figure A.3.4. *^{1}H-NMR traces of R2,3 protons of AlClPc with increasing concentrations of THC.*

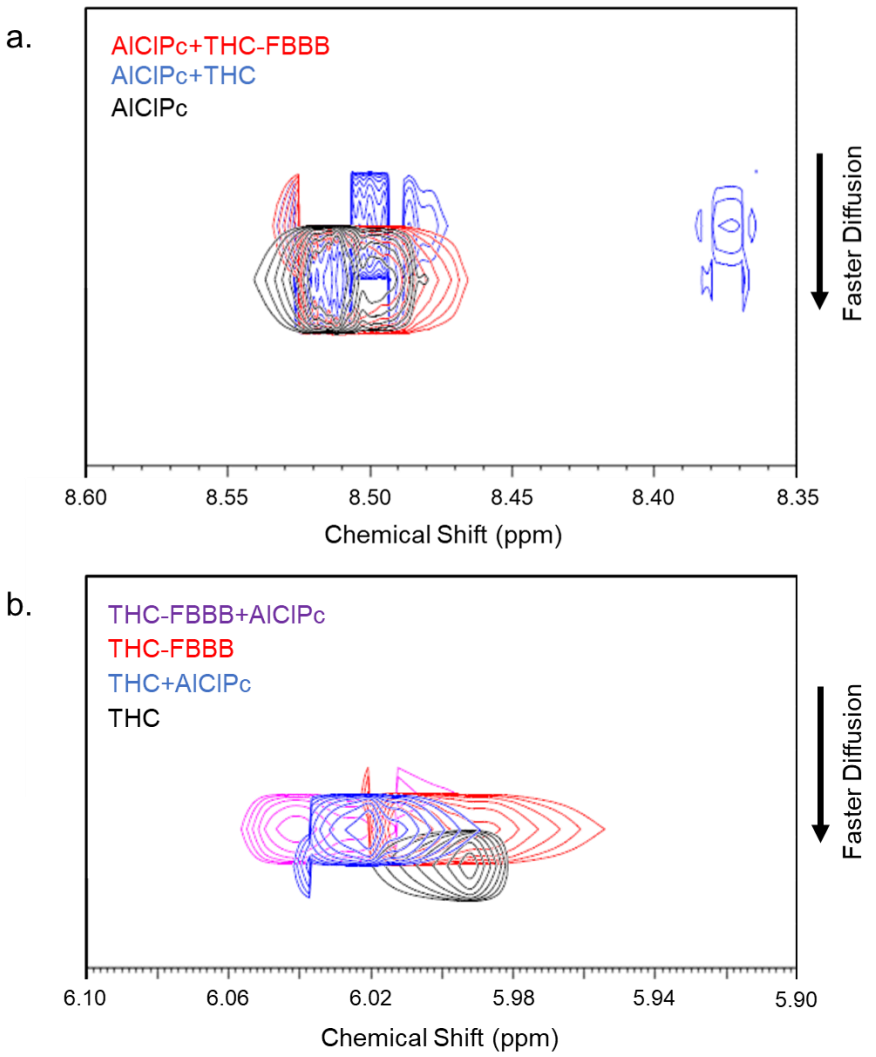

Figure A.3.5. *DOSY spectra of AlClPc, THC, the THC-FBBB(B) conjugate, and AlClPc with THC or the THC-FBBB(B) conjugate. (a) centered at 8.45 ppm, (b) centered at 6.00 ppm (3' THC proton). DOSY experiments were carried out on a Bruker Avance-IIIHD 600 MHz NMR spectrometer equipped with a cryoprobe using standard simulated echo DOSY pulse programs.*

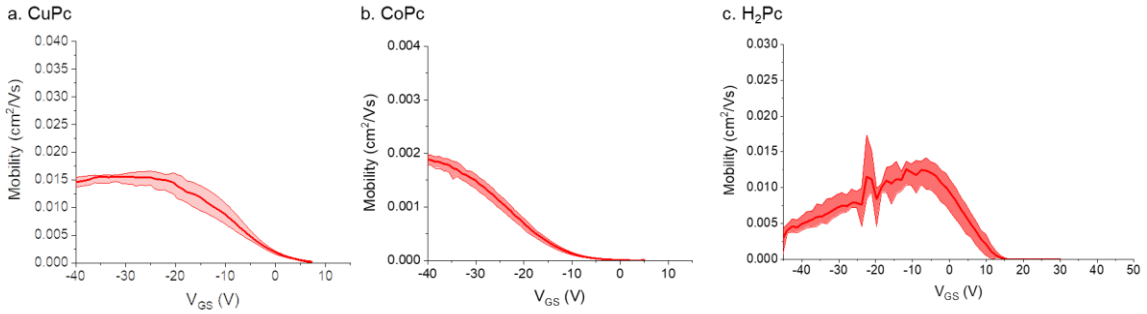

Figure A.3.6. *Effect of FBBB(B) on the field-effect mobility of OTFTs with respect to gate-source voltage (V_{GS}). Field-effect mobility was evaluated for OTFTs consisting of alkaline FBBB (20 µM)-treated (a) CuPc, (b) CoPc, or (c) H_2Pc, semiconductors. Mobility curves represent the mean (solid line) and data range (shaded region) of three V_{GS} sweeps at saturation across four devices with an applied V_{SD} of -50V. Mobilities were calculated between adjacent points of the transfer data using equation 1.*

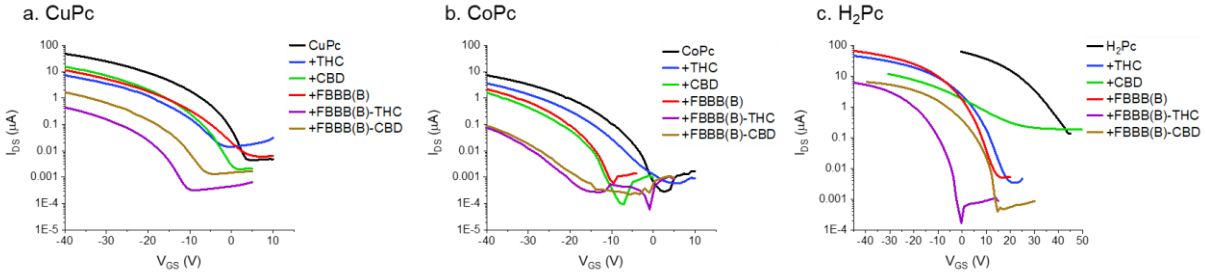

Figure A.3.7. *Effect of THC and CBD on the I_{DS}-V_{GS} curves of alkaline FBBB-treated OTFTs with respect to gate-source voltage (V_{GS}). I_{SD} was evaluated for OTFTs consisting of native and alkaline FBBB (20 µM)-treated (a) CuPc, (b) CoPc, or (c) H_2Pc, semiconductors following the addition of 0.5 µL of 20 µM THC or CBD in ACN with an applied V_{SD} of -50V.*

References

1. Denes, G. Phthalocyanines: Properties and Applications, Volume 4. J. Am. Chem. Soc. 1998, 120, 241– 242, DOI: 10.1021/ja965771a
2. Wöhrle, D.; Schnurpfeil, G.; Makarov, S. G.; Kazarin, A.; Suvorova, O. N. Practical Applications of Phthalocyanines - from Dyes and Pigments to Materials for Optical, Electronic and Photo-electronic Devices. Macroheterocycles 2012, 5, 191– 202, DOI: 10.6060/mhc2012.120990w
3. Urbani, M.; Ragoussi, M. E.; Nazeeruddin, M. K.; Torres, T. Phthalocyanines for Dye-Sensitized Solar Cells. Coordination Chemistry Reviews; Elsevier B.V., February 15, 2019, pp 1– 64
4. de la Torre, G.; Bottari, G.; Torres, T. Phthalocyanines and Subphthalocyanines: Perfect Partners for Fullerenes and Carbon Nanotubes in Molecular Photovoltaics. Adv. Energy Mater. 2017, 7, 1601700, DOI: 10.1002/aenm.201601700
5. Melville, O. A.; Lessard, B. H.; Bender, T. P. Phthalocyanine-Based Organic Thin-Film Transistors: A Review of Recent Advances. ACS Appl. Mater. Interfaces 2015, 7, 13105– 13118, DOI: 10.1021/acsami.5b01718
6. Elkington, D.; Cooling, N.; Belcher, W.; Dastoor, P.; Zhou, X. Organic Thin-Film Transistor (OTFT)-Based Sensors. Electronics 2014, 3, 234– 254, DOI: 10.3390/electronics3020234
7. Melville, O. A.; Grant, T. M.; Lessard, B. H. Silicon Phthalocyanines as N-Type Semiconductors in Organic Thin Film Transistors. J. Mater. Chem. C 2018, 6, 5482– 5488, DOI: 10.1039/c8tc01116h
8. Fahlman, M.; Fabiano, S.; Gueskine, V.; Simon, D.; Berggren, M.; Crispin, X. Interfaces in Organic Electronics. Nat. Rev. Mater. 2019, 4, 627– 650, DOI: 10.1038/s41578-019-0127-y
9. Bohrer, F. I.; Sharoni, A.; Colesniuc, C.; Park, J.; Schuller, I. K.; Kummel, A. C.; Trogler, W. C. Gas Sensing Mechanism in Chemiresistive Cobalt and Metal-Free Phthalocyanine Thin Films. J. Am. Chem. Soc. 2007, 129, 5640– 5646, DOI: 10.1021/ja0689379
10. Boileau, N. T.; Cranston, R.; Mirka, B.; Melville, O. A.; Lessard, B. H. Metal Phthalocyanine Organic Thin-Film Transistors: Changes in Electrical Performance and Stability in Response to Temperature and Environment. RSC Adv. 2019, 9, 21478– 21485, DOI: 10.1039/c9ra03648b
11. Li, L.; Tang, Q.; Li, H.; Hu, W. Molecular Orientation and Interface Compatibility for High Performance Organic Thin Film Transistor Based on Vanadyl Phthalocyanine. J. Phys. Chem. B 2008, 112, 10405– 10410, DOI: 10.1021/jp800879g
12. Anthopoulos, T. D.; Shafai, T. S. Oxygen Induced P-Doping of α-Nickel Phthalocyanine Vacuum Sublimed Films: Implication for Its Use in Organic Photovoltaics. Appl. Phys. Lett. 2003, 82, 1628– 1630, DOI: 10.1063/1.1559649
13. Zhuang, X.; Han, S.; Huai, B.; Shi, W.; Junsheng, Y. Sub-Ppm and High Response Organic Thin-Film Transistor NO2 Sensor Based on Nanofibrillar Structured TIPS-Pentacene. Sens. Actuators, B 2019, 279, 238– 244, DOI: 10.1016/j.snb.2018.10.002
14. Trogler, W. C. Chemical Sensing with Semiconducting Metal Phthalocyanines. Struct. Bond 2012, 142, 91– 118
15. Klyamer, D.; Sukhikh, A.; Gromilov, S.; Krasnov, P.; Basova, T. Fluorinated Metal Phthalocyanines: Interplay between Fluorination Degree, Films Orientation, and Ammonia Sensing Properties. Sensors 2018, 18, 2141, DOI: 10.3390/s18072141
16. Schöllhorn, B.; Germain, J. P.; Pauly, A.; Maleysson, C.; Blanc, J. P. Influence of Peripheral Electron-Withdrawing Substituents on the Conductivity of Zinc Phthalocyanine in the Presence of Gases. Part 1: Reducing Gases. Thin

Solid Films 1998, 326, 245– 250, DOI: 10.1016/s0040-6090(98)00553-7
17. Polat, M. P.; Akyüz, D.; Yasemin Yenilmez, H.; Koca, A.; Altindal, A.; Bayr, Z. A. Sensing Alcohol Vapours with Novel Unsymmetrically Substituted Metallophthalocyanines. Dalton Trans. 2019, 48, 9194– 9204
18. Comeau, Z. J.; Boileau, N. T.; Lee, T.; Melville, O. A.; Rice, N. A.; Troung, Y.; Harris, C. S.; Lessard, B. H.; Shuhendler, A. J. On-the-Spot Detection and Speciation of Cannabinoids Using Organic Thin-Film Transistors. ACS Sens. 2019, 4, 2706– 2715, DOI: 10.1021/acssensors.9b01150
19. Leghissa, A.; Hildenbrand, Z. L.; Schug, K. A. A Review of Methods for the Chemical Characterization of Cannabis Natural Products. J. Sep. Sci. 2018, 41, 398– 415, DOI: 10.1002/jssc.201701003
20. Klyamer, D.; Sukhikh, A.; Gromilov, S.; Krasnov, P.; Basova, T. Fluorinated Metal Phthalocyanines: Interplay between Fluorination Degree, Films Orientation, and Ammonia Sensing Properties. Sensors 2018, 18, 2141, DOI: 10.3390/s18072141
21. Sirringhaus, H. Reliability of Organic Field-Effect Transistors. Adv. Mater. 2009, 21, 3859– 3873, DOI: 10.1002/adma.200901136
22. Hollerer, M.; Lüftner, D.; Hurdax, P.; Ules, T.; Soubatch, S.; Tautz, F. S.; Koller, G.; Puschnig, P.; Sterrer, M.; Ramsey, M. G. Charge Transfer and Orbital Level Alignment at Inorganic/Organic Interfaces: The Role of Dielectric Interlayers. ACS Nano 2017, 11, 6252– 6260, DOI: 10.1021/acsnano.7b02449
23. Olivier, Y.; Muccioli, L.; Lemaur, V.; Geerts, Y. H.; Zannoni, C.; Cornil, J. Theoretical Characterization of the Structural and Hole Transport Dynamics in Liquid-Crystalline Phthalocyanine Stacks. J. Phys. Chem. B 2009, 113, 14102– 14111, DOI: 10.1021/jp9061169
24. Boileau, N. T.; Melville, O. A.; Mirka, B.; Cranston, R.; Lessard, B. H. P and N Type Copper Phthalocyanines as Effective Semiconductors in Organic Thin-Film Transistor Based DNA Biosensors at Elevated Temperatures. RSC Adv. 2019, 9, 2133– 2142, DOI: 10.1039/c8ra08829b
25. Demirbaş, Ü.; Akyüz, D.; Mermer, A.; Akçay, H. T.; Demirbaş, N.; Koca, A. I.; Kantekin, H. The Electrochemical and Spectroelectrochemical Properties of Metal Free and Metallophthalocyanines Containing Triazole/Piperazine Units. Spectrochim. Acta, Part A 2016, 153, 478– 487, DOI: 10.1016/j.saa.2015.08.050
26. Arici, M.; Arican, D.; Uğur, A. L.; Erdoğmuş, A.; Koca, A. Electrochemical and Spectroelectrochemical Characterization of Newly Synthesized Manganese, Cobalt, Iron and Copper Phthalocyanines. Electrochim. Acta 2013, 87, 554– 566, DOI: 10.1016/j.electacta.2012.09.045
27. Yanagisawa, S.; Yasuda, T.; Inagaki, K.; Morikawa, Y.; Manseki, K.; Yanagida, S. Intermolecular Interaction as the Origin of Red Shifts in Absorption Spectra of Zinc-Phthalocyanine from First Principles. J. Phys. Chem. A 2013, 117, 11246– 11253, DOI: 10.1021/jp407608w
28. Rauf, M. A.; Hisaindee, S.; Graham, J. P.; Nawaz, M. Solvent Effects on the Absorption and Fluorescence Spectra of Cu(II)-Phthalocyanine and DFT Calculations. J. Mol. Liq. 2012, 168, 102– 109, DOI: 10.1016/j.molliq.2012.01.008
29. Honório, K. M.; Da Silva, A. B. F. A Theoretical Study on the Influence of the Frontier Orbitals HOMO and LUMO and the Size of C4 and C2 Substituents in the Psychoactivity of Cannabinoid Compounds. J. Mol. Struct.: THEOCHEM 2002, 578, 111– 117, DOI: 10.1016/s0166-1280(01)00690-x
30. Liu, Z.; Zhang, X.; Zhang, Y.; Jiang, J. Theoretical Investigation of the Molecular, Electronic Structures and Vibrational Spectra of a Series of First Transition Metal Phthalocyanines. Spectrochim. Acta, Part A 2007, 67, 1232– 1246, DOI: 10.1016/j.saa.2006.10.013

31. Coropceanu, V.; Cornil, J.; da Silva Filho, D. A.; Olivier, Y.; Silbey, R.; Brédas, J. L. Charge Transport in Organic Semiconductors. Chem. Rev. 2007, 107, 926– 952, DOI: 10.1021/cr050140x
32. Caruso, F.; Atalla, V.; Ren, X.; Rubio, A.; Scheffler, M.; Rinke, P. First-Principles Description of Charge Transfer in Donor-Acceptor Compounds from Self-Consistent Many-Body Perturbation Theory. Phys. Rev. B: Condens. Matter Mater. Phys. 2014, 90, 085141, DOI: 10.1103/PhysRevB.90.085141
33. Mizrahi, A.; Bukuroshi, E.; Vestfrid, J.; Bender, T. P.; Gross, Z. Axial/Peripheral Chloride/Fluoride-Substituted Boron Subphthalocyanines as Electron Acceptors. Inorg. Chem. 2020, 59, 2641– 2645, DOI: 10.1021/acs.inorgchem.9b03529
34. dos Santos, N. A.; Souza, L. M.; Domingos, E.; França, H. S.; Lacerda, V.; Beatriz, A.; Vaz, B. G.; Rodrigues, R. R. T.; Carvalho, V. V.; Merlo, B. B.; Kuster, R. M.; Romão, W. Evaluating the Selectivity of Colorimetric Test (Fast Blue BB Salt) for the Cannabinoids Identification in Marijuana Street Samples by UV–Vis, TLC, ESI(+)FT-ICR MS and ESI(+)MS/MS. Forensic Chem. 2016, 1, 13– 21, DOI: 10.1016/j.forc.2016.07.001
35. Camp, P. J.; Jones, A. C.; Neely, R. K.; Speirs, N. M. Aggregation of Copper(II) Tetrasulfonated Phthalocyanine in Aqueous Salt Solutions. J. Phys. Chem. A 2002, 106, 10725– 10732, DOI: 10.1021/jp026551o
36. Choi, M. T. M.; Li, P. P. S.; Ng, D. K. P. A Direct Comparison of the Aggregation Behavior of Phthalocyanines and 2,3-Naphthalocyanines. Tetrahedron 2000, 56, 3881– 3887, DOI: 10.1016/s0040-4020(00)00326-4
37. Antonov, L.; Gergov, G.; Petrov, V.; Kubista, M.; Nygren, J. UV-Vis Spectroscopic and Chemometric Study on the Aggregation of Ionic Dyes in Water. Talanta 1999, 49, 99– 106, DOI: 10.1016/s0039-9140(98)00348-8
38. Day, P.; Williams, R. J. P. Spectra of Polycrystalline Phthalocyanines in the Visible Spectra and Photo Conduction of Phthalocyanine Complexes (I). Electr. Prop. Phthalocyanines J. Chem. Phys. 1962, 37, 567, DOI: 10.1063/1.1701375
39. Nakai, K.; Usami, J.; Kobayashi, N. Metal Phthalocyanine Showing Four-Peak Q-Band Similar to Metal-Free Phthalocyanines: Nickel 1,4-Di(Trifluorosulfonyl)-Phthalocyanine. J. Porphyr. Phthalocyanines 2007, 11, 222– 227, DOI: 10.1142/s108842460700028x
40. Ueno, L. T.; Machado, A. E. H.; Machado, F. B. C. Theoretical Studies of Zinc Phthalocyanine Monomer, Dimer and Trimer Forms. J. Mol. Struct.: THEOCHEM 2009, 899, 71– 78, DOI: 10.1016/j.theochem.2008.12.013
41. Lessard, B. H.; Al-Amar, M.; Grant, T. M.; White, R.; Lu, Z.-H.; Bender, T. P. From Chloro to Fluoro, Expanding the Role of Aluminum Phthalocyanine in Organic Photovoltaic Devices. J. Mater. Chem. A 2015, 3, 5047– 5053, DOI: 10.1039/c4ta06759b
42. Zagal, J. H.; Bedioui, F. Electrochemistry of N4 Macrocyclic Metal Complexes: Volume 2: Biomimesis, Electroanalysis and Electrosynthesis of MN4 Metal Complexes, 2nd ed; Springer International Publishing, 2016.
43. Li, R.; Zhang, X.; Zhu, P.; Ng, D. K. P.; Kobayashi, N.; Jiang, J. Electron-Donating or -Withdrawing Nature of Substituents Revealed by the Electrochemistry of Metal-Free Phthalocyanines. Inorg. Chem. 2006, 45, 2327– 2334, DOI: 10.1021/ic051931k
44. Yu, B.; Lever, A. B. P.; Swaddle, T. W. Electrochemistry of Metal Phthalocyanines in Organic Solvents at Variable Pressure. Inorg. Chem. 2004, 43, 4496– 4504, DOI: 10.1021/ic040032d
45. Hush, N. S.; Woolsey, I. S. The electronic absorption spectra of phthalocyanine monomers and dimers. Mol. Phys. 1971, 21, 465– 474, DOI: 10.1080/00268977100101641

46. Kumer, A.; Sarkar, N.; Paul, S.; Zannat, A. The Theoretical Prediction of Thermophysical Properties, HOMO, LUMO, QSAR and Biological Indics of Cannabinoids (CBD) and Tetrahhdrocannabinol (THC) by Computational Chemistry. Adv. J. Chem. A 2019, 2, 190– 202
47. Makarov, S. G.; Kazarin, A. S.; Suvorova, O. N.; Ketkov, S. Y.; Lopatin, M. A.; Wöhrle, D. Ionic Interactions between Charged Phthalocyanine and Fullerene Derivatives. Macroheterocycles 2014, 7, 145– 152, DOI: 10.6060/mhc140487m
48. Nevin, W. A.; Liu, W.; Greenberg, l. S.; Hempstead, M. R.; Marcuccio, S. M.; Melnik, M.; Leznoff, l. C.; Lever, A. B. J. Electroanal. Chem., P. C. Van Den Brink; Ultrasound Teach. Cases, 1973; Vol. 15, 891− 899.
49. Salleo, A.; Endicott, F.; Street, R. A. Reversible and Irreversible Trapping at Room Temperature in Poly(Thiophene) Thin-Film Transistors. Appl. Phys. Lett. 2005, 86, 1263505, DOI: 10.1063/1.1968437
50. Aghamohammadi, M.; Rödel, R.; Zschieschang, U.; Ocal, C.; Boschker, H.; Weitz, R. T.; Barrena, E.; Klauk, H. Threshold-Voltage Shifts in Organic Transistors Due to Self-Assembled Monolayers at the Dielectric: Evidence for Electronic Coupling and Dipolar Effects. ACS Appl. Mater. Interfaces 2015, 7, 22775– 22785,
51. Marchl, M.; Edler, M.; Haase, A.; Fian, A.; Trimmel, G.; Griesser, T.; Stadlober, B.; Zojer, E. Tuning the Threshold Voltage in Organic Thin-Film Transistors by Local Channel Doping Using Photoreactive Interfacial Layers. Adv. Mater. 2010, 22, 5361– 5365,

Chapter 4. Organic Thin-Film Transistors as Cannabinoid Sensors: Effect of Analytes on Phthalocyanine Film Crystallization

This chapter is adapted from: ***Z. J. Comeau****, N. A. Rice, C. S. Harris, B. H. Lessard, A. J. Shuhendler, Adv. Funct. Mater. 2022, 32, 21071138.*

Context

While performing the solution characterization experiments of the previous work I was also performing thin-film characterization experiments which had some interesting preliminary findings; specifically, what seemed to be the formation of new Pc polymorphs following analyte exposure and alterations to thin-film morphology. These were features I was keen to explore further, assaying a range of Pc thin films with multiple techniques to establish a correlation between central metal and analyte induced thin-film recrystallization. In a similar fashion to the NMR experiments in my previous study, I experimented with EPR as a complimentary solid-phase technique, which revealed the formation of Pc radicals. Another element I was interested in examining was extracting more data from the transfer curves and relating it to the sensing mechanisms. Calculating the defect density from the sub-threshold slope region helped further corroborate analyte induced recrystallization, and I proposed a sensing mechanism where electrical OTFT responses are a result of the combination of electrochemical solution effects as well as physical recrystallization effects.

Contribution

I performed all experiments barring AFM imaging which was performed by NAR. I authored the manuscript with all co-authors assisting in the editorial process. This work was supervised by BHL and AJS.

Abstract

With a growing international trend of Cannabis legalization, there is a present need for on-the-spot, low cost, and rapid detection of cannabinoids. Here, relationships between thin-films of phthalocyanines (Pcs) with a variety of central, peripheral, and axial substituents and their response to the cannabinoid Δ^9-tetrahydrocannabinol (THC), with and without a cannabinoid-sensitive chromophore (Fast Blue BB) are investigated through organic thin-film transistor (OTFT) performance. X-ray diffraction and UV–vis absorption spectroscopy measurements demonstrate significantly altered film morphologies and the formation of new crystal orientations in response

to analytes, which are corroborated by scanning electron microscopy. Electron paramagnetic resonance further corroborates shifting crystal structures in response to THC and also reveals the formation and promotion of Pc radical species through THC-metal coordination. With exposure to THC, aluminum chloride Pc generates the largest physical film changes as well as the largest changes in OTFT performance. These findings suggest that the semiconductor thin-film morphologies in Pc-based OTFT sensors are not static in the presence of analytes and that the sensing response is driven both by strong analyte-Pc coordination and bulk film restructuring to accommodate these interactions.

Introduction

Phthalocyanines (Pcs) are conjugated macrocyclic molecular dyes that are often deposited as charge transport layers within organic thin-film transistors[1-3] (OTFTs) and organic photovoltaics[4, 5]. Pc-based OTFTs have been demonstrated in a variety of liquid[6-9] and gas[10-12] sensing applications, including the ratiometric detection and differentiation of Δ^9-tetrahydrocannabinol (THC, **Figure 4.1iii**) and cannabidiol (CBD) recently described by our group[13, 14]. The plant *Cannabis sativa* is cultivated for multiple purposes, including its fibers and seed/oil (hemp), but is primarily used for therapeutic and recreational purposes attributed to the pharmacological effects of the unique cannabinoids concentrated within the inflorescence. Among over 100 identified cannabinoids, tetrahydrocannabinolic acid (THCa) and cannabidiolic acid (CBDa) are typically the most abundant, with their respective decarboxylated forms, THC and CBD, the most studied and recognized for their psychoactive and therapeutic potential[15-17]. As THC and CBD are the dominant cannabinoids yet elicit very different effects on consumers, low-cost rapid speciation, and quantification would benefit industry and consumers, alike, but remains a challenge to industry, which still relies on imprecise or resource-intensive methods[18-20]. Colorimetric probes have been developed[21, 22] which rapidly bind to the phenol group of cannabinoids, but the highly reactive nature of these compounds lacks specificity and can yield false positives, making speciation difficult or impossible[23]. 4-Amino-2,5-diethoxybenzanilide diazoated zinc double salt (FBBB, **Figure 4.1iv**) is a common colorimetric cannabinoid detector that rapidly reacts to form a covalent linkage with the cannabinoid through its diazonium group, resulting in extended π-conjugation across the cannabinoid-FBBB conjugate and conferring a color change from yellow to red[22]. For more quantitative commercial speciation and separation, high performance liquid or gas chromatography (HPLC or GC) are used; however, for companies and consumers with limited resources and expertise, these instruments are not an accessible option.

i.

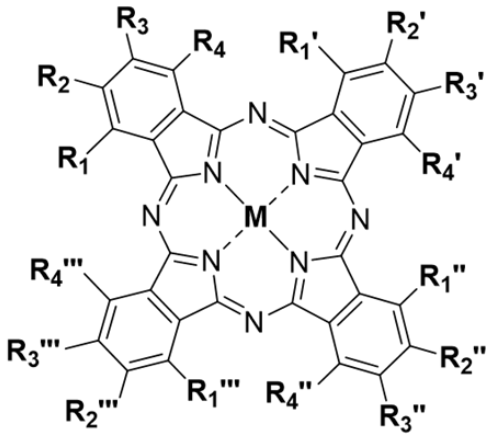

iii.

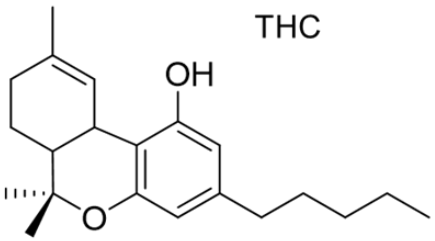

ii.

H_2Pc	M = H_2	R_{1-4} = H
CoPc	M = Co	R_{1-4} = H
CuPc	M = Cu	R_{1-4} = H
F_{16}-CuPc	M = Cu	R_{1-4} = F
tbt-CuPc	M = Cu	$R_{1,2,4}$ = H, R_3= tbt
AlClPc	M = Al-Cl	R_{1-4} = H

iv.

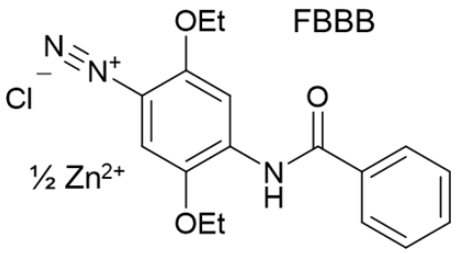

Figure 4.1. *Chemical structures of i) phthalocyanine and ii) the substitutions investigated, iii.) Δ⁹-tetrahydrocannbinol (THC), and iv) 4-amino-2,5-diethoxybenzanilide diazoated zinc double salt (FBBB).*

Semiconducting organic molecules can be solution processed or evaporated at low processing temperatures, enabling their compatibility with a wide variety of substrates and facilitating unique device architectures and fabrication methods[24]. The high thermal stability of Pcs facilitates the use of physical vapor deposition (PVD) to enable rapid deposition of thin-films on a variety of substrates including flexible plastics[25]. Through chemical functionalization of axial or peripheral groups, deposition conditions, and post deposition treatments, the physical properties of Pc thin-films can be tuned to optimize electrical performance[26-29]. Film morphology, grain structure, device architecture, and interface energetics are all critical factors that can influence the electrical performance of Pc-based OTFTs[30-34]. Charge transport through the thin-film can also be manipulated via small molecule doping and atmospheric conditions[7, 34-37]. In a similar fashion, controlled introduction of analytes to the semiconducting layer can affect measured electrical properties, facilitating a sensing response[11, 38, 39]. Changes in π-electron conjugation can influence the frontier orbitals and intermolecular interactions, in turn altering molecular stacking, charge trapping, and charge pathways within a thin-film. As molecular

orientation and film crystallinity are critical to charge transfer, the effects of deposition conditions and substrate material have been generally well characterized[40-42].

Planar Pcs, as well as other aromatic conjugated molecules, are typically oriented as either herringbone or brick layers, with slight variations as the degree of “face-on” or “slipped” interactions changes based on molecular energetics[26, 30]. During PVD at moderate substrate temperatures (≈20–120 °C), unsubstituted Pcs typically align in thin-films as co-facial herringbone stacked α-crystals with a low (≈24.5°) angle of incidence relative to the surface[43]. At elevated temperatures (>200 °C), either during deposition or in a post deposition annealing step, molecular packing can transition to a herringbone β-crystal orientation, characterized by an increased angle of incidence (≈45°), which typically forms larger crystallites[44-46]. Post-deposition, thin-film molecular packing can be altered by exposure to heat, light, solvents, or analytes[43-45, 47]. Conjugated aromatics and small volatile gasses also change both film morphology and measured electrical device performance through disruption of Pc–Pc π-stacking, resulting in molecular re-arrangements[11, 45, 48, 49]. Additionally, both α- and β-crystals frequently coexist within the same film but charge transfer between different crystal domains can be limited, reducing viable charge transport pathways within the film[46]. Finally, deformations of the macrocyclic ring can occur from strong metal-ligand coordination[47] or as a result of larger central metals, promoting unique packing domains[50]. As charge transfer involves discrete particles moving between the π-electron clouds of individual molecules, molecular packing orientation has profound implications on the physical paths of charge transport, enabling or inhibiting different transport regimes, and altering measured electrical properties[30, 51]. Thus, molecular substituents, physical thin-film structures, and charge transport properties are closely interrelated, and the combination of their effects dictates device performance in response to the addition of analytes[29, 33, 44, 52].

Here we examine the effects of THC, with and without FBBB, on thin-film crystallinity and OTFT device performance to identify the role of thin film morphology for THC sensing. We investigated devices comprising thin-films of metal free phthalocyanine (H_2Pc), cobalt phthalocyanine (CoPc), copper phthalocyanine (CuPc), peripherally fluorinated copper phthalocyanine (F_{16}-CuPc), tetra-t-butyl copper phthalocyanine (tbt-CuPc), and aluminum chloride phthalocyanine (AlClPc) (**Figure 4.1i,ii**). Through X-Ray diffraction (XRD), electrical characterization of OTFTs, and UV–vis absorption spectroscopy, we compare analyte effects on crystal structure and molecular packing, with surface morphology investigated by SEM and atomic force microscopy (AFM). We also examine the powder electron paramagnetic resonance (EPR) spectra of the Pcs with analytes to further elucidate changing crystal structures, relating these

effects to thin-film charge transport. Ultimately, we demonstrate the interplay between analyte-induced changes to film crystallinity and device performance, providing insight toward material selection for sensing applications.

Results and Discussion

Thin-Film Characterization

Thin-films (thickness = 200 Å) of six Pcs, classified as unsubstituted (H_2Pc, CoPc, and CuPc), peripherally substituted (F_{16}-CuPc, tbt-CuPc), or axially substituted (AlClPc) were obtained by PVD on octyltrichlorosilane (OTS) treated Si/SiO_2 substrates at room temperature. XRD spectra of each Pc thin-film are displayed in **Figure 4.2**, with broad peaks for the as-deposited unsubstituted H_2Pc (2θ = 6.86°), CoPc (2θ = 6.94°), and CuPc (2θ = 6.84°) corresponding to d-spacings of 12.87, 12.72, and 12.90 Å, respectively, indicating the α-crystal geometry as previously identified[40]. F_{16}-CuPc displays a peak at 2θ = 6.14° corresponding to a d-spacing of 14.38 Å as its peripheral substituents increase the size of the unit cell, altering molecular packing[53]. tbt-CuPc displays a broad, asymmetrical peak at 2θ = 5.97°, corresponding to a d-spacing of 14.80 Å, and suggesting its peripheral substituents result in a poorly aligned film and reduced π–π interactions. AlClPc, with a peak at 2θ = 7.36°, displays the smallest d-spacing of 12.00 Å as the central aluminum chloride bends the Pc ring, conferring a unique translationally ordered packing structure. Upon visualization by AFM and SEM (**Figure 4.3; Figure A.4.1**), both the unsubstituted and peripherally substituted Pcs were observed to form nanometer scale, rounded grains, while AlClPc forms longer ≈100 nm grains with no uniform directionality. The obtained morphologies are typical of respective Pc thin films and are consistent with literature[40,43,54 55].

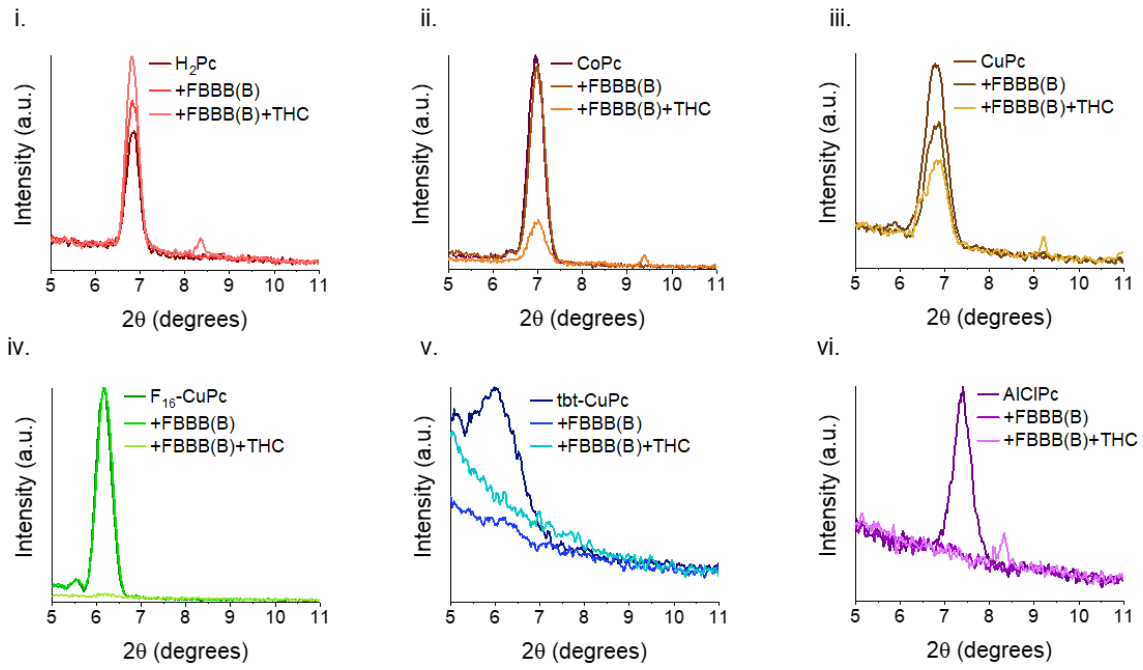

Figure 4.2. *XRD spectra of Pc thin-films upon exposure to FBBB(B) with and without THC. XRD spectra of i) H_2Pc, ii) CoPc, iii) CuPc, iv) F_{16}-CuPc, v) tbt-CuPc, and vi) AlClPc, as deposited, with exposure to 40 µm FBBB with 50 µm of NaOH at pH 9 in ACN, and with subsequent exposure to 40 µm THC.*

Treatment of the Pc thin-films with equal volumes of alkaline FBBB (FBBB(B)) in ACN resulted in an 18% increase in XRD α-peak intensity for H_2Pc, while the α-peaks of CoPc and CuPc decreased in intensity by 8% and 30%, respectively (**Figure 4.2**). The intensity of the F_{16}-CuPc peak is reduced by 1%, tbt-CuPc by 59%, and AlClPc had a complete loss of peak intensity. Subsequent treatment with THC revealed an additional 30% gain in α-peak intensity for H_2Pc, and a 79% and 26% loss of α-peak intensity for CoPc and CuPc, respectively. Additionally, a small secondary peak was visible for H_2Pc (2θ = 8.34°), CoPc (2θ = 9.38°), and CuPc (2θ = 9.20°), corresponding to narrower d-spacings of 10.6, 9.4, and 9.6 Å, respectively. These secondary peaks suggest the formation of new η-crystallites in the H_2Pc films and β-crystallites in the CoPc and CuPc films with subsequent treatments of FBBB(B) and THC[56]. Analyte induced crystal structures can be visualized by SEM (**Figure 4.3; Figure A.4.1**) where the previously featureless H_2Pc film formed round ≈100 nm crystallites, whereas CoPc and CuPc films formed oblong crystals with exposure to FBBB(B) and THC. F_{16}-CuPc had a complete loss of peak intensity with the subsequent addition of THC, indicating the film structure becoming disordered, visualized as mix of rounded and oblong crystals in SEM images. tbt-CuPc had a complete loss of peak intensity when treated with just FBBB(B), however, the low angle intensity of tbt-CuPc increased after addition of THC, which suggests the formation of aggregates[57]. AlClPc displayed a minor peak at 2θ = 8.32° with a corresponding d-spacing of 10.6 Å, and sparse needle-like crystals were

observed on the surface, demonstrating the formation of new crystal morphologies within the film as a result of analyte treatment.

Treatment with exclusively ACN (**Figure A.4.2**) resulted in slight (7 ± 2%) decreases in peak intensity for H_2Pc, CoPc, CuPc, and F_{16}-CuPc, suggesting that the carrier solvent has limited effects on the crystallinity of the film, and that observed differences in XRD spectra (**Figure 4.2**) are primarily due to analyte interactions. tbt-CuPc had a complete loss of peak intensity with exposure to ACN, convoluting the effects of treatment with FBBB(B), however, aggregate formation was only observed after the addition of the FBBB(B) + THC conjugate. AlClPc demonstrated a 55% loss in peak intensity with ACN, suggesting that both the effects of analyte and solvent are responsible for the observed peak shifts.

To explore alternative recrystallization regimes and investigate the rate of response with continuous exposure, thin-film substrates were treated with toluene vapor and XRD spectra were collected after a series of time intervals (**Figure A.4.3**). With exposure to toluene vapor, CoPc and CuPc retained their α-peak intensity over 60 min with only a 2% and 12% decrease respectively; however, a phase transition occurred between 1 and 24 h of continual exposure to solvent vapor, with their respective α-peaks losing 17% and 25% intensity, becoming 86% and 90% narrower, and a sharp β-peak appearing at 9.38 and 9.2° 2θ. Corroborating the intense XRD peak shifts, large micrometer-sized crystals were visible, forming rectangular needle clusters or wire shapes for CoPc and CuPc, respectively (**Figure 4.3; Figure A.4.1**). Though highly crystalline, the β-form is generally poorer performing or non-semiconducting in OTFTs, with mobilities on the order of 10^{-5} cm^2 V^{-1} s^{-1} due to the increased face to face orientation of the Pcs[45, 46]. H_2Pc and F_{16}-CuPc undergo rapid changes, gaining peak intensity within the first 10 min treatment, and continuing to gain peak intensity at each time point, becoming highly α-crystalline after 24 h of exposure to toluene vapor. While no phase angle shift occurs in the XRD spectra, large micrometer scale crystals are again observed in what were previously featureless films. In the first 10 min of toluene vapor exposure, the peak angle of tbt-CuPc initially shifts from 5.97 to 6.53° 2θ before losing peak intensity and a sharp peak appearing at 7.27° 2θ by 24 h, with large aggregates observed in SEM images. Between 1 and 24 h, the peak for AlClPc becomes narrower and shifts to 7.02° 2θ, and large, micrometer-sized rectangular needle cluster are visible on the substrate surfaces.

While the α- to β-crystal transition in CoPc and CuPc films is observed for both FBBB(B) + THC and toluene vapor exposure, an α- to η-transition for H_2Pc is only observed with FBBB(B) + THC exposure. Similarly, while F_{16}-CuPc and tbt-CuPc lose crystallinity with the subsequent

exposure to THC, they become markedly more crystalline with exposure to toluene vapor. Finally, AlClPc demonstrates different crystal forms with subsequent exposure to THC versus toluene vapor. Furthermore, the XRD spectra of H_2Pc, F_{16}-CuPc, and tbt-CuPc films are observed to change within the first 10 min of toluene vapor exposure while CoPc, CuPc, and AlClPc undergo little change in the first hour of treatment, suggesting that the presence of a central metal or peripheral substituents influences the rate of film recrystallization. The immediate, if limited, crystal transitions with exposure to FBBB(B) + THC compared to the lack of changes with only carrier solvent, versus the larger, but slower crystal transitions with toluene vapor suggests that that FBBB(B)–cannabinoid interaction enables rapid detection of THC. These results demonstrate analytes can have varied, specific effects on film structure and in some cases, drive rapid film recrystallization, induce phase transitions, and form micrometer scale crystallites, which are expected to have implications on the charge transport characteristics of the Pc-based OTFTs.

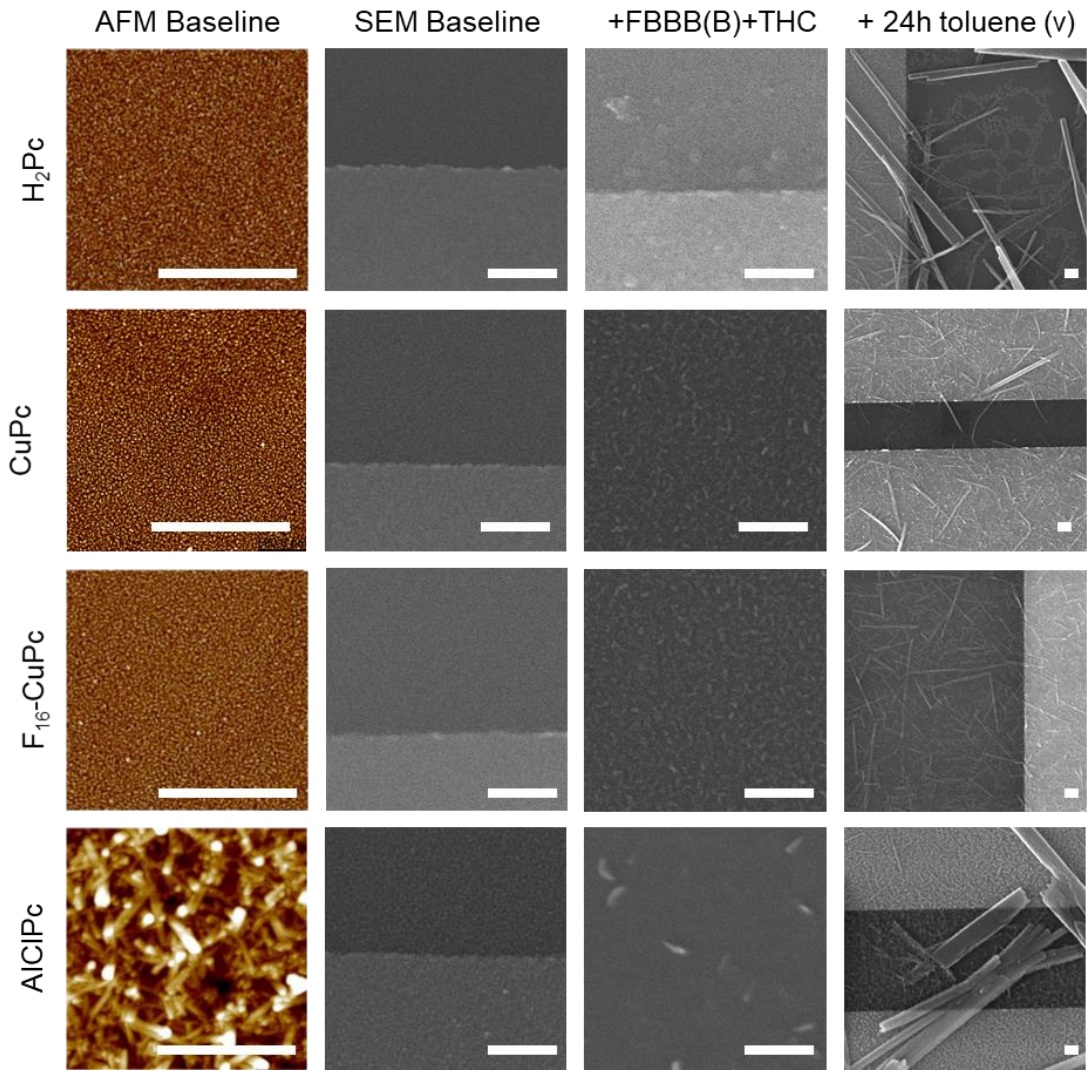

Figure 4.3. *AFM and SEM images of characteristic untreated and treated Pc thin-films. H_2Pc, CuPc, F_{16}-CuPc, and AlClPc, as deposited on OTS treated Si/SiO_2 substrates (Baseline), with exposure to 40 µm FBBB with 50 µm of NaOH at pH 9, and subsequent exposure to 40 µm THC (+FBBB(B) + THC), or after 24 h of exposure to toluene vapor. Scale bars represent 500 nm.*

Solid state UV–vis absorbance spectroscopy was used to further study the progression of molecular interaction in the thin-films when exposed to different analytes (**Figure A.4.4**). As deposited, the unsubstituted Pcs (H_2Pc, CoPc, and CuPc) displayed two broad peaks in the Q band between 600 and 725 nm. F_{16}-CuPc displayed a broad peak at 654 nm and a greater peak intensity at 797 nm, while tbt-CuPc displayed a broad peak at 608 nm and a slightly sharper peak at 678 nm. AlClPc displayed a very broad Q band with limited features, peaking at 775 nm. When exposed to analytes, some Pc films experience disruptions in solid state packing leading to changes in π–π* transitions. With exposure to FBBB(B) there are negligible changes to the UV–vis absorbance spectra of the unsubstituted Pcs (**Figure A.4.4**) but, following addition of THC,

CoPc has a sharp increase in the intensity of its second Q band at 683 nm, suggesting coordination of the FBBB(B) + THC conjugate to the central cobalt, in addition to an increase in relative number of β-crystallites[46, 56]. Upon exposure to both FBBB(B) and THC, CuPc also has an increase in its second Q band (695 nm), albeit much lower in relative intensity to that of CoPc, further suggesting the absorbance peak intensity shifts are a result of strong FBBB(B) + THC conjugate interactions. In our previous work[13], H_2Pc was found to uniquely coordinate with the FBBB(B) + THC conjugate in solution. The absorbance spectra of the H_2Pc thin-film shows the appearance of two additional broad peaks, centered at 499 and 583 nm, when exposed to FBBB(B) + THC, another indication of η-crystal formation. This corroborates the observed α- and η- phase XRD peak[56] and suggests strong interactions between the FBBB(B) + THC conjugate and isoindole groups[26, 58]. Thus, compared to the analyte-induced β-crystal phase shifts of CoPc and CuPc, we can infer that the site of molecular interactions determined by the presence of a central metal plays a key role in the morphology of analyte-induced film recrystallization of unsubstituted Pcs.

F_{16}-CuPc demonstrates negligible Q band changes after addition of FBBB(B) and the subsequent addition of THC, suggesting limited analyte-Pc coordination and random penetration of conjugate throughout the film. The tbt-CuPc Q band becomes increasingly broad, further corroborating the formation of aggregates (**Figure A.4.4**). Both F_{16}-CuPc and tbt-CuPc do not form well-ordered films with FBBB(B) + THC conjugate exposure, possibly as they are limited by their peripheral substituents. With FBBB(B) treatment, AlClPc loses its XRD peak intensity, suggesting a significant change in film morphology. This is corroborated by UV–vis absorbance results, with a sharp peak at 686 nm appearing when FBBB(B) is added, indicating a decrease in bulk molecular order. With the subsequent addition of THC, the peak maximum of AlClPc red shifts from 686 to 689 nm, suggesting altered analyte-Pc coordination states similar to those observed in solution in our previous work[13]. This is further corroborated by the SEM images (**Figure 4.3**), suggesting the unique crystal structure of AlClPc is particularly susceptible to analyte-induced physical film effects. These results provide evidence that metal and substituent differences in the Pcs alter Pc-analyte interactions, resulting in the observed variations of analyte induced crystals.

Electron Paramagnetic Resonance Analysis

To further understand analyte coordinating effects within the Pc thin-films with respect to the metal center and peripheral substituents, continuous wave EPR experiments were conducted on Pc powders in capillary tubes (**Figure 4.4**). The effects of crystal structure and peripheral substituents

were explored with CuPc and its derivatives, which generally demonstrate a lack of hyperfine structure (HFS) associated with an averaging of line splitting of the paramagnetic nuclei through copper coordinating exchange interactions resulting in a $g_{\perp}$ value as summation of all exchange interactions[59]. As a result, CuPc powder as α-crystals (αCuPc) has the broadest peak (**Figure 4.4i**) with a $g_{\perp}$ value of 2.0573, as many co-facial interactions are possible, supporting previously published results[59, 60]. In comparison, F_{16}-CuPc (**Figure 4.4ii**) with its highly electronegative periphery demonstrates a sharp line shape with a $g_{\perp}$ value of 2.0472, as the vibrational modes and co-facial interactions of the central copper atom and associated isoindole nitrogen are limited[59]. tbt-CuPc, with less defined crystal domains, has a broad peak, suggesting a high degree of molecular disorder and a larger range of Pc–Pc coordinating interactions[61]. β-crystalline CuPc (βCuPc) has a sharp peak and $g_{\perp}$ value of 2.0480, as a result of its tightly packed and uniform crystal structure and limiting vibrational modes through increased face-on Pc–Pc orientations[26,59]. CoPc, as a ferromagnetic molecule, demonstrates very broad spectrum, and AlClPc shows a sharp paramagnetic Pc peak with $g_{\perp}$ value of 2.0510, and an additional peak corresponding to the presence of a Pc radical[62] at $g_{\perp}$ value of 2.0020.

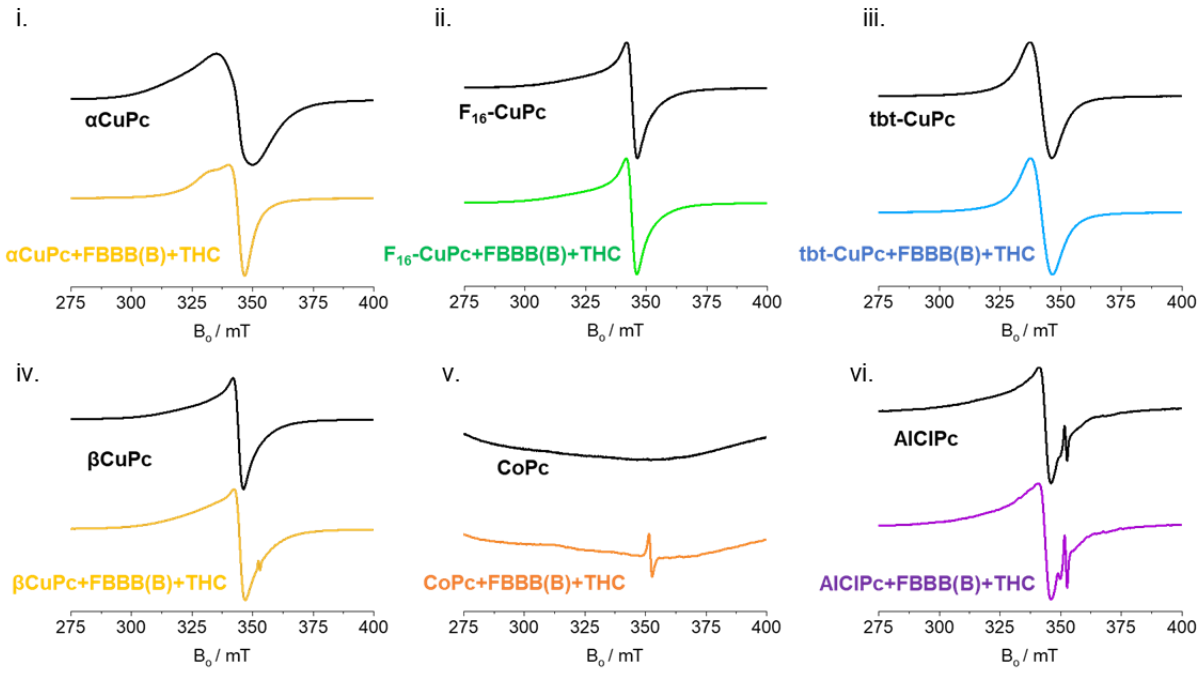

Figure 4.4. *Effects of FBBB(B) + THC conjugate on the EPR signal of MPcs. Sublimed MPcs powder, i) αCuPc, ii) F_{16}-CuPc, iii) tbt-CuPc, iv) βCuPc, v) CoPc, and vi) AlClPc or a rotovap-dried slurry of 20 µmol MPc powder, mixed with 500 µL of ACN containing 40 µm THC and FBBB at pH 9, were loaded into capillary tubes. Each 1D EPR spectrum was collected over 60 s at an attenuation of 30 dB on a Bruker EPR spectrometer.*

Following treatment with FBBB(B) and THC, αCuPc shifts to demonstrate both αCuPc and βCuPc peak, as was observed in XRD experiments. The F_{16}-CuPc and tbt-CuPc peaks become narrower without shifting $g_{\perp}$ value, suggesting that analyte treatment reduces the range of possible Pc–Pc coordinating interactions but, due to the bulky peripheral groups, there is limited copper–analyte coordination. βCuPc and CoPc both show the formation of a Pc radical species, with g values of 2.0001 and 2.0015, respectively. The Pc radical species peak observed for AlClPc increases in relative intensity without shifting $g_{\perp}$ value. It is suggested that while Pc radicals can form as a result of Pc–Pc or Pc–analyte coordinating effects[59, 63], the lack of observed HFS could indicate that the radical becomes trapped on the Pc, suggesting radical formation is induced by Pc–analyte coordination. A radical species is not observed for treated αCuPc as the greater range of Pc–Pc coordinating interactions could prevent trapping. In a similar manner, the peripheral substituents of F_{16}-CuPc and tbt-CuPc may prevent the coordinating interactions necessary to induce radical formation. Thus, the formation of radicals could be indicative of increased defect densities and altered grain boundaries and will have consequences on charge transport in OTFT devices.

Without an exchanging metal center, H_2Pc demonstrates HFS with 16 peaks (**Figure 4.5**), stemming from Pc–Pc co-facial macrocyclic interactions of the four isoindole nitrogens[60]. After treatment with FBBB(B) and THC, H_2Pc loses intensity at the second 4 HFS peaks, suggesting asymmetric interaction at a single isoindole nitrogen[60]. A Pc radical peak with $g_{\perp}$ value 2.0002 is present but does not change in intensity with treatment. To explore coordinating effects on a single CuPc molecule, CuPc was diluted in H_2Pc in a 1:500 ratio, revealing a combination of H_2Pc HFS peaks with a sharp CuPc peak (**Figure 4.5ii**). A Pc radical species at $g_{\perp}$ value 2.0016 is visible, increasing in intensity with FBBB(B) + THC treatment, suggesting that, while the formation of the Pc radical species is not metal dependent, the interaction of the FBBB(B) + THC conjugate with the central metal of the unique Pcs induces or increases the number of radicals. Furthermore, the unique formation of η-crystals in H_2Pc films following FBBB(B) + THC treatment may be a result of the asymmetrical interaction between H_2Pc and the FBBB(B) + THC conjugate. Radicals within the Pc films will have significant consequences on charge transport, potentially acting as pseudo-dopants, changing the energetics of the film, and driving film recrystallization[62, 64, 65].

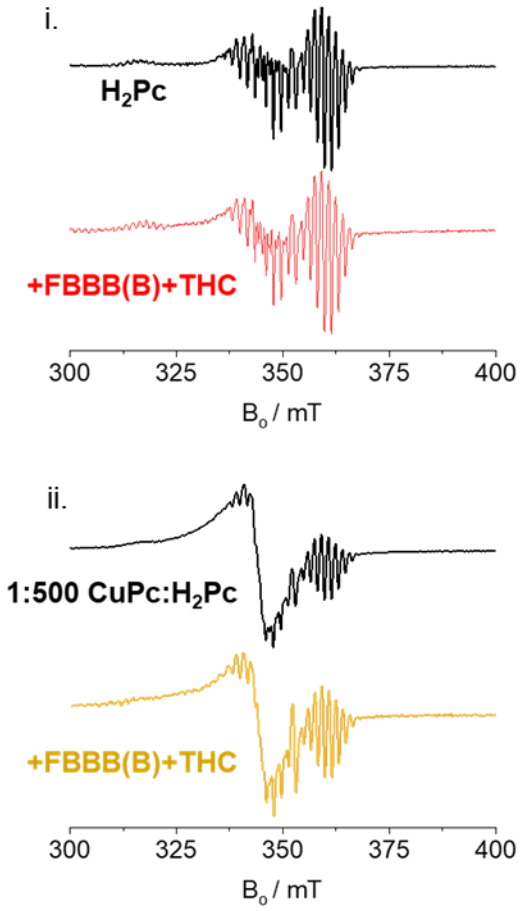

Figure 4.5. *Effects of applied analytes on EPR signal of H_2Pc and CuPc diluted in H_2Pc in a ratio of 1:500. Sublimed Pc powder i) H_2Pc and ii) CuPc mixed with H_2Pc in a 1:500 ratio, or a rotovap-dried slurry of 20 µmol Pc powder, mixed with 500 µL of ACN containing 40 µm THC, and FBBB at pH 9, were loaded into capillary tubes. Each sample's 1D EPR spectrum was collected over 60 s at an attenuation of 30 dB on a Bruker EPR spectrometer.*

OTFT Device Characterization

Bottom gate bottom contact (BGBC) OTFT devices were fabricated by depositing a 200 Å thin-film of each Pc on OTS-treated Si/SiO_2 wafers with pre-deposited gold electrodes. Devices were characterized by discretely sweeping through gate–source biases (V_{GS}) while maintaining a constant source drain bias (V_{SD}) and measuring current between the source and drain electrodes (I_{SD}) generating transfer curves (**Figure A.4.5**, Supporting Information). From the saturated I_{SD} versus V_{GS} data for each condition, mobility of either holes (μ_H) or electrons (μ_E) was calculated according to Equation (3), the threshold voltage (V_T) at which current begins to rapidly increase was determined, and the defect density (N) was calculated according to Equation (4) with the results displayed in **Figure 4.6**. By maintaining a constant V_{GS} and sweeping the V_{SD}, output curves, demonstrating the linear and saturation operating regimes for each Pc OTFT, were

generated and are displayed in **Figure A.4.6**, Supporting Information. Our baseline results are generally in accordance with other sources (**Table A.4.1**)[1, 66-68], with expected performances for BGBC devices on OTS treated Si/SiO_2 dielectrics. To our knowledge this is the first demonstration of tbt-CuPc in OTFTs.

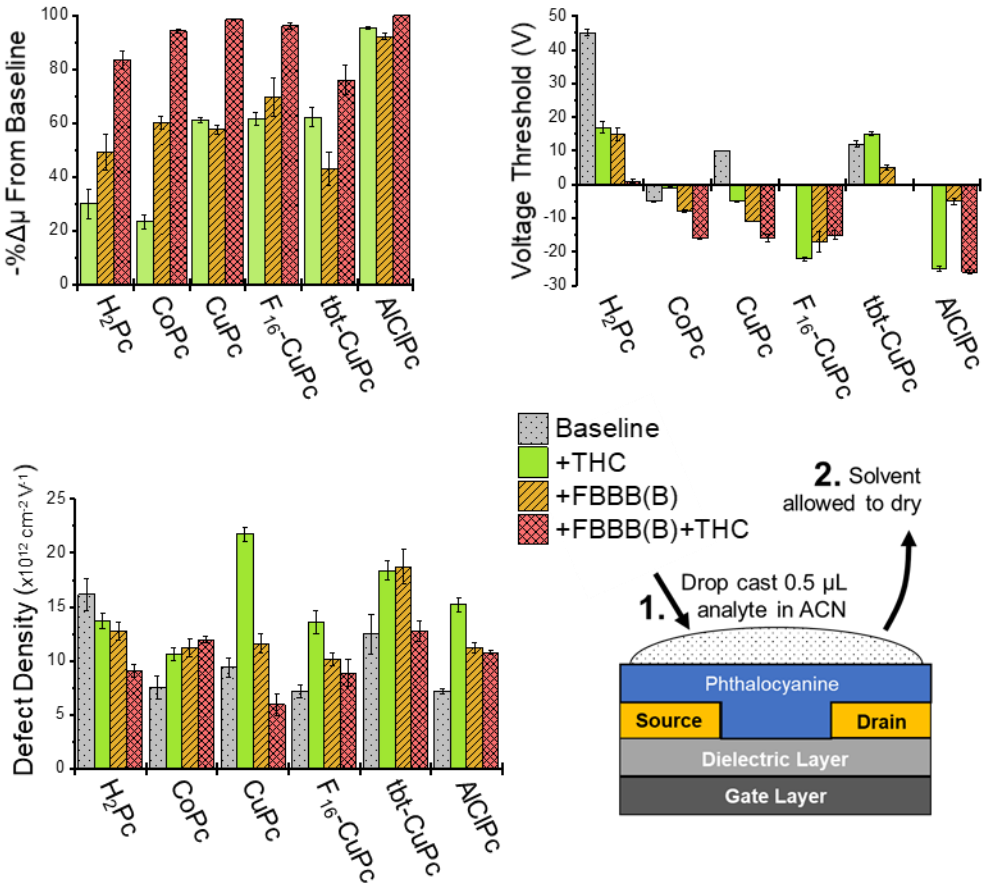

Figure 4.6. *Relative effects of applied analytes on i) field effect mobility, ii) threshold voltage, and iii) defect density in Pc-based OTFTs. Field-effect mobility was evaluated for OTFTs consisting of thin-films of H_2Pc, CoPc, CuPc, F_{16}-CuPc, tbt-CuPc, and AlClPc semiconductors (baseline) prior to addition of 40 µm THC, or 40 µm FBBB with NaOH at pH 9 and subsequent exposure to 40 µm THC. Mobility was calculated from the saturation region of transfer curves while defect density and voltage threshold were estimated from the subthreshold slope. Error bars represent standard deviation of eight devices from two wafers.*

In our previous work, following exposure to FBBB(B), subsequent additions of THC to the surface of OTFTs, at concentrations as low as 200 nm, was found to produce strong effects on device performance, and demonstrated as ratiometric sensors[24], as well as spectroelectrochemical responses for a variety of soluble Pcs[13]. We previously established that the combination of FBBB(B) and THC was necessary to produce large decreases in μ in CuPc and F16-CuPc[24]. In the current study, exposure to only THC resulted in $\Delta\mu_H$ of −30% for H_2Pc

and −23% for CoPc, with more than twice the $\Delta\mu$ response in CuPc ($\Delta\mu_H$ = −61%), F_{16}-CuPc ($\Delta\mu_E$ = −61%), and tbt-CuPc ($\Delta\mu_H$ = −62%) and three times the response for AlClPc ($\Delta\mu_H$ = −95%). Pcs with a copper center display their highest defect densities with THC exposure, suggesting a unique THC-Cu interaction that increases charge traps. CuPc demonstrates the highest defect density, potentially indicating the peripheral substituents of F_{16}-CuPc and tbt-CuPc limit THC-Cu coordination.

Exposure of H_2Pc to FBBB(B) resulted in a 49% decrease in peak μ_H, a lower N, and −15 V change in V_T. Despite H_2Pc becoming more α-crystalline under these conditions, our results show that increasing crystallinity does not necessarily equate to improved μ. While the molecular order of charge transport pathways may be increasing, reducing N, the number of viable charge transport pathways can decrease and thereby reduce μ[69, 70]. CoPc and CuPc, had similar responses to FBBB(B) in all respects, with an average $\Delta\mu_H$ of −59 ± 1%, V_T of −9.5 ± 1.5 V, and an increase in N of 3.0×10^{12} cm^{-2} V^{-1}. Together with the XRD and UV–vis absorbance data, this suggests that FBBB(B) has a similar effect on these materials, and interacts with CoPc and CuPc differently than THC, ultimately producing a greater $-\Delta V_T$. For tbt-CuPc, the higher calculated N value can be explained by the disruption of its large d-spacings by FBBB(B) as observed by XRD. However, the relatively limited percent reduction in μ suggests the number of viable charge transport pathways remains high, with the poor overall performance of tbt-CuPc-derived devices possibly attributed to the large intermolecular spacings due to the peripheral substituents inhibiting molecular packing. While XRD data demonstrated that the crystal packing of F_{16}-CuPc is not significantly influenced by exposure to FBBB(B), a 69.6% decrease in μ_E coupled with a large $-\Delta V_T$ were observed in OTFT devices. As the only electron transporting material in this data set, this suggests that μ_E may be particularly susceptible to the analytes studied here. AlClPc films, with the smallest d-spacings, are also disrupted by FBBB(B), demonstrating a complete loss of XRD peak intensity and the largest μ_H decrease with only a moderate increase in N, suggesting that analytes may have a limited effect on the mechanics of charge transport, instead reducing the number of viable charge transport pathways through disruption of the physical film structure.

Following exposure to both FBBB(B) + THC, the six studied Pcs demonstrate >83% reduction in μ and an additional $-\Delta V_T$. Under these conditions, XRD (**Figure 4.2**) and SEM (**Figure 4.3; Figure A.4.1**) indicate disruptions in the as-deposited film morphologies and the formation of crystallites within the film. Although these crystallites have varied morphologies, with η-crystallites in H_2Pc, β-crystallites in CoPc and CuPc, and new higher angle peak AlClPc, the

formation of new crystal morphologies will dramatically alter grain boundaries and consequently effect charge transport pathways through the film. As a general trend, lower defect densities are observed for the combination of FBBB(B) + THC compared to singular exposure to either FBBB(B) or THC. As a function of sub-threshold slope, the number of defect densities indicates the quality of charge transport pathways[24, 51, 71], supporting that the FBBB(B) + THC reaction induces the formation of locally ordered crystallites within the films, while disrupting bulk film morphology and reducing μ. Negative V_T shifts for each treatment suggests that the introduction of these analytes elicits a pseudo-doping effect, possibly as a result of the induced radical species observed by EPR[36, 72]. We conclude that the application of analytes generally decreases the bulk molecular order by inducing the formation of small localized ordered crystals, occasionally causing phase transitions. These rearrangements are detrimental to device performance, with varied crystal types and domains resulting in increased grain boundaries and limiting the number of viable charge transport pathways[46, 51]. A balance must then be struck between re-arrangement effects and coordinating effects as enhanced sensitivity can limit selectivity.

Conclusions

We demonstrated that analytes, in addition to acting as charge traps, induce physical film transformations that can selectively disrupt the number of charge transport pathways, significantly reducing thin-film semiconducting μ. Exposure to specific analytes is found to disrupt the physical order of a variety of Pc thin-films, in some cases inducing recrystallization, resulting in micrometer-sized crystallites in previously amorphous films. The THC + FBBB(B) conjugate is observed by EPR to uniquely coordinate with the macrocycle of H_2Pc, inducing the formation of η-crystals. The as-deposited films of CoPc and CuPc are disrupted with analyte–metal coordination, resulting in a loss of α-crystallinity, and the formation of β-crystallites and Pc radicals. CoPc and CuPc OTFTs respond differently to THC, while a near identical response is observed to FBBB(B), further evidencing the key role of both the metal center and macrocycle with respect to physical and related electrical responses. The effects of peripheral substituents are explored, where the bulky peripheral substituents of tbt-CuPc and F_{16}-CuPc are demonstrated to inhibit interactions with the Pc macrocycle in thin-films, preventing the formation of Pc radicals, and limiting film recrystallization. tbt-CuPc demonstrated the formation of unique aggregate domains, while thin-films of AlClPc were the most susceptible to all analytes and consequently demonstrated the greatest OTFT performance changes. While AlClPc is observed to form unique crystal structures with different analytes, suggesting the axial substituent and bent Pc ring shape enables unique coordinating interactions, this unfortunately did not translate into discernible OTFT device

performances. Thus, both the physical and electrical characteristics of Pc thin-films are closely intertwined with the nature of analyte–Pc coordination. This work demonstrates that analytes, such as FBBB(B) + THC, can rapidly induce physical changes in Pc films, similar to those observed with solvent vapor or temperature annealing, which could have relevant implications for thin-film engineering and other sensing applications.

Experimental Section

Materials

H_2Pc (metal free phthalocyanine), CuPc (copper(II) phthalocyanine), tbt-CuPc (copper(II) 2,9,16,23-tetra-tert-butyl-phthalocyanine), OTS, and FBBB, were obtained from Sigma Aldrich. CoPc (cobalt phthalocyanine), F_{16}-CuPc (Copper(II) 1,2,3,4,8,9,10,11,15,16,17,18,22,23,24,25-hexadecafluoro phthalocyanine, and AlClPc were obtained from TCI chemicals. All Pcs were purified by train sublimation prior to use. All other materials were used as received. Cannabinoid standards were obtained from Toronto Research Chemicals. All solvents were HPLC grade and purchased from Fischer Scientific.

Thin Film Formation

Substrates with 230 nm thermally grown SiO_2 dielectric on Si, with prepatterned gold source–drain electrodes (W = 2000 µm, L = 10 µm), were purchased from Fraunhofer IPMS and used to fabricate BGBC transistors. Substrates with 230 nm thermally grown SiO_2 dielectric on Si, were purchased from Ossila and used to fabricate thin films for XRD characterization. Each Fraunhofer substrate contained four devices. Wafers were rinsed with acetone and isopropanol, before being dried with an N_2 gas stream, and treated with O_2 plasma for 15 min. Wafers were then rinsed with water, followed by isopropanol, before immersion in a 1% v/v OTS/toluene solution for 1 h at 70 °C. The OTS-treated substrates were rinsed with toluene, followed by isopropanol, before being dried with an N_2 gas stream and a second drying step in a 70 °C vacuum oven for 45 min. The substrates were then transferred to an Angstrom EvoVac thermal evaporator, and one of the six Pcs sublimed onto the surface at a substrate temperature of 25 °C, pressure below 2×10^{-6} torr, and a deposition rate of 0.2 $Å s^{-1}$ to a thickness of 200 Å.

Thin Film Treatments

THC was dissolved in ACN to a yield a concentration of 40 µm THC. FBBB was dissolved in ACN and mixed with NaOH to yield a final concentration of 40 µm FBBB and 50 µm NaOH yielding FBBB(B). Between subsequent treatments of FBBB(B) followed by THC, the carrier solvent (ACN) was allowed to dry completely. For Pc OTFT devices, prepared on Fraunhofer IPMS substrates, 0.5 µL of analyte solution(s) was pipetted directly on the semiconducting

channel and allowed to dry for 3 min before device characterization. The OTFT channels were subsequently imaged by SEM and AFM following device characterization. For XRD characterization of Pc thin-films, prepared on Ossila substrates, 150 µL of analyte solution(s) was pipetted over the entire surface and allowed to dry for at least 15 min before characterization.

XRD Characterization

XRD experiments were carried out on 200 Å Pc films on Si/SiO_2 substrates using a Rigaku Ultima IV powder diffractometer with a Cu-Kα (λ = 1.5418 Å) source. Measurements were taken directly from the thin-film substrates with a scan range of 5° < 2θ < 11° and a rate of 0.5° min^{-1} with no spin. The interplanar (d-spacing) was calculated using Bragg's law, Equation (1),

$$n\lambda = 2d\sin(\theta) \quad (1)$$

where λ is the incident wavelength of 1.5418 Å, θ is the angle of incidence in degrees, n is a positive integer equal to 1, and d is the calculated d-spacing between lattice planes. Toluene vapor treated films were exposed in a custom vapor chamber in ambient conditions.

Thin-Film UV–vis

Square glass microscope slides (25.4 mm, VWR) were cleaned in a sonication bath before PVD was used to deposit a 400 Å layer of Pc on the surface in the same manner as described in the device fabrication section. Thin-film UV–vis spectra were recorded in an Ocean Optics Flame Spectrophotometer with analyte treatments were applied in the same manner described previously for thin-films on Si/SiO_2 substrates.

SEM and AFM

SEM measurements were carried out with a Tescan Vega II on thin-film Pc devices at 20 kV. AFM measurements were carried out with a Bruker Dimension Icon AFM equipped with ScanAsyst-Air tips and images were processed using NanoScope Analysis v.1.8. Scans were performed at a rate of 0.85 Hz, with multiple locations investigated.

Electron Paramagnetic Resonance

EPR spectra were acquired using a Bruker EPR spectrometer with an attenuation of 20 dB. Powder sample or a rotovap-dried slurry of 20 µmol MPc powder, mixed with 500 µL of ACN containing 40 µm THC and FBBB(B) at pH 9, was loaded into capillary tubes and placed inside a quartz EPR sample tube. A 60 s 1D field sweep acquired the spectrum over 3 scans. g values were calculated according to Equation (2):

$$g = h\nu u_o B_o \quad (2)$$

where *h* is Plank's constant, *v* is the microwave frequency, μ_o is the Bohr Magneton, and B_o is the magnetic field strength.

OTFT Characterization

Organic thin film transistors were operated by applying a voltage bias between gate and source electrodes (V_{GS}), causing charge to accumulate in a separating, non-conducting dielectric layer, polarizing the interface between dielectric and semiconducting layers. With a secondary applied voltage bias between source and drain electrodes (V_{SD}), electrons or holes, for n- and p-type semiconductors respectively, could be injected at the source and be transported through the semiconducting material between the source and drain generating current (I_{SD}). The gate-source bias at which current began to rapidly increase, an "on" state, is known as the threshold voltage (V_T) while the maximum over minimum source–drain current is known as the on–off ratio. The speed, or mobility (μ, $cm^2\ V^{-1}s^{-1}$) at which charge transport occurred across the semiconducting channel could be isolated from the plot of I_{SD} versus V_{GS} in the saturation regime as shown in the following, Equation (3):

$$I_{DS}=\mu C_i W/2L\ (V_{GS}-V_T)^2 \quad (3)$$

where C_i is the dielectric capacitance, *W* and *L* are the width and length of the semiconducting channel, respectively. The source-drain electrodes of each device were contacted with BeCu alloy probe tips and electrical characterization was performed using a custom electrical probe station, oesProbe A10000-P290 (Element Instrumentation Inc. and Kreus Design Inc.) with a Keithley 2614B. To mitigate the effects of bias stress, a pulsed gate voltage was applied, at 20 ms intervals with an 80 ms delay. To saturate the devices, six transfer curves were obtained and the final three were averaged to yield a characteristic transfer curve for each device, as shown in **Figure A.4.7**, Supporting Information. Baseline characteristics of each device were obtained prior to analyte exposure and averaged across eight devices.

Defect density (*N*) was determined by Equation (4),

$$N = (S_q kT\ln(10)-1)C_{ox}q \quad (4)$$

where *S* is the subthreshold slope, estimated graphically from the transfer curves, *q* is the electronic charge, *k* is Boltzmann's constant, *T* is temperature, and C_{ox} is the dielectric capacitance.

Supplemental Information

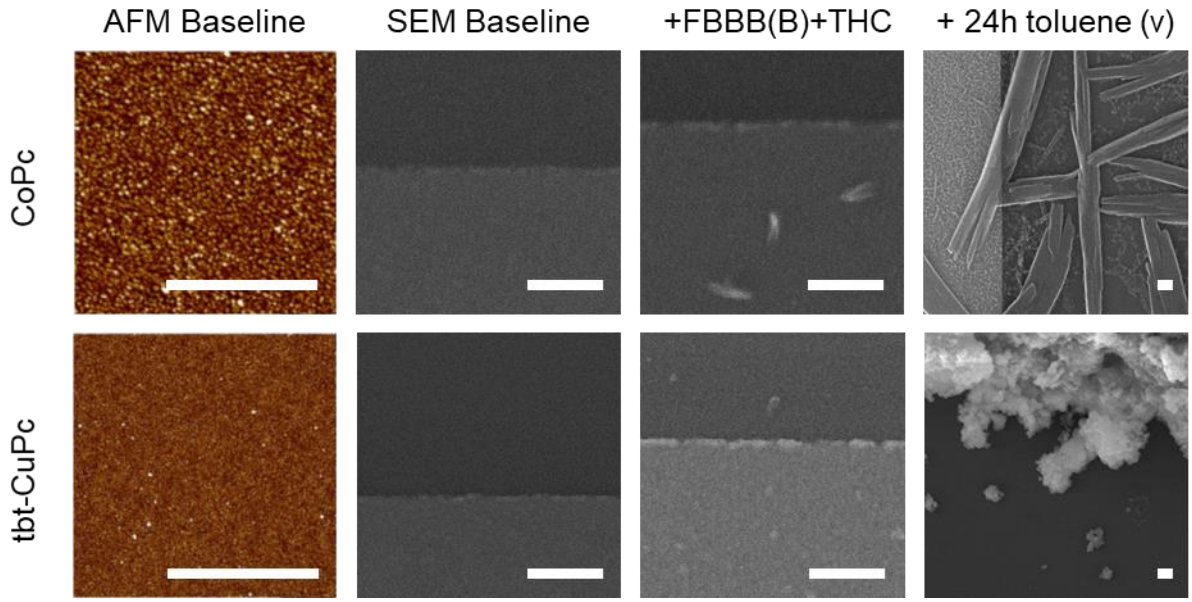

Figure A.4.1. *AFM and SEM images of untreated and treated Pc thin-films. CoPc and tbt-CuPc, as deposited on OTS treated Si/SiO_2 substrates (Baseline), with exposure to 40 µM FBBB with 50 µM of NaOH at pH 9 and subsequent exposure to 40 µM THC (+FBBB(B)+THC), or after 24 hours of exposure to toluene vapor. Scale bars represent 500 nm.*

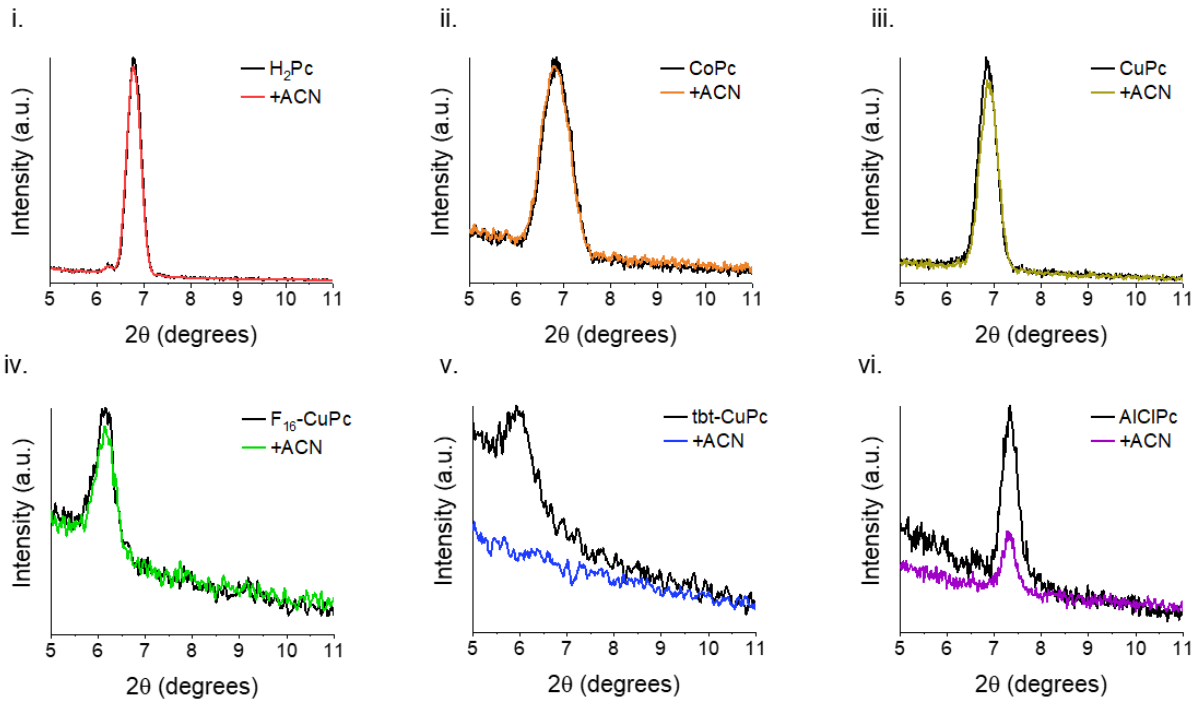

Figure A.4.2. *XRD spectra of phthalocyanine thin-films with exposure to acetonitrile. XRD spectra of (i) H_2Pc, (ii) CoPc, (iii) CuPc, (iv) F_{16}-CuPc, (v) tbt-CuPc, (vi) AlClPc, as deposited, with exposure to 150 µL of acetonitrile which was allowed to evaporate in ambient conditions.*

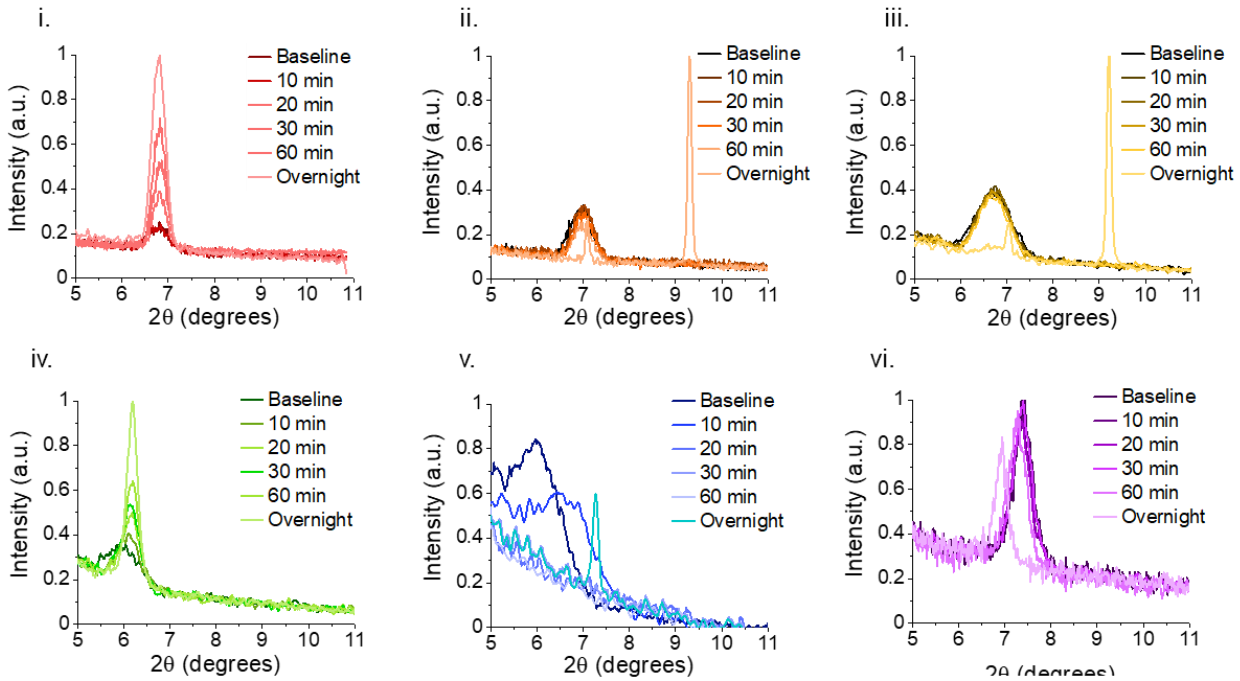

***Figure A.4.3**. XRD spectra of phthalocyanine thin-films with exposure to toluene vapor. XRD spectra of (i) H_2Pc, (ii) CoPc, (iii) CuPc, (iv) F_{16}-CuPc, (v) tbt-CuPc, (vi) AlClPc, as deposited, with exposure to toluene vapor after 10, 20, 30, 60 minutes and 24 hours.*

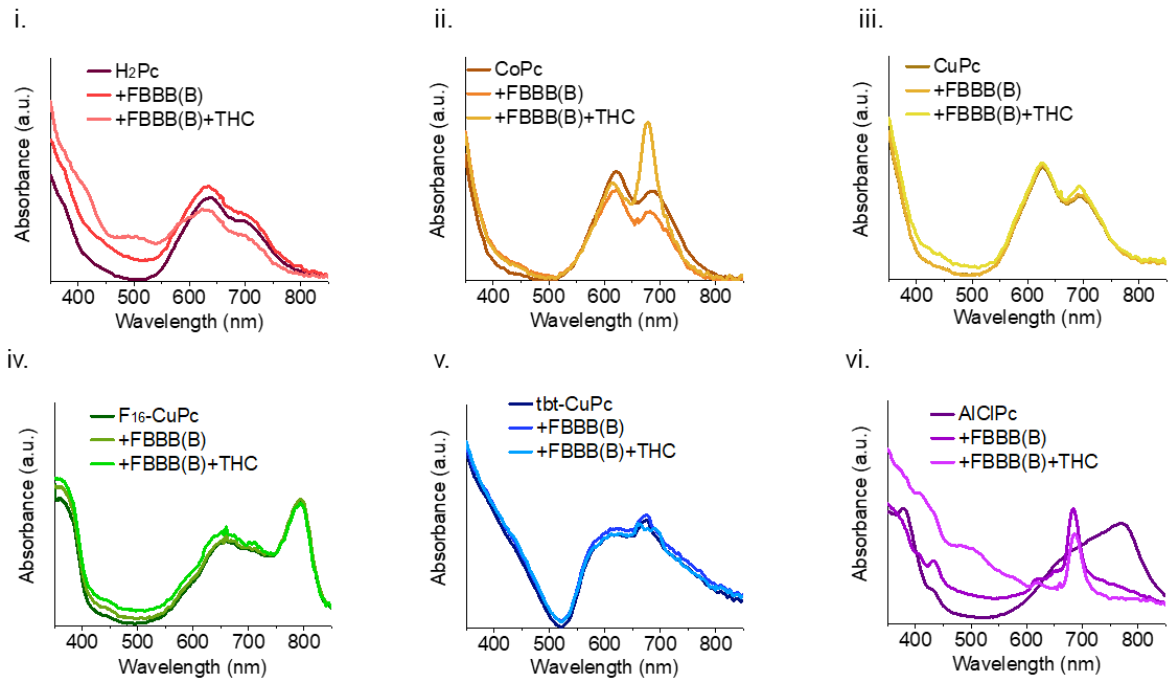

***Figure A.4.4**. UV-Vis spectra of phthalocyanine thin-films (i) H_2Pc, (ii) CoPc, (iii) CuPc, (iv) F_{16}-CuPc, (v) tbt-CuPc, (vi) AlClPc, as deposited, with exposure to 40 µM FBBB with 50 µM of NaOH at pH 9, and with subsequent exposure to 40 µM THC.*

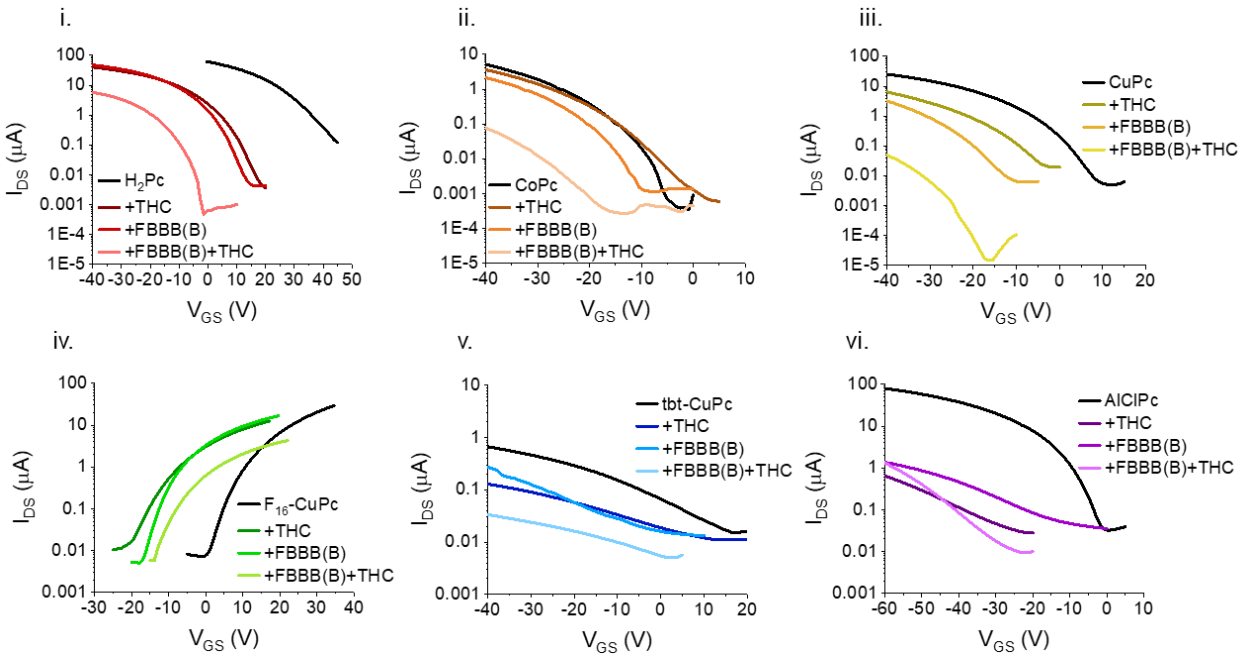

Figure A.4.5. *Relative effects of applied analytes on the transfer curves of Pc-based OTFTs. Transfer data was collected for H_2Pc, CoPc, CuPc, F_{16}-CuPc, tbt-CuPc, and AlClPc semiconductors (baseline) prior to addition of 40 μM THC, or 40 μM FBBB with NaOH at pH 9 and subsequent exposure to 40 μM THC.*

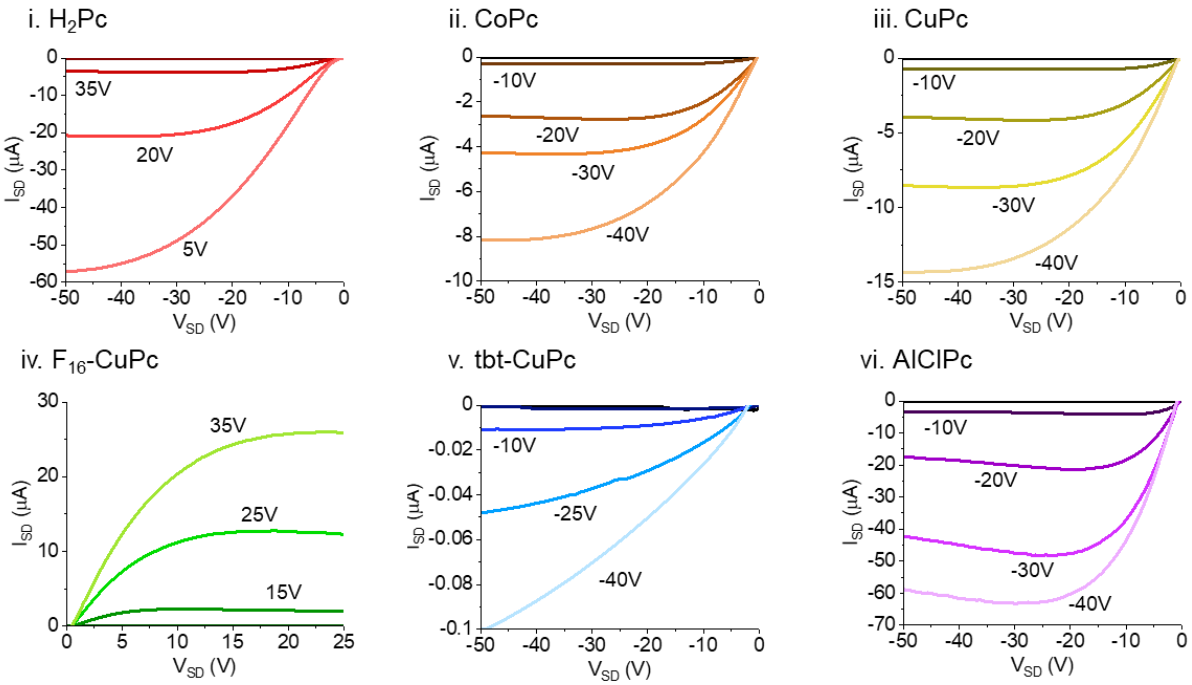

Figure A.4.6. *Sample output curves of Pc-based OTFTs. Output curves were obtained for characteristic H_2Pc, CoPc, CuPc, F_{16}-CuPc, tbt-CuPc, and AlClPc semiconductors.*

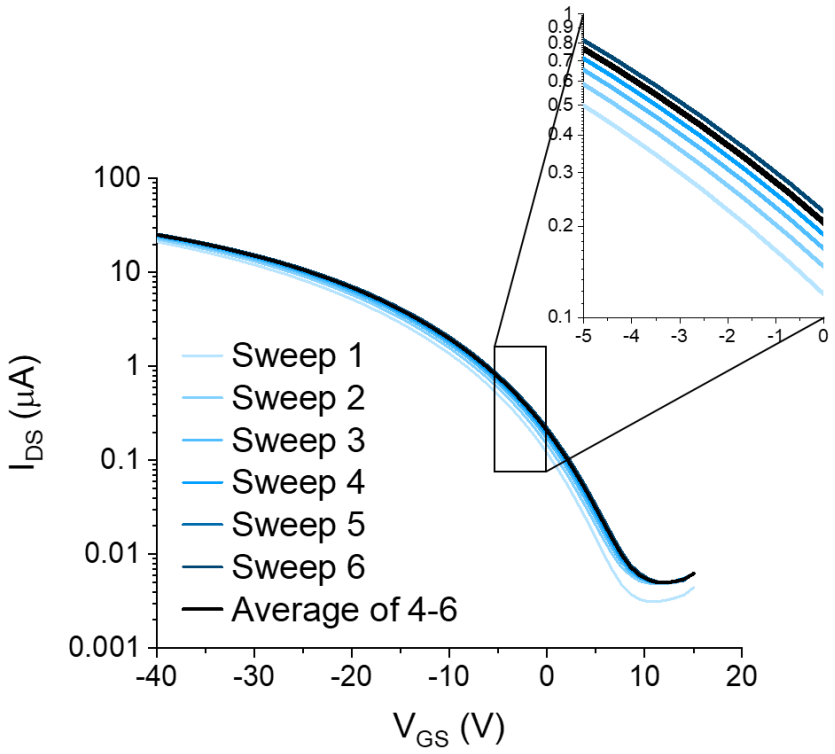

Figure A.4.7. *Bias stress and saturation effects on CuPc transfer curves.*

	μ_H (10^{-2} cm^2 $V^{-1}s^{-1}$)	V_T (V)	N (10^{-12} cm^2 V^{-1})
H_2Pc	2.5	45	16.2
CoPc	0.33	-5	7.5
CuPc	3.0	10	9.4
F_{16}-CuPc	2.7*	0	7.2
tbt-CuPc	0.041	12	12.5
AlClPc	7.3	0	7.2

Table A.4.1. *Baseline hole mobilities (μ_H), voltage threshold (V_T), and defect densities (N) for Pc OTFTs. *μ_E was recorded for F_{16}-CuPc.*

References

1. O. A. Melville, B. H. Lessard, T. P. Bender, ACS Appl. Mater. Interfaces 2015, 7, 13105.
2. W. Zhou, N. J. Yutronkie, B. H. Lessard, J. L. Brusso, Mater. Adv. 2021, 2, 165.
3. L. BH, ACS Appl. Mater. Interfaces 2021, 13, 31321.
4. N. Kaur, M. Singh, D. Pathak, T. Wagner, J. M. Nunzi, Synth. Met. 2014, 190, 20.
5. T. M. Grant, D. S. Josey, K. L. Sampson, T. Mudigonda, T. P. Bender, B. H. Lessard, Chem. Rec. 2019, 19, 1093.
6. J. Liu, M. Agarwal, K. Varahramyan, Sens. Actuators, B 2008, 135, 195.
7. N. T. Boileau, O. A. Melville, B. Mirka, R. Cranston, B. H. Lessard, RSC Adv. 2019, 9, 2133.
8. D. Khodagholy, V. F. Curto, K. J. Fraser, M. Gurfinkel, R. Byrne, D. Diamond, G. G. Malliaras, F. Benito-Lopez, R. M. Owens, J. Mater. Chem. 2012, 22, 4440.
9. G. Seo, G. Lee, M. J. Kim, S.-H. Baek, M. Choi, K. B. Ku, C.-S. Lee, S. Jun, D. Park, H. G. Kim, S.-J. Kim, J.-O. Lee, B. T. Kim, E. C. Park, S. I. Kim, ACS Nano 2020, 14, 5135.
10. Z. Wang, L. Huang, X. Zhu, X. Zhou, L. Chi, Adv. Mater. 2017, 29, 1703192.
11. D. Klyamer, A. Sukhikh, S. Gromilov, P. Krasnov, T. Basova, Sensors 2018, 18, 2141.
12. L. Torsi, A. Dodabalapur, L. Sabbatini, P. G. Zambonin, Sens. Actuators, B 2000, 67, 312.
13. Z. J. Comeau, G. A. Facey, C. S. Harris, A. J. Shuhendler, B. H. Lessard, ACS Appl. Mater. Interfaces 2020, 12, 50692.
14. Z. J. Comeau, N. T. Boileau, T. Lee, O. A. Melville, N. A. Rice, Y. Troung, C. S. Harris, B. H. Lessard, A. J. Shuhendler, ACS Sens. 2019, 4, 2706.
15. C. E. Turner, M. A. Elsohly, E. G. Boeren, J. Nat. Prod. 1980, 43, 169.
16. R. Mechoulam, M. Peters, E. Murillo-Rodriguez, L. O. Hanuš, Chem. Biodivers. 2007, 4, 1678.
17. I. Ujváry, L. Hanuš, Cannabis Cannabinoid Res. 2016, 1, 90.
18. H. Z. Khiabani, J. G. Bramness, A. Bj⊘rneboe, J. M⊘Rland, Traffic Inj. Prev. 2006, 7, 111.
19. A. Stolker, J. Vanschoonhoven, A. Devries, I. Bobeldijkpastorova, W. Vaes, R. Vandenberg, J. Chromatogr. A 2004, 1058, 143.
20. I. Angeli, S. Casati, A. Ravelli, M. Minoli, M. Orioli, J. Pharm. Biomed. Anal. 2018, 155, 1.
21. K. Watanabe, E. Yamaki, I. Yamamoto, H. Yoshimura, Eisei Kagaku 1979, 25, 321.
22. N. A. Dos Santos, L. M. Souza, E. Domingos, H. S. França, V. Lacerda, A. Beatriz, B. G. Vaz, R. R. T. Rodrigues, V. V. Carvalho, B. B. Merlo, R. M. Kuster, W. Romão, Forensic Chem. 2016, 1, 13.
23. G. E. Lester, K. S. Lewers, M. B. Medina, R. A. Saftner, J. Food Compos. Anal. 2012, 27, 102.
24. H. Sirringhaus, Adv. Mater. 2014, 26, 1319.
25. C. G. Claessens, U. Hahn, T. Torres, Chem. Rec. 2008, 8, 75.
26. S. Yanagisawa, T. Yasuda, K. Inagaki, Y. Morikawa, K. Manseki, S. Yanagida, J. Phys. Chem. A 2013, 117, 11246.
27. M. Fahlman, S. Fabiano, V. Gueskine, D. Simon, M. Berggren, X. Crispin, Nat. Rev. Mater. 2019, 4, 627.
28. R. R. Cranston, M. C. Vebber, J. F. Berbigier, N. A. Rice, C. Tonnelé, Z. J. Comeau, N. T. Boileau, J. L. Brusso, A. J. Shuhendler, F. Castet, L. Muccioli, T. L. Kelly, B. H. Lessard, ACS Appl. Mater. Interfaces 2021, 13, 1008.
29. M. Schwarze, K. S. Schellhammer, K. Ortstein, J. Benduhn, C. Gaul, A. Hinderhofer, L. Perdigón Toro, R. Scholz, J. Kublitski, S. Roland, M. Lau, C. Poelking, D. Andrienko, G. Cuniberti, F. Schreiber, D. Neher, K. Vandewal, F. Ortmann, K. Leo, Nat. Commun. 2019, 10, 1.
30. H. Dong, X. Fu, J. Liu, Z. Wang, W. Hu, Adv. Mater. 2013, 25, 6158.
31. O. A. Melville, N. A. Rice, I. Therrien, B. H. Lessard, Dyes Pigm. 2018, 149, 449.

32. B. Shao, Y. Liu, X. Zhuang, S. Hou, S. Han, X. Yu, J. Yu, J. Mater. Chem. C 2019, 7, 10196.
33. .J. Zaumseil, H. Sirringhaus, Chem. Rev. 2007, 107, 1296.
34. H. Sirringhaus, Adv. Mater. 2009, 21, 3859.
35. L. Li, Q. Tang, H. Li, W. Hu, J. Phys. Chem. B 2008, 112, 10405.
36. T. D. Anthopoulos, T. S. Shafai, Appl. Phys. Lett. 2003, 82, 1628.
37. Z.-T. Zhu, J. T. Mason, R. Dieckmann, G. G. Malliaras, Appl. Phys. Lett. 2002, 81, 4643.
38. Y. Zang, F. Zhang, D. Huang, X. Gao, C.-A. Di, D. Zhu, Nat. Commun. 2015, 6, 6269.
39. D. Elkington, N. Cooling, W. Belcher, P. Dastoor, X. Zhou, Electronics 2014, 3, 234.
40. S. Kera, M. B. Casu, K. R. Bauchspieß, D. Batchelor, T. Schmidt, E. Umbach, Surf. Sci. 2006, 600, 1077.
41. A. Popescu, R. A. Younts, B. Hoffman, T. Mcafee, D. B. Dougherty, H. W. Ade, K. Gundogdu, I. V. Bondarev, Nano Lett. 2017, 17, 6056.
42. R. R. Cranston, B. H. Lessard, RSC Adv. 2021, 11, 21716.
43. N. T. Boileau, R. Cranston, B. Mirka, O. A. Melville, B. H. Lessard, RSC Adv. 2019, 9, 21478.
44. D. L. Gonzalez Arellano, E. K. Burnett, S. Demirci Uzun, J. A. Zakashansky, V. K. Champagne, M. George, S. C. B. Mannsfeld, A. L. Briseno, J. Am. Chem. Soc. 2018, 140, 8185.
45. J. Xu, X. Liu, W. Hou, H. Guo, L. Yu, H. Zhang, Bull. Mater. Sci. 2018, 41, 111.
46. T. Mcafee, B. C. Hoffman, X. You, J. M. Atkin, H. Ade, D. B. Dougherty, J. Phys. Chem. C 2016, 120, 18616.
47. G. Van Straaten, M. Franke, S. Soubatch, B. Stadtmüller, D. A. Duncan, T.-L. Lee, F. S. Tautz, C. Kumpf, J. Phys. Chem. C 2018, 122, 8491.
48. A. Ogunsipe, D. Maree, T. Nyokong, J. Mol. Struct. 2003, 650, 131.
49. X. Zhuang, S. Han, B. Huai, W. Shi, Y. Junsheng, Sens. Actuators, B 2019, 279, 238.
50. B. H. Lessard, M. Al-Amar, T. M. Grant, R. White, Z.-H. Lu, T. P. Bender, J. Mater. Chem. A 2015, 3, 5047.
51. Z. Zhou, J. Wang, J. Chen, C. Jiang, L. Li, M. Liu, J. Mater. Chem. C 2021, 9, 649.
52. M. Schwarze, W. Tress, B. Beyer, F. Gao, R. Scholz, C. Poelking, K. Ortstein, A. A. Günther, D. Kasemann, D. Andrienko, K. Leo, Science 2016, 352, 1446.
53. S. M. Yoon, H. J. Song, I.-C. Hwang, K. S. Kim, H. C. Choi, Chem. Commun. 2010, 46, 231.
54. L. Lozzi, S. Santucci, S. La Rosa, B. Delley, S. Picozzi, J. Chem. Phys. 2004, 121, 1883.
55. J. Xu, X. Liu, W. Hou, H. Guo, L. Yu, H. Zhang, Bull. Mater. Sci. 2018, 41, 111.
56. T. Zou, X. Wang, H. Ju, L. Zhao, T. Guo, W. Wu, H. Wang, Crystals 2018, 8, 22.
57. D. Janeba, P. Capkova, Z. Weiss, H. Schenk, Clays Clay Miner. 1998, 46, 63.
58. M. Gouterman, G. H. Wagnière', L. C. Sxyder, J. Mol. Spectrosc. 1963, 11, 108.
59. C. Finazzo, C. Calle, S. Stoll, S. Van Doorslaer, A. Schweiger, Phys. Chem. Chem. Phys. 2006, 8, 1942.
60. S. P. Greiner, D. L. Rowlands, R. W. Kreilick, J. Phys. Chem. 1992, 96, 9132.
61. S. Seelan, M. S. Agashe, D. Srinivas, S. Sivasanker, J. Mol. Catal. A: Chem. 2001, 168, 61.
62. J. M. Assour, S. E. Harrison, J. Phys. Chem. 1964, 68, 872.
63. D. V. Konarev, A. V. Kuzmin, M. A. Faraonov, M. Ishikawa, S. S. Khasanov, Y. Nakano, A. Otsuka, H. Yamochi, G. Saito, R. N. Lyubovskaya, Chem. - Eur. J. 2015, 21, 1014.
64. E. Van Faassen, H. Kerp, Sens. Actuators, B 2003, 88, 329.
65. Y. A. Koksharov, A. I. Sherle, A. N. Tikhonov, Synth. Met. 2005, 149, 19.
66. W. Gu, Y. Hu, Z. Zhu, N. Liu, J. Zhang, J. Wang, Solid-State Electron. 2013, 89, 101.
67. H. Wang, F. Zhu, J. Yang, Y. Geng, D. Yan, Adv. Mater. 2007, 19, 2168.
68. Z. Bao, A. J. Lovinger, A. Dodabalapur, Adv. Mater. 1997, 9, 42.

69. V. Rani, A. Sharma, P. Kumar, B. Singh, S. Ghosh, RSC Adv. 2017, 7, 54911.
70. M. D. Hanwell, T. A. Madison, G. R. Hutchison, J. Phys. Chem. C 2010, 114, 20417.
71. S. H. Kim, I. Kang, Y. G. Kim, H. R. Hwang, Y.-H. Kim, S.-K. Kwon, J. Jang, J. Mater. Chem. C 2013, 1, 2408.
72. Q. Zhang, V. Subramanian, Biosens. Bioelectron. 2007, 22, 3182.

Chapter 5. Surface Engineering Part-Per-Billion Sensitivity of Cannabinoids in Zinc Phthalocyanine Organic Thin-Film Transistors

This chapter is adapted from: *Surface Engineering Part-Per-Billion Sensitivity of Cannabinoids in Zinc Phthalocyanine Organic Thin-Film Transistors*. **Zachary J. Comeau**, Rosemary R. Cranston, Halynne Lamontagne, Cory S. Harris, Adam J. Shuhendler, and Benoît H. Lessard. Submitted, 2022.

Context

I sought to improve OTFT sensitivity by building on the mechanisms established in **Chapter 3**, where I observed the importance of material selection for Pc-cannabinoid interactions, and **Chapter 4**, where I determined that analyte induced recrystallization of thin-film morphology and polymorphs is a major driver of sensing response. By OSC material screening and then controlling deposition conditions, I was able to achieve a 100x increase in sensitivity compared to the devices first characterized in **Chapter 2**. I performed additional experiments to assay the effects cannabinoid exposure in real-time, further building on the previously established mechanisms, and the effects of polymorphism, which were surprising and may warrant additional investigation in future students' projects.

Contribution

I performed all experiments and analysis barring the GIWAXS experiments which were performed by RRC and HL and the AFM experiments which were performed by RRC. I authored the manuscript with editorial contributions by AJS and BHL.

Abstract

Phthalocyanine-based organic thin-film transistors (OTFTs) have been demonstrated as sensors for a range of analytes, including cannabinoids, in both liquid and gas phases. Detection of the primary cannabinoids, Δ^9-tetrahydrocannabinol (THC) and cannabidiol (CBD), is necessary for quality control and regulation, however, current techniques are often not readily available or impractical for consumers, industry, and law-enforcement. The OTFT characteristics, X-ray diffraction (XRD) spectra, and grazing incident wide angle X-ray scattering (GIWAXS) spectra of two copper and three zinc phthalocyanines, with varying degrees of peripheral fluorination, were screened to determine sensitivity to THC vapor. Unsubstituted ZnPc was found to be the most sensitive material and, by tuning thin-film morphology and thickness through altered physical

vapor deposition conditions, we increased the sensitivity to THC by 100x. Real-time electrical characterization of the most THC-sensitive thin-films demonstrated both immediate semi-reversible and sustained irreversible effects which we attributed to analyte induced hole-trapping and physical film restructuring, respectively. Thin-film thickness impacted the magnitude of these effects, where thicker films were found to be less responsive. Additionally, a unique device output for THC relative to a potentially interfering vaporized organic product demonstrated the selectivity and sensitivity of these devices. The sensitivity of different thin-film polymorphs was examined post-exposure and in real-time, demonstrating significant film re-crystallization of the β-ZnPc polymorph upon exposure to THC vapor eliciting an electrical turn-on response. Thus, deposition conditions, and the resulting film morphology, thickness, and polymorph, play a significant role in the sensing properties of the semiconducting material and demonstrate physical, rather than chemical, methods for device sensitization.

Introduction

Phthalocyanines (Pcs) and their derived metal complexes (MPcs) are macrocyclic organic compounds with a variety of industrial applications due to their useful spectral and electronic properties[1,2]. First reported in 1907, Pcs were highlighted for their excellent stability and brilliant color, finding extensive use as dyes and pigments[3–5]. As conjugated aromatic molecules, Pcs are often deposited as charge transport layers within organic thin-film transistors (OTFTs) and organic photovoltaics (OPVs)[6,7]. Pc-based OTFTs have been demonstrated as sensors for a variety of liquid and gas sensing applications[8–12], including our groups' recent demonstration of ratiometric detection and differentiation of Δ^9-tetrahydrocannbinol (THC) and cannabidiol (CBD)[13,14]. The dominant active cannabinoids in *Cannabis sativa* smoke/vapour and consumer products, THC and CBD are used for therapeutic and recreational purposes[15,16], however, as THC and CBD elicit different pharmacological effects, accurate, low-cost quantification and speciation is of interest to industry, law enforcement and consumers[17]. Quantitative commercial speciation can be accomplished with high-performance liquid chromatography (HPLC) or gas chromatography-mass spectrometry (GC-MS), though these techniques are often impractical for companies or individuals with limited resources. In our previous works[13,14,18], we rationally examined a variety of Pc-based OTFT sensors and established that the observed sensing responses were due to a combination of electrochemical interactions and physical effects on thin-film crystallinity. Ultimately, we established a relationship between OTFT sensing characteristics and analyte induced physical thin-film effects, which highlighted the importance of semiconducting material selection.

An advantage of Pcs is the ease by which modifications can be made to the central metal, peripheral, or axial substituents[2,7,19], which allows tuning of the electronic, colorimetric, and solubility properties of the Pc to enable a range of applications. Peripheral tetra- (F_4-MPc), octa- (F_8-MPc), or hexadeca- (F_{16}-MPc) Pc fluorination has been demonstrated for tuning thin-film band structures and crystal morphologies[20–22]. Increased fluorination was also found to confer increased solubility and n-type behavior in OTFTs[20,23,24]. With tuneable solubility and high stability, Pcs have been deposited as semiconducting layers for OTFTs both through solution techniques and physical vapor deposition (PVD)[7,22,25]. Examined with the goal of improving charge transport, deposition conditions generally focus on optimizing intermolecular distances while minimizing the negative effects of grain boundaries, interface energetics, and device architecture[22,26–28]. Electrically, improved charge transport is characterized by high mobility (μ), a voltage threshold (V_T) near 0 V, low hysteresis, a large on/off current ratio (On/Off), and low defect density (N), all of which can be obtained from the transfer characteristics of an OTFT[7,29,30]. Post-deposition annealing can be accomplished with a range of techniques, most commonly heat or solvent vapor, but the goal of improved charge transport, and the mechanisms by which it's achieved, remain the same[31,32]. Thus, in addition to molecular tuning, Pc thin films can be morphologically tuned through film engineering by altering the deposition surface, deposition conditions, or post-deposition annealing to obtain more favorable spectral characteristics or charge transport conditions[33,34].

Post deposition annealing and sensing studies have highlighted zinc phthalocyanine (ZnPc) as a highly tuneable and sensitive material[24,35–38] and we have previously demonstrated that analyte exposure induces structural changes within films, altering, and more often disrupting, charge transport pathways similarly to post deposition annealing techniques[18]. Thus, where analyte exposure can induce altered thin-film nanostructures triggering a larger sensing response, we hypothesize that structurally different films will have altered sensing responses. Here, we examine and screen the effects of THC vapor on thin-film crystallinity and OTFT performance of ZnPc, zinc tetrafluorophthalocyanine (F_4-ZnPc), and zinc hexadecafluorophthalocyanine (F_{16}-ZnPc), and compare the THC sensing performance to our previously evaluated copper phthalocyanine (CuPc), and copper hexadecafluorophthalocyanine (F_{16}-CuPc) devices. We further investigate the most sensitive material by examining the effects of deposition conditions, crystal morphology, and thin-film thickness with the goal of increasing the sensitivity to THC vapor. By X-ray diffraction (XRD), grazing incident wide angle X-ray scattering (GIWAXS), atomic force microscopy (AFM), and scanning electron microscopy (SEM), we interrogate thin-film surface nanostructures and morphology pre- and post-exposure to THC vapor, relating OTFT sensing

characteristics to the physical characteristics of Pc thin films. Additionally, we perform real-time electrical characterization with vapor exposure to further elucidate the role of film thickness and polymorphism with sensing response. Ultimately, through material selection and tuned deposition conditions, we achieve an 100x increase in ZnPc device sensitivity to THC vapor, demonstrating the importance and utility of thin-film structures and engineering.

Results and Discussion

Material optimization

CuPcs and ZnPcs, with various degrees of fluorination (CuPc, F_{16}-CuPc, ZnPc, F_4-ZnPc, F_{16}-ZnPc) (**Figure 5.1**), were deposited as 400 Å thin-films by PVD at 25°C with a rate of 0.2 Å/s on OTS treated Si/SiO_2 substrates with and without prepatterned gold electrodes. Pre-exposure GIWAXS and XRD spectra (**Figure A.5.1**) revealed films with a high intensity (100) plane at q = ~0.50 $Å^{-1}$ and a single XRD peak with 2θ between 6-7°, suggesting a preferential orientation of the Pc ring to the substrate surface of ~75º; typical of α-crystal orientations with co-facial herringbone stacking[21,39]. Pre-exposure output and transfer curves (**Figure A.5.2**) demonstrated OTFT performance in agreement with other sources[7,27,40,41], with complete peripheral fluorination (F_{16}-) of both CuPc and ZnPc conferring n-type OTFT behavior.

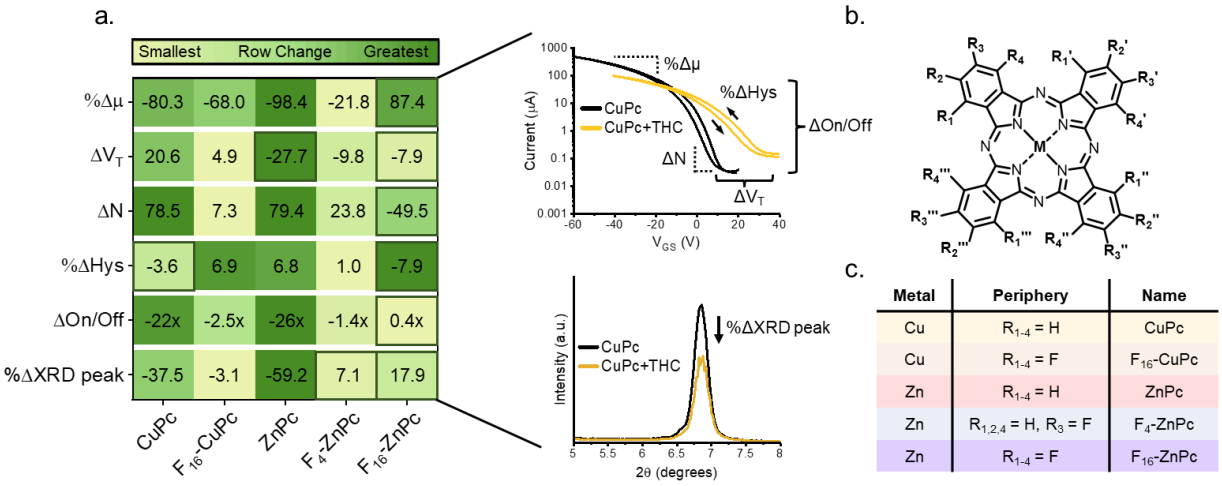

Figure 5.1. *Effects of THC vapor on Pc OTFT electrical characteristics and XRD spectra. CuPc, F_{16}-CuPc, ZnPc, F_4-ZnPc, or F_{16}-ZnPc OTFTs were exposed to 4 ppm THC vapor over a period of 90 seconds (average taken over 20 devices). Boxed regions represent a sign change from the median response. Sample transfer and XRD spectra demonstrate sampled regions. Additionally shown is a general Pc structure and a table of the Pc's studied. Mobility was calculated from the saturation region of the transfer curves while defect density and voltage threshold were estimated from the subthreshold slope.*

Pc thin-films were exposed to 4 ppm THC vapor over a period of 90 seconds and the percent change in peak mobility (%Δμ), voltage threshold shift (ΔV_T), defect density (ΔN),

hysteresis (%ΔHys), on/off current ratio (ΔOn/Off), and peak XRD intensity (%ΔXRD) was determined for each material and displayed in **Figure 5.1a**. As previously established[18], analytes, such as THC, when introduced to Pc thin films, in addition to the effects of intermolecular interactions, can also alter physical characteristics of the thin film, such as crystal packing and morphology, which can cause changes in OTFT performance. Here, with the exception of devices made with F_4-ZnPc, the sign, and magnitude, of the change in XRD peak height correlates to the magnitude of the change in μ and N. By XRD and GIWAXS, the absence of any observed new crystal morphologies suggests that, without the formation of new polymorphs, mobility decreases are related to the degree of change in α-crystallinity of the bulk film. Limited changes in hysteresis and negligible OTFT bias stress effects suggests that exposure of OTFTs to THC vapor results in irreversible and relatively stable physical thin-film changes[29].

In our previous works[14,18], we found that THC, as a π-conjugated molecule with electron donating properties[42], interacts with the central metal of MPcs, and that these interactions are deferential to the species of the central metal. The molecular size, electronegativity, and valence structure of the central metal affects analyte interactions, which, in addition to electrochemical effects, can also result in physical effects, such as distortions to the Pc ring, and induce physical charge traps[38]. Here, CuPc and F_{16}-CuPc based devices both show $+\Delta V_T$ with exposure to THC while the ZnPc, F_4-ZnPc, and F_{16}-ZnPc based devices show $-\Delta V_T$, suggesting that the copper-THC interaction induces electron trapping while the zinc-THC interaction creates deep, but short life-time, hole traps[29,43]. The peripherally fluorinated Pcs demonstrate smaller changes in XRD peak intensity, ΔN, and ΔOn/Off, suggesting limitations to both metal-analyte interactions and film restructuring as a result of their increased size or peripheral electronegativity. With the exception of hysteresis, an overall comparison of the transfer curves and XRD spectra demonstrates that ZnPc devices undergo the greatest changes across all metrics with exposure to THC vapor. This further illustrates the critical impacts of analyte-Pc interactions and thin-film restructuring on over all device performance, highlighting the role of material selection in optimizing sensing responses.

Effects of Morphology

With the greatest changes observed for ZnPc devices, we sought to further examine the effects of thin-film structures by preparing 400 Å α-ZnPc ($2\theta = 6.92°$) OTFTs by altering the PVD rate or deposition substrate temperature, and altering the substrate surface by pre-depositing a monolayer of p-sexiphenyl (p-6P) as a patterning agent to afford varying degrees of α-crystallinity[44,45]. The fastest deposition rate (1 Å/s) at the lowest deposition substrate temperature (25°C) resulted in small uniform grains by AFM, low peak intensity by XRD, and poor transfer

characteristics (**Figure 5.2**). Decreasing deposition rate, increasing deposition substrate temperature, or deposition on p-6P as a patterning agent, led to larger grain sizes, increased XRD peak intensity, and generally improved OTFT transfer characteristics (**Table A.5.1**).

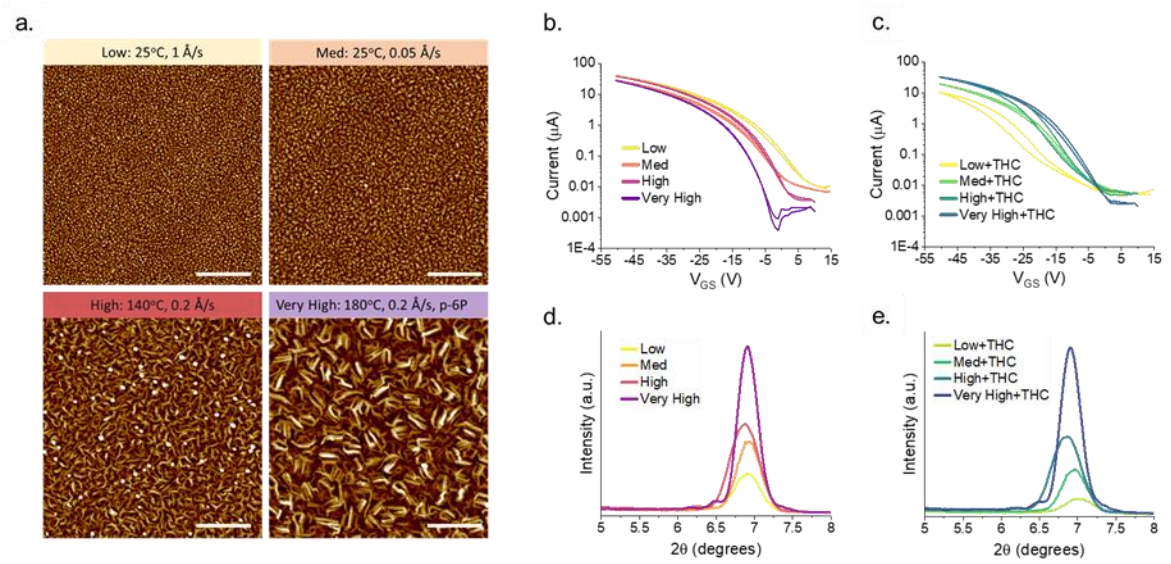

Figure 5.2. *Effect of surface morphology on ZnPc OTFT sensitivity to THC vapor. (a) AFM images, transfer data, and XRD spectra of ZnPc OTFTs with varying degrees of crystallinity (b, d) pre- and (c, e) post-exposure to 400 ppb THC vapor over 90 seconds. Low crystallinity thin-films were deposited at a rate of 1 Å/s and 25°C, medium (med) at 0.05 Å/s and 25°C, high at 0.2 Å/s and 140°C, and very high at 0.2 Å/s and 180°C with a pre-deposited monolayer of p-sexiphenyl (p-6P). Scale bars represent 500 nm.*

Exposure of the least crystalline films to 4 ppm of THC vapor rendered the OTFTs inoperable. Films were instead exposed to 400 ppb THC vapor over a period of 90 seconds, inducing the greatest changes in the least crystalline films, and manifesting as -%$\Delta\mu$, -ΔV_T, an increase in hysteresis, decreased On/Off, and +ΔN (**Table A.5.1**). Increased thin-film crystallinity reduced OTFT sensing responses, with the most crystalline films demonstrating limited changes in charge transport characteristics and negligible changes in XRD intensity. This suggests that smaller grains in the low crystallinity films affords increased surface area for ZnPc-THC interactions and intermolecular forces which facilitate greater changes by XRD and thus greater OTFT sensing responses. Previously, we demonstrated a relationship between different Pcs, their analyte induced physical film changes, and the measured OTFT sensing responses[18]. Here, these findings demonstrate that this relationship between physical thin-film changes and an OTFT sensor response can be applied to a single material, highlighting the importance of thin-film nanostructures for analytes-sensor interactions.

Film Thickness Effects and Real-Time Sensing

To assay the effects of thickness on the most sensitive thin-film conditions, we prepared OTFTs with 200 and 800 Å, low-crystallinity α-ZnPc films (deposition rate 1 Å/s at 25°C) and exposed them to 40 ppb THC vapor over a period of 90 seconds (**Figure A.5.3**). Pre-exposure, OTFTs of both thicknesses demonstrated similar transfer characteristics to low-crystallinity α-ZnPc 400 Å OTFTs, indicating that film thickness between 200-800 Å does not significantly influence the electrical performance of these low-crystallinity OTFTs. Compared to the 200 Å films, XRD spectra shows an expected, 59% more intense α- peak (2θ = 6.92°) for the 800 Å film, as the additional thickness provides additional diffraction signal[46]. The 2D scattering pattern determined by GIWAXS corroborates an α- phase orientation with a highly ordered (100) plane at q = 0.49 $Å^{-1}$ and a preferential Pc orientation to the surface of ~74º. Exposure to THC vapor showed a similar $+\Delta V_T$, increase in hysteresis, $-\Delta N$, and a decrease in XRD peak intensity for OTFTs of both thicknesses. The OTFTs with 200 Å films demonstrated a larger decrease in on-current, greater ΔN, and greater $-\%\Delta\mu$, suggesting greater relative changes in film crystallinity, while changes in V_T and hysteresis suggest Pc-THC interactions which are independent of film thickness.

The initially screened thin-film conditions of 400 Å α-ZnPc OTFTs, deposited at a rate of 0.2 Å/s and 25ºC, demonstrate a negligible response when exposed to 40 ppb THC vapor (**Figure A.5.4**). Comparing the response of the initially screened thin-film conditions to the sensitized response of the thinnest low crystallinity films, we demonstrate a 100x increase in post-exposure sensitivity to THC vapor. Thus, altered surface morphology and semiconductor thickness has a significant effect on OTFT sensitivity.

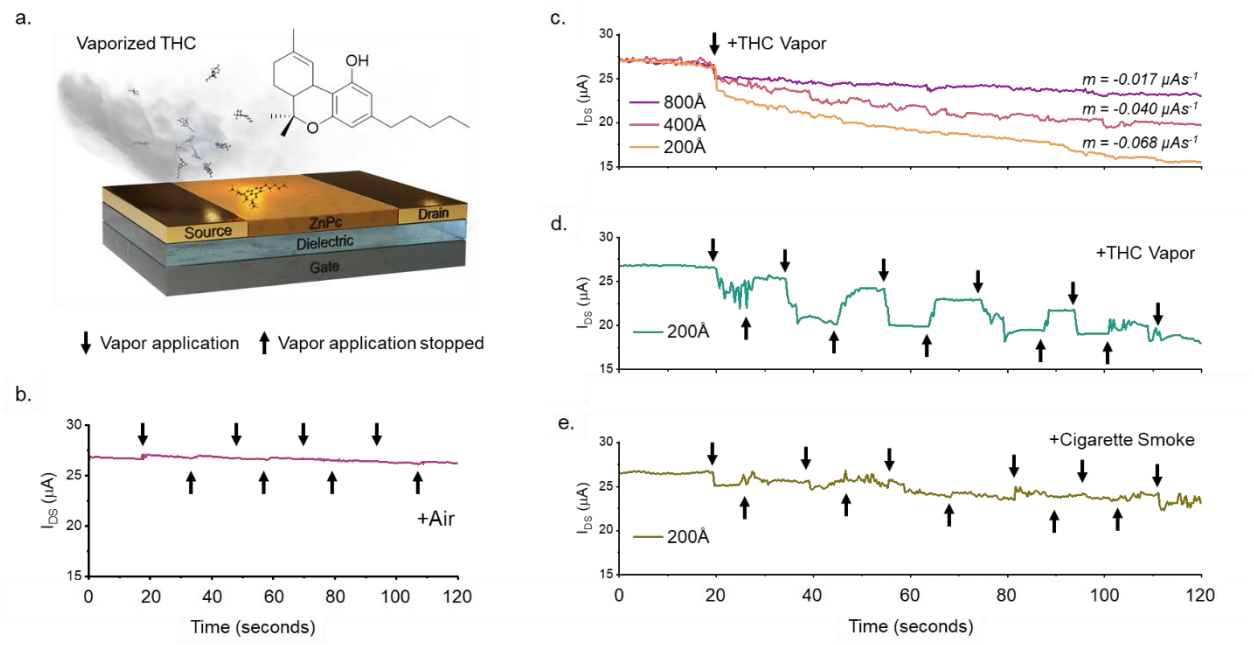

Figure 5.3. *Real-time THC vapor exposure and detection. (a) Schematic showing the application of THC vapor to a ZnPc OTFT, (b) the effects of heated air, (c) the effects of continual THC vapor exposure on 200, 400, and 800 Å ZnPc OTFTs, (d) the effects of periodic THC exposure on a 200 Å ZnPc OTFT, and (e) the effects of 40 ppb cigarette smoke on 200 Å ZnPc OTFTs. A V_{SD} of -50 V was held and a V_{GS} of -40 V and was pulsed at a rate of 20 milliseconds on 80 milliseconds off over a period of 120 seconds while 40 ppb THC vapor was continually or periodically flowed over the surface of the OTFT in a 50 mL chamber. Slope was calculated from 20 to 120 seconds.*

To examine the effects of THC exposure in real time, we operated low crystallinity α-ZnPc OTFTs at fixed saturation biases while they were continually exposed to 40 ppb THC vapor (**Figure 5.3**). At operating biases of V_{SD} = -50 V and V_{GS} = -40 V, continuous THC vapor exposure caused an immediate, sharp, operating current decrease followed by a sustained decrease in operating current at a constant rate, which was mediated by thin-film thickness (**Figure 5.3c**). Pulsed exposure demonstrated a similar effect (**Figure 5.3c and A.5.5**), where the onset of THC vapor induced an immediate decrease in operating current followed by a sustained, thickness mediated, decrease over time. However, after short exposures (~10 seconds), operating current recovered sharply when vapor application was stopped, though not to pre-exposure levels, and subsequent exposures reduced the magnitude of both the operating current decrease and recovery with vapor onset and offset.

The magnitude of the effects of vapor onset, continued exposure, and vapor offset were inversely related to film thickness, where the thinnest, 200 Å films, demonstrated the largest responses, consistent with OTFT sensors made with Cl-AlPc[47]. Additionally, for both pulsed and continual modes of exposure, after 90 seconds, the operating current is consistent with the

operating current of films of the same thickness characterized post-exposure at the same bias conditions, suggesting prolonged exposure limits the observed recovery. Both periodic exposures to forced air and continued device operation in air (**Figure 5.3b**), yielded negligible changes in operating current.

The observed, sharp, but semi-reversible, decreases in operating current with THC vapor onset suggests that the introduction of THC immediately causes hole-trapping effects, lowering the operating current. Sustained, irreversible decreases in operating current with continued THC vapor application then suggests that over time, irreversible structural defects occur within the film, permanently lowering operating current. That both the immediate and sustained decreases in operating current are thickness dependant supports these conclusions, as both the amounts of THC relative to Pc within the film and the THC induced structural defects will be greatest for the thinnest films. Periodic exposure of the 200 Å films to 40 ppb cigarette smoke yields small onset current decreases with smoke application, slight current recovery when smoke application stops, and a slight decrease in current over time (**Figure 5.3e**). However, the magnitude of the operating current decrease was small and the results noisy, indicating that other vaporized organic compounds have different effects on the electrical performance of the substrates, and demonstrating the innate selectivity of ZnPc for this application. Thus, every step of sensor manufacturing impacts device performance, from material selection, deposition conditions, and thin-film thickness.

Effects of Polymorphism

To analyze the effects of crystal polymorphism on sensing response, we prepared β-ZnPc thin-films by treating 400 Å α-ZnPc thin-films with toluene vapor for 24 hours (**Figure 5.4**) resulting in OTFTs with lower peak μ, lower V_T, lower off current, and lower N in comparison to α-ZnPc OTFTs. Additionally, large, μm-scale rectangular crystals are observable by SEM. XRD spectra of the toluene treated films showed two sharp peaks of equal intensity at 2θ = 7.04 and 9.32°, consistent with reported β-Pc morphology[31], and a small shoulder peak at 2θ = 6.84°. The azimuthally-integrated GIWAXS pattern of the films is in good agreement with the β-ZnPc pattern predicted by single crystal XRD (**Figure A.5.6**) confirming complete transition from α- to β- phase. The 2D scattering pattern reveals a highly ordered crystalline thin film with the (100) plane at q = 0.50 $Å^{-1}$ and the (10-2) plane at q = 0.68 $Å^{-1}$ along the q_z axis suggesting multiple molecular orientations however with a preference of the Pc ring aligned ~45º to the surface.

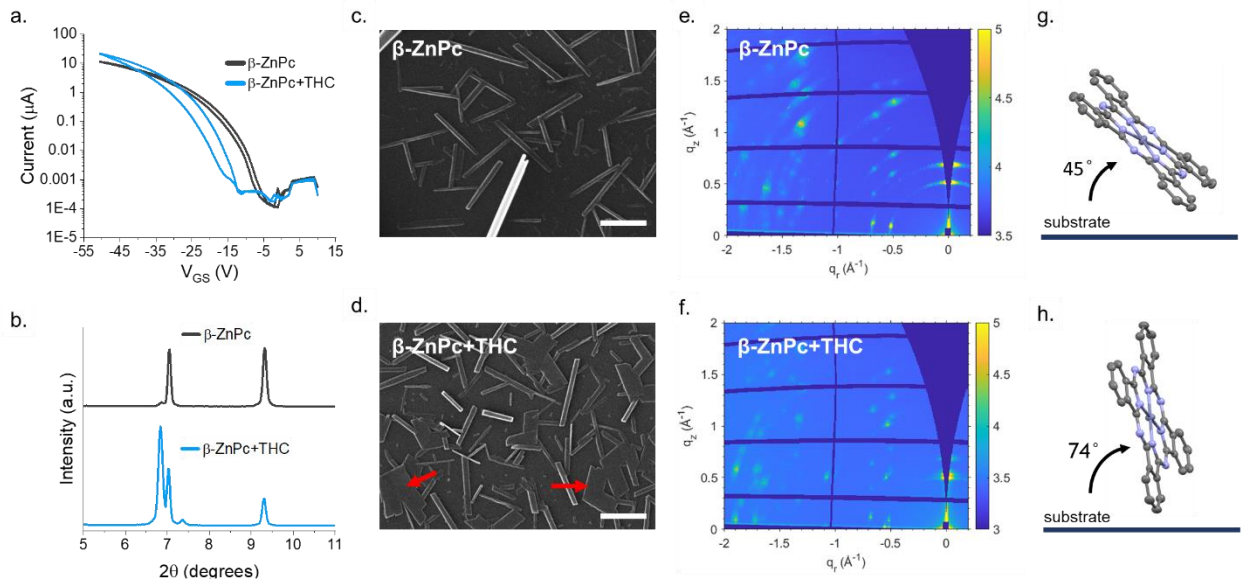

Figure 5.4. *Effect of β- morphology on ZnPc OTFT sensitivity to THC vapor. (a) Transfer data, (b) XRD spectra, and (c,d) SEM images of ZnPc OTFTs after exposure to 400 ppb THC vapor over a period of 90 seconds. Scale bars represent 2 μm and red arrows denote sheet formation. (e, f) 2D scattering patterns (θ = 0.1°) of β-ZnPc thin films deposited on Si substrates and (g, h) a schematic showing GIWAXS determined preferential phase angle to the substrate pre- and post- exposure to THC vapor.*

Exposure to 400 ppb THC vapor over a period of 90 seconds resulted in a 10.3 μA increase in peak operating current, a -7.4 V in ΔV_T, and a 4.1 V increase in hysteresis. By XRD, the intensity of the peak at 2θ = 7.04° does not change while the intensity of the peak at 2θ = 9.32° decreases by 53%. The shoulder peak at 2θ = 6.84° increases in intensity by 20-fold, and a new peak at 2θ = 7.38° appears, indicating morphological changes. Visualized by SEM, previously well ordered, narrow, rectangular crystals become broad and sheet-like post-exposure (red arrows). By GIWAXS we observe a decrease in relative peak intensity corresponding to the (10-2) plane (q = 0.68 Å^{-1}) and peak splitting at q = ~0.50 Å^{-1}, corresponding to the (100) plane (**Figure A.5.6**) in β-ZnPc thin films post-exposure to THC vapor. Additionally, the 2D scattering pattern of post-exposure films exhibit a narrowing of the partial arcs and a change in preferential ZnPc orientation to the surface from ~45º to ~74º.

β-ZnPc, despite being highly crystalline, generally demonstrates poor semiconducting performance due to suboptimal charge transport distances caused by close intermolecular spacing and increased face-on configuration[48]. Thus, the observed increase in operating current as an OTFT “turn-on” response may be a result of partial conversion of β-ZnPc crystals to an α-, or an α-like, polymorph through exposure to THC vapor. Low defect density (N = 5.4•10^{-12}) post-exposure suggests the sheet-like structures provide excellent charge transport pathways, with

hysteresis possibly resulting from the large interfacial areas between the sheets[22,49]. An XRD peak at 2θ = 7.38° for the exposed β-ZnPc films, but not the exposed α-ZnPc films, suggests an intermediate morphology in the THC vapor induced β- to α- ZnPc phase transition[31].

Real-time characterization of the β-ZnPc OTFTs with continual 400 ppb THC vapor exposure (**Figure A.5.7**) demonstrated a turn-off response when operated with V_{SD} of -50 V and V_{GS} of -20 V. Like the α-ZnPc OTFTs, with the onset of THC vapor there is an immediate decrease in operating current, however, rather than a subsequent sustained decrease with constant slope, instead there is a rapid decrease in operating current with a decaying slope. As a large V_T shift is observed for the β-ZnPc OTFTs characterized post-exposure, a decrease in operating current is expected at these bias conditions. Inconsistencies in the pre-exposure operating current and vapor onset effects for the β-ZnPc OTFTs, in comparison to the α-ZnPc OTFTs, are likely a result of uneven distribution and orientation of the β-crystals between OTFT electrodes.

With a V_{GS} bias of -40 V, there is again an immediate decrease in OTFT operating current with the onset of THC vapor with limited change for ~40 seconds, whereupon the operating current begins to fluctuate and trend upwards. Comparing to periodic exposure with the same bias conditions, we observe a similar fluctuating climb in operating current after ~35 seconds of exposure to THC vapor. Fluctuations in operating current suggest that significant μm-scale recrystallization events begin after ~35-40 seconds of exposure, in comparison to the immediate sustained decrease in operating current observed for the α-ZnPc OTFTs. Moreover, sharp decreases in operating current with vapor onset, and recovery with vapor offset, again suggests THC is introducing or acting as a hole-trap within the film. Additionally, where the most crystalline α-ZnPc thin-films demonstrated the least OTFT and XRD changes, highly crystalline β-ZnPc films demonstrated significant re-crystallization with exposure to THC vapor. Thus, the degree of molecular order on the surface is not necessarily indicative of either sensing response or the analyte-induced physical effects. Instead, the lowest crystallinity α-ZnPc OTFTs demonstrated the greatest electrical sensitivity to THC vapor, exhibiting the balance between thin-film morphology, recrystallization, and surface area for intermolecular interactions.

Conclusions

The effects of THC vapor exposure on both the central metal and peripheral fluorination demonstrated that non-fluorinated ZnPc OTFTs exhibited the greatest electrical and structural sensitivity compared to isostructural CuPc OTFTs and devices. Increasing peripheral fluorination was found to limit analyte induced structural changes while the central metal mediated voltage threshold shifts. Preparing α-ZnPc films with varying degrees of crystallinity revealed that the least

crystalline films were the most susceptible to physical alterations upon exposure to analytes and had the largest OTFT electrical changes. Film thickness was also found to effect sensitivity, with 200 Å, low crystallinity films demonstrating sensitivity to 40 ppb THC vapor. Real-time characterization of low crystallinity α-ZnPc OTFTs demonstrated an immediate, reversible hole-trapping effect with the onset of THC vapor and a sustained, irreversible operating current decrease due to physical film restructuring. In contrast, highly crystalline β-ZnPc films demonstrated significant structural changes when exposed to THC vapor. Such films transitioned from large, regular, μm-scale crystals to more sheet-like structures, with a change in preferred substrate angle from 45 to ~74° and demonstrating a turn-on OTFT response. Through film engineering of Pc-based OTFT sensors we achieved a 100x increase in sensitivity over our previously developed CuPc-based devices[13], illustrating the importance of not only material selection, but also thin-film nanostructures, thickness, and polymorphism in Pc-OTFT sensor implementations.

Experimental

Materials

CuPc (copper(II) phthalocyanine), F_{16}-ZnPc (zinc 1,2,3,4,8,9,10,11,15,16,17,18,22,23,24,25-hexadecafluoro phthalocyanine), and tricholoro(octyl)silane were obtained from Sigma Aldrich. F_{16}-CuPc (copper(II) 1,2,3,4,8,9,10,11,15,16,17,18,22,23,24,25-hexadecafluoro phthalocyanine), and ZnPc (zinc phthalocyanine) were obtained from TCI chemicals. F_4-ZnPc was synthesized according to ref. 35 and confirmed by mass spectrometry. All Pcs were purified by train sublimation prior to use. Cannabinoid standards were obtained from Toronto Research Chemicals. All solvents were HPLC grade and purchased from Fischer Scientific.

Thin Film Fabrication

Si substrates with 230 nm thermally grown SiO_2 dielectric and prepatterned gold source-drain electrodes (W = 2000 μm, L = 10 μm), were purchased from Fraunhofer IPMS and used to fabricate bottom-gate bottom-contact (BGBC) transistors. Si substrates with 300 nm thermally grown SiO_2 were purchased from Ossila and used for fabrication of thin films for XRD and GIWAXS. Wafers were prepared as described in ref. 18 before being transferred to an Angstrom EvoVac thermal evaporator where deposition rate and thin-film thickness was controlled by quartz crystal microbalance and substrate temperature was controlled by thermocouple.

β-ZnPc films were generated by exposing 400 Å ZnPc films deposited at 25°C at a rate of 0.2 Å/s to toluene vapor in a custom vapor chamber for 24 hours followed by a baking at 70°C for 45 minutes in a vacuum oven.

Vapor Exposure

THC was dissolved in methanol and loaded on to a steel wool frit where it was allowed to dry before being placed in a Volcano Medic vaporizer set to 210°C temperature. An 8 L balloon was filled completely before being evacuated into a 50 mL volume vapor chamber in which the substrates were placed.

OTFT Characterization

Organic thin film transistors were characterized, and defect density was calculated according to ref. 18.

XRD and GIWAXS

XRD characterization was performed using a Rigaku Ultima IV powder diffractometer with a Cu-Kα (λ = 1.5418 Å) source. Thin-film substrate measurements were taken with a scan range of $5° < 2\theta < 11°$ at a rate of 0.5°/min with a spin rate of 30 rpm.

GIWAXS experiments were performed at the Canadian Light Source (CLS) in Saskatoon, Canada using the Brockhouse Diffraction Sector (BXDS) beamline with a photon energy of 15.1 keV, and the SOLEIL Synchrotron facility in Saint-Aubin, France using the SIRIUS beamline with a photon energy of 10 keV. For data collected at CLS, GIWAXS patterns were collected using a Rayonix MX300 CCD detector (73.242 μm x 73.242 μm pixel size), placed 416 mm from the sample with an angle of incidence of θ = 0.3°. For data collected at SOLEIL, GIWAXS patterns were collected using a PILATUS3 S 1M detector (172 μm x 172 μm pixel size), placed 330 mm from the sample with an angle of incidence of θ = 0.1°. All GIWAXS data was calibrated against a silver behenate standard and a poly(3-hexylthiophene-2,5-diyl) standard and analyzed using the GIXSGUI software package in MATLAB, where both polarization and solid-angle corrections were applied.[50]

AFM and SEM

SEM measurements were performed with a Tescan Vega II on thin-film Pc devices at 20 kV. AFM measurements were performed with a Bruker Dimension Icon AFM, equipped with ScanAsyst-Air tips, and images were processed with NanoScope Analysis v.1.8. Scans were performed at a rate of 0.814 Hz with multiple sites investigated.

Acknowledgments

This work was supported by the National Science and Engineering Council of Canada (RGPIN-2015-05796 and RGPIN-2021-03387 to A. J. S.), and the Canada Research Chairs Program (950-230754 to A. J. S.). We acknowledge the Centre for Research in Photonics at the University of Ottawa (CRPuO) for access to the AFM. The authors would like to thank both the CLS and the SOLEIL Synchrotron facility for providing beamtime, and Adam Leontowich and Arnaud Hemmerle for their expertise and technical support during beamtime at CLS and SOLEIL respectively. CLS is supported by CFI, NSERC, the University of Saskatchewan, the Government of Saskatchewan, Western Economic Diversification Canada, the National Research Council Canada, and the Canadian Institutes of Health Research. SOLEIL is supported by the National Center for Scientific Research (CNRS), the French Alternative Energies and Atomic Energy Commission (CEA), the Île-de-France Regional Council, the Essonne Department Council and the Centre Regional Council.

The authors have no conflicts of interest to declare.

References

1. Lu, H. & Kobayashi, N. Optically Active Porphyrin and Phthalocyanine Systems. Chem. Rev. 116, 6184–6261 (2016).
2. Zhou, W., Yutronkie, N. J., Lessard, B. H. & Brusso, J. L. From chemical curiosity to versatile building blocks: unmasking the hidden potential of main-group phthalocyanines in organic field-effect transistors. Mater. Adv. 2, 165–185 (2021).
3. Braun, A. & Tcherniac, J. Über die Produkte der Einwirkung von Acetanhydrid auf Phthalamid. Berichte der Dtsch. Chem. Gesellschaft 40, 2709–2714 (1907).
4. Dahlen, M. A. The Phthalocyanines A New Class of Synthetic Pigments and Dyes. Ind. Eng. Chem. 31, 839–847 (2002).
5. Claessens, C. G., Hahn, U. & Torres, T. Phthalocyanines: From outstanding electronic properties to emerging applications. Chem. Rec. 8, 75–97 (2008).
6. de la Torre, G., Bottari, G. & Torres, T. Phthalocyanines and Subphthalocyanines: Perfect Partners for Fullerenes and Carbon Nanotubes in Molecular Photovoltaics. Adv. Energy Mater. 7, 1601700 (2017).
7. Melville, O. A., Lessard, B. H. & Bender, T. P. Phthalocyanine-Based Organic Thin-Film Transistors: A Review of Recent Advances. ACS Appl. Mater. Interfaces 7, 13105–13118 (2015).
8. Roberts, M. E., Sokolov, A. N. & Bao, Z. Material and device considerations for organic thin-film transistor sensors. J. Mater. Chem. 19, 3351–3363 (2009).
9. Liu, J., Agarwal, M. & Varahramyan, K. Glucose sensor based on organic thin film transistor using glucose oxidase and conducting polymer. Sensors Actuators B Chem. 135, 195–199 (2008).
10. Seo, G. et al. Rapid Detection of COVID-19 Causative Virus (SARS-CoV-2) in Human Nasopharyngeal Swab Specimens Using Field-Effect Transistor-Based Biosensor. ACS Nano 14, 5135–5142 (2020).
11. Torsi, L., Dodabalapur, A., Sabbatini, L. & Zambonin, P. . Multi-parameter gas sensors based on organic thin-film-transistors. Sensors Actuators B Chem. 67, 312–316 (2000).
12. Boileau, N. T., Melville, O. A., Mirka, B., Cranston, R. & Lessard, B. H. P and N type copper phthalocyanines as effective semiconductors in organic thin-film transistor based DNA biosensors at elevated temperatures. RSC Adv. 9, 2133–2142 (2019).
13. Comeau, Z. J. et al. On-the-Spot Detection and Speciation of Cannabinoids Using Organic Thin-Film Transistors. ACS Sensors 4, 2706–2715 (2019).
14. Comeau, Z. J., Facey, G. A., Harris, C. S., Shuhendler, A. J. & Lessard, B. H. Engineering Cannabinoid Sensors through Solution-Based Screening of Phthalocyanines. ACS Appl. Mater. Interfaces 12, 50692–50702 (2020).
15. Russo, E. B. History of Cannabis and Its Preparations in Saga, Science, and Sobriquet. Chem. Biodivers. 4, 1614–1648 (2007).
16. Gowran, A., Noonan, J. & Campbell, V. A. The Multiplicity of Action of Cannabinoids: Implications for Treating Neurodegeneration. CNS Neurosci. Ther. 17, 637–644 (2011).
17. Stolker, A. A. M. et al. Determination of cannabinoids in cannabis products using liquid chromatography–ion trap mass spectrometry. J. Chromatogr. A 1058, 143–151 (2004).
18. Comeau, Z. J. et al. Organic Thin-Film Transistors as Cannabinoid Sensors: Effect of Analytes on Phthalocyanine Film Crystallization. Adv. Funct. Mater. 32, 2107138 (2022).
19. Cranston, R. R. et al. Highlighting the processing versatility of a silicon

phthalocyanine derivative for organic thin-film transistors. J. Mater. Chem. C 10, 485–495 (2022).
20. Schwarze, M. et al. Band structure engineering in organic semiconductors. Science (80-.). 352, 1446–1449 (2016).
21. Boileau, N. T., Cranston, R., Mirka, B., Melville, O. A. & Lessard, B. H. Metal phthalocyanine organic thin-film transistors: Changes in electrical performance and stability in response to temperature and environment. RSC Adv. 9, 21478–21485 (2019).
22. Cranston, R. R. & Lessard, B. H. Metal phthalocyanines: thin-film formation, microstructure, and physical properties. RSC Adv. 11, 21716–21737 (2021).
23. Klyamer, D., Sukhikh, A., Gromilov, S., Krasnov, P. & Basova, T. Fluorinated metal phthalocyanines: Interplay between fluorination degree, films orientation, and ammonia sensing properties. Sensors (Switzerland) 18, (2018).
24. Schwarze, M. et al. Impact of molecular quadrupole moments on the energy levels at organic heterojunctions. Nat. Commun. 10, 1–9 (2019).
25. Shimoda, T. et al. Solution-processed silicon films and transistors. Nature 440, 783–786 (2006).
26. Tan, J., Sorensen, J., Dong, H. & Hu, W. Fullerene-derivative as interlayer for high performance organic thin-film transistors. J. Mater. Chem. C 6, 6052–6057 (2018).
27. Ye, R., Baba, M., Suzuki, K. & Mori, K. Improved performance of fluorinated copper phthalocyanine thin film transistors using an organic pn junction: Effect of copper phthalocyanine film thickness. Thin Solid Films 517, 3001–3004 (2009).
28. Melville, O. A. et al. Ambipolarity and Air Stability of Silicon Phthalocyanine Organic Thin-Film Transistors. Adv. Electron. Mater. 5, 1900087 (2019).
29. Sirringhaus, H. Reliability of organic field-effect transistors. Adv. Mater. 21, 3859–3873 (2009).
30. Lin, Y. J. & Lin, Y. C. Electrical conduction mechanisms in the transfer characteristics of pentacene thin film transistors. Appl. Phys. Lett. 105, 023506 (2014).
31. Xu, J. et al. Effect of solvent–vapour annealing on morphology, structure of copper(II) phthalocyanine thin films and device performance. Bull. Mater. Sci. 41, 111 (2018).
32. Ogunsipe, A., Maree, D. & Nyokong, T. Solvent effects on the photochemical and fluorescence properties of zinc phthalocyanine derivatives. J. Mol. Struct. 650, 131–140 (2003).
33. Faris, T. et al. Effects of annealing on device parameters of organic field effect transistors using liquid-crystalline tetrasubstituted zinc phthalocyanine. Europhys. Lett. 106, 58002 (2014).
34. Padma, N., Sawant, S. N., Sen, S. & Gupta, S. K. Effect of post deposition annealing on the performance of copper phthalocyanine based organic thin film transistor. AIP Conf. Proc. 1512, 786 (2013).
35. Klyamer, D. D. et al. Influence of fluorosubstitution on the structure of zinc phthalocyanine thin films. Macroheterocycles 11, 304–311 (2018).
36. Zhu, Y. et al. High-Performance NO2 Sensors Based on Ultrathin Heterogeneous Interface Layers. Adv. Mater. Interfaces 7, 1901579 (2020).
37. Gonzalez Arellano, D. L. et al. Phase Transition of Graphene-Templated Vertical Zinc Phthalocyanine Nanopillars. J. Am. Chem. Soc. 140, 8185–8191 (2018).
38. S Saini, G. S. et al. Zinc phthalocyanine thin film and chemical analyte interaction studies by density functional theory and vibrational techniques. (2009) doi:10.1088/0953-8984/21/22/225006.

39. Dong, H., Fu, X., Liu, J., Wang, Z. & Hu, W. 25th Anniversary Article: Key Points for High-Mobility Organic Field-Effect Transistors. Advanced Materials vol. 25 6158–6183 (2013).
40. Yan, X., Wang, H. & Yan, D. An investigation on air stability of copper phthalocyanine-based organic thin-film transistors and device encapsulation. Thin Solid Films 515, 2655–2658 (2006).
41. Jiang, H. et al. Molecular Crystal Engineering: Tuning Organic Semiconductor from p-type to n-type by Adjusting Their Substitutional Symmetry. Adv. Mater. 29, 1605053 (2017).
42. Borges, R. S. et al. Understanding the Molecular Aspects of Tetrahydrocannabinol and Cannabidiol as Antioxidants. Mol. 2013, Vol. 18, Pages 12663-12674 18, 12663–12674 (2013).
43. Gu, G., Kane, M. G., Doty, J. E. & Firester, A. H. Electron traps and hysteresis in pentacene-based organic thin-film transistors. Appl. Phys. Lett. 87, 243512 (2005).
44. Gu, W. et al. Preparing highly ordered copper phthalocyanine thin-film by controlling the thickness of the modified layer and its application in organic transistors. Solid. State. Electron. 89, 101–104 (2013).
45. Wang, T., Yang, J., Wang, H., Zhu, F. & Yan, D. Weak epitaxy growth and phase behavior of planar phthalocyanines on p-sexiphenyl monolayer film. J. Phys. Chem. B 112, 6786–6792 (2008).
46. Chang, J. F., Kuo, H. H., Leu, I. C. & Hon, M. H. The effects of thickness and operation temperature on ZnO:Al thin film CO gas sensor. Sensors Actuators B Chem. 84, 258–264 (2002).
47. Lamontagne, H. et al. Chloro Aluminum Phthalocyanine-based Organic Thin-Film Transistors as Cannabinoid Sensors: Engineering the thin film response. Sensors and Diagnostics (2022).
48. McAfee, T. et al. Morphological, Optical, and Electronic Consequences of Coexisting Crystal Orientations in β-Copper Phthalocyanine Thin Films. J. Phys. Chem. C 120, 18616–18621 (2016).
49. Hanwell, M. D., Madison, T. A. & Hutchison, G. R. Charge Transport in Imperfect Organic Field Effect Transistors: Effects of Explicit Defects and Electrostatics. J. Phys. Chem. C 114, 20417–20423 (2010).
50. Jiang, Z. GIXSGUI: a MATLAB toolbox for grazing-incidence X-ray scattering data visualization and reduction, and indexing of buried three-dimensional periodic nanostructured films. J. Appl. Crystallogr. 48, 917–926 (2015).

Supplemental Information

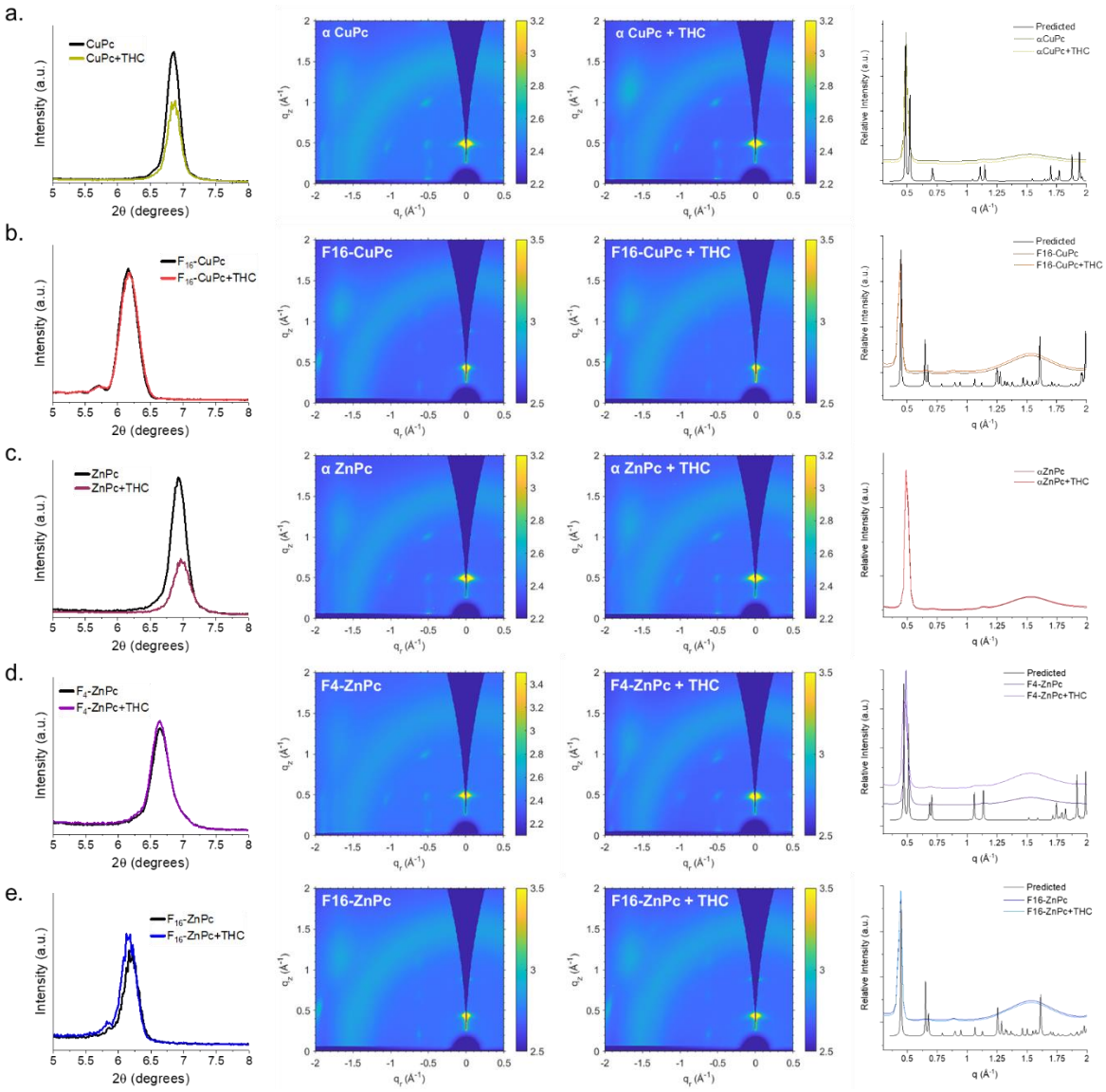

Figure A.5.1. *XRD, 2D scattering patterns (θ = 0.3°), and diffraction patterns predicted from single crystal and determined by GIWAXS of pre- and post- exposure films to THC vapor (a) α-CuPc (CCDC #219250)[1], (b) F_{16}-CuPc (CCDC #698474)[2], (c) α-ZnPc, (d) F_4-ZnPc (CCDC #1818040)[3], and (e) F_{16}-ZnPc (CCDC #1013162)[4].*

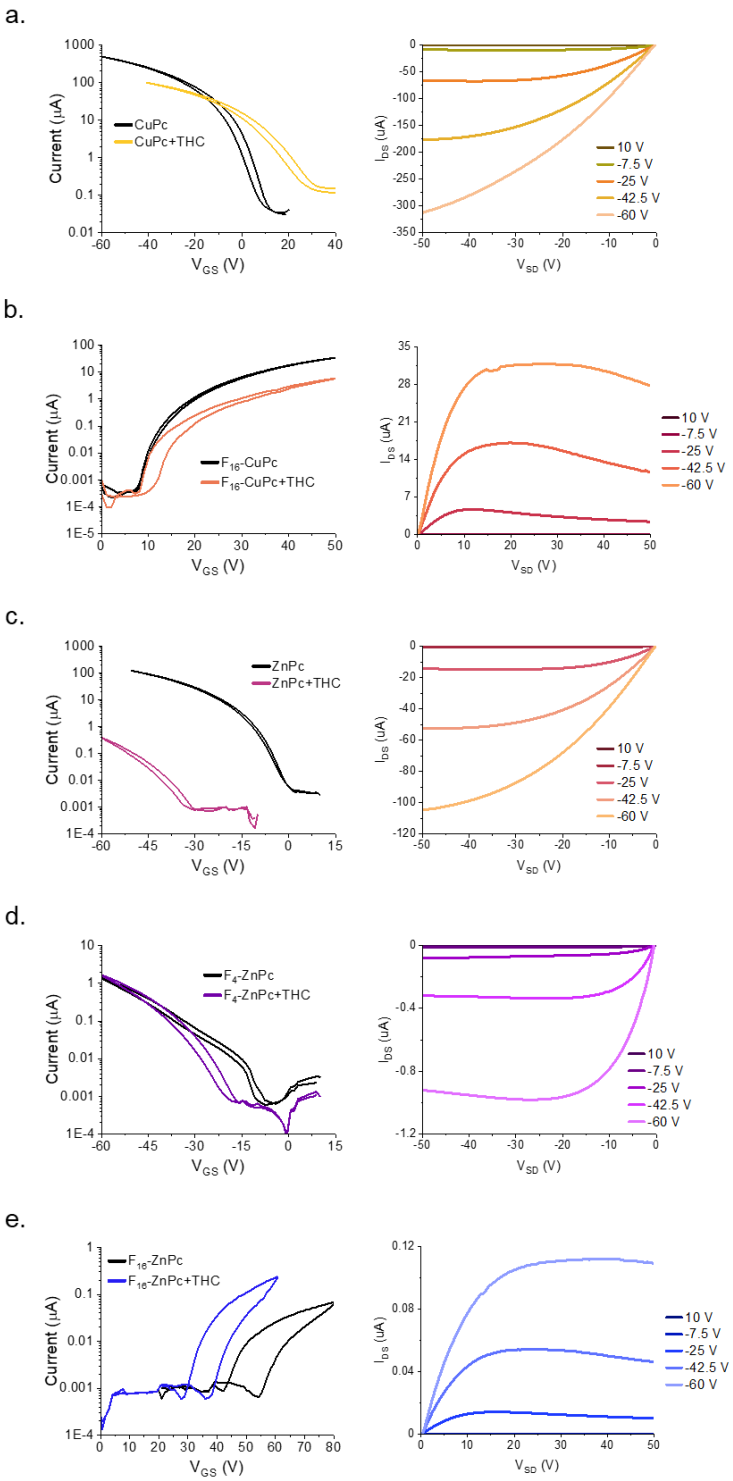

Figure A.5.2. *Characteristic transfer and output curves of Pc thin-films pre- and post- exposure to THC vapor. Twenty (a) CuPc, (b) F_{16}-CuPc, (c) ZnPc, (d) F_4-ZnPc, and (e) F_{16}-ZnPc OTFTs were characterized and then exposed to 4 ppm THC vapor over a period of 90 seconds.*

Table A.5.1. *Calculated transfer data pre- and post- THC vapor exposure for morphologically different films*[a]

	Low		Med		High		Very High	
	Baseline	+THC	Baseline	+THC	Baseline	+THC	Baseline	+THC
Peak Mobility [10^{-2} cm^2/Vs]	2.5±0.2	1.8±0.3	2.4±0.1	2.0±0.2	2.9±0.2	2.6±0.2	2.7±0.1	2.7±0.1
Voltage Threshold [V]	-2.8±0.4	-19.3±2.1	-8.2±0.7	-12.6±0.8	-6.8±1.0	-8.9±0.8	-11.4±1.1	-8.2±1.2
Defect Density [$10^{12}/cm^2V$]	12.3±1.3	21.4±2.3	13.7±0.8	15.4±1.0	7.51±0.5	12.5±0.8	4.23±0.4	9.9±0.7
Maximum Hysteresis [V]	1.6	6.1	1.3	2.5	1.1	3.2	0	2.1
On/Off Ratio	$4•10^3$	$2•10^3$	$4•10^3$	$4•10^3$	$1•10^4$	$7•10^3$	$7•10^4$	$2•10^4$

a. Mobility, voltage threshold, and defect density was calculated from the transfer data of 18 OTFTs for each condition and averaged.

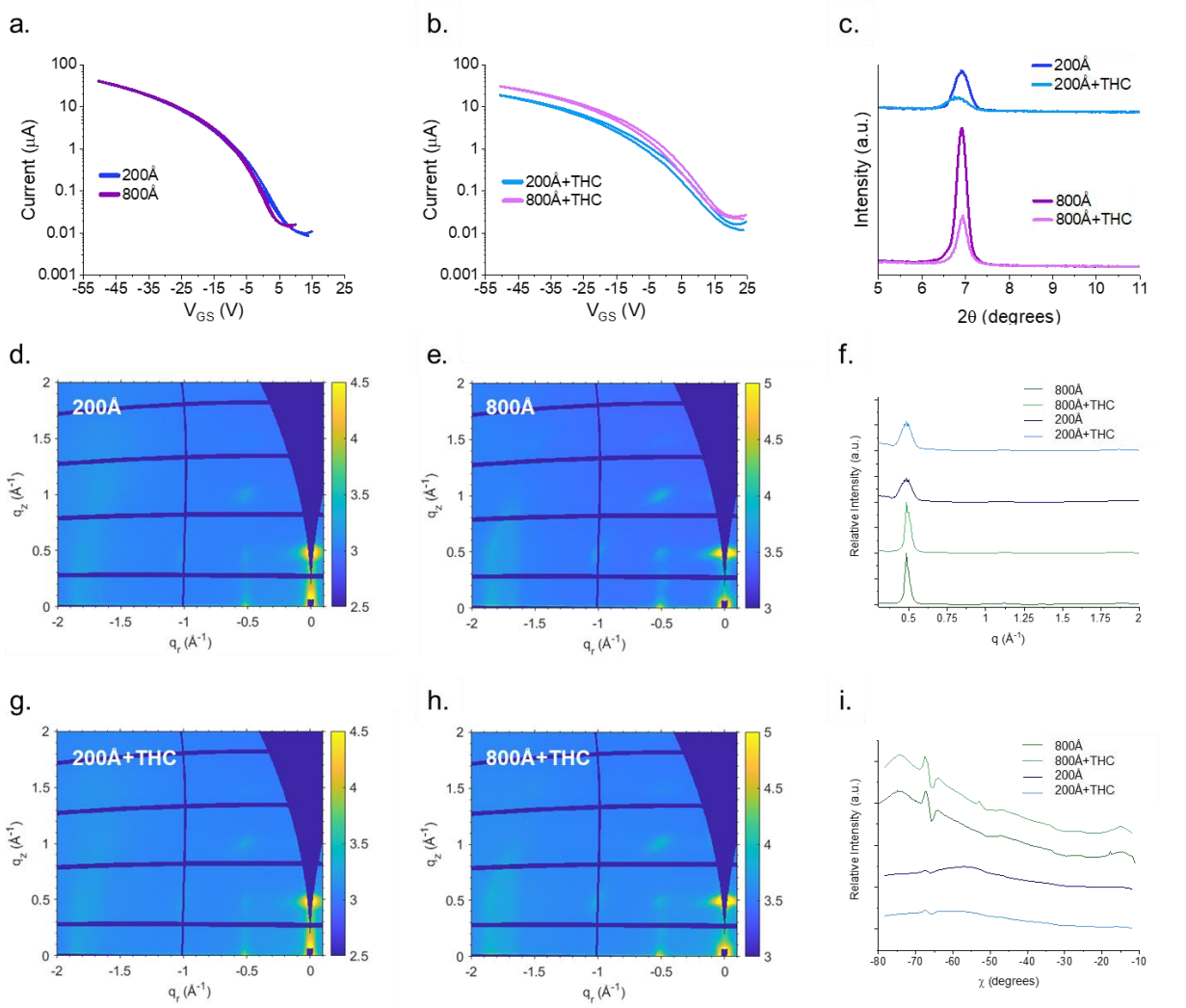

Figure A.5.3. *Effects of thickness on THC vapor sensitivity of ZnPc thin films. Transfer curves of 200 and 800 Å ZnPc OTFTs (a) pre- and (b) post- THC vapor exposure. (c) XRD spectra of thin-films pre- and post-exposure.2D scattering patterns (θ = 0.1°) of (d, g) 200 and (e, h) 800 Å α-ZnPc pre- and post- exposure to THC vapor. (f) Diffraction patterns determined by GIWAXS and (i) linecut profiles with respect to χ using a q range between 1.9-2.1 Å^{-1}.*

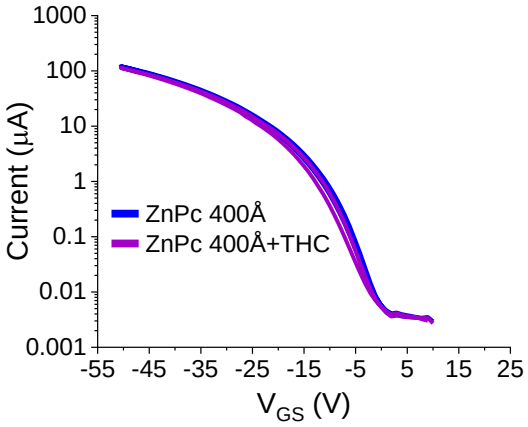

Figure A.5.4: *Initially screened ZnPc OTFT transfer curves pre- and post- exposure to 40 ppb THC vapor for 90 seconds. Films were deposited at a rate of 0.2 Å/s.*

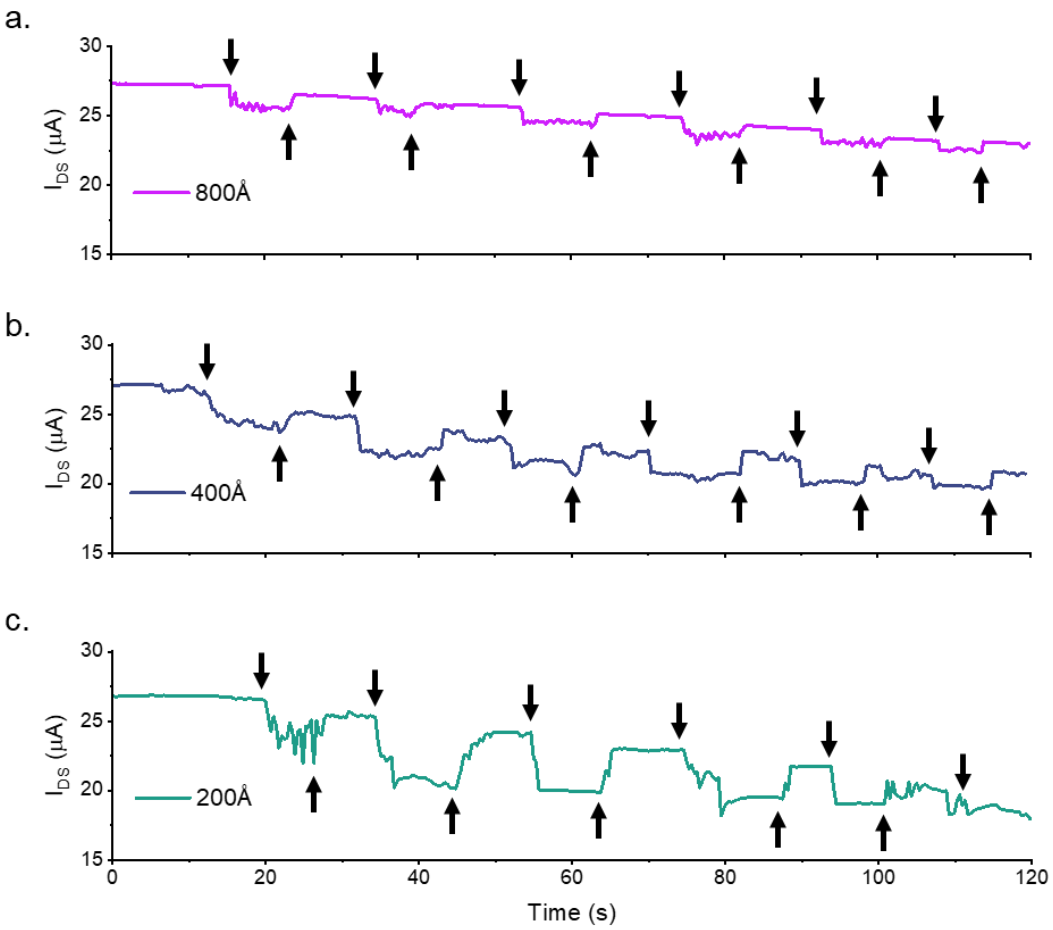

Figure A.5.5. *Periodic in-situ THC vapor exposure and detection. The effects of periodic THC exposure on (a) 800, (b) 400, and (c) 800 Å ZnPc OTFTs. A V_{SD} of -50 V was held and a V_{GS} of -40 V and was pulsed at a rate of 20 milliseconds on 80 milliseconds off over a period of 120 seconds. 40 ppb THC vapor was introduced to a 50 mL chamber.*

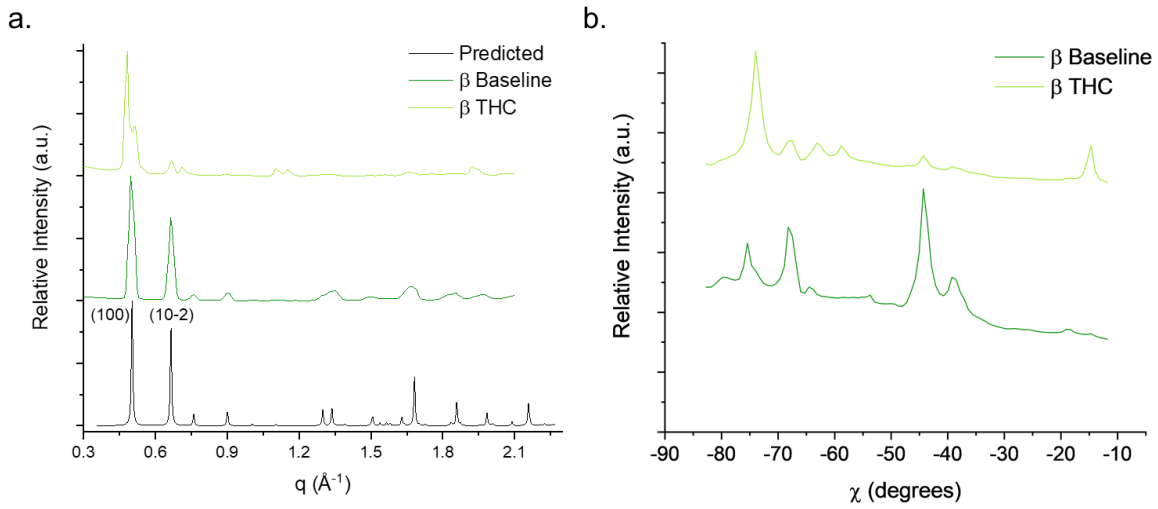

Figure A.5.6. *(a) Diffraction pattern of β-ZnPc predicted from single crystal (CCDC #2098417)[3] and β-ZnPc pre- and post- exposure to THC vapor determined by GIWAXS. (b) Linecut profiles of pre- and post-exposed β-ZnPc with respect to χ using a q range between 1.9-2.1 Å^{-1}.*

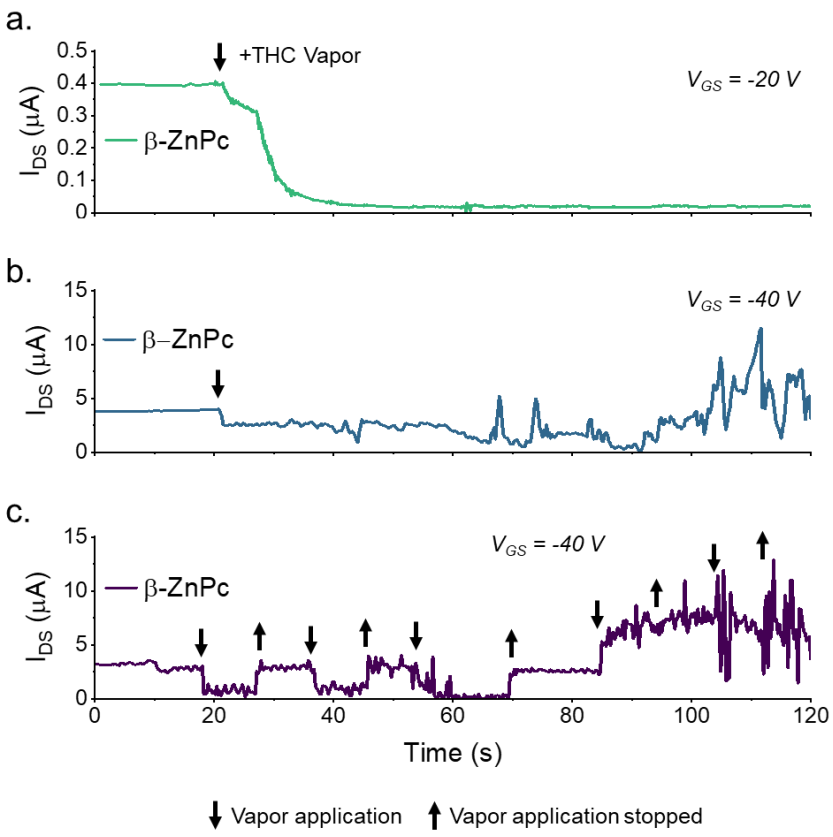

Figure A.5.7. *Continuous and periodic in-situ THC vapor exposure and detection. The effects of (a) continuous THC exposure when V_{GS} = -20V, (b) continuous THC exposure when V_{GS} = -40V, and (c) periodic THC exposure when V_{GS} = -20V on β-ZnPc OTFTs. A V_{SD} of -50 V was held and V_{GS} was pulsed at a rate of 20 ms on 80 ms off over a period of 120 seconds. 400 ppb THC vapor was introduced to a 50 mL chamber.*

References

1. Hoshino, A., Takenaka, Y. & Miyaji, H. Redetermination of the crystal structure of α-copper phthalocyanine grown on KCl. Acta Crystallogr. Sect. B Struct. Sci. 59, 393–403 (2003).
2. Yoon, S. M., Song, H. J., Hwang, I. C., Kim, K. S. & Choi, H. C. Single crystal structure of copper hexadecafluorophthalocyanine (F16CuPc) ribbon. Chem. Commun. 46, 231–233 (2009).
3. Li, D. et al. Green synthesis and characterization of crystalline zinc phthalocyanine and cobalt phthalocyanine prisms by a simple solvothermal route. CrystEngComm 20, 2749–2758 (2018).
4. Jiang, H. et al. Fluorination of Metal Phthalocyanines: Single-Crystal Growth, Efficient N-Channel Organic Field-Effect Transistors and Structure-Property Relationships. Sci. Reports 2014 41 4, 1–6 (2014).

Chapter 6. Future Perspectives and The Need to Pair Molecular Monitoring Devices with Molecular Imaging to Personalize Health

This chapter is adapted from: ***Comeau, Z.J.**, Lessard, B.H. & Shuhendler, A.J. The Need to Pair Molecular Monitoring Devices with Molecular Imaging to Personalize Health. Mol Imaging Biol (2022). DOI: 10.1007/s11307-022-01714-4*

Context to the thesis

It is difficult to overstate the benefits of increased health monitoring, both on societal, but also individual levels. Societally, earlier detection and diagnoses enable earlier, less costly medical intervention, and could significantly reduce the burden of chronic disease, particularly as populations age. Individually, earlier detection and diagnoses can significantly improve an individual's outcome and reduce the number of grieving families experiencing the sudden and unexpected loss of a loved one. I wrote this review alongside the experiments, detailed in **Chapters 3 and 4**, and the sudden passing of my grandmother from pancreatic cancer. While only tenably related to cannabis sensing, I chose to include this review in my thesis as I hope it encapsulates my thoughts to the potential for molecular sensors as a cornerstone of the future of healthcare in addition to some of the challenges that lay ahead.

Contribution

I authored the review with editing and input from AJS and BHL.

Abstract

By enabling the non-invasive monitoring and quantification of biomolecular processes, molecular imaging has dramatically improved our understanding of disease. In recent years, non-invasive access to the molecular drivers of health versus disease has emboldened the goal of precision health, which draws on concepts borrowed from process monitoring in engineering, wherein hundreds of sensors can be employed to develop a model which can be used to preventatively detect and diagnose problems. In translating this monitoring regime from inanimate machines to human beings, precision health posits that continual and on-the-spot monitoring are the next frontiers in molecular medicine. Early biomarker detection and clinical intervention improves individual outcomes and reduces the societal cost of treating chronic and late-stage diseases. However, in current clinical settings, methods of disease diagnoses and monitoring are typically intermittent, based on imprecise risk factors, or self-administered, making optimization of individual patient outcomes an ongoing challenge. Low-cost molecular monitoring devices

capable of on-the-spot biomarker analysis at high frequencies, and even continuously, could alter this paradigm of therapy and disease prevention. When these devices are coupled with molecular imaging, they could work together to enable a complete picture of pathogenesis. To meet this need, an active area of research is the development of sensors capable of point-of-care diagnostic monitoring with an emphasis on clinical utility. However, a myriad of challenges must be met, foremost, an integration of the highly specialized molecular tools developed to understand and monitor the molecular causes of disease with clinically accessible techniques. Functioning on the principle of probe-analyte interactions yielding a transducible signal, probes enabling sensing and imaging significantly overlap in design considerations and targeting moieties, however differing in signal interpretation and readout. Integrating molecular sensors with molecular imaging can provide improved data on the personal biomarkers governing disease progression, furthering our understanding of pathogenesis, and providing a positive feedback loop toward identifying additional biomarkers and therapeutics. Coupling molecular imaging with molecular monitoring devices into the clinical paradigm is a key step toward achieving precision health.

Introduction

The traditional approach to disease management centers around treating symptoms as they present, often as a one-size-fits-all approach for drug therapies and diagnostics, limiting preemptive interventions and clinical flexibility[1, 2]. Though modern disease diagnostics as a facet of precision medicine now better incorporate individual variability through the use of advanced molecular tools, disease screening and chronic disease management often involves rudimentary, sometimes self-administered, screenings based on heuristic risk factors[3]. However, diseases often present molecular biomarkers well before they present outward signs and symptoms, providing an opportunity for early disease diagnosis. Powerful methods, such as metabolomics, gene sequencing, and molecular imaging aided by modern computational tools have enabled us to begin to understand some of the biomarkers that signal disease onset, but practicable implementations have been an ongoing challenge[4, 5]. Nonetheless, an improved understanding of the human model, in addition to the societal and economic value of preventative medicine, has prompted a push toward achieving precision health. Described by Gambhir et al. (2018), the notion of precision health draws on the concepts of engine health monitoring, where a simulated digital twin, constructed with a huge volume of real-world sensor data, forecasts problems to enable preventative repairs. While modern imaging techniques are exponentially increasing the data available, pairing these techniques with continuous sensor data is required to complete the human model. Within clinical settings, molecular imaging, as a part of precision medicine, is being

increasingly used to directly assay an individual's disease state. However, there are still large gaps of time where disease progression or treatment efficacy is largely unknown. Blood analysis or point-of-care tests can reduce the length of these gaps, providing additional data points to draw from for clinical assessments, but the fundamental paradigm remains unchanged. Furthermore, while physiological conditions, such as heart rate, blood O_2, and blood pressure are monitored continuously, with parameters outside accepted limits triggering immediate intervention, this is still often a reactionary intervention within the clinical setting. Molecular monitoring devices able to incorporate additional metrics into this continuous monitoring umbrella could alter the clinical paradigm and, when paired with molecular imaging, could improve clinical assessments by providing a more complete picture of disease pathogenesis. Finally, whereas a jet engine is constantly surveilled in real-time by hundreds of sensors to prevent failure, individuals are encouraged to self-monitor, reporting symptoms as they present, both preventatively and as part of disease management. Accessible molecular sensors are necessary to enable earlier, more objective, and more precise monitoring outside of the clinical setting both pre- and post-diagnosis. By increasingly pairing molecular imaging techniques with molecular monitoring devices, the clinical paradigm can be reimagined as we complete the human model, shifting from reactive to preventative medicine and enabling precision health.

Clinical imaging, including computed tomography (CT), ultrasound (US), magnetic resonance imaging (MRI), and positron emission tomography (PET), among others, are well-established techniques that create a visual representation of the interior of the body. Each technique requires the input of energy into the body, where the energy is differentially modulated by specific body tissue types, and the resulting modulated output energy is captured using specialized detectors or cameras. As a specialized implementation, molecular imaging has been broadly defined as a technique to monitor molecular processes directly or indirectly through the visualization or characterization of biological processes at the molecular and cellular levels. While clinical imaging, including optical techniques (e.g., optical coherence tomography), can provide high-resolution anatomical information, accessing physiological changes at the molecular level has been shown to provide much earlier opportunities for disease diagnosis, monitoring disease progression, or tracking therapeutic outcomes. Such a level of interrogation is achieved through molecular imaging, which differs from traditional anatomical imaging often through the use of injectable imaging agents that bind to or interact with biomolecules of interest, enabling their noninvasive visualization to provide a more complete diagnostic picture for clinicians.

In our view, a molecular monitoring device is broadly defined by any molecular structure used for sensing an analyte where the interaction of device and analyte produces some detectable change. Changes can be transduced, and thus measured optically, by mass, electromagnetically, or electronically. Electronic biosensors are then any molecular sensor engineered to detect a biomolecular analyte and operates by converting the interaction of analyte with the sensor into an electronic signal. Thus, electronic biosensors at their most basic level operate in the same way as molecular imaging techniques: a probe–analyte interaction is transduced into measurable signal and as a result, both molecular imaging and electrical biosensors share many of the same probe design considerations. However, whereas molecular imaging probes are designed to target specific biological systems, biomarker availability guides biosensor design.

Biosensors can be broadly subdivided into two of four categories: single use versus continual; and invasive versus non-invasive. Single use sensors often involve a destructive or covalent binding process, wherein a sample is collected, often invasively, from the patient and introduced to the sensor. Traditional biochemical techniques would fit this definition, however, as they require specific instruments and professional operators their point-of-care applications are limited. Despite their drawbacks, there are applications for novel, invasive, single use sensors, such that they complement clinical point-of-care applications by reducing demand for higher-order analytical imaging techniques. Continual sensors enable persistent monitoring and currently are most often used non-invasively for monitoring key physiological metrics such as heart rate, blood O_2, or blood pressure[6]. Invasive, continual sensors are typically deployed alongside implanted medical devices for treating heart arrhythmias or diabetes; however, noninvasive monitoring techniques are preferred as they improve patient compliance while mitigating risk. From the implementations of biosensors outlined, the concept of precision health requires non-invasive continual monitoring to preemptively detect disease; however, there are many practical hurdles to overcome. Nonetheless, wearable devices are exploding onto the market as non-invasive continual sensors[7]. Driven by affordability and the proliferation of consumer electronics coupled with a growing public desire for health awareness, wearable devices, as non-invasive continuous sensors, are becoming increasingly popular for doctors and individuals to obtain continual medical-quality data. Leveraging existing technology, smart watches and cellphones can monitor a battery of key physiological metrics, including heart rate, activity levels, and blood pressure.

Molecular imaging research is often focused on probe development while electronic biosensing is often focused on achieving increased sensitivity of existing probes via development

of novel sensing platforms. Combining validated molecular imaging probes with biosensing platforms could bridge the gap to provide both pre- and post-diagnosis monitoring. Clinical utility must be a key consideration, such that rapid, point-of-care, molecular sensors can be deployed as diagnostic tools in a non-laboratory setting as complementary or orthogonal methods to sophisticated multimodal molecular imaging techniques. Through multidisciplinary collaboration with clinicians to develop useful tools, the umbrella of clinically monitored physiological metrics can be broadened. In a complimentary manner, drug development can similarly be improved where biosensors can be used to screen the efficacy of therapeutics before clinical validation by molecular imaging. By integrating the precise, in vivo, data afforded by molecular imaging with the broad, continual data generated by multimodal molecular sensing for biomarker characterization, a positive feedback loop could be established. The process of characterizing known disease biomarkers could then identify new disease biomarkers and therapeutic targets as we fill in the gaps of the human model. Multimodal devices that can holistically monitor biomarkers of interest, paired with diagnostic molecular imaging techniques will enrich and modify, but not replace, how we prevent, treat, and monitor chronic diseases such as cancer, heart disease, and diabetes. While many technologies, including immunochromatographic assays, or behavior monitoring through optical scanners and semantic analysis will be necessary facets of the precision health umbrella[8], the aim of this review is to make the case that within the scope of electronic molecular sensors, many of the considerations in the implementation of molecular imaging are shared, and through multidisciplinary pairing of validated molecular imaging probes with electronic sensors we can alter the clinical paradigm and help realize precision health (**Figure 6.1**).

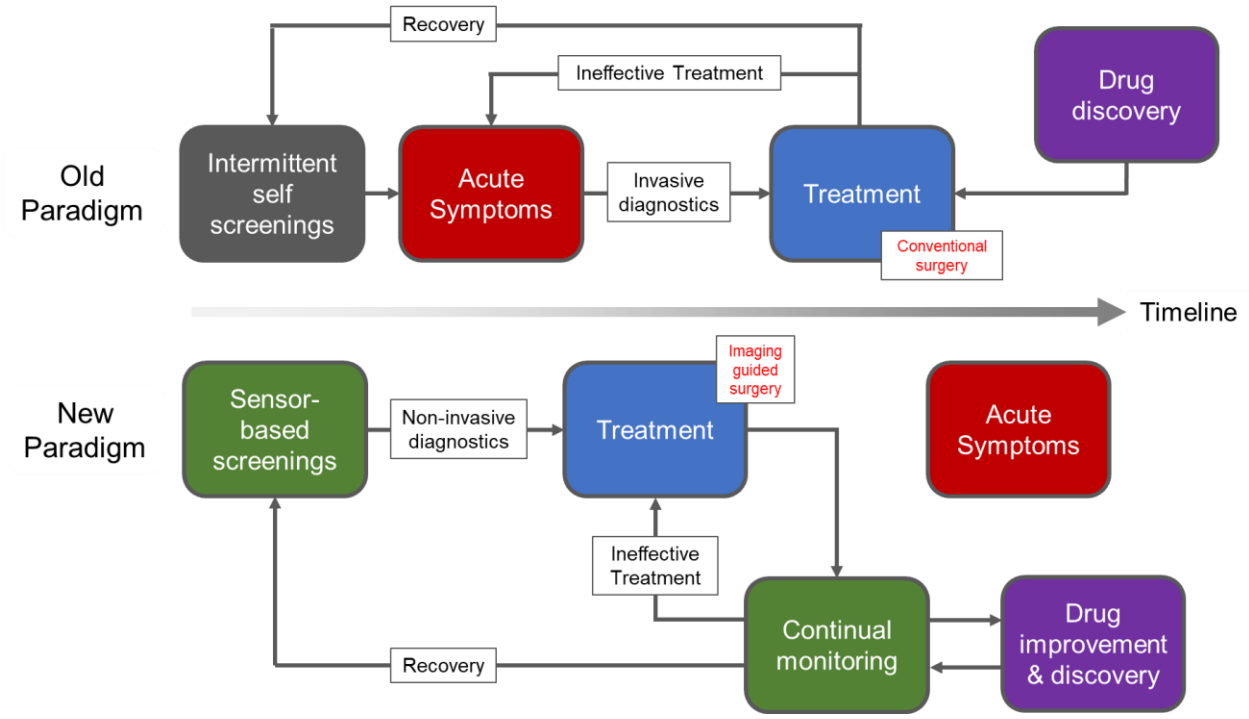

Figure 6.1. *Reimagining the clinical paradigm with paired molecular sensing and imaging. Through early sensor-based screenings and increasing the clinical monitoring umbrella, acute symptoms can be bypassed, and the effectiveness of treatments can be rapidly assessed. Molecular imaging in turn enables non-invasive diagnoses and improves surgical outcomes through increased surgical precision. Drug development and discovery can also be streamlined with both molecular sensing and imaging as more data, more immediately, is available.*

Electronic Sensing

In the broadest sense, an electronic sensor is any device that recognizes changes to its environment by producing or altering an electrical signal that can be transduced into a useful result. Electronic sensors that can recognize biological elements can be termed biosensors and implemented as molecular monitoring devices. For practical implementations, voltage (V), current (I), and resistance (R) are recorded across a material and are dependent on each other by Ohm's law. While many electronic sensors are highly sensitive, the integration of molecular probes as a recognition element is often necessary to achieve useful selectivity. Analytes can interact directly with the sensing material or recognition element in gas or liquid phases, either through direct covalent bonds, indirect molecular interactions, or by altering the ionic potential of the solution, in each case, inducing a measurable change between electrodes (i.e., a change in V)[9]. Additional data points can be collected by modulating operating conditions which can be used to trigger redox reactions, alter resistance, or turn on semiconductors, providing real-time information about dynamic systems. Generally, for two-electrode systems, either V, I, or R, is held constant, and changes are measured in response to analytes, however, as variables dependent on each other,

only having two electrodes limits the ability to perform multiparametric measurements and measurements across a range. By adding a third electrode, measurements can be conducted simultaneously between electrodes and, by maintaining a constant measurement at the intersecting electrode, multiparametric measurements can be taken and a range of potentials assayed. In a three-electrode transistor configuration, a dielectric insulating material between two of the electrodes can be used to generate a buildup of charge carriers at the interface of a semiconducting material across the other electrode junction. This charge buildup then drives charge transport through the semiconducting material, rendering the transistor in an “on” state. Forming the basis of computing and acting as self-amplifiers, transistor-based sensors can be readily integrated into circuits and fabricated on the nanoscale[10,11,12].

Organic semiconductors have been demonstrated for a variety of biosensing applications and are well suited to the task due to their mechanical adaptability. Every part of the three-electrode system (gate, source, and drain electrodes) can be modified with a broad range of materials and architectures to suit specific applications, permitting inherently biocompatible designs. For example, organic thin-film transistors (OTFTs) tend to be solid-state devices while electrolyte gated organic field effect transistors (EGOFETs) have an electrolyte solution as the gating material. The recognition of biological events can occur at the gate, dielectric, or semiconducting layers through functionalization with a probe molecule[12] such that a variety of altered electronic signals can be transduced into a useful readout. Many signal transduction processes elicit some combination of optical, electronic, and physical effects such that one method of signal transduction does not eliminate another. Thus, chemical immobilization of bioactive probes as sensing elements is a common strategy to functionalize the semiconducting channel of OTFTs with antibodies, oligonucleotides, proteins, and chemical probes. Combined with their low cost of manufacturing and implementation, electronic biosensors can readily be paired with the same or analogous sensing elements as molecular imaging probes, however pushing the boundaries of temporal testing resolution, ranging from high frequency to continual sampling of key biomarkers. Ultimately, the commonality of probe design and complementarity of testing regimens between molecular imaging and molecular sensing provides a means to populate the predictive human model that underlies precision health (**Figure 6.2**).

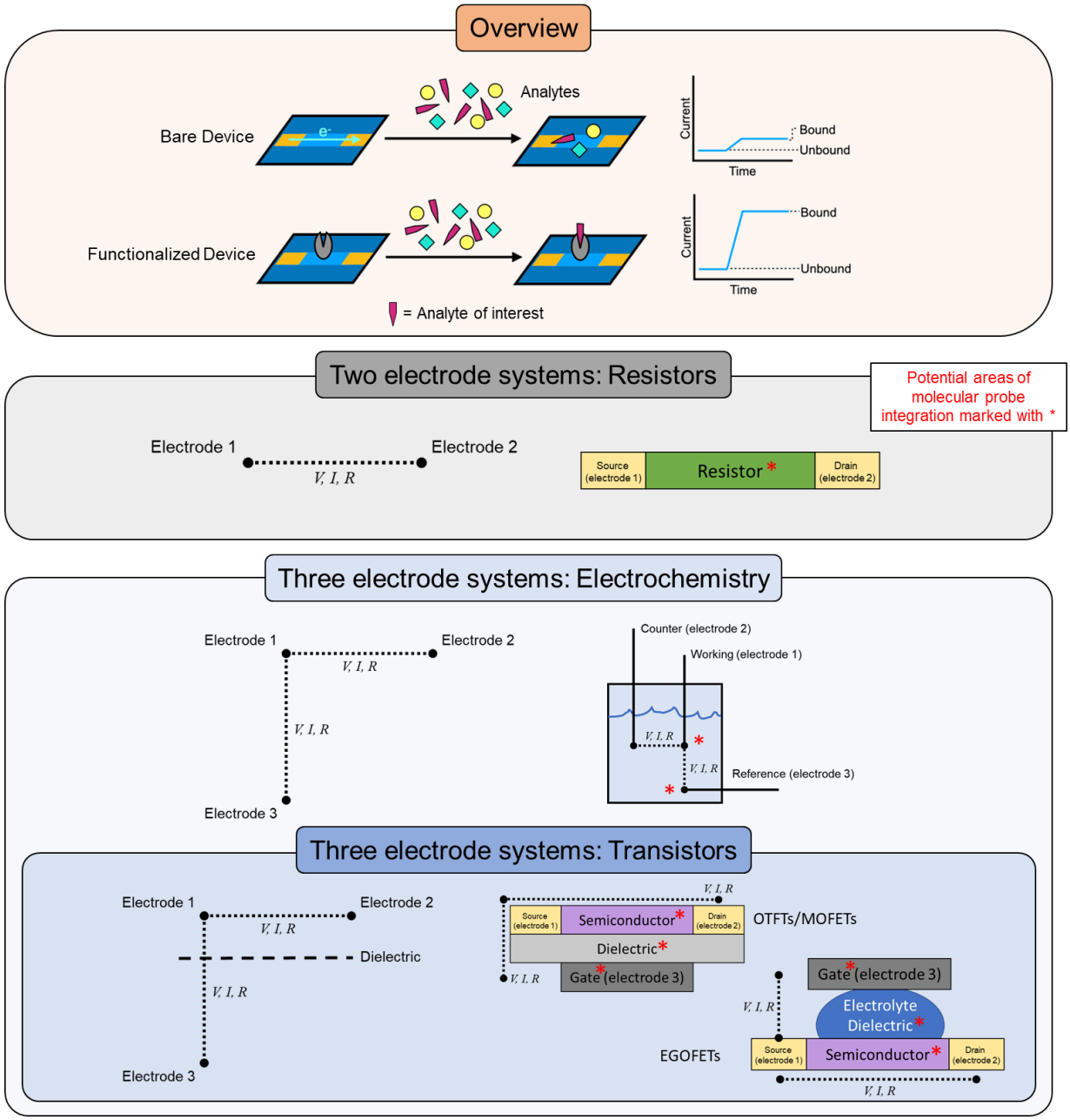

Figure 6.2. *Electronic biosensor architypes and operation. Surface or electrode modifications with exposure to analytes induce altered electrical properties and with functionalization enabling selective responses. Increasing the number of electrodes increases design complexity however it also facilitates multiparametric measurements and complex operations such as electrochemical characterization and transistor operation. Molecular probes can be integrated into almost any components to accommodate a variety of sensor designs and implementations.*

Clinical Opportunities for the Integration of Molecular Imaging with Molecular Sensing Devices

Early detection of cancer and cardiovascular disease (CVD) are perhaps the most compelling arguments for the development of continuous point-of-care diagnostic sensors. The leading cause of death in many countries, these diseases exact a terrible social and economic toll[13]. Cancers are a highly complex group of diseases often only detected in the late stages, which limits therapeutic options and worsens prognoses. CVD is often caused by atherosclerosis resulting in coronary artery disease and ischemic strokes. Many forms of CVD have long asymptomatic phases during which inexpensive treatments or interventions can significantly improve health outcomes and limit the onset of adverse symptoms requiring hospitalization, if only the existence of this silent pathogenesis was identified. For cancers, once detected, a broad range of molecular imaging probes have been developed to assay the extent of disease dissemination and determine treatment options; however, they are limited to a hospital or laboratory setting. In both cases, early intervention significantly improves patient outcomes and reduces the societal cost burden. Thus, there is a critical need for devices for early screening, to facilitate early interventions, and to monitor the effects of treatment to provide early signals that the selected therapy is no longer effective[14].

As a current example, prostate examinations are performed manually and intermittently, with high-risk individuals tested by enzyme-linked immunosorbent assay (ELISA) for prostate-specific antigen (PSA), a biomarker elevated in the presence of some prostate cancers. The standard of care is to perform an ultrasound-guided biopsy; however, negative results do not guarantee a lack of prostate cancer. Increasingly, multiparametric MR imaging, leveraging antibody, aptamer, or small molecule probes, has been demonstrated clinically to assist in prostate cancer biopsies and serve as a diagnostic tool[15-18], with radiolabeled small molecule PET imaging used for post-diagnosis monitoring of severity and potential spread[19-21]. Though these molecular imaging techniques have greatly improved the accuracy of clinical diagnoses and post-diagnosis monitoring, they are limited to the clinical environment, leaving gaps in post-diagnosis monitoring, and an un-met need for pre-diagnosis monitoring. To this end, a variety of electrochemical detection strategies have been developed utilizing functionalized antibodies to achieve clinically relevant detection limits[22-25]. Pyrolytic graphite, carbon nanotube forests, and gold nanoparticles are demonstrated as substrates for differential pulse voltammetry and amperometry-based electrochemical sensing in serum, potentially facilitating rapid detection of PSA in a clinical setting. Alternatively, electrochemiluminescent (ECL) labels have been combined

with antibody-functionalized nanoparticles to amplify square wave voltammogram signal on carbon nanotube forest substrates[25]. Integrating sensors and imaging into the clinical pathway would permit continual screening for PSA or prostate-specific membrane antigen (PSMA), with molecular imaging serving to guide or replace biopsies for diagnosis should further intervention be necessary[16-18, 26]. Minicircles, by delivering exogenously encoded reporter genes into cancer cells, offer an attractive method to endogenously produce both imaging and sensing probes, and could enable multimodal detection of prostate cancer aggressiveness[27]. Other predictive biomarkers (i.e., those that are cancer-predictive but not necessarily cancer-associated) have been identified and demonstrated in electrochemical devices including platelet factor 4 (PF-4), interleukin 6 (IL-6), interleukin 8 (IL-8), and carcinoembryonic antigen (CEA). Thus, during treatment, molecular sensors can be used to monitor the effects of therapies, providing rapid feedback to better direct clinical decisions[28-30]. Advances in molecular imaging and sensing can radically alter clinical workflows, with molecular sensors replacing intermittent invasive clinical monitoring and molecular imaging providing accurate, noninvasive, diagnoses.

As another example, glucose monitoring is critical to diabetes management and the role of glucose utilization as a pathogenic biomarker for of a variety of diseases, including kidney diseases,[31, 32] neurological conditions,[33, 34] and hepatic diseases [35] is well characterized. Through the facile immobilization and implementation of glucose oxidase (GOx) for electrochemical sensing, a range of architectures for electrochemical glucose biosensing have been implemented, including transdermal glucose monitoring. Designed as an alternative to finger prick blood draws, transdermal sensors can noninvasively measure blood glucose concentration in real time, aiding in diabetes management. However, incorporated into CVD therapies, transdermal glucose monitoring facilitates better glycemic control during and post-surgery which has been recently shown to improve patient outcomes[36]. For both cancer and CVD, aided by well-developed chemistry permitting the radiolabeling of glucose for PET imaging, imaging-guided surgery has similarly proved to be an invaluable tool toward improving patient outcomes[4,37-40]. Thus, for surgical applications, molecular imaging and sensing could work in tandem, guiding surgical procedures, minimizing invasiveness, and improving recovery through more precise health monitoring. In addition to the examples described above, a myriad of imaging techniques and sensing platforms have been developed to target a range of diseases (**Table 6.1**).

Table 6.1. A selection of probe types shared between imaging and sensing platforms to assay specific diseases.

Target	Probe Type	Selected Biomarkers	Sensing Modalities	Imaging Modalities
Cancer				
Pan-cancer biomarkers	Antibody	AFP, ferritin, CEA, hCG-β, CA 15-3, CA 125, CA 19-9, carbonic anhydrase IX	Electrochemical[41,42], optoelectronic[25]	PET[43,44], MRI[44], Optical[44]
	Aptamer	AFP, CEA, miRNA, CD30	Optoelectronic[45], Electrochemical[46]	PET[47]
Breast cancer	Antibody	c-erbB-2, CEA, MUC1, TAG-72	OTFT[48]	PET[49,50]
	Aptamer	SK-BR-3, MCF-7	Nanopore[51]	Optical[52]
Lung cancer	Antibody	ANXA2, CKAP4, ENO1, VEGF, NR-LU-10	Impedance[53,54]	PET[55,56], Optical[57]
	Protein	CEA, NSE, KLKB1	Electrochemical[54]	PET[55]
	Small Molecule	VEGF165, EGFR, CK19	Impedance[58]	PET/CT[59]
PSA	Antibody	PSA, PSMA	Electrochemical[23,60,61], OTFT[62]	MRI[63], PET[64]
	Aptamer	PSA	Nanowire[65,66], optoelectronic[45]	MRI[67]
	Protein	PSA	Electrode[68]	
	Small molecule	PSA, PSMA		PET[21,69], MRI[19]
Coronary artery disease				
	Antibody	CRP, TNT-α, IL-6, inflammatory cells	Electrochemical[70], OTFT[71]	PET[72]
	Aptamer	Troponin-T, thrombin, IL-6	Electrochemical[73,74,42]	US[75]
	Small molecule	Lipoproteins, EP-2104R	Electrochemical[76,70]	PET[77,72,78], MRI[72,78]
Neurological				
Alzheimer's disease	Antibody	$A\beta_{42}$, $A\beta_{40}$, p-tau_{181}	Impedance[79,80], CNT Resistor[81]	PET[82–85]
	Aptamer	Thrombin, adenosine, AβO, $A\beta_{40}$	Nanowire[86]	Optical[87]
	Protein	AβO	Electrode[88]	
	Small molecule	Aβ, p-tau_{217}		MRI[89], PET[90–92]
	Quantum Dot	QDAβ	Optoelectronic[93]	
Dopamine dysregulation	Antibody	--	Electrochemical[94]	
	Aptamer	--	OTFT[95], electrochemical[94]	Optical[96]
	Enzyme	--	Biosensors[94]	
	Small molecule	--		PET[97,98]

Shared Probe Design Considerations

Molecular imaging probes are agents used to visualize biochemical processes by providing a signal that can be detected by the camera for the imaging modality of choice. Thus, a signaling agent or beacon specific to the imaging modality is often linked to the targeting moiety which interacts with the biomarker of interest. Similarly, probes for electronic biosensing require a targeting moiety in addition to a handle or linker moiety through which the probe can be conjugated to the surface of the device, allowing the conversion of analyte–probe interaction into an electronic signal and facilitating its transduction to the device. As a result, probe design for molecular imaging shares many of the same considerations as probe design for molecular sensing devices. Molecular imaging and sensing can be complimentary techniques from both a clinical aspect and a design aspect. By targeting the same biomarkers or by using the same recognition agents, advances in either can often be repurposed to potentially innovate in the orthogonal technique. Furthermore, clinically, where molecular imaging can provide focused analysis of disease state in vivo, molecular sensing can complement imaging techniques, providing continuous analysis of disease progression at home or clinically at the bedside (**Figure 6.3**).

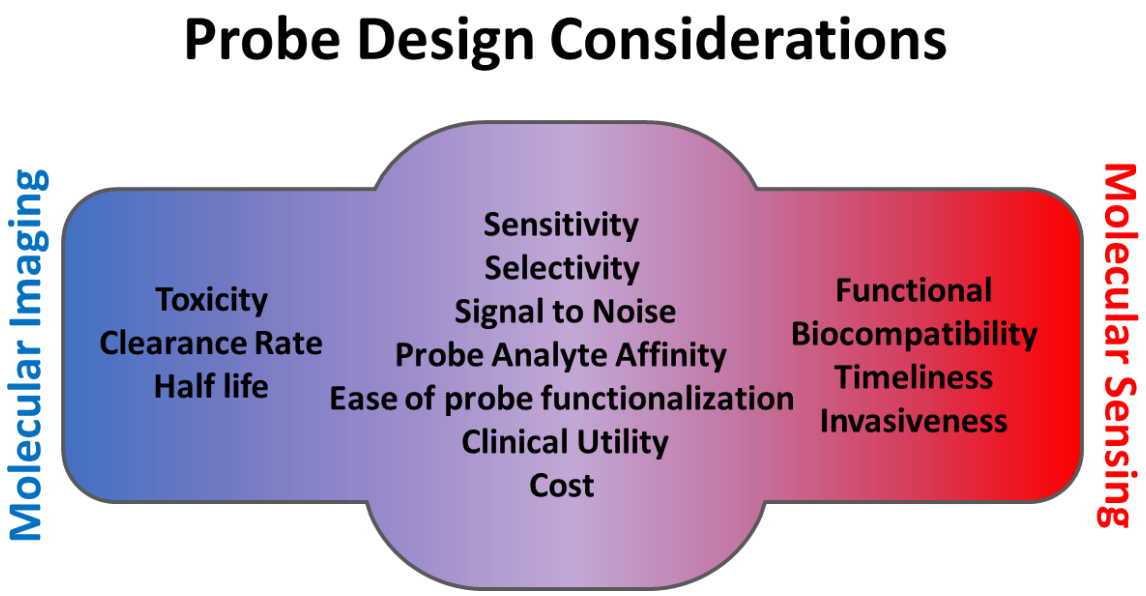

Figure 6.3. *Shared design considerations of molecular imaging and molecular sensing probes. Probes for molecular imaging and molecular sensing share many of the same considerations as they pertain to analyte interaction and signal transduction and thus probes which work for one technique may be applicable to another. Molecular imaging and sensing instead slightly differ in relation to the practical aspects of each technique. Where imaging agents are typically injected into the subject, and thus toxicity, the rate of clearance, and half-life are major concerns, sensors are often outside the subject, interacting only partially with biofluids, and thus necessitate functional biocompatibility, timeliness of response, and minimizing the sampling invasiveness.*

Antibodies

Functionalized antibodies have become popular targeting moieties due to their well-defined structure, specificity, high affinity, and serum stability, positioning them well for use as targeting agents for molecular imaging probes and electronic biosensors. Antibodies generally consist of a constant region, termed heavy chain, a light chain, and a variable region with the antigen-binding site. Through a complex, naturally occurring, V(D)J B-cell recombination process, a staggering diversity of receptors are possible,[99] enabling antibody-based targeting of a broad range of biomarker targets. The constant regions, while not conferring antigen-binding specificity, are essential for mediating the resulting immune response and cytotoxicity. Thus, depending on the organism used to produce the antibodies, they can elicit an unwanted immune response in humans; however, developments in antibody engineering and antibody fragments have addressed some of these challenges without compromising functionality[100]. For both imaging and sensing, site-specific labelling of amino acids guides conjugation strategy, which is a key challenge in employing antibodies as targeting agents and a rapidly expanding area of research[101,102,103]. With smart antibody design and shared click chemistry, a recombinant antibody (rAb) could be clicked to both a sensing platform and an imaging agent, providing instant sensing and imaging of a specific biomarker. The affinity and specificity of the antigen-binding region would be maintained, facilitating orthogonal imaging and sensing of a specific antigen provided appropriate antigen bioavailability. Enabling imaging of intracellular targets, antibody fragments can facilitate click chemistry while also limiting background signal and non-specific accumulation; however, their practical use is still an on-going challenge[44, 104, 105].

As an example of the potential flexibility of antibody-based detection agents, functionalized hafnium oxide (HfO_2) substrates were demonstrated for hybrid field effect transistor-immunofluorescent detection of human interleukin (IL)-10,[106] a biomarker associated with inflammation and adverse cardiovascular events[107]. Detecting IL-10 electronically by conjugating the antibody to the HfO_2 surface, rather than optically, afforded a 30-fold increase in device sensitivity versus fluorescence detection[108]. In both cases, a harsh silane treatment was used to functionalize the surface with available aldehydes enabling mild covalent antibody coupling. While a variety of alternative techniques exist for antibody-device surface coupling (e.g., thiol, glycan, non-covalent immobilization, or affinity-based immobilization), a key aspect to consider however with any site non-specific method is a reduction in the availability of antigen-binding sites due to random immobilization. Antibody fragments obtained from rAbs can again be used to limit this effect with the additional advantage of enabling a higher density of antigen-binding sites on the substrate surface.

Upstream in the development process, electronic biosensors with immobilized rAb targets on their substrate surface could find a role for rAb evaluation, providing additional screening data on their specificity and affinity. Electronic sensors can then assist antibody imaging both by facilitating the selection of lead rAbs and providing a complimentary assay technique for disease specific antigens. With their advantages for both imaging and sensing, antibody fragments are well positioned to potentially serve to generate paired molecular imaging agents and molecular monitoring devices[109-111].

Oligonucleotides

Oligonucleotides, either as immobilized strands of DNA or RNA, have been demonstrated as recognition elements in a variety of electrical biosensors[112] and imaging probes. Functionalization is facilitated by chemically modifying either the 3' or 5' ends of oligonucleotides with well-established chemistry. Oligonucleotides can be readily labelled, enabling application to a broad range of imaging modalities while producing few changes in the behavior of the molecules. Oligonucleotides are produced with great facility and at lower costs in comparison with enzyme- or antibody-based methods for analyte recognition. With limited immunogenicity or off-target toxicity, oligonucleotide-based probes offer an attractive alternative to other probe systems. Uniquely, oligonucleotides provide rapid and highly specific hybridization to complementary strands amenable to the growing interest in cell-free RNA and DNA as biomarkers of disease. Oligonucleotide functionalization is not without challenges as the probes can have short half lives in vivo and must have a well-defined orientation that is accessible for hybridization.

Independently from hybridization (i.e., base–base recognition), but rather as unique oligonucleotide folding conformations, aptamers can provide highly specific recognition sites enabling their use as molecular imaging and sensing probes. Selectively screened from a complex library in vitro for high affinity and specificity, aptamers can bind with a broad range of biomolecular targets and have been demonstrated in OTFT sensors to detect a range of small molecules, peptides, and proteins[11, 95, 113, 114]. Aptamers can be fabricated cost-effectively and afford enhanced stability in response to pH, temperatures, and solutions of high ionic strength with in vivo stability in the range of hours[115]. This combination of ease of production, consistent structure, and stability positions aptamers well as a flexible imaging and sensing recognition agent[73, 116,117,118].

Small Molecules

Small molecule probes have found broad applications in a variety of imaging modalities through incorporation of an imaging beacon, and they are also readily immobilized on electronic

devices to afford analyte sensing. Advances in PET and SPECT imaging and radiochemistry have enabled incorporation of ^{11}C and ^{18}F radionuclei, among other radioisotopes, into small molecule structures enabling the study of complex metabolic pathways with the advantage of limiting disruptions in molecular behavior. As targeting agents for sensing, small molecules that form covalent bonds or undergo redox reactions with the analyte at an electrode interface is often all that is required to produce a measurable sensing response[119-122] in some capacities, enabling single molecule sensing[123]. However, while sensitivity can be as high as single molecule detection, selectivity and specificity is a core challenge to broader sensor use. As a result, significant effort has been directed at developing a variety of sensing platforms to target small molecules, often by interpreting specific analyte–probe interaction-induced conformational changes as electrical signals[124-126]. Electronic noses, wherein an array of slightly varied sensors facilitates deconvolution of non-specific molecular events, can be used to improve selectivity. We demonstrated the integration of a colorimetric cannabinoid probe as sensitizing agent with OTFT-based sensors and then through material selection were able to selectively determine cannabinoid ratios from a complex solution[127]. Other colorimetric probes have been integrated into optoelectronic noses[128], most commonly for airborne small-molecule targets such as aldehydes and ketones.

As sensing targets, aldehyde and ketone dysregulation and their associated enzymes have been used as an index of oxidative stress and inflammation and therefore can be used as biomarkers for a variety of disease states[129-131]. Aldehydes represent a promising target for molecular sensing as they have high bioavailability in biological fluids that can be sampled relatively non-invasively. Additionally, specific environmental aldehydes can cause negative health effects, affording their use as indicators of pollution and spoiled food. Acetaldehyde and ketone breath sensors, using metal-oxide semiconductor field-effect transistor (MOSFET) devices as the electronic transducer, are widely available as breathalyzers to analyze alcohol consumption and to monitor ketogenic diets, respectively[132]. Imaging aldehydic load could provide a more holistic approach toward understanding disease pathogenesis, and non-invasively measuring aldehyde concentration in available biofluids has been demonstrated as a useful diagnostic metric. Shuhendler and coworkers have developed a series of aldehyde probes, leveraging hydrazone formation to provide rapid aldehyde complexation without a catalyst[133]. While their clinical use and utility is still limited, volatile organic compound (VOC) breath or environmental sensors can fit into the umbrella of precision health by providing additional complimentary data to small molecule imaging studies.

Enzymes and Reporter Genes

Since the demonstration of immobilized glucose oxidase (GOx) in 1962 as a glucose sensor, a popular technique for electrochemical biosensing is monitoring electroactive enzymatic products via oxidation or reduction reactions. Through the generation of oxygen by GOx, the activity, and thus the concentration of glucose, can be monitored electronically in real time. Glucose test strips expanded on this principle, miniaturizing and commercializing the technology in the late 1980s. Recently, transdermal, continuous glucose monitoring has been demonstrated for diabetes and surgical monitoring, improving individuals' quality of life and surgical outcomes, respectively[36].

Reporter genes are a key part of molecular imaging as efficient tools to monitor the efficacy of gene delivery, gene expression, and facilitating imaging of challenging molecular targets. In this way, enzymatic activity can be imaged in vivo. As an example, [18F]-trimethoprim ([18F]-TMP) was used to image the expression of Escherichia coli dihyrofolate reductase enzyme (eDHFR) enabling the trafficking of human chimeric antigen receptor T cells to be followed in mice [134]. TMP is a popular antibiotic used alongside sulfamethoxazole (SMX) to treat urinary tract and ear infections. Electrochemical sensors have been developed and demonstrated to simultaneously detect SMX and TMP in urine[135] potentially facilitating multimodal, and continuous monitoring of TMP pharmacodynamics. Minicircle plasmids have demonstrated tumor activatable paired sensing and imaging reporter gene, producing easily assayed biomarkers for sensing in combination with imaging markers, and demonstrating the potential of pairing molecular imaging and sensing from the design stage[27, 136, 137].

Sensor-functionalized enzymes can play an important role in drug development through real-time assaying of enzymatic activity, corroborating in vivo imaging studies. Xanthine oxidase (XO) catalyzes the oxidation of hypoxanthine (HYP) to xanthine (XAN), which is then further oxidized to uric acid as the final degradation product in the human purine catabolic pathway. Overproduction of these degradation products can lead to xanthinuria, hyperuricemia, high blood pressure, gout, and renal failure. Allopurinol (1H-pyrazolo[3,4-d] pyrimidin-4-ol) is a XO inhibitor in clinical use to treat gout and improve long-term outcomes following ischemic strokes[119, 138]; however, as established through molecular imaging studies, there can be a variety of strong side effects[139, 140]. Through simple and sensitive amperometric biosensors with surface functionalized XO, the chemical mechanism of allopurinol inhibition was determined[141]. Building on the premise, allopurinol alternatives for XO inhibition were able to be rapidly tested ex vivo[142]. Thus, molecular sensors can assist with drug development before molecular imaging can be used to validate

clinical effectiveness. With the ability to detect the downstream products of XO activity, these sensors could also fill a role in disease monitoring.

Monitoring the Human Engine—Blood, Sweat, and Tears

Molecular imaging is focused on finding specific biomolecular targets in living systems and thus key considerations of imaging probe design are focused on delivery, specificity, and clearance. Analyte availability is a secondary concern in so far that the targeted analyte is usually found in the highest concentrations at the site of interest (e.g., site of disease initiation). For molecular sensing, particularly when developed in combination with imaging probes, analyte availability and its biodistribution are the primary concerns such that the concentrations of analytes available in sampled biological fluids can be detected, and that the analyte levels evaluated from a biological sample are reflective of the disease state. To this end, the routes by which biomarkers are shed, processed, and excreted, and the invasiveness by which the biofluids in that process can be sampled, is a key consideration of molecular sensor design. Compartmentalization, both in respect to cells and larger bodily systems is an additional concern. To draw on the analogy of an engine, an issue with the engine oil is unlikely to be detected in the wiper fluid; thus, analyte bioavailability is particularly relevant in the context of pairing molecular imaging probes with sensors. Whereas molecular imaging probes can target specific processes or intracellular analytes, molecular sensors are exclusively limited, for now, to extracellularly available analytes. Finally, functional biocompatibility is a necessary consideration when designing sensors, specifically, designing for electronics for operation in aqueous, and often ionic environments (**Figure 6.4**).

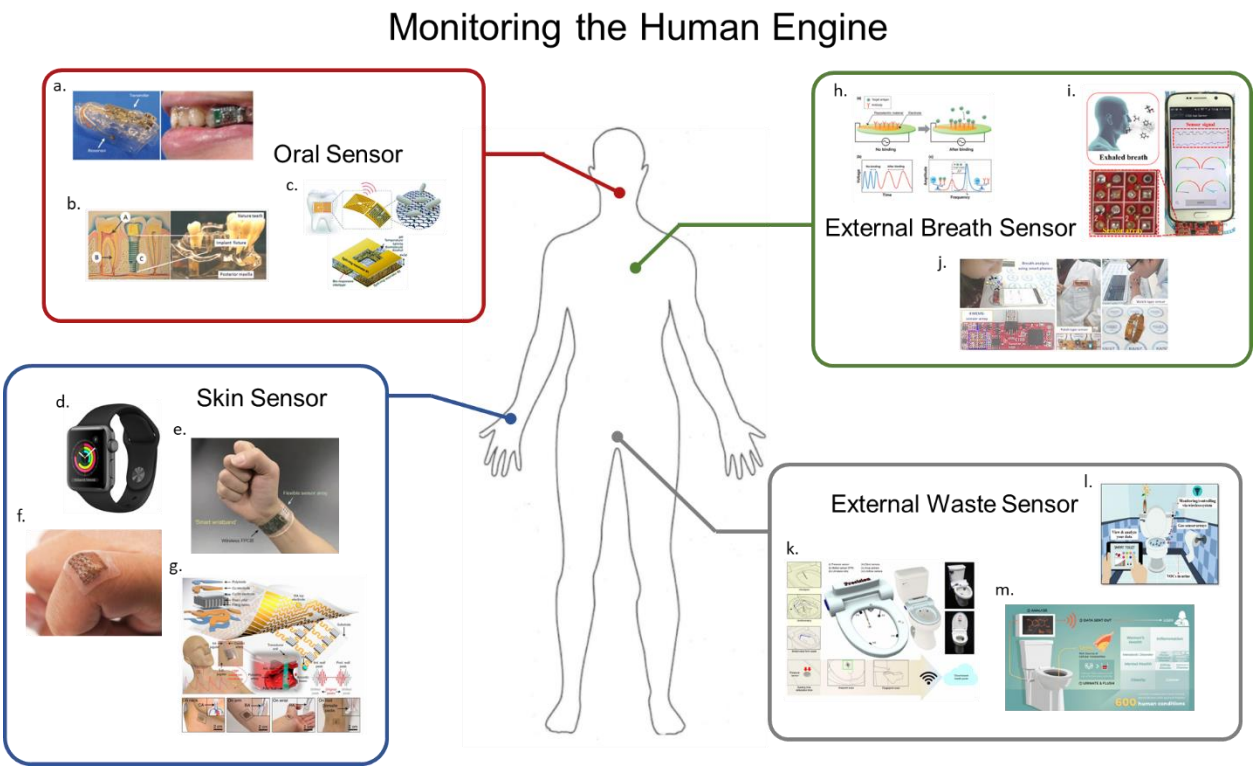

Figure 6.4. *Monitoring the human engine. Examples of recent works to incorporating non-invasive technologies to molecularly monitor a battery of health metrics. While physiological monitoring has become ubiquitous there is a current need for monitoring devices to provide clinically actionable diagnostic data. Complex biomarker monitoring is possible with molecular imaging but still limited in capacity with molecular sensing. (a) Schematic image of a glucose biosensor with mouthguard support and oral implementation (adapted from ref.145). (b) Proposed intra-oral dental implant system with an integrated three-electrode electrochemical biosensor (from ref.146). (c) Biotransferrable graphene wireless nanosensor (adapted from ref.147). (d) Apple Watch Series 3 with integrated heart rate and blood pressure sensors. (e) A wearable fully integrated sensor array on a subjects wrist for in-situ perspiration analysis (adapted from ref.148). (f, g) Stretchable ultrasonic devices and design schematic for monitoring the central blood pressure waveform (adapted from ref.149). (h) Function of a immuno-piezoelectric biosensor (adapted from ref.150). (i) Electrochemiresistive breath sensing with apoferritin encapsulated nanoparticles (from ref.151) (j) Real-time breath analysis via portable functionalized electrochemical sensing platforms (from ref.152). (k) A mountable toilet system for personalized health monitoring (from ref.153). (l) Real-time health monitoring through urine metabolomics (from ref.154). (m) Urine odor detection by electronic nose for smart toilet applications (from ref.155).*

Breath

Thousands of volatile organic compounds (VOCs) have been identified in human breath, providing an array of biomarkers that can potentially be targeted for analysis[154]. Alcohols, ketones, and aldehydes are popular VOC-based biomarkers for breath analysis as they can be detected directly by an electrode and somewhat selectively without the need of an intervening recognition element. However, a variety of human factors may influence breath sampling, including breathing route, exhalation rate, airway pressure, and posture[155]. Additionally, breath is not a homogenous

mixture of gases[156]. Instead, biomarkers stemming from the oral cavity will be in higher concentrations in early breath (such as H_2S for halitosis[157]), while end-tidal breath will have higher concentrations of blood-borne biomarkers (such as acetone[158]). Thus, flow restrictors are often necessary to achieve a consistent and prolonged exhalation for meaningful and reproducible analysis. Nonetheless, metal-oxide chemiresistors, borrowing ideas from industrial gas monitoring, have been sensitized to detect biologically relevant levels of VOCs for monitoring metabolic disorders. To simultaneously analyze a broad range of aldehydes, optoelectronic noses have been developed, leveraging an array of dyes to electro-optically determine specific aldehydes and ketones[128]. Probe molecules incorporating a hydrazine binding moiety have been demonstrated for molecular imaging of aldehydes, converting an aldehyde binding event into fluorescent, MRI, or PET-detectable signal[135, 159,160,161]. Further sensitization can be achieved through device design, where hollow structure nanomaterials[162], carbon nanotube structures[163], adsorption traps[164], or buffering[165] are tailored to improve analyte delivery to the sensor. Breath sensing is a promising option to detect slowly progressing diseases with few early indicators[166], such as cancer[167], diabetes[168], or renal dysfunctions[169].

Saliva

Saliva is being increasingly recognized as a useful diagnostic fluid for biomarker analysis as it can be easily and noninvasively sampled[170]. Human oral fluid is mainly composed of saliva produced by three pairs of major salivary glands and a large number of minor salivary glands. Each salivary gland secretes a characteristic type of saliva with variations observed in the concentrations of salts, ions, and total proteins[171-173]. Additionally, saliva contains crevicular fluids, oropharyngeal mucosae, blood-derived compounds, and food debris, with the average healthy adult producing 500–1500 mL per day[170]. For sensing purposes, saliva is almost universally collected and analyzed whole, as separation or precise collection is often not practicable. Salivary glucose, lactate, phosphate, alpha-amylase, hormones, and antibodies have been demonstrated as sensing targets[170, 174, 175]. Miniaturized GOx sensors have been developed for noninvasive sampling of salivary glucose as well as crevicular fluid glucose, correlating these measurements to blood glucose concentrations with the aim of noninvasive monitoring for diabetes management[176, 177]. Using the same principle as glucose measurements, salivary lactate can also be measured by electrochemical measurement of H_2O_2 generation from immobilized lactate oxidase. Elevated levels of salivary lactate can be indicative of lactic acidosis, a biomarker that can signal an impending heart attack[178, 179]. Several salivary lactate electronic biosensors have been reported, as electrochemical sensors[179] as well as miniaturized cavity-type sensors meant to be worn in the mouth, reporting salivary lactate levels in real-time wirelessly[180]. Salivary

lactate concentrations also have consequences on sports performance, with a three-electrode monitoring system printed on the inside of a mouth guard demonstrating a sensitive and stable response[181]. Electrochemical immobilized enzyme sensors have also been reported for salivary phosphate[175], a cardiovascular calcification biomarker[182], and salivary alpha-amylase[174, 183], a stress biomarker[184]. Many blood serum hormones which can also function as biomarkers have been detected in saliva, suggesting promising noninvasive alternatives to blood serum testing. Electrochemical immunosensors have been demonstrated for monitoring adrenal biomarkers (cortisol[185, 186], testosterone[187]), cancer biomarkers (IL-8[188], IL-1[189], CD-59[190]), and other disease biomarkers such as cytokine interferon[191], and SARS-CoV-2[192]. With the popularity of oral implants for orthodontic purposes, non-invasive oral implants or sensors integrated into dentures have been demonstrated to provide real-time passive health monitoring.

Sweat

The average adult human produces 500–700 mL of sweat under most climate conditions per day[193]. Easily accessible, sweat can provide a range of physiological data including electrolyte levels, and metabolites[194]. It can be sampled continually and noninvasively with a skin patch, often preferable to a dental implant, and significantly preferable to blood collection. Gao et al. (2016) demonstrated a flexible integrated sensing array able to continually monitor glucose, lactate, sodium, potassium, and temperature in sweat, leveraging existing GOx and LOx enzyme-based electrochemical sensors in combination with NaCl and KCl ion sensitive electrodes. Temperature measurements were used to calibrate the activity of the other sensors and were able to continually monitor sweat produced during vigorous exercise. Sebum, the oily substance produced by sebaceous glands, contains non-invasively accessible lipids which have been demonstrated as neurodegenerative disease biomarkers[195, 196]. While a plethora of physiological information is present in sweat[146], there have been limited validated correlations of compartmental analyte availability and the relationships to physiological levels[197]. Recent advances in wearable electronics have begun to address these shortcomings but there is a need for paired imaging studies to validate the clinical value of sweat-borne biomarkers[146, 198]. Thus, the continuous physiological monitoring umbrella could be expanded from heart rate, blood pressure, and blood O_2 to include blood glucose, lactate, and ions to improve overall health monitoring.

Urine and Feces

Monitoring of human waste has gained increased attention as a complementary alternative to blood plasma sampling. Blood plasma is controlled through tight homeostatic mechanisms, with deviations often signaling a major issue, and as a result the biomarkers found

within are often short lived in vivo, limiting their use for early detection and continual monitoring. Waste, specifically urine, comprises objects cleared of the blood homeostasis mechanism, and can potentially better reflect in vivo changes. Additionally, the urine proteome is relatively low, facilitating analysis and validation of potential biomarkers. Broad, multiplexed urinalysis and the implementation of machine learning algorithms have found promising biomarkers to detect the early onset of a variety of diseases and infections[199-201], potentially facilitating early interventions of colorectal and prostate cancers. By leveraging the renal clearance of many therapeutics, including molecular imaging agents, additional information toward their effectiveness can be obtained. Acute kidney injury (AKI) is a common and serious complication following significant medical events and its early detection and treatment can reduce mortality and improve recovery following surgery[202-204]. It has been suggested that urine could be passively monitored from within the home in a similar fashion to CO monitoring, where out of bounds biomarker levels could trigger an alarm and further investigation. Changes to an individual's hydration and activity levels can act as a confounding factor and fouling can be an issue. "Smart toilets," leveraging a multi-sensor design, offer an interesting option for passive, noninvasive home health monitoring[81, 205]. By combining an array of existing waste monitoring sensors with machine learning, significant health data can be collected in a facile non-intrusive way. Integration of sensors for a specific purpose, such as a guaiac fecal occult blood test (gFOBT), microbiome, or biochemical analyses could enable early disease detection and long-term monitoring. Fecal tracking has been deployed extensively throughout the COVID-19 pandemic and large-scale waste monitoring can provide significant state level public health data for population modeling[206]. Thus, "smart toilets" are expected to have significant impacts on health monitoring research and public health planning.

Blood

Blood plasma is considered to be the main target of research for biomarker analysis with proteomics and lipidomics identifying tens of thousands of molecular species and thousands of potential biomarkers for a wide variety of diseases. Repeat, comprehensive analysis of an individual's blood metabolome is impractical for clinical applications, necessitating targeted testing. Additionally, blood sampling requires invasive procedures and is available in limited quantities. Finger pricks are tolerable however analyte concentrations will be very low. Large (mL volume) blood draws are currently used for "blood work" as a stopgap. Whole blood samples often further require separation steps, removing platelets and red blood cells to yield either plasma (with clotting factors) or serum (without clotting factors). It is preferential to avoid requiring a blood draw; however, alternative methods of biomarker acquisition may be impossible or impractical. Continuous blood and interstitial fluid monitoring has been demonstrated with implantable

devices,[207] with advances in biocompatible implant materials bringing such devices closer to routine clinical use. With implantable devices currently being mostly experimental, external molecular sensors could be deployed alongside other medical implants, such as pacemakers, or insulin pumps. Limiting the risks of infection and inflammation post-implant are still significant outstanding issues toward integration, in addition to challenges with wireless communication and regulations. Many implantable devices are classified as Class III devices by the FDA, necessitating a lengthy and stringent testing process to ensure reliability and safety. Implementation and integration of implantable devices into the clinical paradigm will require multidisciplinary collaboration to overcome the hurdles presented (**Figure 6.5**).

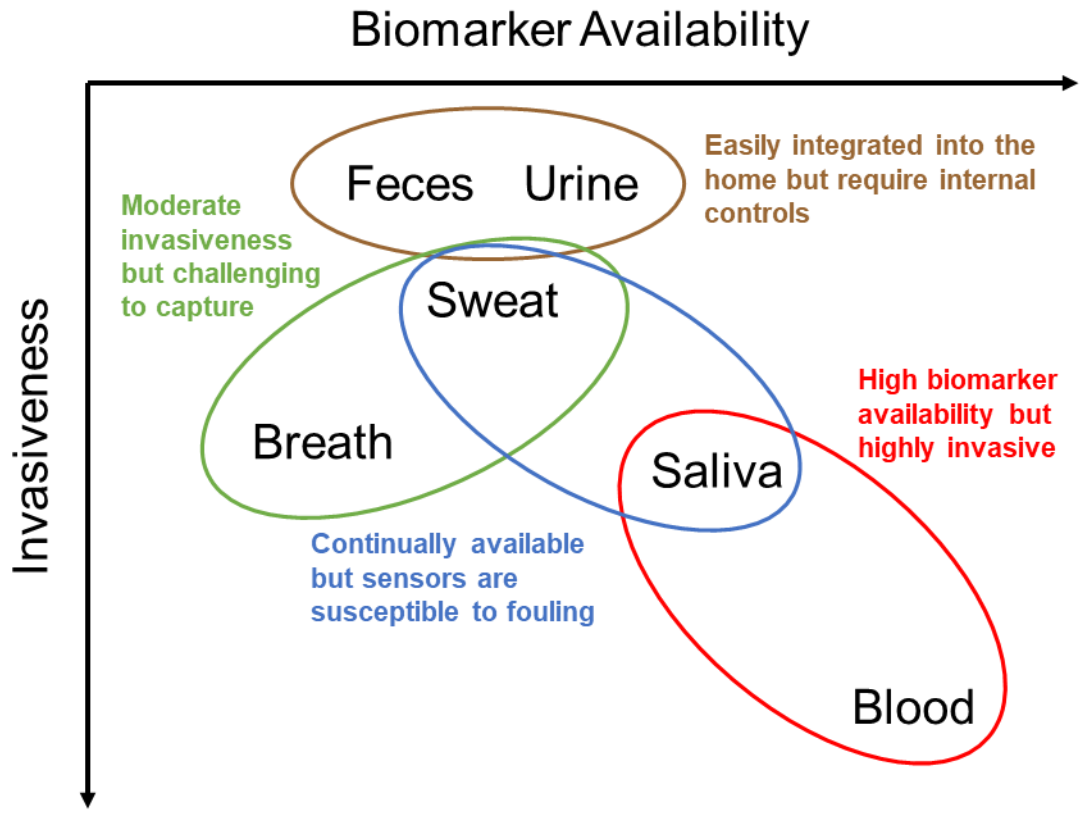

Figure 6.5. *Advantages and disadvantages of commonly assayed biofluids. Biomarker availability is plotted against invasiveness and time to biomarker expression. Where molecular imaging provides a snapshot of an individual's disease state, biomarkers found in feces, as an example, could provide more holistic analysis as they are generated and cleared on a longer time scale. Blood and breath then can provide more rapid feedback on acute injuries.*

Wearables

With the proliferation and miniaturization of cell phones and wearable devices, smart watches have become increasingly popular in the consumer market. Coupled with a growing societal focus on health, there is demand for additional personal health monitoring. However, many wearable devices available to consumers are only incorporating technology that has been available for decades. There have been marked improvements in miniaturization, ergonomics, and implementation, but the majority of the biosensors discussed herein have yet to be implemented for consumer, or even clinical use. As sensors, the usual considerations of sensitivity, selectivity, and feasibility apply, however, as long term, external, continuous sensors operating outside of a clinical environment they must also overcome environmental factors without fouling. Additionally, a bottleneck for future sensor implementation, particularly implantable sensors, is power supply. While modern batteries can last years, this limits the power draw of implantable sensors and thus their complexity. Both self-powered sensors and wireless charged sensors are in development to offer potential solutions to this challenge. Non-invasive sensors are preferred as they can be implemented with less risk of injury or side effects, and ultimately improve patient compliance.

Conclusions

Advances in molecular imaging have been a major driver toward changing clinical methods to better accommodate individual differences, personalizing medicine. This has prompted a recent push toward achieving precision health, shifting the clinical paradigm from reactive medicine to preventative medicine. To this end, molecular imaging is still generally limited to the clinical setting. By pairing molecular imaging with molecular sensing, design considerations and analyte recognition performance gleaned from imaging probes for validated biomarkers can be applied to the development of molecular monitoring devices and moved out of the clinical setting and into the home. Though still limited in consumer available implementations, improvements in wearable health technology, its increased use in our daily lives, and further integration with clinician available electronic health records will dramatically change how we diagnose, monitor, and treat disease. With earlier disease diagnoses, patient outcomes are improved, while societal and economic health burdens are lessened. Within clinical settings, molecular imaging integrated with molecular sensing could broaden our understanding of disease progression, generate data necessary to complete the human model, and create positive feedback loops toward identifying earlier biomarkers and better therapeutics.

References

1. Gambhir, S. S., Ge, T. J., Vermesh, O. & Spitler, R. Toward achieving precision health. Sci. Transl. Med. 10, (2018).
2. Gambhir, S. S., Ge, T. J., Vermesh, O., Spitler, R. & Gold, G. E. Continuous health monitoring: An opportunity for precision health. Sci. Transl. Med. 13, (2021).
3. Collins, F. S. & Varmus, H. A New Initiative on Precision Medicine. N. Engl. J. Med. 372, 793–795 (2015).
4. Wang, C. et al. Advanced Nanotechnology Leading the Way to Multimodal Imaging-Guided Precision Surgical Therapy. Adv. Mater. 31, 1904329 (2019).
5. Terris, M. Evolution of Public Health and Preventive Medicine in the United States. Am. J. Public Health 65, 161–169 (1975).
6. Mendelson, Y. Pulse Oximetry: Theory and Applications for Noninvasive Monitoring. Clin. Chem. 38, 1601–1607 (1992).
7. Bandodkar, A. J. & Wang, J. Non-invasive wearable electrochemical sensors: a review. Trends Biotechnol. 32, 363–371 (2014).
8. Scott, R. T. et al. Beyond Low Earth Orbit: Biomonitoring, Artificial Intelligence, and Precision Space Health.
9. Sokolov, A. N., Roberts, M. E. & Bao, Z. Fabrication of low-cost electronic biosensors. Mater. Today 12, 12–20 (2009).
10. Roberts, M. E., Sokolov, A. N. & Bao, Z. Material and device considerations for organic thin-film transistor sensors. J. Mater. Chem. 19, 3351–3363 (2009).
11. Kubota, R., Sasaki, Y., Minamiki, T. & Minami, T. Chemical Sensing Platforms Based on Organic Thin-Film Transistors Functionalized with Artificial Receptors. ACS Sensors 4, 2571–2587 (2019).
12. Wang, N., Yang, A., Fu, Y., Li, Y. & Yan, F. Functionalized Organic Thin Film Transistors for Biosensing. Acc. Chem. Res. (2019) doi:10.1021/acs.accounts.8b00448.
13. Girgis, A., Lambert, S., Johnson, C., Waller, A. & Currow, D. Physical, psychosocial, relationship, and economic burden of caring for people with cancer: A review. J. Oncol. Pract. 9, 197–202 (2013).
14. Sandbhor Gaikwad, P. & Banerjee, R. Advances in point-of-care diagnostic devices in cancers. Analyst vol. 143 1326–1348 (2018).
15. Rais-Bahrami, S. et al. Diagnostic value of biparametric magnetic resonance imaging (MRI) as an adjunct to prostate-specific antigen (PSA)-based detection of prostate cancer in men without prior biopsies. BJU Int. 115, 381–388 (2015).
16. Hambrock, T. et al. Magnetic Resonance Imaging Guided Prostate Biopsy in Men With Repeat Negative Biopsies and Increased Prostate Specific Antigen. J. Urol. 183, 520–528 (2010).
17. Kuhl, C. K. et al. Abbreviated biparametric prostate MR imaging in men with elevated prostate-specific antigen. Radiology 285, 493–505 (2017).
18. Turkbey, B. et al. Prostate cancer: Can multiparametric mr imaging help identify patients who are candidates for active surveillance? Radiology 268, 144–152 (2013).
19. Cimitan, M. et al. [18F]fluorocholine PET/CT imaging for the detection of recurrent prostate cancer at PSA relapse: Experience in 100 consecutive patients. Eur. J. Nucl. Med. Mol. Imaging 33, 1387–1398 (2006).
20. Sarkar, S. & Das, S. A Review of Imaging Methods for Prostate Cancer Detection. Biomed. Eng. Comput. Biol. 7, 1 (2016).

21. Fortuin, A., De Rooij, M., Zamecnik, P., Haberkorn, U. & Barentsz, J. Molecular and Functional Imaging for Detection of Lymph Node Metastases in Prostate Cancer. Int. J. Mol. Sci. 2013, Vol. 14, Pages 13842-13857 14, 13842–13857 (2013).
22. Zani, A., Laschi, S., Mascini , M. & Marrazza, G. A New Electrochemical Multiplexed Assay for PSA Cancer Marker Detection. Electroanalysis 23, 91–99 (2011).
23. Mani, V., Chikkaveeraiah, B. V., Patel, V., Gutkind, J. S. & Rusling, J. F. Ultrasensitive immunosensor for cancer biomarker proteins using gold nanoparticle film electrodes and multienzyme-particle amplification. ACS Nano 3, 585–594 (2009).
24. Yu, X. et al. Carbon nanotube amplification strategies for highly sensitive immunodetection of cancer biomarkers. J. Am. Chem. Soc. 128, 11199–11205 (2006).
25. Sardesai, N., Pan, S. & Rusling, J. Electrochemiluminescent immunosensor for detection of protein cancer biomarkers using carbon nanotube forests and [Ru-(bpy)3] 2+-doped silica nanoparticles. Chem. Commun. 0, 4968–4970 (2009).
26. Turkbey, B. et al. Multiparametric prostate magnetic resonance imaging in the evaluation of prostate cancer. CA. Cancer J. Clin. 66, 326–336 (2016).
27. Wang, T. D., Chen, Y. & Ronald, J. A. A novel approach for assessment of prostate cancer aggressiveness using survivin-driven tumour-activatable minicircles. Gene Ther. 2019 265 26, 177–186 (2019).
28. Hussain, T. et al. Surgical molecular navigation with ratiometric activatable cell penetrating peptide for intraoperative identification and resection of small salivary gland cancers. Head Neck 38, 715–723 (2016).
29. Johansson, G. et al. Monitoring circulating tumor-DNA during surgical treatment in patients with gastrointestinal stromal tumors. Mol. Cancer Ther. molcanther.0403.2021 (2021) doi:10.1158/1535-7163.MCT-21-0403.
30. Kinross, J. M., Holmes, E., Darzi, A. W. & Nicholson, J. K. Metabolic phenotyping for monitoring surgical patients. Lancet 377, 1817–1819 (2011).
31. Sobngwi, E. et al. Continuous interstitial glucose monitoring in non-diabetic subjects with end-stage renal disease undergoing maintenance haemodialysis. Diabetes Res. Clin. Pract. 90, 22–25 (2010).
32. Zelnick, L. R. et al. Continuous Glucose Monitoring and Use of Alternative Markers To Assess Glycemia in Chronic Kidney Disease. Diabetes Care 43, 2379–2387 (2020).
33. Block, C. D., Manuel-y-Keenoy, B., Rogiers, P., Jorens, P. & Gaal, L. Van. Glucose Control and Use of Continuous Glucose Monitoring in the Intensive Care Unit: A Critical Review. Curr. Diabetes Rev. 4, 234–244 (2008).
34. Butterfield, D. A. & Halliwell, B. Oxidative stress, dysfunctional glucose metabolism and Alzheimer disease. Nat. Rev. Neurosci. 2019 203 20, 148–160 (2019).
35. Peeks, F. et al. A retrospective in-depth analysis of continuous glucose monitoring datasets for patients with hepatic glycogen storage disease: Recommended outcome parameters for glucose management. J. Inherit. Metab. Dis. 44, 1136–1150 (2021).
36. Chuang, H. et al. Pilot studies of transdermal continuous glucose measurement in outpatient diabetic patients and in patients during and after cardiac surgery. J. Diabetes Sci. Technol. 2, 595–602 (2008).

37. Chetrit, M. et al. Imaging-Guided Therapies for Pericardial Diseases. JACC Cardiovasc. Imaging 13, 1422–1437 (2020).
38. Namikawa, T., Sato, T. & Hanazaki, K. Recent advances in near-infrared fluorescence-guided imaging surgery using indocyanine green. Surg. Today 2015 4512 45, 1467–1474 (2015).
39. Zghaib, T. et al. Standard Ablation Versus Magnetic Resonance Imaging–Guided Ablation in the Treatment of Ventricular Tachycardia. Circ. Arrhythmia Electrophysiol. 11, 5973 (2018).
40. Mauri, G. et al. Technical success, technique efficacy and complications of minimally-invasive imaging-guided percutaneous ablation procedures of breast cancer: A systematic review and meta-analysis. Eur. Radiol. 2016 278 27, 3199–3210 (2017).
41. Wilson, M. S. & Nie, W. Multiplex Measurement of Seven Tumor Markers Using an Electrochemical Protein Chip. Anal. Chem. 78, 6476–6483 (2006).
42. Wu, J. et al. Lab-on-a-chip platforms for detection of cardiovascular disease and cancer biomarkers. Sensors (Switzerland) vol. 17 2934 (2017).
43. Wu, A. M. & Olafsen, T. Antibodies for molecular imaging of cancer. Cancer J. 14, 191–197 (2008).
44. Warram, J. M. et al. Antibody-based imaging strategies for cancer. Cancer Metastasis Rev. 33, 809–822 (2014).
45. Qi, L. et al. Simultaneous Detection of Multiple Tumor Markers in Blood by Functional Liquid Crystal Sensors Assisted with Target-Induced Dissociation of Aptamer. Anal. Chem. 92, 3867–3873 (2020).
46. Yang, C. et al. Multiplexed and Amplified Electronic Sensor for the Detection of MicroRNAs from Cancer Cells. Anal. Chem. 86, 11913–11918 (2014).
47. Zeng, Z. et al. Specific and Sensitive Tumor Imaging Using Biostable Oligonucleotide Aptamer Probes. Theranostics 4, 945 (2014).
48. Chen, K. H. et al. c-erbB-2 sensing using AlGaN⁄GaN high electron mobility transistors for breast cancer detection. Appl. Phys. Lett. 92, 192103 (2008).
49. Goldenberg, D. M. & Nabi, H. A. Breast cancer imaging with radiolabeled antibodies. Semin. Nucl. Med. 29, 41–48 (1999).
50. Stipsanelli, E. & Valsamaki, P. Monoclonal antibodies: old and new trends in breast cancer imaging and therapeutic approach. Hell. J. Nucl. Med. 8, 103–108 (2005).
51. Li, X. et al. Detection of Circulating Tumor Cells in Breast Cancer Patients by Nanopore Sensing with Aptamer-Mediated Amplification. ACS Sensors 5, 2359–2366 (2020).
52. Liu, M. et al. An Aptamer-Based Probe for Molecular Subtyping of Breast Cancer. Theranostics 8, 5772 (2018).
53. Li, P., Zhang, B. & Cui, T. Towards intrinsic graphene biosensor: A label-free, suspended single crystalline graphene sensor for multiplex lung cancer tumor markers detection. Biosens. Bioelectron. 72, 168–174 (2015).
54. Roointan, A. et al. Early detection of lung cancer biomarkers through biosensor technology: A review. J. Pharm. Biomed. Anal. 164, 93–103 (2019).
55. Machac, J., Krynyckyi, B. & Kim, C. Peptide and antibody imaging in lung cancer. Semin. Nucl. Med. 32, 276–292 (2002).
56. Breitz, H. B., Sullivan, K. & Nelp, W. B. Imaging lung cancer with radiolabeled antibodies. Semin. Nucl. Med. 23, 127–132 (1993).
57. Huang, X. et al. CKAP4 Antibody-Conjugated Si Quantum Dot Micelles for Targeted Imaging of Lung Cancer.

Nanoscale Res. Lett. 16, 1–12 (2021).
58. Khatoon, Z. et al. Feasibility study of doped SnO2 nanomaterial for electronic nose towards sensing biomarkers of lung cancer. J. Mater. Sci. Mater. Electron. 31, 15751–15763 (2020).
59. Ambrosini, V. et al. PET/CT imaging in different types of lung cancer: An overview. Eur. J. Radiol. 81, 988–1001 (2012).
60. Mishra, S. et al. Tailored Biofunctionalized Biosensor for the Label-Free Sensing of Prostate-Specific Antigen. ACS Appl. Bio Mater. 2020, (2020).
61. Chen, S. et al. Microfluidic Device Directly Fabricated on Screen-Printed Electrodes for Ultrasensitive Electrochemical Sensing of PSA. Nanoscale Res. Lett. 14, 1–7 (2019).
62. Lerner, M. B. et al. Hybrids of a genetically engineered antibody and a carbon nanotube transistor for detection of prostate cancer biomarkers. ACS Nano 6, 5143–5149 (2012).
63. Bander, N. H. Technology Insight: monoclonal antibody imaging of prostate cancer. Nat. Clin. Pract. Urol. 2006 34 3, 216–225 (2006).
64. Wiehr, S. et al. Pharmacokinetics and PET imaging properties of two recombinant anti-PSMA antibody fragments in comparison to their parental antibody. Prostate 74, 743–755 (2014).
65. Savory, N., Abe, K., Sode, K. & Ikebukuro, K. Selection of DNA aptamer against prostate specific antigen using a genetic algorithm and application to sensing. Biosens. Bioelectron. 26, 1386–1391 (2010).
66. Zheng, G., Patolsky, F., Cui, Y., Wang, W. U. & Lieber, C. M. Multiplexed electrical detection of cancer markers with nanowire sensor arrays. Nat. Biotechnol. 2005 2310 23, 1294–1301 (2005).
67. Wang, A. Z. et al. Superparamagnetic Iron Oxide Nanoparticle–Aptamer Bioconjugates for Combined Prostate Cancer Imaging and Therapy. ChemMedChem 3, 1311 (2008).
68. Abbasy, L., Mohammadzadeh, A., Hasanzadeh, M. & Razmi, N. Development of a reliable bioanalytical method based on prostate specific antigen trapping on the cavity of molecular imprinted polymer towards sensing of PSA using binding affinity of PSA-MIP receptor: A novel biosensor. J. Pharm. Biomed. Anal. 188, 113447 (2020).
69. Sciarra, A. et al. Advances in Magnetic Resonance Imaging: How They Are Changing the Management of Prostate Cancer. Eur. Urol. 59, 962–977 (2011).
70. Altintas, Z., Fakanya, W. M. & Tothill, I. E. Cardiovascular disease detection using bio-sensing techniques. Talanta 128, 177–186 (2014).
71. Justino, C. I. L. et al. Disposable immunosensors for C-reactive protein based on carbon nanotubes field effect transistors. Talanta 108, 165–170 (2013).
72. Sanz, J. & Fayad, Z. A. Imaging of atherosclerotic cardiovascular disease. Nat. 2008 4517181 451, 953–957 (2008).
73. Willner, I. & Zayats, M. Electronic Aptamer-Based Sensors. Angew. Chemie Int. Ed. 46, 6408–6418 (2007).
74. Kumar, V. et al. Nanostructured aptamer-functionalized black phosphorus sensing platform for label-free detection of myoglobin, a cardiovascular disease biomarker. ACS Appl. Mater. Interfaces 8, 22860–22868 (2016).
75. Nakatsuka, M. A., Mattrey, R. F., Esener, S. C., Cha, J. N. & Goodwin, A. P. Aptamer-Crosslinked Microbubbles: Smart Contrast Agents for Thrombin-Activated

Ultrasound Imaging. Adv. Mater. 24, 6010–6016 (2012).
76. Gupta, S., Sharma, A. & Verma, R. S. Polymers in biosensor devices for cardiovascular applications. Curr. Opin. Biomed. Eng. 13, 69–75 (2020).
77. Sogbein, O. O. et al. New SPECT and PET radiopharmaceuticals for imaging cardiovascular disease. Biomed Res. Int. 2014, (2014).
78. Jaffer, F. A., Libby, P. & Weissleder, R. Molecular imaging of cardiovascular disease. Circulation 116, 1052–1061 (2007).
79. Kim, K., Lee, C. H. & Park, C. B. Chemical sensing platforms for detecting trace-level Alzheimer's core biomarkers. Chem. Soc. Rev. 49, 5446–5472 (2020).
80. Lien, T. T. N., Takamura, Y., Tamiya, E. & Vestergaard, M. C. Modified screen-printed electrode for development of a highly sensitive label-free impedimetric immunosensor to detect amyloid beta peptides. Anal. Chim. Acta 892, 69–76 (2015).
81. Kim, K. et al. Clinically accurate diagnosis of Alzheimer's disease via multiplexed sensing of core biomarkers in human plasma. Nat. Commun. 2020 111 11, 1–9 (2020).
82. Viola, K. L. et al. Towards non-invasive diagnostic imaging of early-stage Alzheimer's disease. Nat. Nanotechnol. 2014 101 10, 91–98 (2014).
83. van Dyck, C. H. Anti-Amyloid-β Monoclonal Antibodies for Alzheimer's Disease: Pitfalls and Promise. Biol. Psychiatry 83, 311–319 (2018).
84. Sehlin, D. et al. Antibody-based PET imaging of amyloid beta in mouse models of Alzheimer's disease. Nat. Commun. 2016 71 7, 1–11 (2016).
85. Reiman, E. M. & Jagust, W. J. Brain imaging in the study of Alzheimer's disease. Neuroimage 61, 505–516 (2012).
86. Kutovyi, Y. et al. Amyloid-beta peptide detection via aptamer-functionalized nanowire sensors exploiting single-trap phenomena. Biosens. Bioelectron. 154, 112053 (2020).
87. Farrar, C. T., William, C. M., Hudry, E., Hashimoto, T. & Hyman, B. T. RNA Aptamer Probes as Optical Imaging Agents for the Detection of Amyloid Plaques. PLoS One 9, e89901 (2014).
88. Qin, J., Kim, S., Cho, M. & Lee, Y. Hierarchical and ultra-sensitive amyloid beta oligomer sensor for practical applications. Chem. Eng. J. 401, 126055 (2020).
89. Choi, G. et al. Multifunctional imaging of amyloid-beta peptides with a new gadolinium-based contrast agent in Alzheimer's disease. J. Ind. Eng. Chem. 83, 214–223 (2020).
90. Nordberg, A. PET imaging of amyloid in Alzheimer's disease. Lancet Neurol. 3, 519–527 (2004).
91. Vlassenko, A. G., Benzinger, T. L. S. & Morris, J. C. PET amyloid-beta imaging in preclinical Alzheimer's disease. Biochim. Biophys. Acta - Mol. Basis Dis. 1822, 370–379 (2012).
92. Leuzy, A. et al. Biomarker-Based Prediction of Longitudinal Tau Positron Emission Tomography in Alzheimer Disease. JAMA Neurol. (2021) doi:10.1001/JAMANEUROL.2021.4654.
93. Tokuraku, K., Marquardt, M. & Ikezu, T. Real-Time Imaging and Quantification of Amyloid-β Peptide Aggregates by Novel Quantum-Dot Nanoprobes. PLoS One 4, e8492 (2009).
94. Liu, X. & Liu, J. Biosensors and sensors for dopamine detection. View 2, 20200102 (2021).
95. Liang, Y., Guo, T., Zhou, L., Offenhäusser, A. & Mayer, D. Label-Free Split Aptamer Sensor for Femtomolar Detection of Dopamine

by Means of Flexible Organic Electrochemical Transistors. Materials (Basel). 13, (2020).
96. McConnell, E. M. et al. In Vivo Use of a Multi-DNA Aptamer-Based Payload/Targeting System to Study Dopamine Dysregulation in the Central Nervous System. ACS Chem. Neurosci. 10, 371–383 (2019).
97. Badgaiyan, R. D. Imaging dopamine neurotransmission in live human brain. Prog. Brain Res. 211, 165 (2014).
98. Shen, L. H., Liao, M. H. & Tseng, Y. C. Recent Advances in Imaging of Dopaminergic Neurons for Evaluation of Neuropsychiatric Disorders. J. Biomed. Biotechnol. 2012, (2012).
99. Schatz, D. G. & Ji, Y. Recombination centres and the orchestration of V(D)J recombination. Nature Reviews Immunology vol. 11 251–263 (2011).
100. Harding, F. A., Stickler, M. M., Razo, J. & DuBridge, R. B. The immunogenicity of humanized and fully human antibodies: Residual immunogenicity resides in the CDR regions. MAbs 2, 256–265 (2010).
101. Xu, W., Wang, D., Li, D. & Liu, C. C. Recent Developments of Electrochemical and Optical Biosensors for Antibody Detection. Int. J. Mol. Sci. 2020, Vol. 21, Page 134 21, 134 (2019).
102. Casalini, S. et al. Multiscale sensing of antibody-antigen interactions by organic transistors and single-molecule force spectroscopy. ACS Nano 9, 5051–5062 (2015).
103. Wujcik, E. K. et al. Antibody nanosensors: a detailed review. RSC Adv. 4, 43725–43745 (2014).
104. Gao, S., Guisán, J. M. & Rocha-Martin, J. Oriented immobilization of antibodies onto sensing platforms - A critical review. Anal. Chim. Acta 1189, 338907 (2022).
105. Warram, J. M. et al. Antibody-based imaging strategies for cancer. Cancer Metastasis Rev. 33, 809–822 (2014).
106. Kaur, S. et al. Recent trends in antibody-based oncologic imaging. Cancer Lett. 315, 97–111 (2012).
107. Lee, M. et al. A novel biosensor based on hafnium oxide: Application for early-stage detection of human interleukin-10. Sensors Actuators, B Chem. 175, 201–207 (2012).
108. Mälarstig, A. et al. Raised interleukin-10 is an indicator of poor outcome and enhanced systemic inflammation in patients with acute coronary syndrome. Heart 94, 724–729 (2008).
109. Chen, Y. W., Liu, M., Kaneko, T. & McIntyre, P. C. Atomic layer deposited hafnium oxide gate dielectrics for charge-based biosensors. Electrochem. Solid-State Lett. 13, G29 (2010).
110. Xenaki, K. T., Oliveira, S. & van Bergen en Henegouwen, P. M. P. Antibody or Antibody Fragments: Implications for Molecular Imaging and Targeted Therapy of Solid Tumors. Front. Immunol. 0, 1287 (2017).
111. Freise, A. C. & Wu, A. M. In vivo imaging with antibodies and engineered fragments. Mol. Immunol. 67, 142–152 (2015).
112. Bates, A. & Power, C. A. David vs. Goliath: The Structure, Function, and Clinical Prospects of Antibody Fragments. Antibodies 2019, Vol. 8, Page 28 8, 28 (2019).
113. Hammock, M. L., Knopfmacher, O., Naab, B. D., Tok, J. B.-H. & Bao, Z. Investigation of Protein Detection Parameters Using Nanofunctionalized Organic Field-Effect Transistors. ACS Nano 7, 3970–3980 (2013).
114. Agarwal, D. K., Kandpal, M. & Surya, S. G. Characterization and detection of cardiac Troponin-T protein by using ‘aptamer’ mediated biofunctionalization of ZnO thin-film

transistor. Appl. Surf. Sci. 466, 874–881 (2019).
115. Liang, Y., Guo, T., Zhou, L., Offenhäusser, A. & Mayer, D. Label-free split aptamer sensor for femtomolar detection of dopamine by means of flexible organic electrochemical transistors. Materials (Basel). 13, (2020).
116. Kratschmer, C. & Levy, M. Effect of Chemical Modifications on Aptamer Stability in Serum. Nucleic Acid Ther. 27, 335 (2017).
117. Chen, H. et al. A review on electronic bio-sensing approaches based on non-antibody recognition elements. Analyst 141, 2335–2346 (2016).
118. Song, S., Wang, L., Li, J., Fan, C. & Zhao, J. Aptamer-based biosensors. TrAC Trends Anal. Chem. 27, 108–117 (2008).
119. Schoukroun-Barnes, L. R. et al. Reagentless, Structure-Switching, Electrochemical Aptamer-Based Sensors. http://dx.doi.org/10.1146/annurev-anchem-071015-041446 9, 163–181 (2016).
120. Harrad, L. El, Bourais, I., Mohammadi, H. & Amine, A. Recent advances in electrochemical biosensors based on enzyme inhibition for clinical and pharmaceutical applications. Sensors (Switzerland) 18, 164 (2018).
121. Magliulo, M. et al. Part per Trillion Label-Free Electronic Bioanalytical Detection. Anal. Chem. 85, 3849–3857 (2013).
122. Takao Someya, *,†,ǁ, Ananth Dodabalapur*, †,‡, Alan Gelperin, †, Howard E. Katz, *,† and & Bao†, Z. Integration and Response of Organic Electronics with Aqueous Microfluidics. Langmuir 18, 5299–5302 (2002).
123. Mabeck, J. T. & Malliaras, G. G. Chemical and biological sensors based on organic thin-film transistors. Anal. Bioanal. Chem. 2005 3842 384, 343–353 (2005).
124. Xin, N. et al. Concepts in the design and engineering of single-molecule electronic devices. Nat. Rev. Phys. 2019 13 1, 211–230 (2019).
125. Lin, M. et al. Electrochemical detection of nucleic acids, proteins, small molecules and cells using a DNA-nanostructure-based universal biosensing platform. Nat. Protoc. 2016 117 11, 1244–1263 (2016).
126. Yen, Y. K. & Chiu, C. Y. A CMOS MEMS-based Membrane-Bridge Nanomechanical Sensor for Small Molecule Detection. Sci. Reports 2020 101 10, 1–8 (2020).
127. Wang, X., Qin, L., Zhou, M., Lou, Z. & Wei, H. Nanozyme Sensor Arrays for Detecting Versatile Analytes from Small Molecules to Proteins and Cells. Anal. Chem. 90, 11696–11702 (2018).
128. Comeau, Z. J. et al. On-the-Spot Detection and Speciation of Cannabinoids Using Organic Thin-Film Transistors. ACS Sensors 4, 2706–2715 (2019).
129. Li, Z., Fang, M., LaGasse, M. K., Askim, J. R. & Suslick, K. S. Colorimetric Recognition of Aldehydes and Ketones. Angew. Chemie 129, 9992–9995 (2017).
130. Cagle, B. S., Crawford, R. A. & Doorn, J. A. Biogenic Aldehyde-Mediated Mechanisms of Toxicity in Neurodegenerative Disease. Curr. Opin. Toxicol. 13, 16 (2019).
131. Wang, W., Wang, C., Xu, H. & Gao, Y. Aldehyde dehydrogenase, liver disease and cancer. Int. J. Biol. Sci. 16, 921–934 (2020).
132. O'Brien, P., Siraki, A. & Shangari, N. Aldehyde Sources, Metabolism, Molecular Toxicity Mechanisms, and Possible Effects on Human Health. http://dx.doi.org/10.1080/10408440591002183 35, 609–662 (2008).
133. Alkedeh, O. & Priefer, R. The Ketogenic Diet: Breath Acetone

Sensing Technology. Biosensors 11, (2021).
134. Dang, T. et al. Hydrazo-CEST: Hydrazone-Dependent Chemical Exchange Saturation Transfer Magnetic Resonance Imaging Contrast Agents. Chem. - A Eur. J. 24, 9148–9156 (2018).
135. Sellmyer, M. A. et al. Imaging CAR T Cell Trafficking with eDHFR as a PET Reporter Gene. Mol. Ther. 28, 42–51 (2020).
136. Sgobbi, L. F., Razzino, C. A. & Machado, S. A. S. A disposable electrochemical sensor for simultaneous detection of sulfamethoxazole and trimethoprim antibiotics in urine based on multiwalled nanotubes decorated with Prussian blue nanocubes modified screen-printed electrode. Electrochim. Acta 191, 1010–1017 (2016).
137. Wang, T. D., Chen, Y. & Ronald, J. A. A novel approach for assessment of prostate cancer aggressiveness using survivin-driven tumour-activatable minicircles. Gene Ther. 2019 265 26, 177–186 (2019).
138. Robinson, E. R. et al. Minicircles for a two-step blood biomarker and PET imaging early cancer detection strategy. J. Control. Release 335, 281–289 (2021).
139. Ronald, J. A., Chuang, H. Y., Dragulescu-Andrasi, A., Horia, S. S. & Gambhira, S. S. Detecting cancers through tumor-activatable minicircles that lead to a detectable blood biomarker. Proc. Natl. Acad. Sci. U. S. A. 112, 3068–3073 (2015).
140. Dawson, J. et al. Xanthine oxidase inhibition for the improvement of long-term outcomes following ischaemic stroke and transient ischaemic attack (XILO-FIST) – Protocol for a randomised double blind placebo-controlled clinical trial. Eur. Stroke J. 3, 281–290 (2018).
141. Liu, D., Wang, D., Yang, W. & Meng, D. Potential anti-gout constituents as xanthine oxidase inhibitor from the fruits of Stauntonia brachyanthera. Bioorganic Med. Chem. 25, 3562–3566 (2017).
142. Patoulias, D. et al. Meta-Analysis Assessing the Effects of Allopurinol on Left Ventricular Mass and Other Indices of Left Ventricular Remodeling as Evaluated by Cardiac Magnetic Resonance Imaging. Am. J. Cardiol. 138, 129–132 (2021).
143. Hason, S. et al. Simultaneous electrochemical monitoring of metabolites related to the xanthine oxidase pathway using a grinded carbon electrode. Anal. Chem. 81, 4302–4307 (2009).
144. El Harrad, L. & Amine, A. Amperometric biosensor based on prussian blue and nafion modified screen-printed electrode for screening of potential xanthine oxidase inhibitors from medicinal plants. Enzyme Microb. Technol. 85, 57–63 (2016).
145. Arakawa, T. et al. Mouthguard biosensor with telemetry system for monitoring of saliva glucose: A novel cavitas sensor. Biosens. Bioelectron. 84, 106–111 (2016).
146. Li, Y. J. & Lu, C. C. A Novel Scheme and Evaluations on a Long-Term and Continuous Biosensor Platform Integrated with a Dental Implant Fixture and Its Prosthetic Abutment. Sensors 2015, Vol. 15, Pages 24961-24976 15, 24961–24976 (2015).
147. Mannoor, M. S. et al. Graphene-based wireless bacteria detection on tooth enamel. Nat. Commun. 2012 31 3, 1–9 (2012).
148. Gao, W. et al. Fully integrated wearable sensor arrays for multiplexed in situ perspiration analysis. Nature 529, 509–514 (2016).
149. Wang, C. et al. Monitoring of the central blood pressure waveform via a conformal ultrasonic device. Nat. Biomed. Eng. 2018 29 2, 687–695 (2018).

150. Rodelo, C. G. et al. Zinc associated nanomaterials and their intervention in emerging respiratory viruses: Journey to the field of biomedicine and biomaterials. Coord. Chem. Rev. 457, 214402 (2022).
151. Kim, S. J., Choi, S. J., Jang, J. S., Cho, H. J. & Kim, I. D. Innovative Nanosensor for Disease Diagnosis. Acc. Chem. Res. 50, 1587–1596 (2017).
152. Choi, S. J. et al. WO3 Nanofiber-Based Biomarker Detectors Enabled by Protein-Encapsulated Catalyst Self-Assembled on Polystyrene Colloid Templates. Small 12, 911–920 (2016).
153. Park, S. min et al. A mountable toilet system for personalized health monitoring via the analysis of excreta. Nat. Biomed. Eng. 2020 46 4, 624–635 (2020).
154. Miller, I. J. et al. Real-time health monitoring through urine metabolomics. npj Digit. Med. 2019 21 2, 1–9 (2019).
155. Choden, P., Seesaard, T., Dorji, U., Sriphrapradang, C. & Kerdcharoen, T. Urine odor detection by electronic nose for smart toilet application. ECTI-CON 2017 - 2017 14th Int. Conf. Electr. Eng. Comput. Telecommun. Inf. Technol. 190–193 (2017) doi:10.1109/ECTICON.2017.8096205.
156. Usman, F. et al. A Review of Biosensors for Non-Invasive Diabetes Monitoring and Screening in Human Exhaled Breath. IEEE Access 7, 5963–5974 (2019).
157. Risby, T. H. & Solga, S. F. Current status of clinical breath analysis. Appl. Phys. B Lasers Opt. 85, 421–426 (2006).
158. Sukul, P., Trefz, P., Kamysek, S., Schubert, J. K. & Miekisch, W. Instant effects of changing body positions on compositions of exhaled breath. J. Breath Res. 9, 047105 (2015).
159. Sterer, N. & Rosenberg, M. Origin, Diagnosis, and Management Breath Odors.
160. King, J. et al. Isoprene and acetone concentration profiles during exercise on an ergometer. J. Breath Res. 3, 027006 (2009).
161. Yuen, L. H., Saxena, N. S., Park, H. S., Weinberg, K. & Kool, E. T. Dark Hydrazone Fluorescence Labeling Agents Enable Imaging of Cellular Aldehydic Load. ACS Chem. Biol. 11, 2312–2319 (2016).
162. Dang, T. et al. Hydrazo-CEST: Hydrazone-Dependent Chemical Exchange Saturation Transfer Magnetic Resonance Imaging Contrast Agents. Chem. - A Eur. J. 24, 9148–9156 (2018).
163. Akam, E. A. et al. Improving the reactivity of hydrazine-bearing MRI probes for in vivo imaging of lung fibrogenesis. Chem. Sci. 11, 224–231 (2019).
164. Chen, H. H. et al. Molecular imaging of oxidized collagen quantifies pulmonary and hepatic fibrogenesis. JCI Insight 2, (2017).
165. Moon, H. G. et al. Hollow Pt-Functionalized SnO2 Hemipill Network Formation Using a Bacterial Skeleton for the Noninvasive Diagnosis of Diabetes. ACS Sensors 3, 661–669 (2018).
166. Salehi, S., Nikan, E., Khodadadi, A. A. & Mortazavi, Y. Highly sensitive carbon nanotubes-SnO2 nanocomposite sensor for acetone detection in diabetes mellitus breath. Sensors Actuators, B Chem. 205, 261–267 (2014).
167. Bajtarevic, A. et al. Noninvasive detection of lung cancer by analysis of exhaled breath. BMC Cancer 9, 348 (2009).
168. Herbig, J., Titzmann, T., Beauchamp, J., Kohl, I. & Hansel, A. Buffered end-tidal (BET) sampling - A novel method for real-time breath-gas analysis. J. Breath Res. 2, 37008 (2008).

169. Güntner, A. T. et al. Breath Sensors for Health Monitoring. ACS Sensors 4, 268–280 (2019).
170. Schiffman, J. D., Fisher, P. G. & Gibbs, P. Early Detection of Cancer: Past, Present, and Future. https://doi-org.proxy.bib.uottawa.ca/10.14694/EdBook_AM.2015.35.57 57–65 (2015) doi:10.14694/EDBOOK_AM.2015.35.57.
171. Kraniotou, C., Karadima, V., Bellos, G. & Tsangaris, G. T. Predictive biomarkers for type 2 of diabetes mellitus: Bridging the gap between systems research and personalized medicine. J. Proteomics 188, 59–62 (2018).
172. Wouters, O. J., O'Donoghue, D. J., Ritchie, J., Kanavos, P. G. & Narva, A. S. Early chronic kidney disease: diagnosis, management and models of care. Nat. Rev. Nephrol. 2015 118 11, 491–502 (2015).
173. Chiappin, S., Antonelli, G., Gatti, R. & De Palo, E. F. Saliva specimen: A new laboratory tool for diagnostic and basic investigation. Clinica Chimica Acta vol. 383 30–40 (2007).
174. Chicharro, J. L., Lucía, A., Pérez, M., Vaquero, A. F. & Ureña, R. Saliva composition and exercise. Sports Medicine vol. 26 17–27 (1998).
175. Malon, R. S. P., Sadir, S., Balakrishnan, M. & Córcoles, E. P. Saliva-Based Biosensors: Noninvasive Monitoring Tool for Clinical Diagnostics. BioMed Research International vol. 2014 (2014).
176. Kalk, W. W. I. et al. Sialometry and sialochemistry: A non-invasive approach for diagnosing Sjögren's syndrome. Ann. Rheum. Dis. 61, 137–144 (2002).
177. Aluoch, A. O., Sadik, O. A. & Bedi, G. Development of an oral biosensor for salivary amylase using a monodispersed silver for signal amplification. Anal. Biochem. 340, 136–144 (2005).
178. Kwan, R. C. H. et al. Amperometric biosensor for determining human salivary phosphate. Anal. Biochem. 343, 263–267 (2005).
179. Yamaguchi, M. et al. Non-invasive monitoring of gingival crevicular fluid for estimation of blood glucose level. Med. Biol. Eng. Comput. 42, 322–327 (2004).
180. Guilbault, G. G., Palleschi, G. & Lubrano, G. Non-invasive biosensors in clinical analysis. Biosens. Bioelectron. 10, 379–392 (1995).
181. Ballesta Claver, J., Valencia Mirón, M. C. & Capitán-Vallvey, L. F. Disposable electrochemiluminescent biosensor for lactate determination in saliva. Analyst 134, 1423–1432 (2009).
182. Palleschi, G., Faridnia, M. H., Lubrano, G. J. & Guilbault, G. G. Determination of lactate in human saliva with an electrochemical enzyme probe. Anal. Chim. Acta 245, 151–157 (1991).
183. Piechotta, G., Albers, J. & Hintsche, R. Novel micromachined silicon sensor for continuous glucose monitoring. Biosens. Bioelectron. 21, 802–808 (2005).
184. Valdés-Ramírez, G. et al. Non-invasive mouthguard biosensor for continuous salivary monitoring of metabolites. Analyst 139, 1632–1636 (2014).
185. Zheng, C.-M., Lu, K.-C., Wu, C.-C., Hsu, Y.-H. & Lin, Y.-F. Association of Serum Phosphate and Related Factors in ESRD-Related Vascular Calcification. Int. J. Nephrol. 2011, 1–8 (2011).
186. Shetty, V., Zigler, C., Robles, T. F., Elashoff, D. & Yamaguchi, M. Developmental validation of a point-of-care, salivary α-amylase biosensor. Psychoneuroendocrinology 36, 193–199 (2011).
187. Kalman, D. S. et al. Effect of a proprietary Magnolia and Phellodendron extract on stress

levels in healthy women: A pilot, double-blind, placebo-controlled clinical trial. Nutr. J. 7, 1–6 (2008).
188. Sun, K., Ramgir, N. & Bhansali, S. An immunoelectrochemical sensor for salivary cortisol measurement. Sensors Actuators, B Chem. 133, 533–537 (2008).
189. Dhull, N., Kaur, G., Gupta, V. & Tomar, M. Highly sensitive and non-invasive electrochemical immunosensor for salivary cortisol detection. Sensors Actuators, B Chem. 293, 281–288 (2019).
190. Mitchell, J. S. & Lowe, T. E. Ultrasensitive detection of testosterone using conjugate linker technology in a nanoparticle-enhanced surface plasmon resonance biosensor. Biosens. Bioelectron. 24, 2177–2183 (2009).
191. Aydın, M., Aydın, E. B. & Sezgintürk, M. K. A highly selective electrochemical immunosensor based on conductive carbon black and star PGMA polymer composite material for IL-8 biomarker detection in human serum and saliva. Biosens. Bioelectron. 117, 720–728 (2018).
192. Sánchez-Tirado, E. et al. Electrochemical immunosensor for simultaneous determination of interleukin-1 beta and tumor necrosis factor alpha in serum and saliva using dual screen printed electrodes modified with functionalized double–walled carbon nanotubes. Anal. Chim. Acta 959, 66–73 (2017).
193. Choudhary, M. et al. CD 59 Targeted Ultrasensitive Electrochemical Immunosensor for Fast and Noninvasive Diagnosis of Oral Cancer. Electroanalysis 28, 2565–2574 (2016).
194. Sánchez-Tirado, E., González-Cortés, A., Yáñez-Sedeño, P. & Pingarrón, J. M. Electrochemical immunosensor for the determination of the cytokine interferon gamma (IFN-γ) in saliva. Talanta 211, 120761 (2020).
195. Fabiani, L. et al. Magnetic beads combined with carbon black-based screen-printed electrodes for COVID-19: A reliable and miniaturized electrochemical immunosensor for SARS-CoV-2 detection in saliva. Biosens. Bioelectron. 171, 112686 (2021).
196. Essentials of Exercise Physiology - William D. McArdle, Frank I. Katch, Victor L. Katch - Google Books. https://books.google.ca/books?hl=en&lr=&id=L4aZIDbmV3oC&oi=fnd&pg=PA1&ots=WonZs6Bn4P&sig=WOhrlAUZ0QtTt2w3JSzIPqp1xnQ&redir_esc=y#v=onepage&q&f=false.
197. Montain, S. J., Cheuvront, S. N. & Lukaski, H. C. Sweat mineral-element responses during 7 h of exercise-heat stress. Int. J. Sport Nutr. Exerc. Metab. 17, 574–582 (2007).
198. Briganti, S. et al. Application of Sebum Lipidomics to Biomarkers Discovery in Neurodegenerative Diseases. Metab. 2021, Vol. 11, Page 819 11, 819 (2021).
199. Sinclair, E. et al. Metabolomics of sebum reveals lipid dysregulation in Parkinson's disease. Nat. Commun. 2021 121 12, 1–9 (2021).
200. Chung, M., Fortunato, G. & Radacsi, N. Wearable flexible sweat sensors for healthcare monitoring: A review. Journal of the Royal Society Interface vol. 16 (2019).
201. Kim, J., Campbell, A. S., de Ávila, B. E. F. & Wang, J. Wearable biosensors for healthcare monitoring. Nature Biotechnology vol. 37 389–406 (2019).
202. Kwong, G. A. et al. Mass-encoded synthetic biomarkers for multiplexed urinary monitoring of disease. Nat. Biotechnol. 31, 63 (2013).
203. Gadalla, A. A. H. et al. Identification of clinical and urine biomarkers for uncomplicated urinary tract infection using machine learning algorithms. Sci. Reports 2019 91 9, 1–11 (2019).

204. Grayson, K., Gregory, E., Khan, G. & Guinn, B.-A. Urine Biomarkers for the Early Detection of Ovarian Cancer – Are We There Yet? https://doi.org/10.1177/1179299X19830977 11, 1179299X1983097 (2019).
205. Koyner, J. L. et al. Urinary Biomarkers in the Clinical Prognosis and Early Detection of Acute Kidney Injury. Clin. J. Am. Soc. Nephrol. 5, 2154 (2010).
206. Jin, K. et al. Intensive Monitoring of Urine Output Is Associated with Increased Detection of Acute Kidney Injury and Improved Outcomes. Chest 152, 972–979 (2017).
207. Lachance, P. et al. Association between e-alert implementation for detection of acute kidney injury and outcomes: a systematic review. Nephrol. Dial. Transplant. 32, 265–272 (2017).
208. Park, S. min, Ge, T. J., Won, D. D., Lee, J. K. & Liao, J. C. Digital biomarkers in human excreta. Nat. Rev. Gastroenterol. Hepatol. 18, (2021).
209. Farkas, K., Hillary, L. S., Malham, S. K., McDonald, J. E. & Jones, D. L. Wastewater and public health: the potential of wastewater surveillance for monitoring COVID-19. Curr. Opin. Environ. Sci. Heal. 17, 14–20 (2020).
210. Arroyo-Currás, N. et al. Real-time measurement of small molecules directly in awake, ambulatory animals. Proc. Natl. Acad. Sci. 114, 645–650 (2017).

Chapter 7: Additional, Ongoing, and Future Work

Summary of Contributions

The development and implementation of OTFT sensors is a promising area of research with a variety of broad applications environmental and health sensing. Pc-OTFTs represent a highly tunable sensor platform with high versatility and applicability. In this thesis, Pc-based OTFT sensing and chemotyping of cannabinoids is established and explored to elucidate a mechanism by which the sensing responses are achieved, hopefully providing a guide for future Pc-OTFT biosensing applications.

In **Chapter 2**, sensing, and differentiating cannabinoids with Pc-OTFTs is reported for the first time. In combination with a cannabinoid sensitive colorimetric probe, large changes to mobility and voltage threshold were observed with CuPc and F_{16}-CuPc OTFTs were exposed to cannabinoids. By generating standard curves, ratios of THC to CBD were able to be determined electronically from a rapidly extracted liquid plant sample with HPLC accuracy. Vapor phase sensing was also explored, and cannabinoids were able to be differentiated from other potentially interfering vaporized compounds. This study highlighted the potential utility, sensitivity, and selectivity of Pc-OTFT sensors, but opened questions regarding the mechanism by which the sensing responses were achieved.

In **Chapter 3**, a spectroelectrochemical set-up and procedure was devised and used to assay molecular interactions between cannabinoids, Pcs, and the colorimetric probe to gain further insights into the observed OTFT sensing responses. Strong interactions between Pcs and cannabinoids were observed, with 2D-NMR revealing specific sites of coordination. By relating spectroelectrochemical changes to electrical changes in the OTFT characterization data it was demonstrated that spectroelectrochemistry could be used as a rapid screening tool for Pc sensors.

In **Chapter 4**, the effects of analytes on thin-film morphology and polymorphs were explored and a relationship between analyte-Pc electrochemical interactions, physical changes to thin-film morphology, and the resulting electrical OTFT data was established. Additionally, EPR revealed the formation of long-lived Pc radical species when exposed to analytes, corroborating some of the spectroelectrochemical phenomenon observed, and further demonstrating the strength of the electrochemical interactions.

Building on the previous works, in **Chapter 5**, OTFTs with ZnPc or CuPc with varying degrees of peripheral fluorination were screened against THC, such that the most sensitive material, unsubstituted ZnPc, was selected for further sensor optimization. By tuning the thin-film morphology, polymorph, and thickness a ppb level sensitivity was achieved. Real-time sensing demonstrated a two-part sensor response, with an initial, immediate phase attributed to electrochemical interactions and a slower phase, attributed to slower, physical recrystallization effects.

The additional projects I have initiated or contributed to, detailed further in this chapter, can be generally subdivided as those pertaining to phthalocyanine thin-films or electrochemical characterization of other small organic compounds. The former studies were focused on either analyte or annealing induced changes to thin-film morphology while the latter were focused on determining electrochemical mechanisms of redox processes. As extensions of the techniques developed and studied throughout the cannabinoid sensing projects, I hope they highlight the versatility therein, and offer inspiration for methods of modifying and characterizing other thin-film biosensor devices.

Ultimately, this thesis contains the first reports of an OTFT cannabinoid sensor. In particular, the efforts to understand the sensing mechanisms and improve sensor responses represents a significant contribution to the field of OTFT sensors and Pc thin-film engineering. Spectroelectrochemical characterization of both Pcs and other small molecules involved in sensing or electrochemical processes is a technique with high utility for understanding charge transfer properties. Thin-film engineering has broad applicability and I hope that in doing so I have laid the groundwork for many exciting biosensing applications with Pc-OTFTs.

Thin-Film Engineering of Solution-Processable n-Type Silicon Phthalocyanines for Organic Thin-Film Transistors

Rosemary R. Cranston, Mário C. Vebber, Jônatas Faleiro Berbigier, Nicole A. Rice, Claire Tonnelé, **Zachary J. Comeau**, Nicholas T. Boileau, Jaclyn L. Brusso, Adam J. Shuhendler, Frédéric Castet, Luca Muccioli, Timothy L. Kelly, and Benoît H. Lessard.

ACS Applied Materials and Interfaces, **2021**, 12, 1, 1008-1020

Abstract

Metal and metalloid phthalocyanines are an abundant and established class of materials widely used in the dye and pigment industry as well as in commercial photoreceptors. Silicon phthalocyanines (SiPcs) are among the highest-performing n-type semiconductor materials in this family when used in organic thin-film transistors (OTFTs) as their performance and solid-state arrangement are often increased through axial substitution. Herein, we study eight axially substituted SiPcs and their integration into solution-processed n-type OTFTs. Electrical characterization of the OTFTs, combined with atomic force microscopy (AFM), determined that the length of the alkyl chain affects device performance and thin-film morphology. The effects of high-temperature annealing and spin coating time on film formation, two key processing steps for fabrication of OTFTs, were investigated by grazing-incidence wide-angle X-ray scattering (GIWAXS) and X-ray diffraction (XRD) to elucidate the relationship between thin-film microstructure and device performance. Thermal annealing was shown to change both film crystallinity and SiPc molecular orientation relative to the substrate surface. Spin time affected film crystallinity, morphology, and interplanar d-spacing, thus ultimately modifying device performance. Of the eight materials studied, bis(tri-*n*-butylsilyl oxide) SiPc exhibited the greatest electron field-effect mobility (0.028 $cm^2\ V^{-1}\ s^{-1}$, a threshold voltage of 17.6 V) of all reported solution-processed SiPc derivatives.

Contribution

For this study I assisted in preparing substrates for OTFT characterization, assisted with, and performed XRD characterization, as well as data analysis and editing.

Transition Metal Heteropolynuclear Complexes as Super-atomic MRI Redox Rulers

Alexandros A. Kitos, Raúl Castañeda, **Zachary J. Comeau**, Niki Mavragani, Alexia Kirby, Nick D. Calvert, Paco Martinez, Benoit H. Lessard, Timothy J. Scholl, Muralee Murugesu, Adam J. Shuhendler, Jaclyn L. Brusso.

Submitted manuscript under review

Abstract

Transition metal molecular clusters hold great promise as MRI probes due to their enhanced tunability in size, shape and total spin state given the collection of metal ions can act as a single entity; however, a key challenge limiting the application of polynuclear clusters as MRI contrast agents remains, namely the molecular engineering of super-atomic contrast agents that oppose dissociation/speciation in biological media. To resolve this challenge, the N-2-pyrimidylimidoyl-2-pyrimidylamidine chelate was employed to selectively bind 3d metal ions to form highly stable mixed metal clusters. Advantageously, the sensitivity of valence electron configurations of 3d metal complexes to their microenvironment allows for the rational design of smart contrast agents capable of reporting a variety of biochemical changes. Through spectroscopic, electrochemical and magnetic analysis along with in vitro and in vivo studies, the data presented support the application of iron and manganese homo- and heterometallic triskelion-shaped complexes as MRI contrast agents capable of mapping tumor redox status through a simple T_{1w}/T_{2w} ratiometric approach. The contrast agent design strategy presented here introduces heteropolynuclear transition metal super-atomic complexes suitable for semi-quantitative in vivo MR imaging of tissue redox status and opens up new avenues for non-invasive characterization of the tumor environment by MRI.

Contribution

For this study, I performed spectral and electrochemical characterization of the potential contrast agents, comparing the effects of electrochemical potentials to the effects of reducing agents with various redox potentials. Additionally, I analyzed the spectroelectrochemical data against MRI phantom data to assist in determining a mechanism governing the redox mediated MRI contrast effects, writing those sections of the manuscript.

Context

Magnetic resonance imaging (MRI) is a key technique in the clinical umbrella, as, when paired with a contrast agent (CA), MRI can provide non-invasive molecular imaging of disease pathogenesis. Currently however, all commercially available MRI contrast agents, nine in use in

the USA and six available within the European Union, utilize Gd^{III}-based complexes with linear or macrocyclic ligands (GBCAs). Unfortunately, it has been identified that Gd can cause severe nephrogenic systemic fibrosis (NSF), particularly in people with impaired kidney function. To address this, there has been considerable research towards non-Gd based contrast agents that can offer safer, and more biocompatible, alternatives. Other transition metal complexes, particularly Mn, are promising candidates thanks to their inherent biocompatibility, capability to enhance nuclear relaxation, and high thermodynamic stability. Some molecular clusters have shown promising results; however, they are hampered by low aqueous solubility. N-2-pyrimidylimidoyl-2-pyrimidylamidine (Pm_2ImAm) chelates enable the controlled binding of first row transition metals as mono-, di-, tri-, tetra-, and hexanuclear homometallic systems, facilitating strategic ligand architectures. Areas with a high level of cellular metabolism, particularly tumors and cancerous growth, often have higher concentrations of redox species as a byproduct. Thus, detecting *in vivo* regions of high redox activity can allow tumor mapping. In this study, $MnMn_3$ and $FeMn_3$ were found to provide redox microenvironment sensitive MRI contrast both *in vitro* as well as *in vivo*, and a mechanism was determined with spectroscopic and electrochemical characterization on $MnMn_3$, $FeMn_3$, and $FeZn_3$.

Examining the electrochemical, spectroscopic, and T_1w/T_2w MRI properties of $FeMn_3$, $MnMn_3$, and $FeZn_3$ in aqueous redox environments revealed that the outer Mn is necessary to provide MRI contrast. Additionally, while the inner metal does not directly coordinate with water to provide contrast, there is strong intramolecular signaling between the central and peripheral metals, whereby the identity of the central metal mediates the contrast effects observed. Exposing each CA to known concentrations of redox agents demonstrated, in combination with cyclic voltammetry, that $FeMn_3$ had greater sensitivity to reducing environments while $MnMn_3$ had greater sensitivity to oxidizing environments. Building on this principle, we generated a redox ruler for each compound, which was used observe redox-driven alterations to MRI contrast *in vivo*, allowing mapping of tumor redox microenvironments. These CAs were additionally demonstrated to have both high stability and low cell toxicity, marking them as an exciting development towards generating non-Gd CAs. In the context of this thesis, this study demonstrates the power and utility of spectroelectrochemical characterization to elucidate molecular mechanisms of charge transport and redox processes.

Chloro Aluminum Phthalocyanine-based Organic Thin-Film Transistors as Cannabinoid Sensors: Engineering the thin film response

Halynne R. Lamontagne, **Zachary J. Comeau**, Rosemary R. Cranston, Nicholas T. Boileau, Cory S. Harris, Adam J. Shuhendler and Benoît H. Lessard.

*Sensors and Diagnostics, **2022**, Advance Article, DOI: 10.1039/d2sd00071g*

Abstract

Cannabis producers, retailers, and law enforcement increasingly need low-cost point-of-source cannabinoid sensors. Organic thin-film transistor (OTFT) based sensors are a promising technology that can provide rapid speciation and detection of Δ^9-tetrahydrocannabinol (THC) while maintaining low manufacturing costs and ease of use. Herein, chloro aluminum phthalocyanine (Cl-AlPc) OTFTs were optimized through engineering film thickness (30, 50 or 100 nm) and the device source-drain geometry (W/L = 100, 200, 400, 800 and 1000), as these parameters have been shown to strongly influence OTFT performance. Optimized Cl-AlPc OTFT based sensors were exposed to both THC liquid and THC vapor, demonstrating that improved device performance was not directly correlated with increased sensitivity. Grazing-incidence wide-angle X-ray scattering (GIWAXS) and atomic force microscopy (AFM) were used to interrogate thin-film morphology. While little change in molecular orientation resulted from film thickness or exposure to THC, the data suggest that the improved sensing response of Cl-AlPc-derived devices is directly related to increased thin-film surface area resulting from increased roughness and reduced film thickness.

Contribution

Building on the data in **Chapters 3** and **4,** where AlClPc demonstrated strong interactions with cannabinoids, I instructed and assisted an undergraduate, now PhD student, in designing and carrying out a study on the effects of device architecture and thin-film thickness on sensing response.

Context

In this study, AlClPc OTFTs were optimized by changing the source-drain electrode configuration and the OSC thin-film thickness. It was found that increasing semiconducting channel W/L improved peak mobility and I_{on}, however, it led to a higher V_T, and an increase in defect density suggesting an increase in channel resistance. Additionally, the 30 nm films demonstrated improved charge transport characteristics compared to the thicker films, but again, with lower peak mobility and I_{on}. AFM imaging and GIWAXS analysis revealed that the 30 nm films had improved grain ordering. Greater surface roughness for the 50 nm films suggests that

under these deposition conditions, AlClPc thin films undergoes mixed growth modes, forming islands first, up to approximately 50 nm in thickness, whereupon subsequently deposited material fills in the gaps, leaving a smoother film with more charge transport pathways, but lower molecular order. These findings, in conjunction with the findings of **Chapter 5**, serve to illustrate the importance of not only deposition conditions on thin-film morphology, but also the potential effects of film thickness.

When exposed to THC in solution, W/L did not have an effect on the sensor response, however, the thinner films displayed higher sensitivity. No changes in molecular orientation were observed for the 30 and 100 nm films, but slight changes in molecular orientation were observed for the 50 nm films. For the 50 nm films this did not lead to significant changes in OTFT performance compared to the other thicknesses. When exposed to THC vapor, W/L appeared to have a slight effect, with the largest channel size exhibiting slightly larger changes in transfer characteristics. This suggests that the total amount of analyte captured within the channel is related to the sensing response instead of the relevant amount of analyte capture. Additionally, the thinnest films were once again the most sensitive. No changes in thin-film morphology were observed with THC vapor exposure. Thus, we established that thin-film thickness can affect thin-film morphology as well as sensitivity to analytes however within the scope of this study we were unable to extract the two parameters. In a broader context, I trained a new student on OTFT manufacture as well as the techniques and sensing protocols I established for our group such that she can continue work for other biosensing applications.

Arrays of functionalized graphene field-effect transistors for selective sensing of volatile organic compounds

Natalia Alzate-Carvajal, Jaewoo Park, Ranjana Rautela, **Zachary J. Comeau**, Lukas Scarfe, Jean-Michel Ménard, Seth B. Darling, Benoît Lessard, Adina Luican-Mayer.

Submitted manuscript under review.

Abstract

Real-time detection of volatile organic compounds (VOCs) is being spotlighted for its importance in environmental monitoring and disease detection from breath. However, the selective detection of VOCs in a small form factor gas sensor remains a challenge. Here, we present the VOC sensing performance of phthalocyanine (Pc) functionalized graphene field-effect transistors (FETs) supported by the theoretical prediction of Pc's VOC interactions. Pc functionalization, with and without metalation, was studied parametrically with varying deposition parameters to explore impacts on gas sensing response toward VOCs as a function of substrate coverage. Sensing data were collected to establish fingerprint signatures for a variety of VOCs. Improvement in selectivity is shown by successfully differentiating the VOCs from each other when combined into a gas sensor array tested with acetone, ethanol, formaldehyde, and toluene.

Contribution and Context

For this study I deposited Pc thin-films to functionalize graphene FETs and performed XRD measurements and analysis to confirm thin-film morphology. A combination of metal-free and copper Pc functionalized FETs was found to provide selectivity to a variety of VOC analytes.

Magnetic annealing for improved phthalocyanine organic thin-film transistors

Zachary J. Comeau, Rosemary R. Cranston, Halynne Lamontagne, Adam J. Shuhendler, Benoit H. Lessard

Manuscript in progress

Abstract

Thin-film microstructure, morphology, and polymorphism can be controlled and optimized to facilitate charge transport and improve overall performance of carbon-based printed and flexible electronics. Thermal or solvent vapor annealing are common post-deposition processing techniques; however, they can be difficult to control or destructive to the active layer or substrates. Here, we demonstrate the use of a static, strong magnetic field (SMF) as a non-destructive process for the improvement of phthalocyanine (Pc) thin-film microstructure, increasing organic thin-film transistor (OTFTs) mobility by two-fold. Grazing incident wide angle X-ray scattering (GIWAXS), X-ray diffraction (XRD), and atomic force microscopy (AFM) elucidate the effect of SMF on both para- and diamagnetic Pc thin-films when subjected to a magnetic field parallel or perpendicular to the substrate, in both air and nitrogen environments. A SMF is found to increase the concentration of oxygen induced radical species within the Pc thin-film, lending a paramagnetic character to ordinarily diamagnetic metal-free Pc, and resulting in magnetic field induced changes to its thin-film microstructures. In an ambient air environment, the SMF processing reduces the effects of oxygen degradation, and in a nitrogen environment, without the competing degradation effects of molecular oxygen, SMF processing was found to favorably improve charge transport characteristics and increase OTFT mobility. For the materials studied, post-deposition thermal annealing was found to have a negative effect on the thin-film properties for charge transport, reducing XRD peak intensity and lowering peak OTFT mobility. Thus, we present post-deposition thin-film annealing with a magnetic field as an alternative and promising technique for future thin-film engineering applications.

Contribution

I conceived of and performed all experiments for this study with the exception of GIWAXS characterization. R.R.C. and H.L. performed GIWAXS experiments, assisted with data analysis, and aided in authorship of the manuscript.

Context

The effects of a magnetic field on Pc thin film deposition have been characterized, however there is limited literature on the effects of a strong magnetic field on Pc thin-film microstructure and crystallinity post-deposition. During deposition, it has been demonstrated that a SMF can align Pc molecules providing favorable charge transport conditions. Thus, as a non-destructive technique in comparison to thermal annealing, magnetic field annealing could be potentially useful to align grain structures in some materials to optimize charge transport.

For this study, I examined the effects of a SMF that was applied post-deposition of ZnPc, CuPc, and H_2Pc, perpendicular and parallel relative to the substrate surface for 24h, comparing to the effects of thermal annealing at 220ºC for 20 minutes. When a strong magnetic field (SMF) is applied parallel to the substrate, GIWAXS alterations to the thin-film microstructures are observed for the each of the materials studied. However, when a SMF is applied perpendicular to the substrate no changes are observed. GIWAXS observed microstructural changes to H_2Pc, an ordinarily diamagnetic Pc, suggested some secondary effect that was sensitizing the H_2Pc to the magnetic field.

EPR was used to observe an increase in the concentration of radical species within an H_2Pc sample in the presence of oxygen. As molecular oxygen, and potentially other environmental gases, diffuse into the Pc thin films, they induce the formation of radical anionic species within the film. These radical anions are known to facilitate p-type charge transport and are stabilized across the Pc macrocycle, causing slight deformations in molecular structure. Notably, these radial anions confer paramagnetism to diamagnetic Pcs, which we hypothesize renders them susceptible to magnetic fields. Furthermore, SMFs are described to alter the reaction kinetics of radical species, slowing down reaction processes that require a change in spin states, increasing the concentration and duration of radical species.

OTFTs characterized in air demonstrated expected oxygen degradation effects that were somewhat mitigated by exposure to a parallel SMF. H_2Pc devices showed no response when SMF annealed under nitrogen and characterized, corroborating the EPR experiments. Notably, CuPc OTFTs exposed to a parallel SMF and characterized under nitrogen, without the competing effects of oxygen degradation, demonstrated a two-fold increase in mobility. In comparison to the thermally annealed OTFT samples which showed decreases in OTFT performance, this demonstrated that SMF annealing could have significant utility as a non-destructive annealing technique.

Ongoing and Future Projects

Magnetoelectrochemical Mechanism for Redox Sensitivity of TEMPO-based Probes

Oxidanyl, more commonly known as TEMPO, is a heterocyclic compound with a stable aminoxyl radical that is both MRI active and redox sensitive. As previously mentioned, due to potential toxicity, there is a drive towards generating non-Gd CAs for MRI imaging and thus, TEMPO based MRI probes are then an attractive alternative for MRI contrast enhancement without the use of metal chelates. While a radical, TEMPO displays MRI contrast activity, however, it loses activity once reduced and thus, when conjugated with a molecular targeting agent, can provide redox sensitive MRI contrast.

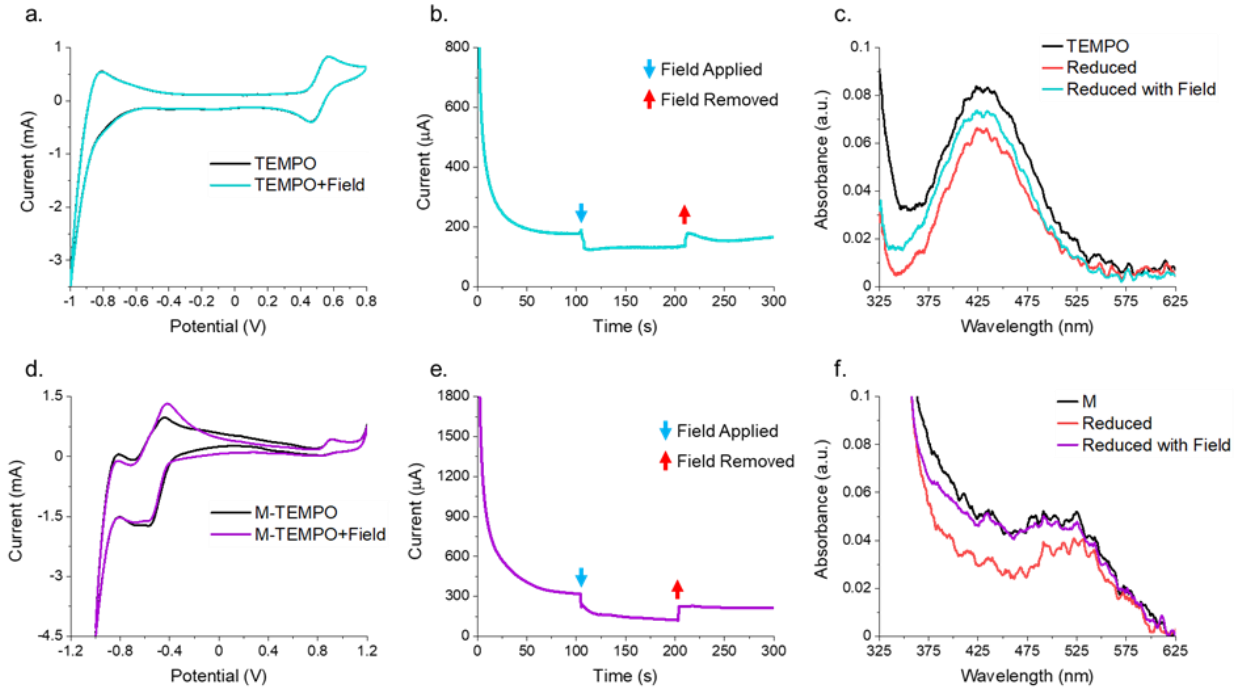

Figure 7.1. *Cyclic voltammograms, chronopotentiometry, and spectroelectrochemistry of TEMPO and TEMPO-based MRI probe in the presence of a strong magnetic field.*

During MRI phantom experiments, it was observed that TEMPO, and TEMPO-based probes, maintained longer contrast activity in the presence of a field. Examining this phenomenon with magnetoelectrochemistry, I observed sharp decreases in measured current with an applied magnetic field and a fixed reducing bias. When the field was removed there was a similarly sharp recovery. That current sharply decreases suggests this is not a result of magnetohydrodynamics altering the size of the diffusion layer, where we would expect to see a current increase, but rather a mechanistic change in the redox behavior of TEMPO. Magnetospectroelectrochemical characterization demonstrates smaller changes in spectral characteristics over time,

corroborating that in the presence of a magnetic field the redox mechanisms of TEMPO are altered. This is in agreement with theoretical mechanisms of biological radical activity and further suggests that the TEMPO reduction mechanism requires a change in electron spin states. As TEMPO is a popular moiety for MRI probes these results have significance and could potentially point to avenues to prolong the contrast activity of TEMPO-based MRI probes once *in vivo*. Finally, these results pose some interesting questions about *in vivo* ROS and chronic exposure to magnetic fields which could warrant further investigation.

Gravity Annealing of Phthalocyanine Thin-Films

While examining the effects of cannabinoids on thin-film morphology and polymorphs as detailed in **Chapters 4 and 5**, I became interested in other post deposition techniques to control and manipulate thin-film crystallinity. Thermal post-deposition annealing is perhaps the most common method and is widely used by our group in Pc OTFT fabrication, however, it can be destructive, or, in some cases, result in an unwanted, poorly semiconducting, polymorph. An alternative, solvent vapor annealing (SVA), can facilitate much larger changes to thin-film morphology and polymorphs (as demonstrated in **Chapters 4 and 5** where SVA with toluene was used to transition as deposited α-Pc films to β-Pc films). However, SVA necessitates the introduction of solvent into the thin-film microstructures, which must be subsequently removed before OTFT characterization, and can be destructive to substituted Pcs. Thus, I sought out alternative non-destructive methods for controllable post-deposition annealing of Pc thin films.

A colleague presented some interesting data on the effects of spin time for spin coating, demonstrating that longer spin times could result in different thin-film morphologies which I was curious to investigate in already deposited thin-films. An examination of the literature showed that the effects microgravity on thin-film structure during Pc deposition have been characterized and, in some cases, revealed the formation of new polymorphs. However, the effects of a strong gravitational force for post deposition annealing of Pc thin films has not been well demonstrated. Building custom centrifuge holders, I was able to control the direction of gravitational force through the film as either perpendicular, parallel, or at an angle to the film. Preliminary examination by AFM and XRD demonstrated potential effects, with the appearance of an alignment in the thin-film microstructures for AlClPc when exposed to 5000x g at an angle of 30°, which correlated to an increase in XRD peak intensity (**Figure 7.2**). Under the same conditions, spinning a co-evaporated mix of CuPc/CoPc demonstrated, by AFM, a flattening of the thin-film microstructure, resulting in a loss of XRD peak intensity. For both AlClPc and the co-evaporated Pcs, XRD and GIWAXS measurements both demonstrated no changes in thin-film polymorphism.

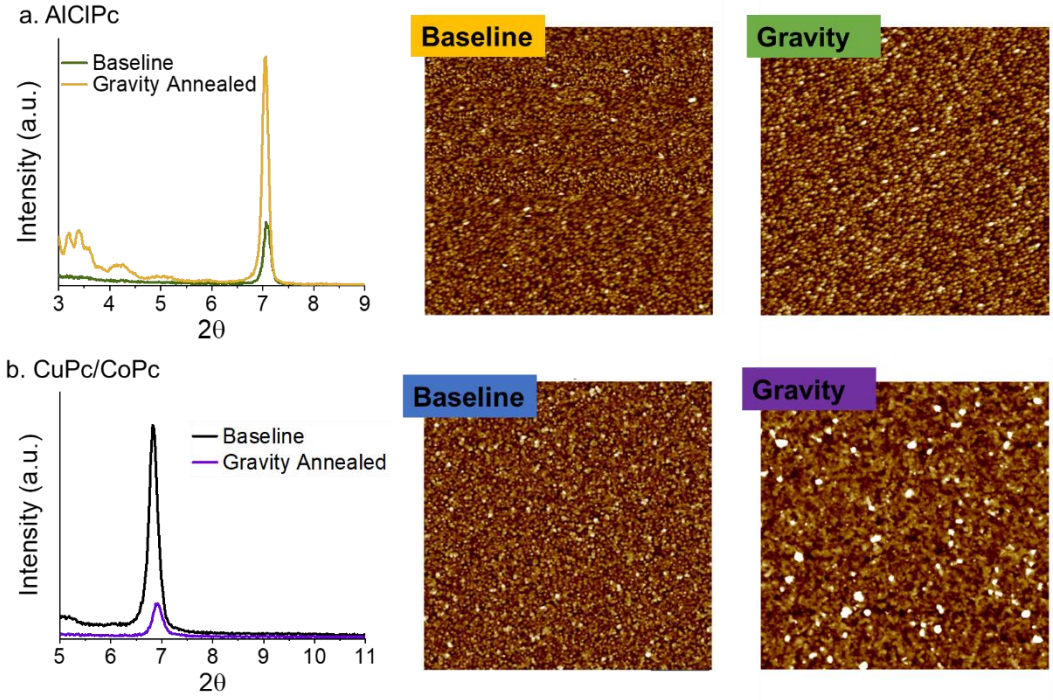

Figure 7.2. *Effects of high gravity on Pc thin films. (a) AlClPc and (b) co-evaporated CuPc/CoPc thin films were spun at 5000x g for 210 minutes in a fixed rotor centrifuge where the force of gravity was at a 30º angle to the substrate.*

As a preliminary study, the use of gravity as a non-destructive process to align thin-film microstructures, and the different effects between planar and cone-like Pcs, showed interesting results that could warrant further investigation. Effects of varying forces and spin time could be two first variables to assay, however, further characterization of material effects, or the effects of the dielectric surface and the relative energetics to the Pc-film could also be of interest. The ultimate step would be relating alterations to the thin-film microstructure to OTFT performance, such that specific gravitational conditions can be used to improve OTFT performance, perhaps by aligning grain microstructures with the electrode macrostructures.

Molecular Tuning of Axial X-AlPcs for Biosensing

As a continuation of AlClPc THC sensing, a colleague in training and I performed preliminary examinations of sensing murine biofluids with AlClPc OTFTs. We examined saliva, urine, fecal matter, and various phases of blood to determine what biofluids may be compatible with rapid OTFT sensing. Unfortunately, all biofluids, with the exception of fecal matter rendered OTFTs inoperable as a rapid test, demonstrating the necessity of a preliminary liquid-liquid extraction. Fecal matter, extracted with hexanes, demonstrated promising OTFT responses, and we were able to differentiate a natural extraction from an extraction spiked with THC. These were

promising preliminary results that open the door to future biosensing applications. The second phase of this project is novel substitutions to the axial position of the Al to tune sensing response. This is currently ongoing with Ph-AlPc demonstrating, for the first time, functional OTFTs with a peak mobility of μ = ~0.2 cm^2/Vs. The ultimate goal of this project is to generate a number of novel substituted X-AlPcs which can be screened against a range of analytes through spectroelectrochemistry, before tuning the deposition properties to optimize thin-film sensitivity.

Positron Detection with Pc-Based OTFTs

As highly conjugated aromatic molecules, it has been suggested that Pcs can be sensitive to radiation exposure and Pc-based dosimeters have been demonstrated. While dosimetry is both useful and necessary for many applications, numerous, more sensitive, dosimeters are already implemented for radiation monitoring throughout industry. Positron emission tomography (PET) is an imaging technique whereby a series of detectors register coincident gamma rays that result from positron annihilation produced by a radiotracer, such that the site of emission to be computationally determined, allowing visualization of the location of emission. Presently, PET detectors often use scintillation crystals in combination with photomultiplier tubes which are limited both in size and dead-time which in turn limits resolution and count-rate performance. Pc-based OTFTs, were they to be sensitive to positrons, could then be an order of magnitude smaller than current detectors, increasing PET resolution, and more numerous, allowing higher rate counts. Pc-based OTFTs for PET could then also carry their low-cost and high throughput fabrication advantages, dramatically reducing the cost of a PET detector. Thus, it was deemed worthwhile to investigate Pc-based OTFTs for PET.

As a preliminary study, I exposed ZnPc, CoPc, AlClPc, F_{16}-CuPc, H_2Pc, and CuPc OTFTs to a gamma emitter and observed changes in the transfer characteristics post exposure. For CuPc, ZnPc, and AlClPc there was a slight p-doping effect, similar to that previously reported. CoPc and F_{16}-CuPc demonstrated deterioration with exposure and H_2Pc demonstrated negligible changes. A substituted SnPc, found to degrade with exposure to light, was analyzed by GIWAXS, demonstrating polymorph changes post radiation exposure. These were promising preliminary results, so I carried out experiments similar to those of **Chapter 5**, where constant biases were maintained, and OTFT operating current was monitored over time while devices were exposed to ionizing radiation. Unfortunately, the results were inconsistent, possibly due to the ad-hoc nature of the experiment. Future experiments will be conducted with increased control over the position of the radio-source relative to the electrode channel such that we can also confirm emission events as a positive control.

Copyright Permissions

Chapter 2:

Reprinted with permissions from:

> **On-the-Spot Detection and Speciation of Cannabinoids Using Organic Thin-Film Transistors.** Zachary J. Comeau, Nicholas T. Boileau, Tiah Lee, Owen A. Melville, Nicole A. Rice, Yen Troung, Cory S. Harris, Benoît H. Lessard, and Adam J. Shuhendler. *ACS Sensors* **2019** 4 (10), 2706-2715. DOI: 10.1021/acssensors.9b01150.

Copyright 2019 American Chemical Society.

Chapter 3:

Reprinted with permissions from:

> **Engineering Cannabinoid Sensors through Solution-Based Screening of Phthalocyanines.** Zachary J. Comeau, Glenn A. Facey, Cory S. Harris, Adam J. Shuhendler, and Benoît H. Lessard. *ACS Applied Materials & Interfaces* **2020** 12 (45), 50692-50702. DOI: 10.1021/acsami.0c17146

Copyright 2020 American Chemical Society.

Chapter 4:

Reprinted with permissions from:

> **Organic Thin-Film Transistors as Cannabinoid Sensors: Effect of Analytes on Phthalocyanine Film Crystallization.** Zachary J. Comeau, Nicole A. Rice, Cory S. Harris, Adam J. Shuhendler, Benoît H. Lessard. *Adv. Funct. Mater.*, **2022**, 32, 2107138. DOI: 10.1002/adfm.202107138

Copyright 2022 Wiley Online Library.

Chapter 5:

Currently unpublished work

Chapter 6:

Reprinted with permissions from:

> Comeau, Z.J., Lessard, B.H. & Shuhendler, A.J. **The Need to Pair Molecular Monitoring Devices with Molecular Imaging to Personalize Health.** Mol Imaging Biol (2022). DOI: 10.1007/s11307-022-01714-4

Copyright 2022 Springer Nature.